



**US Army Corps
of Engineers®**
Engineer Research and
Development Center

Waves, Currents, and Sediment Transport in the Surf Zone along Long, Straight Beaches

Yoshimitsu Tajima and Ole S. Madsen

August 2005

Waves, Currents, and Sediment Transport in the Surf Zone along Long, Straight Beaches

Yoshimitsu Tajima and Ole S. Madsen

*Massachusetts Institute of Technology
Department of Civil Engineering
Cambridge, MA 02139*

Final report

Approved for public release; distribution is unlimited

Prepared for Coastal and Hydraulics Laboratory
U.S. Army Engineer Research and Development Center
3909 Halls Ferry Road, Vicksburg, MS 39180-6199

ABSTRACT:

This study presents a theoretical model for predictions of nearshore hydrodynamic characteristics and the local sediment transport rate along long, straight beaches. The wave may be periodic or random, the beach may be plane or barred, and the bed may be concrete or covered with movable natural sand grains. The present model must be efficient and flexible so that it can accommodate iterative computations for time-varying and, hence, arbitrary beach profiles.

The nearshore hydrodynamics model consists of wave, surface roller, and nearshore current models. Both wave and surface roller models are based on simple energy balance equations and, based on these models, the nearshore current is determined from two-layer 2DH momentum equations. Coupled with a simple turbulent eddy viscosity model, vertical profiles of mean shear current are analytically obtained. The model accounts for advective interactions between waves, surface rollers, and currents and, coupled with the surface roller model, explain the shoreward shift of the peak longshore current velocity. The model applies a modified version of Madsen's (1994) wave-current bottom boundary layer model to specify the bottom boundary condition from knowledge of equivalent bottom roughness scaled by a sediment diameter.

Introducing the predicted nearshore hydrodynamic characteristics, we extend the conceptual bedload and associated suspended load sediment transport models (Madsen 2001) to the surf zone. The extended sediment transport model accounts for breaking wave effects such as an increase of turbulence due to broken waves and change of the momentum force balances due to breaking waves and surface rollers. The model predicted the peaks of longshore sediment transport observed near the shoreline and the wave breaking point for plunging breakers.

DISCLAIMER: The contents of this report are not to be used for advertising, publication, or promotional purposes. Citation of trade names does not constitute an official endorsement or approval of the use of such commercial products. All product names and trademarks cited are the property of their respective owners. The findings of this report are not to be construed as an official Department of the Army position unless so designated by other authorized documents.

Waves, Currents, and Sediment Transport in the Surf Zone along Long, Straight Beaches

by

Yoshimitsu Tajima

Submitted to the Department of Civil and Environmental Engineering
on February 3rd, 2004, in partial fulfillment of the
requirements for the degree of
Doctor of Philosophy in Civil and Environmental Engineering

Abstract

This study presents a theoretical model for predictions of nearshore hydrodynamic characteristics and the local sediment transport rate along long, straight beaches. The wave may be periodic or random, the beach may be plane or barred, and the bed may be concrete or covered with movable natural sand grains. The present model must be efficient and flexible so that it can accommodate iterative computations for time-varying and, hence, arbitrary beach profiles.

The nearshore hydrodynamics model consists of wave, surface roller, and nearshore current models. Both wave and surface roller models are based on simple energy balance equations and, based on these models, the nearshore current is determined from two-layer 2DH momentum equations. Coupled with a simple turbulent eddy viscosity model, vertical profiles of mean shear current are analytically obtained. The model accounts for advective interactions between waves, surface rollers, and currents and, coupled with the surface roller model, explain the shoreward shift of the peak longshore current velocity. The model applies a modified version of Madsen's (1994) wave-current bottom boundary layer model to specify the bottom boundary condition from knowledge of equivalent bottom roughness scaled by a sediment diameter.

Introducing the predicted nearshore hydrodynamic characteristics, we extend the conceptual bedload and associated suspended load sediment transport models (Madsen 2001) to the surf zone. The extended sediment transport model accounts for breaking wave effects such as an increase of turbulence due to broken waves and change of the momentum force balances due to breaking waves and surface rollers. The model predicted the peaks of longshore sediment transport observed near the shore line and the wave breaking point for plunging breakers.

Thesis Supervisor: Ole S. Madsen

Title: Professor, Department of Civil and Environmental Engineering

Preface

This study was funded by Headquarters, U.S. Army Corps of Engineers, under Contract No. DACA42-01-C-0017, through the “Advanced Nearshore Circulation and Sediment Transport” and “Large-Scale Laboratory Investigation of Longshore Sediment Transport” Work Units of the Navigation Systems Research Program. The research was conducted under the general supervision of Mr. Thomas Richardson, Director, Coastal and Hydraulics Laboratory (CHL); Dr. William D. Martin, Deputy Director, CHL; Mr. Bruce Ebersole, Chief, Flood and Storm Protection Division; Mr. Ty Wamsley, Chief, Coastal Processes Branch; Dr. Sandra Knight, Technical Director, Navigation Systems Research Program; and Mr. James Clausner, Program Manager, Navigation Systems Research Program.

This report is a dissertation by Dr. Yoshimitsu Tajima in partial fulfillment of the requirements for the degree of Doctor of Philosophy from the Massachusetts Institute of Technology, Cambridge, MA. Dr. Ole S. Madsen served as advisor to Dr. Tajima.

The authors would like to thank Dr. Heidi M. Nepf, MIT, and Dr. John H. Trowbridge, Woods Hole Oceanographic Institution, for evaluation of the study and review of the dissertation, and Dr. Chiang C. Mei, MIT, for fruitful discussions on the topic. Messrs. Ebersole and Ernest R. Smith, CHL, and Dr. Jane M. Smith, CHL, are acknowledged for their assistance with providing data for the study. Dr. Tajima sincerely thanks Penta-Ocean Construction Co., Ltd., particularly Dr. Takuzo Shimizu and Dr. Tsunehiro Sekimoto, for their support.

At the time of publication of this report, Dr. James R. Houston was Director of ERDC, and COL James R. Rowan, EN, was Commander and Executive Director.

Contents

1	Introduction	31
1.1	General Remarks	31
1.2	Thesis Outline	35
2	Wave Model	37
2.1	Non-Linear Wave Model	39
2.1.1	Equivalent Linear Wave	39
2.1.2	Numerical Experiments	40
2.1.3	Non-Linear Wave Parameters	43
2.1.4	Reconstruction of the Non-Linear Near-Bottom Wave Orbital Velocity Profile	45
2.2	Breaking Wave Model	48
2.2.1	Model Concept	49
2.2.2	Modeling Fitting Function	49
2.2.3	Experimental Data	51
2.2.4	Complete Breaking Criteria	53
2.3	Broken Waves	57
2.3.1	Determination of K_b	58
2.3.2	Evaluation of γ_s and γ_r	59
2.4	Model Application	60
2.4.1	H_* is Known	61
2.4.2	H_* is Unknown	61
2.5	Extension of the Model to Random Waves	62

2.6	Comparison with Experimental Results	63
2.6.1	Wave Heights and Wave Set-up	63
2.6.2	Slope-Dependency of the Wave Attenuation	68
2.6.3	Non-linear Velocity Parameters	68
2.6.4	Non-Linear Near-Bottom Wave Orbital Velocity Profiles	73
2.7	Summary and Conclusions	77
3	Surface Roller Model	81
3.1	Model Development	83
3.1.1	Volume Flux and Depth-Averaged Return Flow Velocity	84
3.1.2	Momentum Flux	84
3.1.3	Energy Balance Equation for Surface Roller	85
3.1.4	Determination of K_{sr} and Physical Implications	87
3.2	Extension of the Model to Random Waves	89
3.3	Numerical Application of the Model	90
3.4	Test of the Model	90
3.5	Summary and Further Implications	96
4	Nearshore current model	101
4.1	Introduction	101
4.2	Wave Model	105
4.2.1	Volume Flux and Momentum Forcings	106
4.2.2	Model Extension to Random Waves	107
4.3	Surface Roller Model	107
4.3.1	Volume Fluxes and Momentum Forcings	108
4.4	Near-Shore Mean Current Model	109
4.4.1	Governing Equation	110
4.4.2	Turbulent Eddy Viscosity Model	111
4.4.3	Bottom Boundary Condition	114
4.4.4	Solution for Mean Current Profiles	115
4.4.5	Integrated Momentum Equations	117

4.5	Model Test	120
4.5.1	Undertow Velocity Profiles	120
4.5.2	Longshore Current Profiles	131
4.6	Effect of Bottom Roughness	142
4.6.1	Fixed Bed (“Known” Roughness Case)	147
4.6.2	Comparison with Longuet-Higgins’ (1970) Model	150
4.6.3	Movable Bed Bottom Roughness	153
4.6.4	Model Application to LSTF Movable Bed Experiments	163
4.7	Summary and Conclusions	166
5	Sediment Transport Model	175
5.1	Introduction	175
5.2	Bedload Sediment Transport	176
5.2.1	Sediment Transport Roughness and Shear Stress	177
5.2.2	Net Bedload Sediment Transport Rate	180
5.3	Suspended Sediment Transport	180
5.3.1	Further Simplifications	181
5.4	Mean Concentration Distribution	182
5.4.1	Turbulent Eddy Diffusivity.	182
5.4.2	Bottom Boundary Condition	183
5.4.3	Mean Concentration Profiles	188
5.4.4	Mean Longshore Suspended Sediment Transport	188
5.5	Grain Size Effect on Suspended Sediment	191
5.6	Model Application to LSTF Experiments	192
5.6.1	Sediment Characteristics	193
5.6.2	Bedload Sediment Transport	197
5.6.3	Suspended Sediment Transport	210
5.6.4	Total Sediment Transport	228
5.7	Summary and Conclusion	243
6	Summary and Concluding Remarks	245

A	Derivation of Expressions for Trough and Bottom Shear Stress	253
A.1	Pressure Force	253
A.2	Some simplifications	254
A.3	Mean Pressure	256
A.4	Trough Shear Stress	258
A.5	Momentum forces due to surface roller	259
A.6	Mean vertical momentum flux at trough level	260
A.7	Mean Trough Shear Stress	261
A.8	Mean Bottom Shear Stress	261
A.9	Simplifications for Depth-Integrated Momentum Equations	263
B	Model Application for Numerical Computations	265
B.1	Waves and Surface Rollers	265
B.1.1	Effective Bottom Slope	266
B.2	Nearshore Mean Current	268
B.2.1	Boundary Conditions	270
C	Predictions of Ripple Geometry	273
C.1	Introduction	273
C.2	Existing Models	274
C.3	Model Comparisons	279
D	Estimation of Skin Friction Shear Stress under Combined Wave and Current Fields	289

List of Figures

2-1	Concept of the equivalent linear wave.	40
2-2	Geometrical conditions for the numerical experiment.	42
2-3	Non-linear characteristics of near-bottom wave orbital velocity and definitions of non-linear wave parameters, T_c , $T_{c'}$, u_{c*} , and U_{b*}	44
2-4	Non-linear wave characteristics parameters, H_*/H and U_{b*}/U_b as functions of H_0/L_0 , h/L_0 with $\tan \beta_0 = 1/35$; simulations (full line) and fitting formulae (dotted line).	45
2-5	Non-linear wave characteristics parameters, $T_{c'}/T$, T_c/T and u_{c*}/U_{b*} as functions of H_0/L_0 , h/L_0 with $\tan \beta_0 = 1/35$; simulations (full line) and fitting formulae (dotted line).	46
2-6	Modeling for reconstructions of the non-linear near-bottom wave orbital velocity profile	47
2-7	$kH_b/\tanh kh_b$ vs. h_b/L_0 (experimental data)	52
2-8	Comparisons of the present model and measurements of breaking wave parameter, $kH_b/\tanh kh_b$ as functions of h_b/L_0 and $\tan \beta_0$; Present index (full line), Watanabe et al.'s (1984) index (dotted line) and measurements on various slopes (circles, triangles, and diamonds)	54
2-9	Comparisons of the present model and measurements of relative breaking water depth, h_b/H_0 as functions of H_0/L_0 and $\tan \beta_0$; Present index (full line), Watanabe et al.'s (1984) index (dotted line) and measurements on various slopes (circles, triangles, and diamonds)	55
2-10	Relative errors of breaking water depth, h_b , between model and data as functions of H_0/L_0 and $\tan \beta_0$	56

2-11	Comparisons of H_{b*}/h_b as functions relative breaking water depth, h_b/L_0 , and the bottom slope, β_0 , predicted by Goda's (1970) model and the present model; Present model (full line) and Goda's (1970) model (dotted line and circles).	57
2-12	γ_s vs. $\tan \beta$; experiments (circles) and Eq.(2.25) (full line)	60
2-13	Comparison of measured and predicted wave heights and wave set-up (Cox and Kobayashi, 1996); measurements (circles), predicted non-linear wave heights (full line), and predicted equivalent linear wave heights (dotted line).	64
2-14	Comparison of measured and predicted significant wave heights and wave set-up (Okayasu and Katayama, 1992); measurements (circles) and predictions (full line).	65
2-15	Comparison of measured and predicted significant wave heights and wave set-up (Wang et al., 2002, spilling breaker); measurements (circles) and predictions (full line).	66
2-16	Comparison of measured and predicted significant wave heights and wave set-up (Wang et al., 2002, plunging breaker); measurements (circles) and predictions (full line).	67
2-17	Comparisons of predicted (full line) and measured wave heights on uniform slopes. Measurements were reported by Mizuguchi et al. (1978), Okayasu and Katayama (1992), Cox and Kobayashi (1996), and Stive and Wind (1986) for $\tan \beta_0 = \partial h_0 / \partial x = 1/10, 1/20, 1/35$, and $1/40$	69
2-18	Measured and predicted non-linear wave characteristics of near-bottom orbital velocity profiles. (Cox and Kobayashi, 1996); measurements (circles) and predictions (full line)	70
2-19	Comparisons of measured and predicted wave heights, H_* , near-bottom wave orbital velocity height, U_{b*} , asymmetry, T_c/T , and skewness, u_{c*}/U_{b*} , for periodic waves on plane 1 on 30 sloping beach. Measurements by Hamilton and Ebersole (2001): Test 6A-N	72

2-20	Comparisons of measured and predicted wave heights, H_* , near-bottom wave orbital velocity height, U_{b*} , asymmetry, T_c/T , and skewness, u_{c*}/U_{b*} , for random waves on plane 1 on 30 sloping beach. Measurements by Hamilton and Ebersole (2001): Test 8A-E	74
2-21	Comparisons of measured and predicted wave heights, H_* , near-bottom wave orbital velocity height, U_{b*} , asymmetry, T_c/T , and skewness, u_{c*}/U_{b*} , for random waves on movable bed beach. Measurements by Wang et al. (2002): Test 1, spilling breaker.	75
2-22	Comparisons of measured and predicted wave heights, H_* , near-bottom wave orbital velocity height, U_{b*} , asymmetry, T_c/T , and skewness, u_{c*}/U_{b*} , for random waves on movable bed beach. Measurements by Wang et al. (2002): Test 3, plunging breaker.	76
2-23	Comparisons of measured (dashed lines) and predicted (full lines) near-bottom wave orbital velocity profiles for periodic waves on plane 1 on 35 sloping beach. Measurements by Cox and Koabayshi (1996) (at stations 1, 2, and 3).	78
2-24	Comparisons of measured (dashed lines) and predicted (full lines) near-bottom wave orbital velocity profiles for periodic waves on plane 1 on 35 sloping beach. Measurements by Cox and Koabayshi (1996) (at stations 4, 5, and 6).	79
3-1	Sketch of the surface roller	83
3-2	Comparisons of measured and predicted non-dimensional volume flux with periodic waves incident on uniform slopes. Resources of the experimental data were the same referred in Figure 2-17, i.e. by Mizuguchi et al. (1978), Okayasu and Katayama (1992), Cox and Kobayashi (1996), and Stive and Wind (1986) for $\tan \beta_0 = \partial h_0 / \partial x = 1/10, 1/20, 1/35$, and $1/40$; Present Model (full line) and Dally and Brown's Model (dashed line).	88

3-3	Comparisons of measured and predicted wave heights, wave set-up, and depth-averaged undertow velocity for periodic waves on plane 1 on 35 sloping beach. Measurements by Cox and Kobayashi (1996) (circles); Predictions with surface roller (full line) and without (dashed line).	92
3-4	Comparisons of measured and predicted wave heights, H_* , wave set-up, $\bar{\eta}$, and depth-averaged return flow velocity, $-\bar{U}$, for periodic waves obliquely incident on plane 1 on 30 sloping beach. Measurements (Test 6A-N) Hamilton and Ebersole (2001) (circles); Predictions with surface roller (full line) and without (dashed line).	93
3-5	Comparisons of measured and predicted wave heights, wave set-up, and depth-averaged undertow velocity for random waves on plane 1 on 20 sloping beach. Measurements by Okayasu and Katayama (1992) (circles); Predictions with surface roller (full line) and without (dashed line).	94
3-6	Comparisons of measured and predicted wave heights, H_{rms} , wave set-up, $\bar{\eta}$, and depth-averaged return flow velocity, $-\bar{U}$, for random waves obliquely incident on plane 1 on 30 sloping beach. Measurements (Test 8A-E) Hamilton and Ebersole (2001) (circles); Predictions with surface roller (full line) and without (dashed line).	95
3-7	Comparisons of measured and predicted wave heights, wave set-up, and depth-averaged undertow velocity for random waves on barred beach profile. Measurements by Okayasu and Katayama (1992) (circles); Predictions with surface roller (full line) and without (dashed line).	97
4-1	Illustration of the near-shore mean current model	110
4-2	Turbulent Eddy Viscosity Model	113
4-3	Modified wave-current bottom boundary layer model proposed by Madsen (1994)	116

4-4	Comparison of measured and predicted wave heights, H_* , wave set-up, $\bar{\eta}$, and vertical profiles of undertow velocity for periodic waves on plane 1 on 35 sloping beach with bottom roughness $k_N = 1\text{mm}$. Measurements by Cox and Kobayashi (1996) (full circles indicate measurements below and open circles above trough level) and predictions (full line). Dotted line in set-up is the prediction neglecting the bottom shear stress and mean momentum forces.	121
4-5	Comparisons of the cross-shore forcing terms in (4.49) for Cox and Kobayashi's (1996) experiment: (a) external forcings and hydrostatic pressure forces; (b) mean-current-associated forces; (c) total forces. .	124
4-6	Comparisons of the cross-shore forcing terms in (4.33) for Cox and Kobayashi's (1996) experiment: (a) external forcings and hydrostatic pressure forces; (b) mean-current-associated forces; (c) total forces. .	125
4-7	Comparison of measured and predicted wave heights, H_{rms} , wave set-up, $\bar{\eta}$, and vertical profiles of undertow velocity for random waves on plane 1 on 20 sloping beach with smooth concrete bed. Measurements(Case 2) by Okayasu and Katayama (1992) (full circles indicate measurements below and open circles above trough level) and predictions (full line). Dotted line in set-up is the prediction neglecting the bottom shear stress and mean momentum forces.	128
4-8	Comparisons of the cross-shore forcing terms in (4.49) for Okayasu and Katayama's (1992) experiment (Case 2): (a) external forcings and hydrostatic pressure forces; (b) mean-current-associated forces; (c) total forces.	129
4-9	Comparisons of the cross-shore forcing terms in (4.33) for Okayasu and Katayama's (1992) experiment: (a) external forcings and hydrostatic pressure forces; (b) mean-current-associated forces; (c) total forces. .	130

4-10	Comparison of measured and predicted wave heights, H_{rms} , wave set-up, $\bar{\eta}$, and vertical profiles of undertow velocity for random waves on barred beach with smooth concrete bed. Measurements (Case 3) by Okayasu and Katayama (1992) (full circles indicate measurements below and open circles above trough level) and predictions (full line). Dotted line in set-up is the prediction neglecting the bottom shear stress and mean momentum forces.	131
4-11	Comparisons of measured and predicted wave heights, H_* , wave set-up, $\bar{\eta}$, vertical profiles of undertow and longshore current velocity, and depth-averaged longshore current velocity, \bar{V} , for periodic waves on plane 1 on 30 sloping beach. Measurements (Test 6A-N) by Hamilton and Ebersole (2001) (full circles) and predictions (full line).	133
4-12	Comparisons of the longshore forcing terms in (4.50) for LSTF experiment (Test 6A-N): (a) external forcings and hydrostatic pressure forces; (b) mean-current-associated forces; (c) total forces.	135
4-13	Comparisons of the longshore forcing terms in (4.41) for LSTF experiment (Test 6A-N): (a) external forcings and hydrostatic pressure forces; (b) mean-current-associated forces; (c) total forces.	138
4-14	Comparisons of the depth-averaged longshore current velocity for LSTF experiment (Test 6A-N): measurements (full circles) and predictions by the present model when following terms are accounted: (1) only wave forces; (2) (1) plus the turbulent lateral mixing; (3) (1) plus surface roller forces; (4) (3) plus the turbulent lateral mixing; (5) all terms except mean-current associated forcing terms above the trough; and (6) all terms.	141
4-15	Comparisons of measured and predicted wave heights, H_{rms} , wave set-up, $\bar{\eta}$, vertical profiles of undertow and longshore current velocity, and depth-averaged longshore current velocity, \bar{V} , for random waves on plane 1 on 30 sloping beach. Measurements (Test 8A-E) by Hamilton and Ebersole (2001) (full circles) and predictions (full line).	143

4-16	Comparisons of the longshore forcing terms in (4.50) for LSTF experiment (Test 8A-E): (a) external forcings and hydrostatic pressure forces; (b) mean-current-associated forces; (c) total forces.	144
4-17	Comparisons of the longshore forcing terms in (4.41) for LSTF experiment (Test 8A-E): (a) external forcings and hydrostatic pressure forces; (b) mean-current-associated forces; (c) total forces.	145
4-18	Comparisons of the depth-averaged longshore current velocity for LSTF experiment (Test 8A-E): measurements (full circles) and predictions by the present model when following terms are accounted: (1) only wave forces; (2) (1) plus the turbulent lateral mixing; (3) (1) plus surface roller forces; (4) (3) plus the turbulent lateral mixing; (5) all terms except mean-current associated forcing terms above the trough; and (6) all terms.	146
4-19	Comparisons of measured and predicted depth-averaged longshore current velocity, \bar{V} , for periodic waves on plane 1 on 20 sloping beach with different bottom roughness. Measurements (Cases 4 and 7 above and Cases 5 and 8 below) by Visser (1991) (Concrete bed (Cases 4 and 5) by open circles and gravel bed (Case 7 and 8) by full circles) and predictions (Concrete bed (Cases 4 and 5) by dashed line and gravel bed (Case 7 and 8) by full line).	149
4-20	Comparison of predicted undertow velocity profiles with different bottom roughness for periodic waves on plane 1 on 20 sloping beach (Corresponding to experimental Case 4 and 7 by Visser, 1991). $k_N=0.1\text{mm}$ (dashed line) and $k_N=6\text{mm}$ (full line).	150

4-21	Comparisons of measured and predicted depth-averaged longshore current velocity, \bar{V} , for periodic waves on plane 1 on 20 sloping beach with different bottom roughness. Measurements (Cases 4 and 7 above and Cases 5 and 8 below) by Visser (1991) (Concrete bed (Cases 4 and 5) by open circles and gravel bed (Case 7 and 8) by full circles) and predictions (Concrete bed (Cases 4 and 5) by dashed line and gravel bed (Case 7 and 8) by full line). Heavy lines are the predictions by the present model with $k_N = 5\text{mm}$ (full) and $k_N = 0.1\text{mm}$ (dashed) and thin lines are the predictions by the best-fit LH model.	154
4-22	Relative equivalent bottom roughness, k_N/D vs. $\psi'_{w,rms}$. Measurements (full rectangles) presented by Madsen et al. (1993) and models by Herrmann (2004) (full circles); Wilson (1989) (open circles); Xu and Wright (1995) (triangles); and Coastal Engineering Manual (2002) (diamonds).	161
4-23	Cross-shore distributions of (a) depth-averaged longshore current velocity, (b) ripple heights, (c) equivalent bottom roughness, and (d) water depth; Experiments (full circles) presented by Wang et al. (2002) (Test 1) and predictions with roughness represented by Herrmann's (2004) (full line); Madsen(2001) (thin dashed line); and $k_N = \eta_r$ (heavy dashed line).	165
4-24	Cross-shore distributions of (a) depth-averaged longshore current velocity, (b) ripple heights, (c) equivalent bottom roughness, and (d) water depth; Experiments (full circles) presented by Wang et al. (2002) (Test 3) and predictions with roughness represented by Herrmann's (2004) (full line); Madsen(2001) (thin dashed line); and $k_N = \eta_r$ (heavy dashed line).	168

4-25	Comparisons of measured and predicted wave heights, H_{rms} , wave set-up, $\bar{\eta}$, vertical profiles of undertow and longshore current velocity, and depth-averaged longshore current velocity, \bar{V} , for random waves barred beach with movable sand bed. Measurements (Test 1: spilling breaker) by Wang et al. (2002) (full circles) and predictions (full line).	169
4-26	Comparisons of measured and predicted wave heights, H_{rms} , wave set-up, $\bar{\eta}$, vertical profiles of undertow and longshore current velocity, and depth-averaged longshore current velocity, \bar{V} , for random waves barred beach with movable sand bed. Measurements (Test 3: plunging breaker) by Wang et al. (2002) (full circles) and predictions (full line).	170
5-1	Cross-shore locations of measured longshore current velocity profiles; LSTF experiments by Wang et al. (2002) (Test 1)	194
5-2	Cross-shore locations of measured longshore current velocity profiles; LSTF experiments by Wang et al. (2002) (Test 3)	194
5-3	Cumulative distributions of sampled sand used in LSTF experiment (Wang et al., 2002)	196
5-4	Weight fractions of each diameter class. Open circles are the dominant six classes applied to represent the sediment characteristics.	196
5-5	Time-varying profiles of (a) linear sinusoidal near-bottom wave orbital velocity and corresponding profiles of (b) sediment transport shear stress, (c) cross-shore (x) and (d) longshore (y) bedload sediment transport rates at Station 4 in Test 1 of LSTF experiments. Full and dashed lines in (c) and (d) are when the bottom slope effect is accounted for and neglected, respectively. (case (A), $\tau_{ws}(t) \sim u_{bm} \cos(\omega t - \pi)$) . . .	199

5-6	Time-varying profiles of (a) linear sinusoidal near-bottom wave orbital velocity and corresponding profiles of (b) sediment transport shear stress, (c) cross-shore (x) and (d) longshore (y) bedload sediment transport rates at Station 4 in Test 3 of LSTF experiments. Full and dashed lines in (c) and (d) are when the bottom slope effect is accounted for and neglected, respectively. (case (A), $\tau_{ws}(t) \sim u_{bm} \cos(\omega t - \pi)$) . . .	200
5-7	Time-varying profiles of (a) non-linear near-bottom wave orbital velocity and corresponding profiles of (b) sediment transport shear stress, (c) cross-shore (x) and (d) longshore (y) bedload sediment transport rates at Station 4 in Test 1 of LSTF experiments. Full and dashed lines in (c) and (d) are when the bottom slope effect is accounted for and neglected, respectively. (case (B), $\tau_{ws}(t) \sim u_{bw}(t)$)	203
5-8	Time-varying profiles of (a) non-linear near-bottom wave orbital velocity and corresponding profiles of (b) sediment transport shear stress, (c) cross-shore (x) and (d) longshore (y) bedload sediment transport rates at Station 4 in Test 3 of LSTF experiments. Full and dashed lines in (c) and (d) are when the bottom slope effect is accounted for and neglected, respectively. (case (B), $\tau_{ws}(t) \sim u_{bw}(t)$)	204
5-9	Time-varying profiles of (a) non-linear near-bottom wave orbital velocity and corresponding profiles of (b) sediment transport shear stress, (c) cross-shore (x) and (d) longshore (y) bedload sediment transport rates at Station 4 in Test 1 of LSTF experiments. Full and dashed lines in (c) and (d) are when the bottom slope effect is accounted for and neglected, respectively. (case (C), $\tau_{ws}(t) \sim u_{bw}(t) u_{bw}(t)$)	205
5-10	Time-varying profiles of (a) non-linear near-bottom wave orbital velocity and corresponding profiles of (b) sediment transport shear stress, (c) cross-shore (x) and (d) longshore (y) bedload sediment transport rates at Station 4 in Test 3 of LSTF experiments. Full and dashed lines in (c) and (d) are when the bottom slope effect is accounted for and neglected, respectively. (case (C), $\tau_{ws}(t) \sim u_{bw}(t) u_{bw}(t)$)	206

5-11	Cross-shore distributions of the net bedload sediment transport rates in the cross-shore (x) and the shore-parallel (y) directions (Test 1). Predictions are based on: (A) $\tau_{ws}(t) \sim u_{bm} \cos(\omega t)$ (thin dashed line); (B) $\tau_{ws}(t) \sim u_{bw}(t)$ (thin full line); (C) $\tau_{ws}(t) \sim u_{bw}(t) u_{bw}(t)$ (heavy full line); and (D) same as (C) without bottom slope effects (heavy dashed line). Full circles are the longshore bedload sediment transport rates obtained from the measurements and open circles denote the cross-shore locations where measured suspended sediment transport rates exceed the measured total LSST.	208
5-12	Cross-shore distributions of the net bedload sediment transport rates in the cross-shore (x) and the shore-parallel (y) directions (Test 3). Predictions are based on: (A) $\tau_{ws}(t) \sim u_{bm} \cos(\omega t)$ (thin dashed line); (B) $\tau_{ws}(t) \sim u_{bw}(t)$ (thin full line); (C) $\tau_{ws}(t) \sim u_{bw}(t) u_{bw}(t)$ (heavy full line); and (D) same as (C) without bottom slope effects (heavy dashed line). Full circles are the longshore bedload sediment transport rates obtained from the measurements and open circles denote the cross-shore locations where measured suspended sediment transport rates exceed the measured total LSST.	209
5-13	Time-varying profiles of linear sinusoidal near-bottom wave orbital velocity and corresponding profiles of sediment transport shear stress and reference concentrations at Station 4 in Test 1. Full and dashed lines in the reference concentration are when the bottom slope effect is accounted for and neglected, respectively.	211
5-14	Time-varying profiles of linear sinusoidal near-bottom wave orbital velocity and corresponding profiles of sediment transport shear stress and reference concentrations at Station 4 in Test 3. Full and dashed lines in the reference concentration are when the bottom slope effect is accounted for and neglected, respectively.	212

5-15	Time-varying profiles of non-linear near-bottom wave orbital velocity and corresponding profiles of sediment transport shear stress and reference concentrations at Station 4 in Test 1. Profiles are (B) (heavy dashed line), (C) (heavy full line), and (C) without bottom slope effects (thin dashed line). Straight dashed and full lines in the reference concentrations are the mean reference concentrations for (B) and (C), respectively.	214
5-16	Time-varying profiles of non-linear near-bottom wave orbital velocity and corresponding profiles of sediment transport shear stress and reference concentrations at Station 4 in Test 3. Profiles are (B) (heavy dashed line), (C) (heavy full line), and (C) without bottom slope effects (thin dashed line). Straight dashed and full lines in the reference concentrations are the mean reference concentrations for (B) and (C), respectively.	215
5-17	Cross-shore distributions of the mean reference concentration (Test 1). Predictions are based on: (A) $\tau_{ws}(t) \sim u_{bm} \cos(\omega t)$ (thin dashed line); (B) non-linear profile with $\tau_{ws}(t) \sim u_{bw}(t)$ (thin full line); (C) $\tau_{ws}(t) \sim u_{bw}(t) u_{bw}(t)$ (heavy full line); and (D) same as (C) without bottom slope effects (heavy dashed line).	216
5-18	Cross-shore distributions of the mean reference concentration (Test 3). Predictions are based on: (A) $\tau_{ws}(t) \sim u_{bm} \cos(\omega t)$ (thin dashed line); (B) non-linear profile with $\tau_{ws}(t) \sim u_{bw}(t)$ (thin full line); (C) $\tau_{ws}(t) \sim u_{bw}(t) u_{bw}(t)$ (heavy full line); and (D) same as (C) without bottom slope effects (heavy dashed line).	217
5-19	Comparisons of the predicted and measured mean suspended sediment concentrations. Measurements (circles) are obtained by Wang et al., (2002) (Test 1) and predictions (six full lines in each figure) are when D_4 to D_9 were applied respectively. The highest concentrations in each figure is when the finest diameter, $D = D_4$, is applied and the predicted concentration lowers as D changes from D_4 to D_9	218

5-20	Comparisons of the predicted and measured mean suspended sediment concentrations. Measurements (circles) are obtained by Wang et al., (2002) (Test 1) and predictions are when following diameters were applied: D_{n50} (thin dashed line); D_5 , D_6 , and D_7 (thin full line); D_4 to D_9 (heavy dashed line); and all diameter classes (heavy full line). . . .	220
5-21	Comparisons of the predicted and measured mean suspended sediment concentrations. Measurements (circles) are obtained by Wang et al., (2002) (Test 3) and predictions are when following diameters were applied: D_{n50} (thin dashed line); D_5 , D_6 , and D_7 (thin full line); D_4 to D_9 (heavy dashed line); and all diameter classes (heavy full line). . . .	222
5-22	Cross-shore distributions of the net cross-shore, $\bar{q}_{SS,x}$, and longshore, $\bar{q}_{SS,y}$, suspended sediment transport rates for LSTF experiments (Test 1). Measurements (circles) and predictions are when following sediment size-classes are accounted for: (i) D_{n50} (thin dashed line); (ii) D_5 , D_6 , and D_7 (thin full line); (iii) D_4 through D_9 (havy dashed line); and (iv) all diameter classes (heavy full line).	225
5-23	Cross-shore distributions of the net cross-shore, $\bar{q}_{SS,x}$, and longshore, $\bar{q}_{SS,y}$, suspended sediment transport rates for LSTF experiments (Test 3). Measurements (circles) and predictions are when following sediment size-classes are accounted for: (i) D_{n50} (thin dashed line); (ii) D_5 , D_6 , and D_7 (thin full line); (iii) D_4 through D_9 (havy dashed line); and (iv) all diameter classes (heavy full line).	226
5-24	Cross-shore distributions of the measured cross-shore suspended sediment transport rates (open circles) and the predicted bedload (thin full line), suspended load (dashed line), and the total sediment transport rate (heavy full line) in the cross-shore direction for Test 1. (prediction case (B) $\tau_{ws}(t) \sim u_{bw}(t)$)	231

5-25	Cross-shore distributions of the measured cross-shore suspended sediment transport rates (open circles) and the predicted bedload (thin full line), suspended load (dashed line), and the total sediment transport rate (heavy full line) in the cross-shore direction for Test 3. (prediction case (B), $\tau_{ws}(t) \sim u_{bw}(t)$)	232
5-26	Cross-shore distributions of the measured cross-shore suspended sediment transport rates (open circles) and the predicted bedload (thin full line), suspended load (dashed line), and the total sediment transport rate (heavy full line) in the cross-shore direction for Test 1. (prediction case (C), $\tau_{ws}(t) \sim u_{bw}(t) u_{bw}(t)$)	233
5-27	Cross-shore distributions of the measured cross-shore suspended sediment transport rates (open circles) and the predicted bedload (thin full line), suspended load (dashed line), and the total sediment transport rate (heavy full line) in the cross-shore direction for Test 3. (prediction case (C), $\tau_{ws}(t) \sim u_{bw}(t) u_{bw}(t)$)	234
5-28	Cross-shore distributions of the predicted bedload (thin full line), suspended load (dashed line), and the total sediment transport rate (heavy full line) in the shore-parallel for Test 1. Measurements (circles, suspended load; and triangles, total LSST) are obtained by Wang et al. (2002).	237
5-29	Cross-shore distributions of the predicted bedload (thin full line), suspended load (dashed line), and the total sediment transport rate (heavy full line) in the shore-parallel for Test 3. Measurements (circles, suspended load; and triangles, total LSST) are obtained by Wang et al. (2002).	238
5-30	Comparisons of longshore bedload and suspended load transport rates between Test 1 (spilling breakers, full line) and Test 3 (plunging breakers, dashed line).	242
B-1	Concept of the effective bottom slope	268

C-1	Cross-shore distributions of measured ripple height, η_r , steepness, η_r/λ , and water depth. Measurements (Test 1: spilling breakers) by Wang et al. (2002) (full circles) and local average (dashed lines).	280
C-2	Cross-shore distributions of measured ripple height, η_r , steepness, η_r/λ , and water depth. Measurements (Test 3; plunging breakers) by Wang et al. (2002) (full circles) and local average (dashed lines).	281
C-3	Comparisons of predicted and measured ripple height, η_r , and steepness, η_r/λ , as a function of non-dimensional parameter, $Z = \psi'_{w,rms}/S_*$ for the experimental case by Wang et al. (2002) (Test 1; spilling breakers). Measurements outside the surf zone ($X(m) < -14$, triangles), inside the surf zone ($-14 < X(m) < -5$, full circles), and near the shoreline ($X(m) > -5$, open circles). Models are WM91F (Wikramanayake and Madsen, 1991, field), WM91L (Wikramanayake and Madsen, 1991, laboratory), SG02 (Styles and Glenn, 2002), L96 (Li et al., 1996), N81 (Nielsen, 1981), and WH94 (Wiberg and Harris, 1994).	284
C-4	Comparisons of predicted and measured ripple height, η_r , and steepness, η_r/λ , as a function of non-dimensional parameter, $Z = \psi'_{w,rms}/S_*$ for the experimental case by Wang et al. (2002) (Test 3; plunging breakers). Measurements outside the surf zone ($X(m) < -14$, triangles), inside the surf zone ($-14 < X(m) < -5$, full circles), and near the shoreline ($X(m) > -5$, open circles). Models are WM91F (Wikramanayake and Madsen, 1991, field), WM91L (Wikramanayake and Madsen, 1991, laboratory), SG02 (Styles and Glenn, 2002), L96 (Li et al., 1996), N81 (Nielsen, 1981), and WH94 (Wiberg and Harris, 1994).	285
C-5	Cross-shore distributions of measured and predicted ripple height, η_r , steepness, η_r/λ , and water depth. Measurements (Test 1: spilling breakers) by Wang et al. (2002) (full circles) and predictions by Wikramanayake and Madsen (1991) (dashed line based on $\psi'_{w,rms}$; full line based on ψ'_m).	286

C-6	Cross-shore distributions of measured and predicted ripple height, η_r , steepness, η_r/λ , and water depth. Measurements (Test 3: plunging breakers) by Wang et al. (2002) (full circles) and predictions by Wikramanayake and Madsen (1991) (dashed line based on $\psi'_{w,rms}$; full line based on ψ'_m).	287
-----	---	-----

List of Tables

1.1	Experimental cases in LSTF applied to test the present model (Hamilton and Ebersole, 2001; Wang et al., 2002).	34
2.1	Summary of the numerical experiments	41
2.2	Summary of experimental data (N is the number of data available) .	52
2.3	Means and standard deviations of relative errors between predicted and measured breaking water depth.	54
4.1	Root-mean-square errors (m/s) between predicted and measured depth-averaged longshore current velocity (C6-N).	141
4.2	Root-mean-square errors (m/s) between predicted and measured depth-averaged longshore current velocity (C8-E).	144
4.3	Root-mean-square errors of the present model and the best-fit LH model, and best-fit empirical coefficients for the LH model for experiments (Cases 4, 7, 5, and 8) presented by Visser (1991) and LSTF experiments (Tests 6A-N and 8A-E) reported by Hamilton and Ebersole (2001). Predictions for the present model are based on $k_N = 0.1\text{mm}$ (Cases 4 and 5) and $k_N = 5\text{mm}$ (Cases 7 and 8). For the random wave case (Test 8A-E), breaking characteristics of the equivalent periodic wave, applied to the LH model, are determined from: (A) rms; and (B) significant incident wave heights, respectively.	162
4.4	Apparent roughness, k_{Na} , obtained from field data (Madsen, et al., 1993)	162
4.5	Equivalent roughness, k_N/D , obtained from field data (Madsen et al., 1993)	167

4.6	Mean errors of predicted and standard deviations of measured long-shore current velocity (Test 1: spilling breaker). Predictions are (1) Herrmann (2004), (2) Madsen (2001), and (3) $k_N = \eta_r$	167
4.7	Mean errors of predicted and standard deviations of measured long-shore current velocity (Test 3: plunging breaker). Predictions are (1) Herrmann (2004), (2) Madsen (2001), and (3) $k_N = \eta_r$	171
5.1	Characteristics of bottom sediments in each grain size class	195
5.2	Predicted hydrodynamic characteristics at Station 4 for Test 1 and Test 3.	197
5.3	Comparisons of measured and predicted suspended load transport rates in the cross-shore and longshore directions at seven Stations and their relative errors (Test 1, spilling breakers). Predictions (A) and (B) are only for case (iv) and the values at Station 3 ($X = -13.1\text{m}$) are excluded for the average values.	224
5.4	Comparisons of measured and predicted suspended load transport rates in the cross-shore and longshore directions at seven Stations and their relative errors (Test 3, plunging breakers). Predictions (A) and (B) are only for case (iv) and the values at Station 3 ($X = -13.1\text{m}$) are excluded for the average values.	227
5.5	Measured and predicted local LSST and the total LSST integrated over the cross-shore (x) axis and their relative errors (Test 1, spilling breakers). Predictions are based on (A) $\tau_{ws}(t) \sim \cos \omega t$, (B) $\tau_{ws}(t) \sim u_{bw}(t)$, and (C) $\tau_{ws}(t) \sim u_{bw}(t) u_{bw}(t)$	239
5.6	Measured and predicted local LSST and the total LSST integrated over the cross-shore (x) axis and their relative errors (Test 3, plunging breaker). Predictions are based on (A) $\tau_{ws}(t) \sim \cos \omega t$, (B) $\tau_{ws}(t) \sim u_{bw}(t)$, and (C) $\tau_{ws}(t) \sim u_{bw}(t) u_{bw}(t)$	240
5.7	Number of data points (out of 18 measured locations) whose relative errors fall within specified error ranges for the prediction case (C). . .	240

5.8	Measured and predicted bed load, suspended load and total LSST integrated over the entire cross-shore region, Q_{SBY} , Q_{SSY} , and $Q_{SY} = Q_{SBY} + Q_{SSY}$, respectively. Units of the measured and predicted LSST are in (m^3/year).	242
-----	--	-----

Chapter 1

Introduction

1.1 General Remarks

The estimation of beach erosion, which is caused by local imbalance of the sediment transport, is one of the most significant concerns to coastal engineers. Sediment transport is generally expressed as a vector of two horizontal components in the cross-shore and longshore directions. Since the large magnitude of either component of sediment transport is caused around the surf zone, it is essential to develop a predictive model for sediment transport inside the surf zone.

Longshore sediment transport (LSST) is mainly caused by the longshore current, which is induced by the longshore forcing due to breaking waves. Since LSST has a significant influence on beach erosion for a longer time-scale and wider area, intensive efforts have been made to obtain reasonably accurate predictions. In the United States, the “CERC formula” is generally used to predict the total LSST (*Shore Protection Manual*, 1977, 1984). The CERC formula, which is based on Savage (1962), empirically determines the total LSST as a function of the breaking wave characteristics. Although the formula is simple and easy to use, it has considerable uncertainty regarding applications to various conditions such as sediment grain size, different bottom slopes as well as bar-type topography, and breaker types, i.e., plunging or spilling. For instance, Madsen et al. (2003) pointed out, from their order-of-magnitude analysis, that the CERC-type formula does not appropriately account

for the contribution of suspended sediment transport and therefore applicability of the formula is questionable when the suspended sediment transport dominates the total sediment transports, such as during severe storm. Although the cross-shore distributions of LSST have been proposed (e.g., Bodge and Dean, 1987), their predictions do not agree well with field measurements especially for the location of the peak LSST (*Coastal Engineering Manual*, 2001). Based on these total LSST models, numerous coastline evolution models, such as GENESIS (Hanson and Kraus, 1989 and Gravens et al., 1991), N-line models (Perlin and Dean, 1983; Scheffner and Rosati, 1987; and Kobayashi and Han, 1988), have been proposed. Since the concept of these models is based on empirically determined LSST model such as the CERC formula, they have the same problems of uncertainty when applied for various conditions.

Cross-shore sediment transport (CSST) is mainly caused by wave orbital velocity and undertow. CSST can be either shoreward or seaward depending on the wave and undertow intensity. For example, storm waves tend to yield seaward sediment transport while milder waves cause shoreward sediment transport. Because of this feature, CSST generally causes relatively rapid topographical changes compared to LSST and, in the long run, the cross-shore ward sediment transport is considered to be balanced. This is one reasons why only LSST is considered in most models for predictions of long term beach evolutions, with less effort and attention being devoted to the evaluation of CSST (e.g., GENESIS and N-line models). When wave characteristics are uniform along the shoreline, however, CSST becomes more important. Moreover, in order to determine LSST for a barred beach, CSST is essential to estimate the proper cross-shore beach profile.

For the estimation of local sediment transport, the energetics-based approach has often been applied. As an example of this approach, the Bailard (1981) model, which is an improved version of Bagnold (1963) model, is well known. Assuming that a portion of fluid energy is expended in maintaining a sediment transport, the model determines sediment transport as a function of local wave, bottom and sediment characteristics. The model accounts for both bedload and suspended sediment transport and the percent of the contributions of each sediment transport mode is determined

empirically. Although the model is relatively simple and easy to use, the model has the following weaknesses: (i) since the model was originally established for uniform steady flow, there is no justification for its direct application to oscillatory flow conditions; (ii) empirical coefficients are hard to quantify and have been shown to fluctuate with varying hydrodynamic conditions (Nairn and Southgate, 1993); (iii) the model has no threshold for sediment motion, i.e., the model can be used only for large wave conditions. In addition to these weaknesses, Gallagher et al. (1998) pointed out that the energetics model cannot predict the slow shoreward migration observed during milder waves when observed local current conditions are utilized to evaluate local CSST.

The eventual goal of this research is therefore to develop a predictive model for the local sediment transport rate on a long, straight beach. In order to refine the model applicability, a process-based approach should be taken. We thus apply the conceptual bedload sediment transport model and associated suspended sediment transport model (Madsen, 2001), both of which were originally developed for non-breaking wave conditions. Since these models are based on considerations of physical processes, it is expected that these models can be extended to application inside the surf zone once the appropriate hydrodynamics are obtained.

In this sense, an ability to accurately predict the surf zone hydrodynamics is vital to develop a process-based sediment transport model. For example, time-varying near-bottom velocity determines the bottom shear stress, which induces bedload sediment transport. Skewness and asymmetry of the near-bottom non-linear wave orbital velocity, which are dominant features for near-breaking and broken waves, may play significant roles in yielding net bedload sediment transport in the shoreward direction. The bottom shear stress also acts to entrain bottom sediments into the water column where the turbulence due to wave breaking keeps a potentially large amount of sediments suspended and available for transport by the near-shore mean current in the seaward and longshore directions by the undertow and longshore current, respectively.

In this research, we first develop a model for predictions of the surf zone hydrodynamics. The model consists of predictions of breaking wave characteristics,

Table 1.1: Experimental cases in LSTF applied to test the present model (Hamilton and Ebersole, 2001; Wang et al., 2002).

Case	Test 6A-N	Test 8A-E	Test 1	Test 3
Wave	periodic	random		
Bed	concrete plane		movable sand	
T (s)	2.5	2.5	1.5	3.0
H_0/L_0	0.019	0.017	0.054	0.012

near-bottom wave orbital velocities, and wave-induced currents, i.e., undertow and longshore current. In order to explain the excess volume flux and the momentum forcings observed in the surf zone, a surface roller evolution model is also developed. Finally, the predicted near-shore hydrodynamics are applied to the conceptual sediment transport model (Madsen, 2001) to evaluate the characteristics of the local sediment transports.

The predictive skills of the present model is examined through comparison with unique experimental data sets obtained by the U.S. Army Corps of Engineers in their large-scale Longshore Sediment Transport Facility (LSTF) (Hamilton and Ebersole, 2001, Wang et al., 2002). In the LSTF, uniform longshore currents on a long, straight beach are achieved by installing multiple pumps at one end of the beach. Using this facility, they have measured wave characteristics, horizontal current velocities and sediment concentrations at various points at multiple elevations for regular and random waves obliquely incident on parallel contour beaches of both concrete and fine sand. Table 1.1 summarizes the experimental conditions used to compare with the present model. A complete description of the facility can be found in Hamilton, et al. (2001): <http://libweb.wes.army.mil/uhtbin/hyperion/CHL-TR-01-22.pdf>. From the measurements, we have access to time-series of surface profiles and near-bottom wave orbital velocities as well as profiles of time-averaged longshore currents, undertow velocity profiles and suspended sediment concentrations. Equilibrium beach profiles and total LSST are also available for the movable bed cases. Therefore, their experiments are suited for the model examinations because we can confirm the consistency of our model for each of various physical mechanisms, which contribute to

the sediment transport processes.

1.2 Thesis Outline

In Chapter 2, we introduce the wave models (Tajima and Madsen, 2002). For practical reasons, all models are constructed based on linear wave theory. We explore the relationship between non-linear and an equivalent linear wave through numerical experiments and develop a model for reconstruction of non-linear wave characteristics such as skewness and asymmetry of near-bottom orbital velocity from knowledge of the equivalent linear wave characteristics. Shoaling, breaking, and broken wave characteristics are then determined based on equivalent linear wave concept from a simple energy balance equation. A simple model extension to random waves is also discussed. The applicability of these models is examined through comparison of their predictions with measured experimental data, which have not been used to calibrate the model coefficient.

In Chapter 3, the surface roller model (Tajima and Madsen, 2003) is developed. Since the wave model is based on the energy balance equation with linear wave theory, evolution of the surface roller is also determined from an energy balance equation. The local surface roller energy, obtained in this manner, characterizes the volume flux and momentum forcings, which are applied to the near-shore mean current model. The applicability of the model is also tested through comparison with measured experimental data.

Chapter 4 discusses the development of a near-shore mean shear current model based on the present wave and surface roller models. The near-shore current model consists of two-layer two-dimensional-horizontal (2DH) momentum equations, integrated above the wave trough level and over the entire depth, which determine mean shear stresses at the trough level and over the entire depth, respectively. Coupled with a simple turbulent eddy viscosity model, analytical solutions are obtained for the vertical mean shear current profiles. The model account for the convective acceleration forces due to current-current, wave-current, and surface roller-current interactions.

The bottom boundary condition for the near-shore current model is specified from the knowledge of equivalent bottom roughness by application of a modified version of Madsen's (1994) wave-current bottom boundary layer model. Model predictions are also compared with experimental observations.

In Chapter 5, we first summarize the conceptual bedload and associated suspended load sediment transport models (Madsen, 2001). Introducing surf zone hydrodynamic characteristics predicted from the present hydrodynamic models, we extend the sediment transport models to the surf zone. Applicability of the present model is then tested against the LSTF experiments (Wang et al., 2002). Influence of wave non-linearity and bottom slopes on the net bedload sediment transport rates are examined and their relative importance are discussed. Sensitivity of the predicted suspended sediment concentrations to the sediment grain size is also investigated. Finally, we compare the predicted bedload, suspended load and the total sediment transport balance in the cross-shore (x) and longshore (y) directions and discuss about the future modifications of the model.

In Chapter 6, finally, all models and results are summarized and their physical implications are discussed.

Chapter 2

Wave Model

As discussed in Chapter 1, an ability to accurately predict near-shore hydrodynamics is essential to capture the characteristics of sediment transport processes and ultimately to forecast features of coastal morphology. Time-varying near-bottom velocity determines the bottom shear stress, which induces bedload sediment transport. Skewness and asymmetry of the near-bottom non-linear wave orbital velocity, which are dominant features for near-breaking and broken waves, may play significant roles in yielding net bedload sediment transport in the shoreward direction. In this sense, one of the vital features required for the wave model is to predict the time-varying profiles of near-bottom non-linear wave orbital velocity.

A number of numerical models for predictions of the non-linear wave characteristics have been proposed and their predictive performance has also been examined through comparison with experimental data (e.g., Nwogu, 1993; Isobe, 1994; and Nadaoka et al., 1994). Among these non-linear wave models, the Boussinesq equations, first derived by Peregrine (1967) is most widely used. Wei et al. (1995) however pointed out that the use of the standard Boussinesq equations is restricted to shallow water areas and to small non-linear effects because the standard Boussinesq equations are based on the assumptions of weak dispersion and weak non-linearity. Instead of depth-averaged velocity used in Peregrine's (1967) Boussinesq equations, Nwogu (1993) introduced the velocity at a certain depth as a dependent variable and significantly improved linear dispersion properties in intermediate water depth. Nwogu

(1996) furthermore extended his modified Boussinesq model to the broken waves in the surf zone and run-up of waves in the swash zone. Although the improvement of the dispersion relationships allowed an extension of the model to relatively deep water, Nwogu's (1993) modified Boussinesq equations still can not yield appropriate predictions in the vicinity of the breaking point where strong non-linear effects are not negligible. Wei et al. (1995) and Madsen et al. (1996) pointed out this feature and proposed the fully non-linear Boussinesq equations. These fully non-linear Boussinesq equations have been extended to the surf zone as well as swash zone (e.g., Madsen et al., 1997a and 1997b; Kirby et al., 1998; and Chen et al., 2000) and these models were recently applied in a sediment transport model by Wen and Kirby (2003). However, adoption of the higher order terms in the modified Boussinesq equations trades off computational stability and efficiency. Especially for practical use of a model for the prediction of beach morphology changes requires computational efficiency and flexibility so that it can accommodate iterative computations under arbitrary beach profile conditions.

Our goal in this Chapter is therefore to develop computationally efficient and practically flexible models for predictions of nearshore wave characteristics including the surf zone. Because of its simplicity and practical applicability, we apply linear wave theory to estimate wave shoaling and refraction up to the breaking point. After the waves reach breaking, a broken wave attenuation model is applied. Predictive schemes for retrieving non-linear wave characteristics from computed linear wave characteristics must be developed to make our model complete.

A number of breaking wave models based on linear wave theory have been developed and the validity of these models has been examined through comparison with measured broken wave heights. As discussed previously, one of the primary goals of our wave model is to predict appropriate non-linear near-bottom wave orbital velocity profiles that significantly contribute to the sediment transport processes. Because most breaking wave dissipation models are calibrated only in terms of the broken wave heights, however, it is not clear how one can obtain these non-linear features from knowledge of the wave height alone. From consideration of conservation of wave

energy, non-linear wave heights are usually larger than the corresponding linear wave heights. Thus, if one uses a measured or predicted non-linear wave height, as if it were a linear wave height, to calculate wave energy or wave energy flux from linear theory, these quantities will generally be overpredicted. In this sense, broken wave models based on linear wave theory must be calibrated with linear wave heights that somehow are equivalent to the measured, non-linear, wave heights.

In this chapter, we first introduce the concept of an equivalent linear wave and explore the relationship between non-linear and equivalent linear wave characteristics through numerical experiments. Non-linear wave characteristics are then determined as functions of equivalent linear wave characteristics. The equivalent linear wave concept is applied to develop a breaking wave dissipation model, which is applicable to arbitrary beach slope conditions. This breaking wave dissipation model is developed for simple periodic waves but its application is extended to random, narrow-banded spectral waves. Finally, the validity of the model is examined through comparison with experimental data, which have not been used to develop the model.

2.1 Non-Linear Wave Model

In order to develop a non-linear wave model, we introduce the concept of an equivalent linear wave, which defines the relationship between actual non-linear waves and corresponding linear waves. Based on this concept, equivalent linear wave characteristics are simply predicted by linear wave theory and, if necessary, non-linear wave characteristics may be determined as functions of predicted equivalent linear wave characteristics.

2.1.1 Equivalent Linear Wave

Figure 2-1 illustrates the concept of the equivalent linear wave. The equivalent linear wave is defined as the linear wave having the identical energy flux as actual non-linear progressive waves. Since non-linear effects are most pronounced as waves enter shallow water, it is assumed that the non-linear and equivalent linear waves have the

Linear vs. Non-Linear

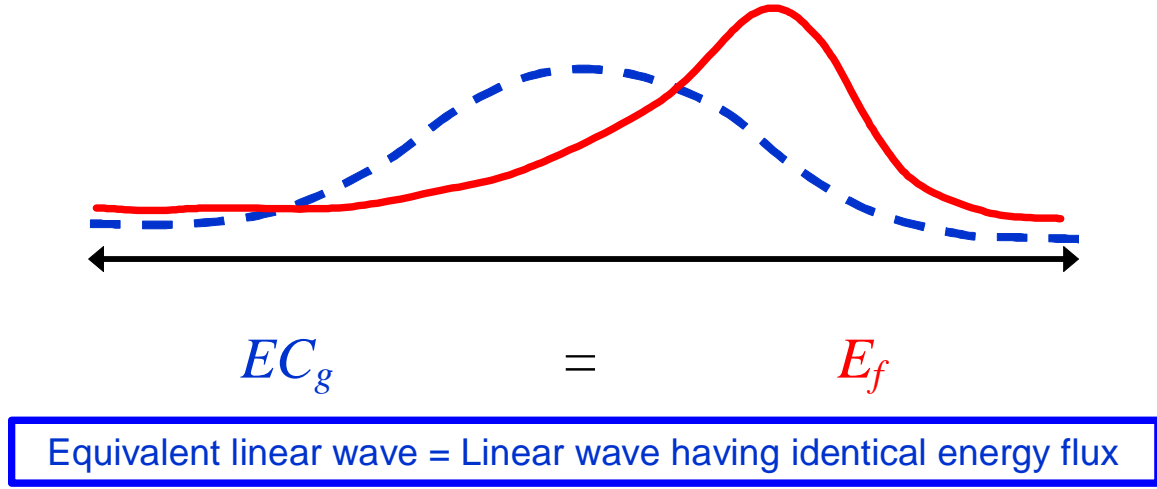


Figure 2-1: Concept of the equivalent linear wave.

same deep water characteristics, L_0 and H_0/L_0 . Shoaling of the equivalent linear wave produces an equivalent linear wave height H which may be transformed to the non-linear wave height, H_* , by applying a transform relationship which is obtained from numerical experiments.

2.1.2 Numerical Experiments

In order to explore the relationship between non-linear and equivalent linear wave characteristics, numerical experiments were performed. Nwogu's (1993) modified Boussinesq equations were applied to compute wave shoaling on plane beaches of various slopes, $\tan \beta_0 = 1/100, 1/50, 1/35, 1/20$, and $1/10$, for a range of deep water wave steepness, $H_0/L_0 = 0.001, 0.002, 0.005, 0.01, 0.02$, and 0.05 . Table 2.1 summarizes the numerical experimental cases. Incident wave profiles were obtained from 5th order Stokes Wave Theory (Isobe, 1978) or Stream Function Theory with 19 terms (Dean, 1965).

The geometrical conditions for the computations are shown in Figure 2-2. In order to introduce stable and appropriate incident waves into the system, the constant depth

Table 2.1: Summary of the numerical experiments

SLOPE	CASE	H_0/L_0	Offshore water depth(m)	Incident wave height(m)	Incident wave theory
1/10	A1	0.001	10.0	0.093	STK5th
	A2	0.002	10.0	0.186	SFM 19
	A3	0.005	10.0	0.466	SFM 19
	A4	0.010	10.0	0.931	SFM 19
	A5	0.020	15.0	1.824	SFM 19
	A6	0.050	20.0	4.583	STK5th
1/20	B1	0.001	10.0	0.093	STK5th
	B2	0.002	10.0	0.186	SFM 19
	B3	0.005	10.0	0.466	SFM 19
	B4	0.010	10.0	0.931	SFM 19
	B5	0.020	15.0	1.824	SFM 19
	B6	0.050	20.0	4.583	STK5th
1/35	C1	0.001	10.0	0.093	STK5th
	C2	0.002	10.0	0.186	SFM 19
	C3	0.005	10.0	0.466	SFM 19
	C4	0.010	10.0	0.931	SFM 19
	C5	0.020	15.0	1.824	SFM 19
	C6	0.050	20.0	4.583	STK5th
1/50	D1	0.001	10.0	0.093	STK5th
	D2	0.002	10.0	0.186	SFM 19
	D3	0.005	10.0	0.466	SFM 19
	D4	0.010	10.0	0.931	SFM 19
	D5	0.020	15.0	1.824	SFM 19
	D6	0.050	20.0	4.583	STK5th
1/100	E1	0.001	10.0	0.093	STK5th
	E2	0.002	10.0	0.186	SFM 19
	E3	0.005	10.0	0.466	SFM 19
	E4	0.010	10.0	0.931	SFM 19
	E5	0.020	15.0	1.824	SFM 19
	E6	0.050	20.0	4.583	STK5th

*STK5:Stokes 5th order wave theory / SFM 19:Stream function of 19th order

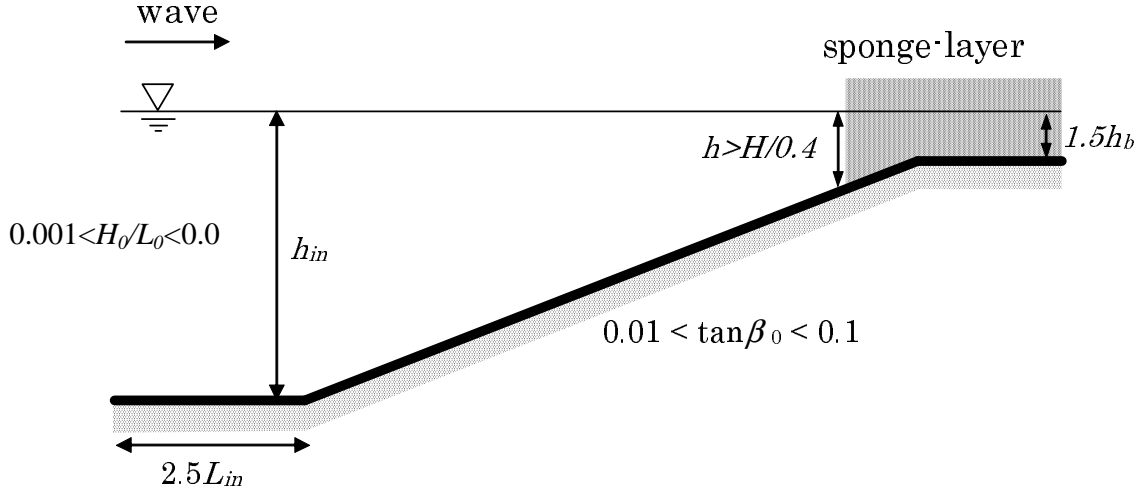


Figure 2-2: Geometrical conditions for the numerical experiment.

region was set at the offshore boundary. The length of this region is $2.5L_{in}$ with L_{in} , the incident wave length. The constant offshore depth, h_{in} , which is shown in Table 2.1 for each case, was selected so as to keep the Ursell number less than 10 and h_{in}/L_{in} less than 0.2. This condition allows us to apply both Boussinesq equation and Stokes wave theory. Near the onshore boundary, constant depth is again assumed and a sponge layer was introduced in order to absorb the waves and avoid reflected waves. The constant depth at the onshore boundary was chosen about 50% larger than the wave breaking depth, which is determined from incident wave conditions by Goda's (1970) breaking wave criteria. The starting point of the sponge layer was adjusted as shallow as possible for the numerical computation keeps stable. As for the sponge-layer conditions for the numerical computation, we applied the model proposed by Cruz et al. (1993). The simulations were carried out up to the value of $H_*/h < 0.4$ since the Boussinesq approximation is known to yield unreliable results for bottom orbital velocities when $H_*/h > 0.4$. Further details of the numerical scheme are given by Tajima (2001).

2.1.3 Non-Linear Wave Parameters

Shoaling non-linear wave characteristics, including near-bottom orbital velocities, are predicted as functions of deep water wave steepness, H_0/L_0 , relative depth, h/L_0 , and the bottom slope, β_0 . These non-linear characteristics, identified by an asterisk subscript, are expressed as dimensionless parameters, H_*/H and U_{b*}/U_b where H denotes the equivalent linear wave height, obtained by shoaling the same deep water wave to the relative depth, h/L_0 , and U_b is the near-bottom velocity "height" predicted from linear theory for the equivalent linear wave, i.e.,

$$U_b = \frac{H\omega}{\sinh kh} \quad (2.1)$$

where $\omega = 2\pi/T$ and $k = 2\pi/L$ is the wave number predicted from the linear dispersion relationship. The asymmetry and skewness of the near-bottom velocity variation are represented by T_c/T , $T_{c'}/T$, and u_{c*}/U_{b*} , where u_{c*} , T_c , and $T_{c'}$ are defined in Figure 2-3. Both T_c and $T_{c'}$ are the time for which the near-bottom wave orbital velocity rises in the wave propagating direction. T_c may be nearly equivalent to $T_{c'}$ if the waves are forward-leaning in shape, i.e. wave asymmetry is relatively strong on the slope. For the waves with relatively small asymmetry (forward-leaning) but with large skewness, such as solitary waves propagating on non-sloping beaches, T_c becomes larger than $T_{c'}$. For example, T_c of Stokes or Cnoidal-type waves should be $T/2$ while $T_{c'}$ should be equal or smaller than $T/2$ depending on the intensity of wave non-linearity.

Figures 2-4 and 2-5 show predicted non-linear wave parameters as functions of h/L_0 and H_0/L_0 for $\tan \beta_0 = 1/35$. Similar figures are obtained with different β . In Figure 2, solid lines are the recorded values from the numerical simulations and dotted lines are the following fitting formulae, which are extrapolated and assumed valid up to the predicted breaking point.

$$\begin{aligned} H_*/H &= 1 + a_1 \exp[-a_2 h/L_0] \\ a_1 &= (2.2 + 2 \tanh(55 \tan \beta_0)) \tanh \left[\left(1.6 \tan^{-\frac{3}{2}} \beta_0 + 25 \right) H_0/L_0 \right] \end{aligned} \quad (2.2)$$

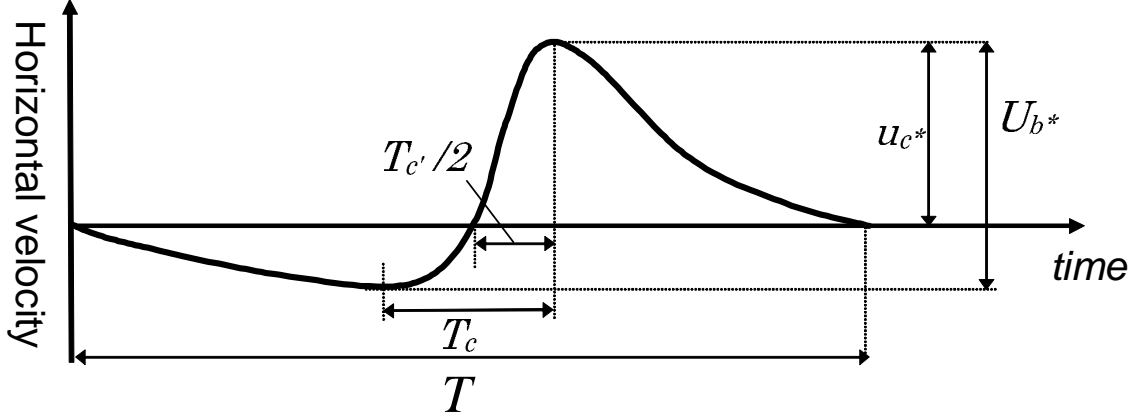


Figure 2-3: Non-linear characteristics of near-bottom wave orbital velocity and definitions of non-linear wave parameters, T_c , $T_{c'}$, u_{c*} , and U_{b*} .

$$\begin{aligned}
 & +30 \tan^{\frac{1}{10}} \beta_0 H_0 / L_0 \\
 a_2 &= 9.5 (H_0 / L_0)^{-0.5} + 10 \\
 U_{*b} / U_b &= 1 - b_1 \exp [-b_2 h_0 / L_0] + b_3 \exp [-b_4 h / L_0] \tag{2.3}
 \end{aligned}$$

$$\begin{aligned}
 b_1 &= 5.4 (H_0 / L_0)^{0.75} \\
 b_2 &= 80 (H_0 / L_0)^{-0.1} - 90 \\
 b_3 &= 49 [(95 + 1100 \exp [-60 \tan \beta_0]) H_0 / L_0]^2 \\
 & \quad \times \exp \left[-4 \sqrt{95 + 1100 \exp (-60 \tan \beta_0) H_0 / L_0} \right] \\
 b_4 &= 8 (H_0 / L_0)^{-0.5} \\
 T_c / T &= 0.5 - c_1 \exp [-c_2 h / L_0] \tag{2.4}
 \end{aligned}$$

$$\begin{aligned}
 c_1 &= \{33 + 110 \exp [-30 \tan \beta_0]\} H_0 / L_0 + 0.69 \exp [-8.7 \tan \beta_0] \\
 c_2 &= 40 + 60 \exp [-30 \tan \beta_0] + 0.3 (H_0 / L_0)^{-0.8} \\
 T_{c'} / T &= 0.5 - c_3 \exp [-c_4 h / L_0] \tag{2.5}
 \end{aligned}$$

$$\begin{aligned}
 c_3 &= 0.5 + 14 H_0 / L_0 + (0.1 - 0.4 \tanh (10 \tan \beta_0)) \exp [-300 H_0 / L_0] \\
 c_4 &= 30 + 0.3 (H_0 / L_0)^{-0.8} \\
 u_{c*} / U_{b*} &= 0.5 + d_1 \exp [-d_2 h / L_0] \tag{2.6} \\
 d_1 &= \exp [-\exp (-1.3 + 3.6 \exp (-30 \tan \beta_0))] \\
 & \quad \times \exp [-(0.3 + 0.25 \exp (-10 \tan \beta_0)) \ln (H_0 / L_0)]
 \end{aligned}$$

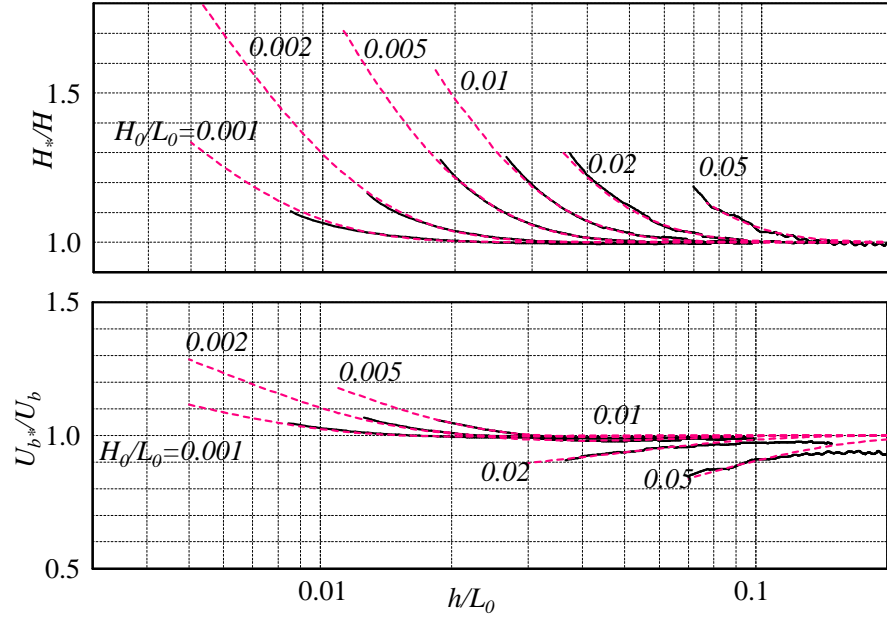


Figure 2-4: Non-linear wave characteristics parameters, H_*/H and U_{b*}/U_b as functions of H_0/L_0 , h/L_0 with $\tan \beta_0 = 1/35$; simulations (full line) and fitting formulae (dotted line).

$$d_2 = \exp [2.4 - 0.5 \exp (-45 \tan \beta_0)] (H_0/L_0)^{-(0.18+0.24 \exp (-25 \tan \beta_0))}$$

As seen in Figures 2-4 and 2-5, non-linear effects become stronger in shallower water (smaller h/L_0) or as H_0/L_0 increases. Validity of the formulae in the extrapolated range is examined later through comparison with measured data.

2.1.4 Reconstruction of the Non-Linear Near-Bottom Wave Orbital Velocity Profile

Introducing the non-linear wave parameters obtained in the Section 2.1.3, approximate bottom orbital velocity profiles can be modeled as a combination of four sinusoidal waves. Figure 2-6 illustrates the approximated velocity profile. Each of the four sinusoidal curves is numbered. The model outline is as follows.

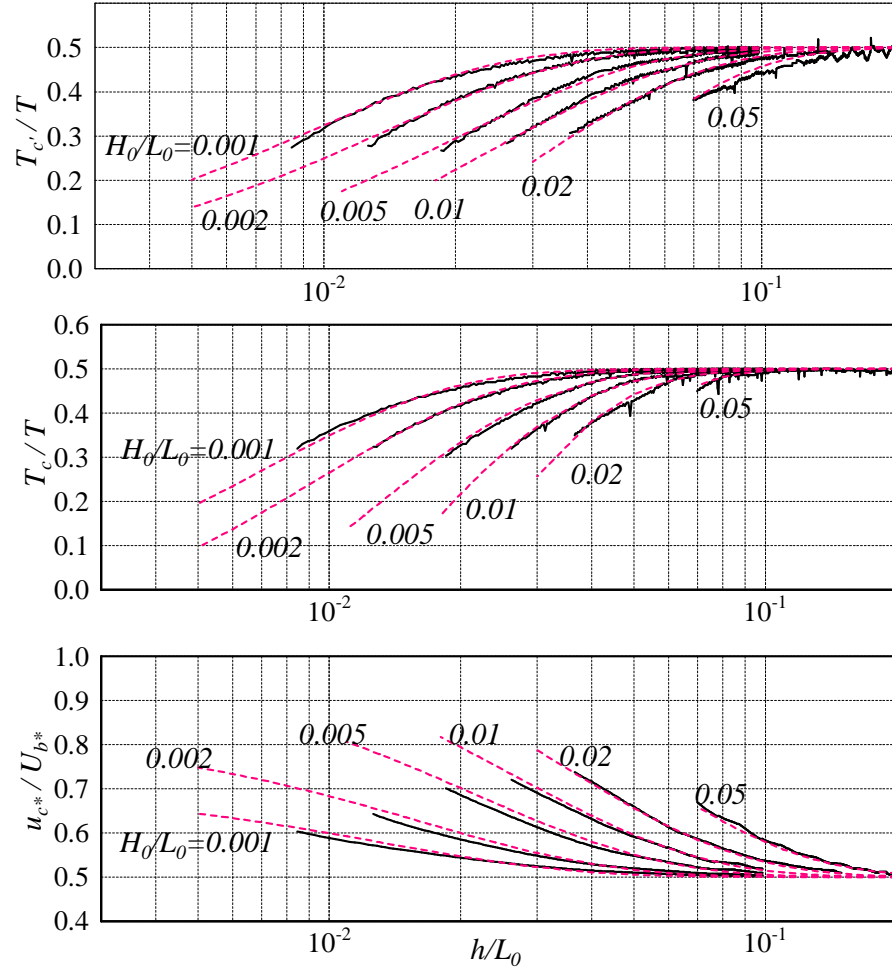


Figure 2-5: Non-linear wave characteristics parameters, $T_{c'}/T$, T_c/T and u_{c^*}/U_{b^*} as functions of H_0/L_0 , h/L_0 with $\tan \beta_0 = 1/35$; simulations (full line) and fitting formulae (dotted line).

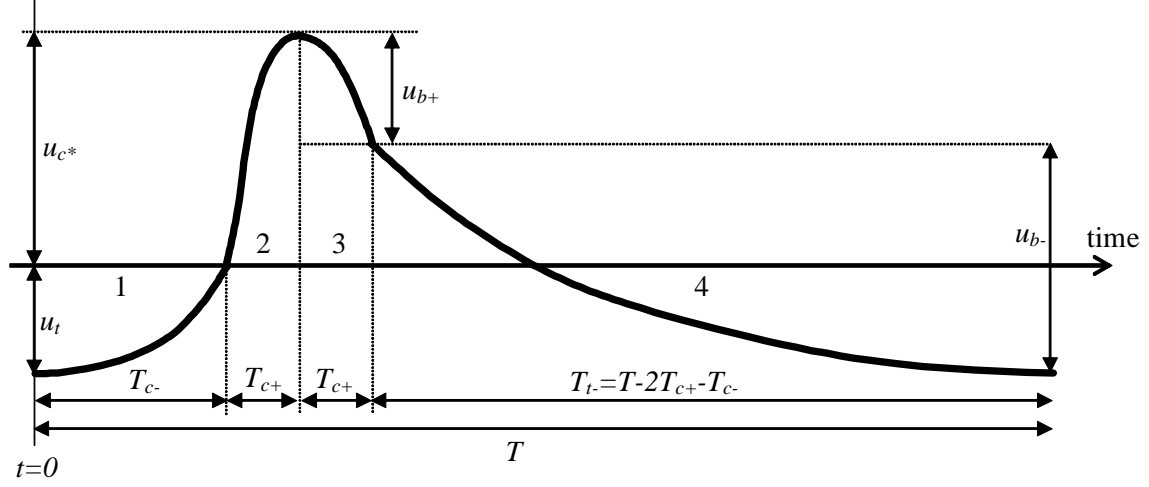


Figure 2-6: Modeling for reconstructions of the non-linear near-bottom wave orbital velocity profile

In the figure, each sinusoidal curves is expressed as

$$\begin{aligned}
 1 : \quad u_w &= -u_t \cos\left(\frac{\pi}{2T_{c-}}t\right) & (0 \leq t \leq T_{c-}) \\
 2 : \quad u_w &= u_{c*} \sin\left(\frac{\pi}{2T_{c+}}(t - T_{c-})\right) & (T_{c-} \leq t \leq T_c) \\
 3 : \quad u_w &= u_{b+} \cos\left(\frac{\pi}{2T_{c+}}(t - T_c)\right) + u_{c*} - u_{b+} & (T_c \leq t \leq T_c + T_{c+}) \\
 4 : \quad u_w &= -u_{b-} \cos\left(\frac{\pi}{2T_{t-}}(t - T_c - T_{c+})\right) + u_{c*} - u_{b+} & (T_c + T_{c+} \leq t \leq T)
 \end{aligned} \tag{2.7}$$

Here, u_t , T_{c-} , T_{c+} , and T_{t-} shown in Figure 2-6 are estimated from the wave non-linear parameters from (2.3) through (2.6) as

$$u_t = U_{b*} - u_{c*} \tag{2.8}$$

$$T_{c-} = T_c - T_{c'}/2 \tag{2.9}$$

$$T_{c+} = T_{c'}/2 \tag{2.10}$$

$$T_{t-} = T - 2T_{c+} - T_{c-} \tag{2.11}$$

The last two unknown parameters, u_{b+} and u_{b-} are determined by requiring (2.7) to be zero if averaged over the wave period and $u_{b+} + u_{b-}$ to be a velocity “height,” U_{b*} ,

as

$$u_{b+} = u_{c*} - \frac{u_{c*}T_{c'}}{(1 - \pi/2)(T - T_{c1})} + \frac{u_t}{1 - \pi/2} \quad (2.12)$$

$$u_{b-} = \frac{u_{c*}T_{c'}}{(1 - \pi/2)(T - T_{c1})} - \frac{u_t\pi/2}{1 - \pi/2} \quad (2.13)$$

Applicability of the presented non-linear wave orbital velocity profile model is examined later in Section 2.6.4.

2.2 Breaking Wave Model

Based on the present equivalent linear wave concept, linear wave theory determines the shoaling of the equivalent linear waves up to the breaking point. Once the wave reaches the breaking point, a broken wave model should be applied to evaluate wave attenuation inside the surf zone. Since the wave characteristics dramatically change beyond the breaking point, accurate prediction of the breaking point is vital. Since the present wave model is based on linear wave theory, a breaking wave criterion should also be cast in terms of linear wave theory for compatibility.

Most of well-known breaking criteria models (e.g. Michell, 1893 and Miche, 1951) characterize the breaking limit by actual, i.e. non-linear, breaking wave height, H_{b*} , as functions of the still water bottom slope, β_0 , wave period, T , and the local breaking water depth, h_b . Since strong wave non-linearity is expected near the wave breaking point, predictions of the non-linear wave heights around the breaking point may contain certain errors. In this sense, even if we could specify the exact breaking wave heights from existing breaking criteria, we may not be able to locate the right breaking point because of uncertainty in predicted non-linear wave heights. Watanabe et al. (1984) also pointed out that most existing breaking criteria, such as Iversen's (1951) and Goda's (1970) criteria, may not be applicable to compound waves because these models are based on observations of a single wave train propagating on a sloping bed. Watanabe et al. (1984) discussed physical mechanisms of breaking waves and suggested that the ratio of water particle velocity at the wave crest and the wave

phase velocity, u_c/C , in stead of H_{b*}/h_b , may characterize the breaking criteria for both single train and compound waves. Since Watanabe et al.'s (1984) breaking criteria, $(u_c/C)_b$, is based on the linear wave theory, their model is ideally suited for application in conjunction with our equivalent linear wave. Thus, we follow Watanabe et al.'s (1984) concept and modify their model adding recently obtained breaking wave data.

2.2.1 Model Concept

Similar to Watanabe et al.'s (1984) model, we characterize the breaking criteria by a ratio of water particle velocity near the wave crest and the wave phase velocity,

$$\left(\frac{2u_c}{C}\right)_b = \frac{k_b H_b}{\tanh k_b h_b} = f(h_b/L_0, \tan \beta_0) \quad (2.14)$$

where $k_b = 2\pi/L_b$ is a wave number at the breaking point. Note that the left hand side of (2.14) becomes $k_b H_b = 2\pi (H_b/L_b)$ for the deep water limit, $\tanh k_b h_b \rightarrow 1$, and it approaches H_b/h_b for the shallow water limit, $\tanh k_b h_b \rightarrow k h_b$. These features are consistent with well-known existing breaking indices. For instance, Michell (1893) characterized the deep water breaking criteria by wave steepness, H_b/L_b and Battjes (1974) proposed multiple values of $\gamma_b = H_b/h_b$ for nearshore breaking waves depending on breaker types, such as plunging and spilling breakers. Hence the use of (2.14) should serve as a general breaking index applicable to both deep and shallow water conditions.

2.2.2 Modeling Fitting Function

The fitting function, f , in (2.14) is modeled so that the model satisfies Michell's (1893) deep water breaking wave criteria. According to Michell (1893), breaking wave steepness in the deep water becomes constant,

$$\frac{H_{b*}}{L_{b*}} = 0.142 \quad (2.15)$$

Transforming (2.15) to the equivalent linear wave characteristics yields

$$\frac{H_b}{L_b} = 0.17 \quad (2.16)$$

Imposing our model to assure (2.16), the fitting function f must converge to a constant value, $f \rightarrow 2\pi H_b/L_b = 2\pi \times 0.17 \sim 1.07$, for a deep water limit, $h_b/L_0 > 0.5$. Requiring this condition, define the form of f by

$$f = 1.07 - a_1 \exp \left[-a_2 \left(\frac{h_b}{L_0} \right)^{b_1} \right] + a_3 \tan^{b_2} \beta_0 \exp \left[-a_4 \left(\frac{h_b}{L_0} \right)^{b_6} \right] \quad (2.17)$$

This form is similar to Isobe's (1986) breaking formula, which is fitted to Watanabe et al.'s (1984) breaking criteria. Best-fit parameters, a_i and b_i are obtained through Monte-Carlo least-square inversion method with the following constraints in deep and shallow water limit.

Constraint in deep water limit

As discussed in the general concepts, the model has to become constant when $h_b/L_0 > 0.5$, which is the deep water wave condition. In order to ensure this feature, we included the constraint stated by

$$|1.07 - f(h_b/L_0)| < 0.01 \quad \text{for } kh > 0.5 \quad (2.18)$$

Constraint in shallow water limit

As discussed later in Section 2.3, it is observed that, well-inside the surf zone, broken waves stop breaking and recover when the ratio of wave height and the water depth, $\gamma = H/h$, reaches its recovery value, γ_r . From this observation, breaking wave height must be larger than this recovery wave height, i.e.

$$f > \gamma_r = 0.3 \quad \text{for } kh \rightarrow 0 \quad (2.19)$$

Any combinations of parameters that violate either (2.18) or (2.19) were discarded through Monte-Carlo method. Experimental data used to obtain optimum coefficients for (2.17) are summarized in the following section.

2.2.3 Experimental Data

In order to determine the fitting function, $f(h_b/L_0, \tan \beta_0)$ introduced in (2.17), we need to know dimensionless parameters of h_b/L_0 , $\tan \beta_0$, and $k_b H_b / \tanh k_b h_b$. Among these parameters, the breaking water depth, h_b , deep water wave length, L_0 and the bottom slope, $\tan \beta_0$, are directly obtained from the experimental conditions and observed data. The wave number at the breaking point, k_b , can also be determined by linear wave theory from h_b and the wave period, T . Finally, the equivalent linear breaking wave height, H_b , is computed from incident wave conditions measured near the wave maker by linear wave theory with Hunt's (1952) wave attenuation formula due to friction along side walls and bottom.

Table 2.2 summarizes the experimental data used in this study. In Table 2.2, N is the number of data sets available in each experiment and H'_0/L_0 is a deep water wave steepness equivalent to the linear breaking wave height, H_b . Equivalent linear breaking wave height, H_b , obtained from incident wave conditions should be smaller than measured, i.e., non-linear breaking wave heights, $H_{b*,meas}$, because the non-linear wave height is usually larger than equivalent linear wave height. However, as is also pointed out by Goda (1970), some data sets shown in the table exhibited $H_b > H_{b*,meas}$. This contradiction may be partially due to underestimation of the wave attenuation by Hunt's (1952) formula. While Hunt's (1952) model is based on laminar boundary layer conditions, actual wave attenuation may be larger because of the intensive turbulence especially near the breaking point. To avoid obtaining an unrealistic breaking criteria, we excluded these experimental data.

Figure 2-7 shows the distributions of $k_b H_b / \tanh k_b h_b$ obtained from the experimental data as functions of $\tan \beta_0$ and h_b/L_0 . As seen in the figure, $k_b H_b / \tanh k_b h_b$ decreases as h_b/L_0 and $\tan \beta_0$ decrease.

Table 2.2: Summary of experimental data (N is the number of data available)

Authors	N	$\tan \beta_0$	H'_0/L_0
Iversen (1951)	63	1/10, 20, 30, 50	0.0023–0.073
Goda (1964)	33	1/100	0.0026–0.048
Toyoshima et al. (1967)	68	1/20, 30	0.0035–0.061
Bowen et al. (1968)	11	1/12	0.0071–0.049
Nagayama (1983)	1	1/20	0.025
Hansen and Svendsen (1984)	1	1/34.25	0.017
Okayasu (1988)	9	1/20	0.0087–0.049
Sato et al. (1988)	3	1/20	0.029–0.048
Cox and Kobayashi (1996)	1	1/35	0.014

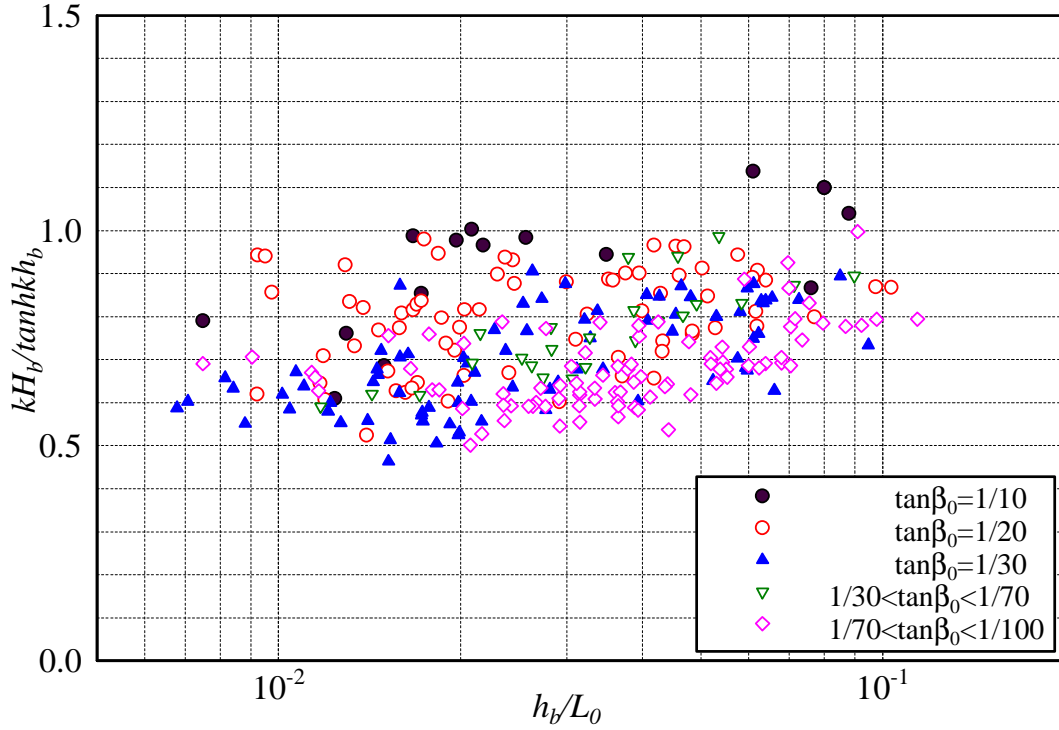


Figure 2-7: $kH_b / \tanh kh_b$ vs. h_b / L_0 (experimental data)

2.2.4 Complete Breaking Criteria

Finally, the best-fit curve, f , satisfying (2.18) and (2.19) is calibrated and the complete breaking wave criteria is expressed by

$$\begin{aligned} \frac{k_b H_b}{\tanh k_b h_b} = & 1.07 - 0.59 \exp \left(-8.6 \frac{h_b}{L_0} \right) \\ & + 2.59 \tan \beta_0 \exp \left(-15.1 \left(\frac{h_b}{L_0} \right)^{1.5} \right) \end{aligned} \quad (2.20)$$

Figure 2-8 shows the comparisons of the present index, (2.20), Watanabe et al.'s (1984) index, and the experimental data used in this study. As seen in the figure, the present breaking criteria reasonably represents the experimental data. Comparing with Watanabe et al.'s (1984) index, the present breaking model tends to predict a larger breaking parameter, $k_b H_b / \tanh k_b h_b$, in deeper water, $h_b / L_0 > 0.1$, and smaller $k_b H_b / \tanh k_b h_b$ in relatively shallow water, $h_b / L_0 < 0.1$. This difference is physically more intuitive if the breaking indices are transferred to relative depth, h_b / H_0 , in terms of H_0 / L_0 and $\tan \beta_0$ as shown in Figure 2-9. This index directly predicts the breaking water depth once the bottom slope and the deep water wave characteristics are specified. As seen in the figure, the present criteria agree well with experimental data and predicts larger breaking water depth than Watanabe et al.'s (1984) criteria when H_0 / L_0 is relatively small. Figure 2-10 shows the relative errors of predicted and measured breaking water depth for each bottom slopes ($1 - h_{b,data} / h_{b,pred.}$) and Table 2.3 shows the means (μ) and the standard deviations (σ) of these relative error in each bottom slope and in all the data sets. The table also shows the same relative error analysis for Watanabe et al.'s breaking criteria. As seen in Figure 2-10, the errors are evenly distributed around the predictions along wide range of H_0 / L_0 and $\tan \beta_0$. From Table 2.3, the mean error (bias) of the predictions against the entire data sets is less than one percent and its standard deviation is less than 10 percent.

Figure 2-11 shows the distribution of H_{b*} / h_b as a function of h_b / L_0 and the uniform bottom slope, β_0 . The present model first determines H_b / h_b from (2.20) and (2.2) is applied to evaluate the equivalent non-linear breaking wave height, H_{b*} , and finally

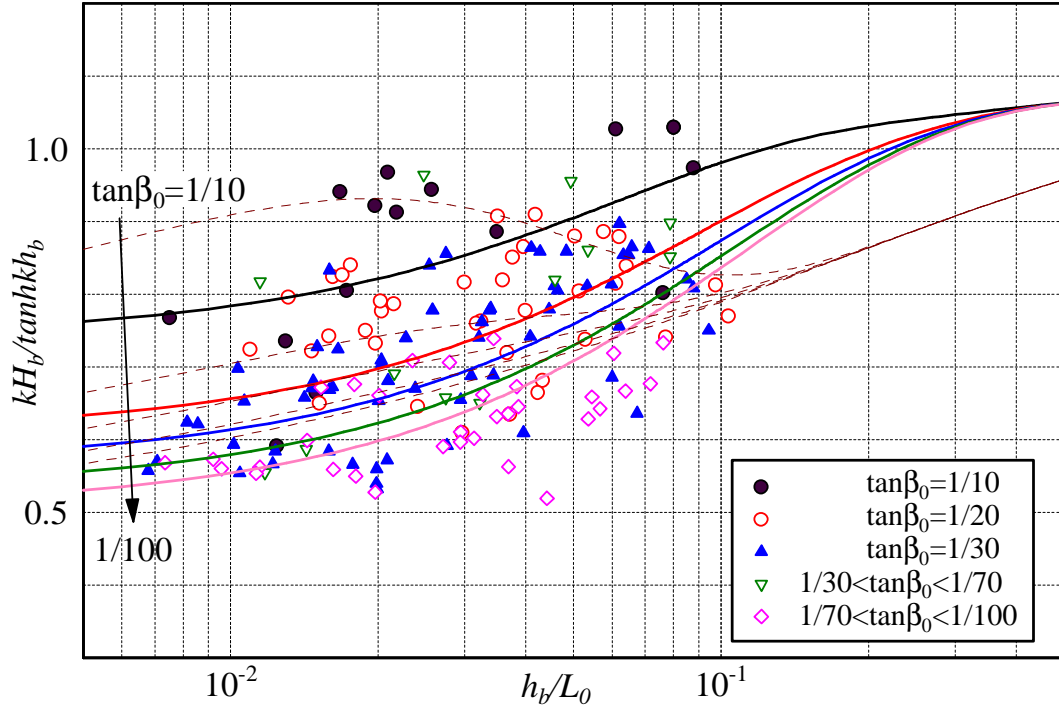


Figure 2-8: Comparisons of the present model and measurements of breaking wave parameter, $kH_b / \tanh kh_b$ as functions of h_b / L_0 and $\tan \beta_0$; Present index (full line), Watanabe et al.'s (1984) index (dotted line) and measurements on various slopes (circles, triangles, and diamonds)

Table 2.3: Means and standard deviations of relative errors between predicted and measured breaking water depth.

$\tan \beta_0$	Present Model		Watanabe et al.(1984)	
	μ (%)	σ (%)	μ (%)	σ (%)
1/10	0.38	11.09	-5.90	18.11
1/20	1.97	9.51	-2.27	9.27
1/30	0.79	8.90	-4.61	11.08
1/30 - 1/70	8.28	13.71	3.16	13.04
1/70 - 1/100	-2.31	8.31	-10.95	13.59
Total	0.95	9.60	-4.91	12.27

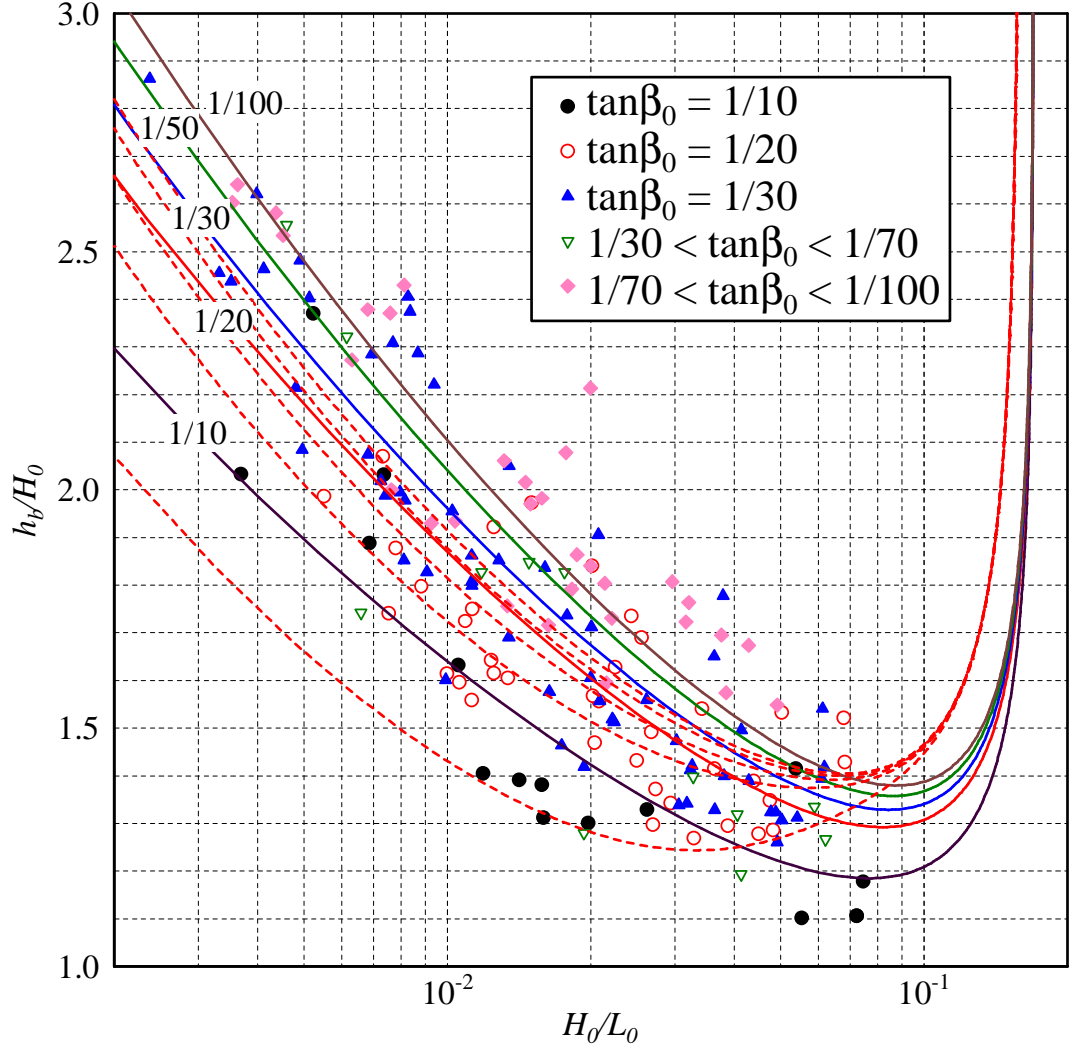


Figure 2-9: Comparisons of the present model and measurements of relative breaking water depth, h_b/H_0 as functions of H_0/L_0 and $\tan \beta_0$; Present index (full line), Watanabe et al.'s (1984) index (dotted line) and measurements on various slopes (circles, triangles, and diamonds)

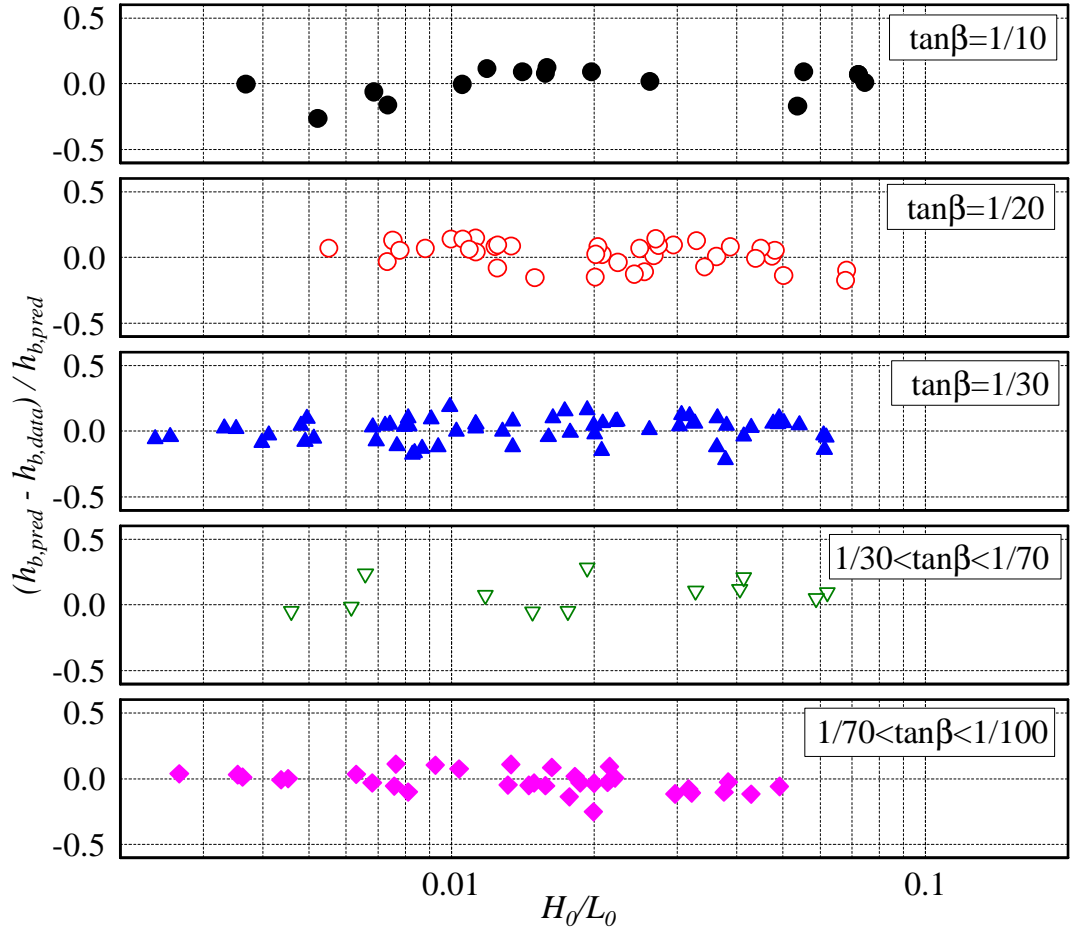


Figure 2-10: Relative errors of breaking water depth, h_b , between model and data as functions of H_0/L_0 and $\tan\beta_0$.

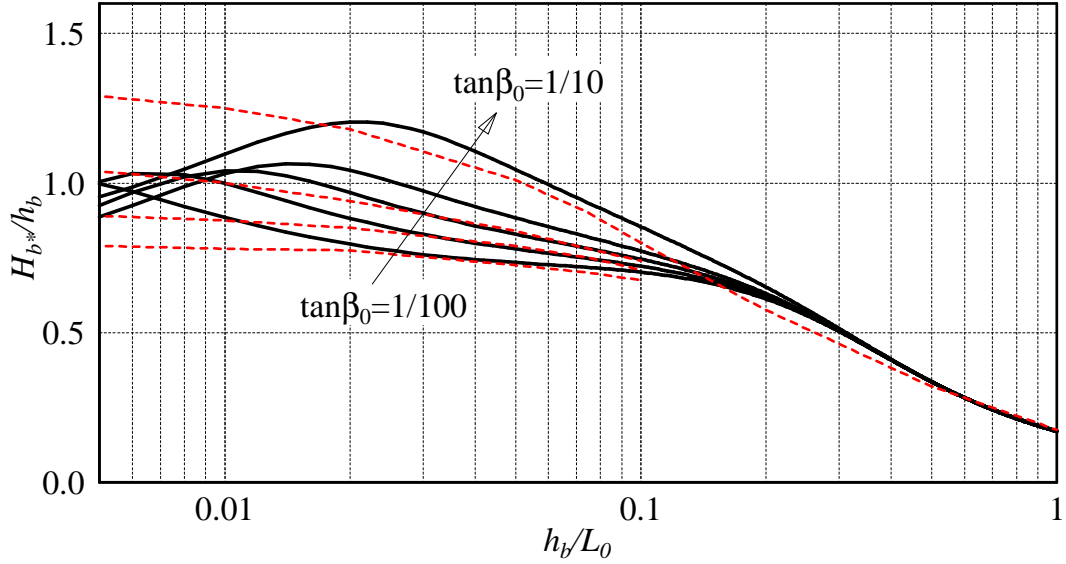


Figure 2-11: Comparisons of H_{b*}/h_b as functions relative breaking water depth, h_b/L_0 , and the bottom slope, β_0 , predicted by Goda's (1970) model and the present model; Present model (full line) and Goda's (1970) model (dotted line and circles).

yield H_{b*}/h_b . In the figure, solid lines are predictions of the present model and circles were obtained from Goda's (1970) breaking criteria. As seen in the figure, our model agrees very well with Goda's empirical curves, which are based on a number of experimental data. It should be stressed that we are not using the measured non-linear breaking wave height, H_{b*} to construct our breaking criteria. Figures 2-9, 2-10, and 2-11 therefore verify the validity of both non-linear wave and linear breaking criteria models, i.e. equations (2.2) and (2.20).

2.3 Broken Waves

Once the wave reaches the breaking point and progresses beyond breaking, energy dissipation must be introduced in the wave energy balance equation in order to evaluate the attenuation of the broken wave heights. We adopt Dally et al.'s (1985)

formulation for the breaking wave energy dissipation model

$$\frac{\partial (EC_g)}{\partial x} = -K_b \frac{C_g}{h} (E - E_r) \quad (2.21)$$

where K_b is a proportionality constant, C_g is the (linear) group velocity, $E = \rho g H^2 / 8$ is local wave energy where $H = \gamma h$ is the equivalent linear wave height and E_r is the wave energy based on the recovery wave height, $H_r = \gamma_r h$, of the broken wave if it were to continue to travel in the local depth, h . As seen from (2.21), the energy dissipation rate is assumed to be proportional to the amount by which the local wave energy flux exceeds its recovery value.

Wave set-up, $\bar{\eta}$, is computed from the cross-shore force balance given by

$$\frac{\partial \bar{\eta}}{\partial x} = -\frac{1}{\rho g h} \frac{\partial S_{xx}}{\partial x} \quad (2.22)$$

where

$$S_{xx} = E \left(2 \frac{C_g}{C} - \frac{1}{2} \right) \quad (2.23)$$

is the radiation stress.

2.3.1 Determination of K_b

In contrast to Dally et al. (1985), who took $K_b = \text{constant}$, we follow a similar procedure to that of Watanabe and Dibajnia (1988), whose dissipation model is different from (2.21), and determine K_b as a function of bottom slope conditions. In order to determine K_b , we make use of the experimental observations that broken waves on a plane beach, well inside the surf zone, approach a constant wave height to depth ratio (e.g. Figure 6 in Horikawa and Kuo, 1966). In other words, we assume that, well inside the surf zone, $H = \gamma_s h$ with $\gamma_s = \text{constant}$, i.e., $\partial \gamma_s / \partial x = 0$ where x is the horizontal axis in the wave propagation direction. Substituting this condition into (2.21) and applying linear long wave theory, K_b is derived as

$$K_b = -\frac{5}{2} \frac{\gamma_s^2}{\gamma_s^2 - \gamma_r^2} \frac{\partial h}{\partial x} = \frac{5}{2} \frac{\gamma_s^2 \tan \beta}{\gamma_s^2 - \gamma_r^2} \quad (2.24)$$

where $\tan \beta = \partial h / \partial x = \partial (h_0 + \bar{\eta}) / \partial x$ is the slope of the mean water depth. As seen in Eq. (2.24), K_b is now a function of effective beach slope, β , which is an improvement of Dally et al.'s (1985) model.

2.3.2 Evaluation of γ_s and γ_r

The information we now require to complete (2.24) is the values of γ_s and γ_r . Since our breaking wave dissipation model is based on linear wave theory, γ_s and γ_r should also be the values corresponding to the equivalent linear wave heights. In order to determine these values, we use existing experimental data on broken wave heights well inside the surf zone on plane beaches for various slopes, β . The data used were obtained by Horikawa and Kuo (1966), Nadaoka et al. (1982), Nagayama (1983), Hansen and Svendsen (1984), Okayasu et al. (1988), Sato et al. (1988), and Okayasu and Katayama (1992) and for each data set only the broken wave height closest to shoreline, i.e., well inside the surf zone, is used. From these experimental data, we obtain the ratio, γ_{s*} , of measured and therefore non-linear wave height, H_* , to local depth, h , for a variety of bottom slopes. For $\beta = 0$, i.e., broken waves traveling into water of constant depth, $\gamma_{s*}(\beta = 0) = \gamma_{r*}$ represents the non-linear recovery wave height. Using the experimental information on β , h/L_0 , and H_0/L_0 , Eq.(2.2) is used to transform the measured non-linear wave heights to their linear equivalents. Details of this procedure are explained in the following section on Model Application when H_* is known. In this manner, the ratio, γ_s , of equivalent linear wave height to water depth is obtained for different slopes (with $\gamma_{s*}(\beta = 0) = \gamma_{r*}$). Figure 2-12 shows the distribution of γ_s as a function of β . Figure 2-12, in which 180 γ_s -values are plotted, shows a relatively small scatter and clearly demonstrates that γ_s is a rather well-defined function of β . Moreover, since γ_r and γ_s values were found not to exhibit any systematic dependency on other parameters, such as H_0/L_0 and h/L_0 , we simply determine γ_s as a function of β by linear regression of the data shown in Figure 2-12. The resulting expression for γ_s and γ_r are then given as

$$\gamma_s = \gamma_r + A \tan \beta = 0.3 + 4 \tan \beta \quad (2.25)$$

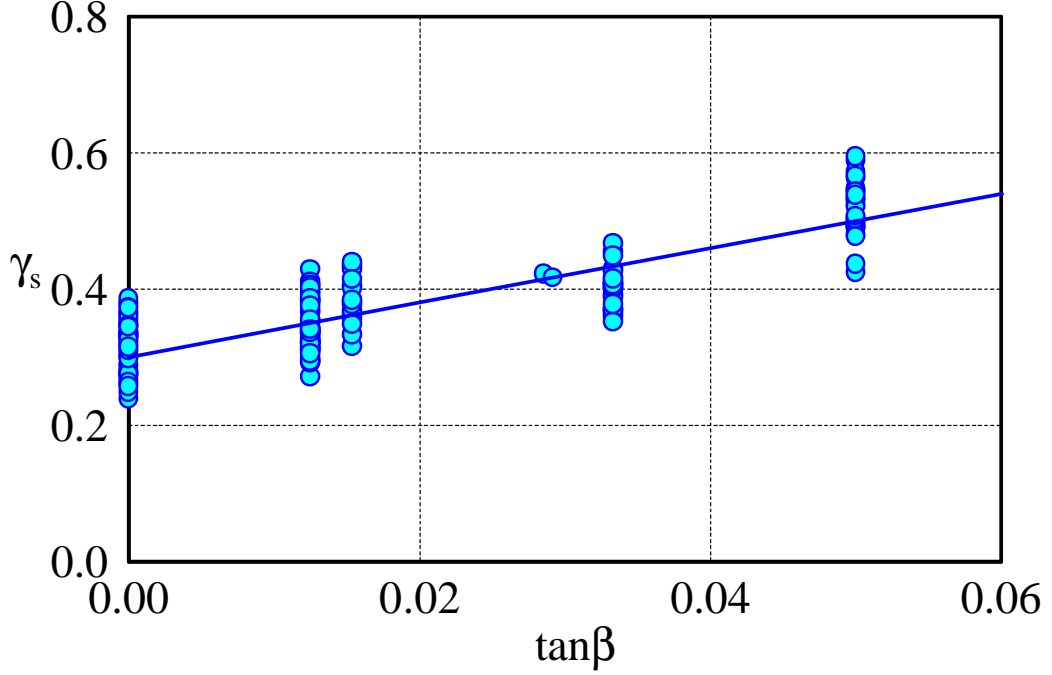


Figure 2-12: γ_s vs. $\tan\beta$; experiments (circles) and Eq.(2.25) (full line)

For negative slopes, $\beta < 0$, e.g. corresponding to the landward slope of an offshore bar, (2.24) is evaluated as if $\beta = 0$ for which the present model, in contrast to the model by Watanabe and Dibajnia (1988), gives a non-zero value of $K_b = 0.094$. Validity of this procedure when $\beta < 0$ is examined later through comparison with measured data.

2.4 Model Application

Since the present model is based entirely on the equivalent linear wave, it is relatively simple to apply. If information on local measured (non-linear) wave height is available, we may use this information to evaluate the equivalent linear wave and then other non-linear wave characteristics such as near-bottom orbital velocity. Otherwise, equivalent linear wave conditions will be directly predicted by linear theory coupled

with the breaking wave model. Non-linear wave characteristics are then determined from predicted equivalent linear wave characteristics. Computational methodologies for these two scenarios are outlined in the following sections.

2.4.1 H_* is Known

If local non-linear wave height, H_* , local water depth, h , and local bottom slope, β_0 , are known, we first guess the equivalent linear wave height, H' , which may be slightly smaller than H_* . From given H' , h , and wave period, T , corresponding h/L_0 and H'_0/L_0 are computed by linear theory. Here, H'_0 is determined as the deep water wave height that through linear shoaling to the given water depth, h , results in the linear wave height, H' , i.e., $H'_0 = H'/K_s$, where K_s is the linear shoaling coefficient, no matter how the wave has traveled and deformed to arrive at that particular location. The non-linear wave height, H'_* , is then predicted by substituting H' , h/L_0 , H'_0/L_0 and β_0 into (2.2). If H'_* is not identical to H_* , the value of H' is modified and the same procedures repeated until $H'_* = H_*$ is obtained. Once $H'_* = H_*$, the equivalent linear wave height is determined as $H = H'$ and $H_0 = H/K_s$ after which other non-linear wave characteristics may be evaluated from (2.3) to (2.6).

2.4.2 H_* is Unknown

For given deep water (linear) wave conditions, linear theory is used to shoal the waves up to the breaking-point which conveniently is expressed by (2.20) in terms of the equivalent linear wave characteristics. After the breaking point, (2.21) is solved numerically, with K_b locally given by (2.24), to obtain the variation of the equivalent linear wave height shoreward of the break-point. If the local bottom slope becomes negative, $\beta_0 = 0$ is assumed. Wave set-up is also numerically computed by (2.22) and change of the mean water level is reflected in the mean water depth as numerical computation proceeds landward. Non-linear wave characteristics are evaluated from (2.2) to (2.6). Similar to the procedure when H_* is known, H_0 is determined from the linear shoaling coefficient, i.e., $H_0 = H/K_s$, where H is the predicted local equivalent

linear wave height.

2.5 Extension of the Model to Random Waves

Since the breaking wave dissipation model is based on linear wave theory, it is possible to make a simple extension of the model to random wave conditions. In order to develop the breaking random wave dissipation model, we first make the following three assumptions: (i) random waves are narrow-banded and represented by a single period; (ii) wave heights are Rayleigh distributed; and (iii) only waves of heights larger than the local breaking wave height are breaking. Under these assumptions, the averaged energy balance equation (2.21) for the random waves is expressed as

$$\frac{\partial}{\partial x} \int_0^\infty p(\xi) E C_g d\xi = -\frac{K_b}{h} C_g \int_{\xi_b}^\infty p(\xi) (E - E_r) d\xi \quad (2.26)$$

where $p(\xi) = 2\xi \exp(-\xi^2)$, $\xi = H/H_{rms}$ and $\xi_b = H_b/H_{rms}$. The left hand side of (2.26) is identical to the periodic equation (2.21) with the wave height being replaced by the rms value for the random wave conditions. The right hand side of (2.26), however, receives contributions only from individual waves with heights greater than the breaking wave height corresponding to the local depth. This contribution is evaluated from the assumed Rayleigh distributed wave heights, and the model is readily applied for random waves to predict local rms wave heights, $H_{rms} = \gamma_{rms} h$, by the following formula

$$\frac{\partial (E C_g)}{\partial x} = -K_b \frac{C_g}{h} \exp(-\xi_b^2) [E (1 + \xi_b^2) - E_r] \quad (2.27)$$

where $E = \rho g H_{rms}^2 / 8$, $E_r = \rho g (\gamma_r h)^2 / 8$ with γ_r determined from (2.25) and H_b used in ξ_b is determined by use of (2.20).

2.6 Comparison with Experimental Results

2.6.1 Wave Heights and Wave Set-up

Figure 2-13 shows a comparison of predicted (non-linear) and measured wave heights and wave set-up obtained from (2.22) for the experiment with periodic waves normally incident on a straight beach reported by Cox and Kobayashi (1996). In the figure, predicted equivalent linear wave heights are also shown. As seen in the Figure, predicted equivalent linear wave heights are clearly smaller than the measured wave heights while predicted non-linear wave heights agree well with the experimental data. It is emphasized that $H_*/h \simeq 0.8$ in the vicinity of the breaking point. Thus, the excellent agreement between measured and predicted non-linear wave heights in the vicinity of the breaking point verifies the applicability of our extrapolated transform formula for wave heights, (2.2), beyond the computed range of $H_*/h < 0.4$. Figure 2-14 shows a comparison of predicted and measured significant wave heights and wave set-up for one of the experiments with random waves normally incident on a barred concrete beach profile reported by Okayasu and Katayama (1992). Figures 2-15 and 2-16 show the same comparisons for the experiments with random waves obliquely incident on barred movable bed beach profiles reported by Wang et al. (2002). The angle of incidence in the experiments reported by Wang et al (2002) is small, less than 10° , so the effect of oblique incidence is safely neglected in the breaking wave and set-up model which treats the waves as normally incident. As seen in Figures 2-14 through 2-16, predictions of both wave heights and mean water level agree well with measured data even where the water depth is increasing, i.e., $\beta < 0$, on the landward side of the bar. Moreover, it should be pointed out that all predictions agree well with measurements in spite of none of these experiments having been used to calibrate the model coefficients.

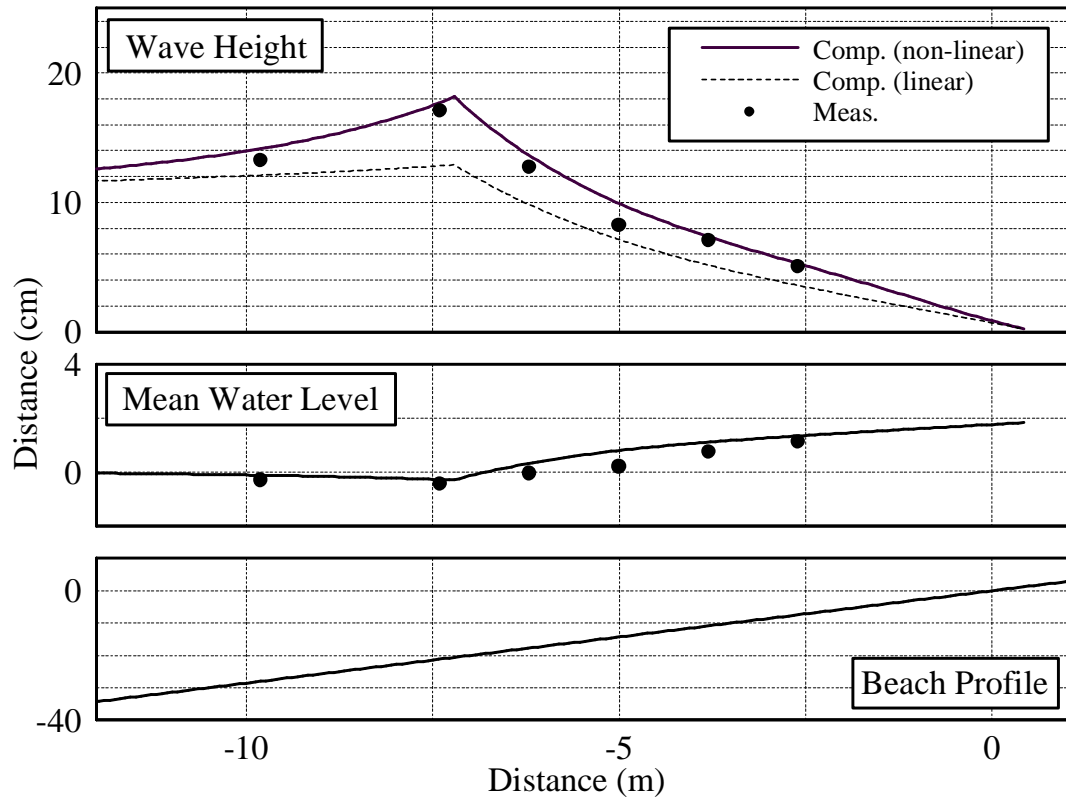


Figure 2-13: Comparison of measured and predicted wave heights and wave set-up (Cox and Kobayashi, 1996); measurements (circles), predicted non-linear wave heights (full line), and predicted equivalent linear wave heights (dotted line).

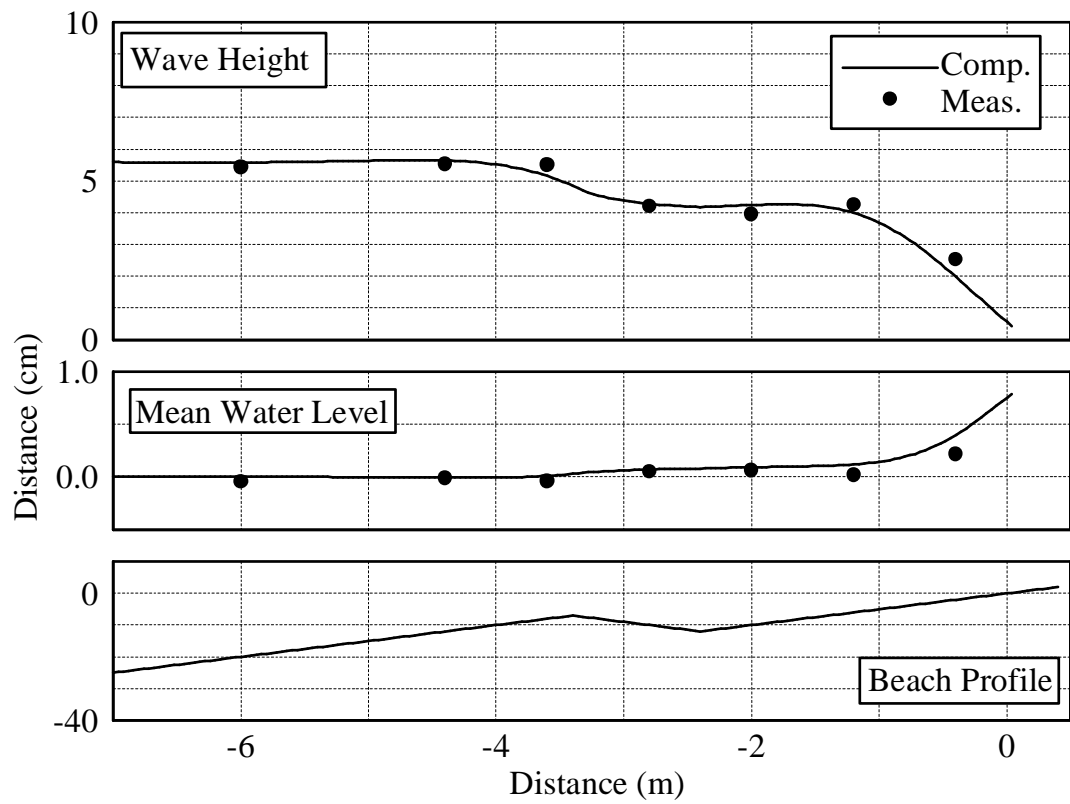


Figure 2-14: Comparison of measured and predicted significant wave heights and wave set-up (Okayasu and Katayama, 1992); measurements (circles) and predictions (full line).

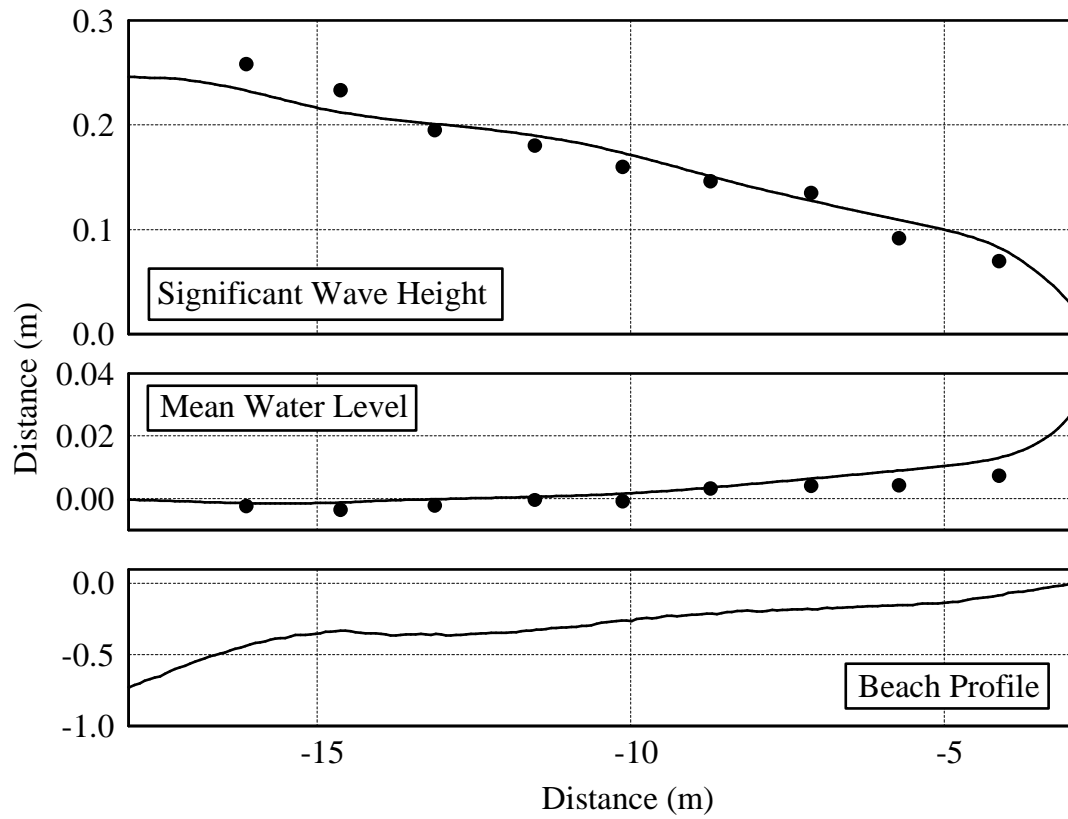


Figure 2-15: Comparison of measured and predicted significant wave heights and wave set-up (Wang et al., 2002, spilling breaker); measurements (circles) and predictions (full line).

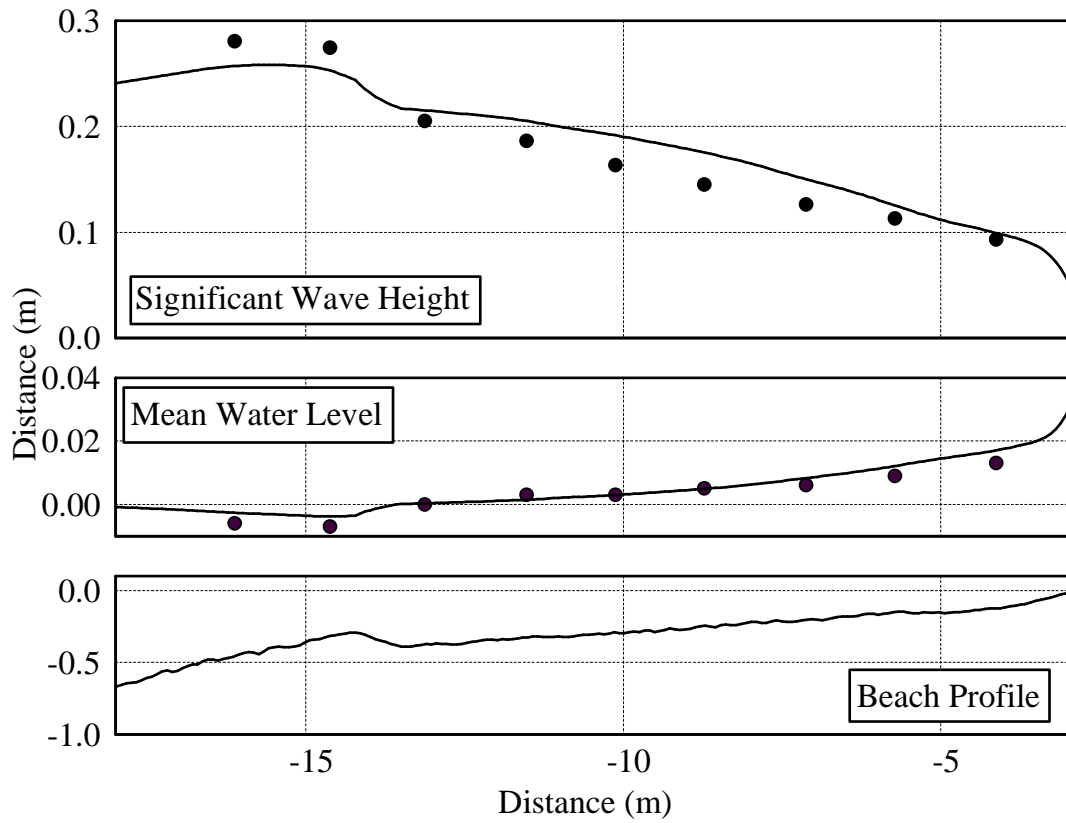


Figure 2-16: Comparison of measured and predicted significant wave heights and wave set-up (Wang et al., 2002, plunging breaker); measurements (circles) and predictions (full line).

2.6.2 Slope-Dependency of the Wave Attenuation

In order to examine the slope-dependency of the present model, the model was applied to different bottom slope conditions. Figure 2-17 shows the comparisons of wave heights predicted by the present and Dally et al.'s (1985) models with experimental data for periodic waves incident on straight beaches with various slopes. In the figure, non-linear wave heights predicted by the present model are compared with the measurements. For the computations of Dally et al.'s model the present non-linear wave and wave breaking models were applied up to the breaking point since their model does not determine the non-linear breaking wave heights. Experimental data were obtained by Mizuguchi et al. (1978), Okayasu and Katayama (1992), Cox and Kobayashi (1996) and Stive and Wind (1986) for $1/10$, $1/20$, $1/35$ and $1/40$, respectively. From the comparisons with data, the present model predicts reasonable non-linear wave heights up to the breaking point. In the surf zone, agreement of broken wave heights between data and the present model is also excellent while Dally et al.'s model, which applies a constant K_b , over-predicts broken wave heights when $\tan \beta = 1/10$, for which larger K_b is required for better predictions. This comparison therefore verifies the slope-dependency of K_b as proposed in the present model.

2.6.3 Non-linear Velocity Parameters

Figure 2-18 shows the comparison of non-linear parameters of the near-bottom wave orbital velocity for the experiment by Cox and Kobayashi (1996), which is the same experiment used in Figure 2-13. In this figure circles are the values obtained from the measured data and solid lines are the predictions obtained from (2.3) to (2.6) using predicted equivalent linear wave heights. Again it is noted that the excellent agreement near the breaking point, where $H_*/h \simeq 0.8$, supports our use of the extrapolated transform formulae for non-linear near-bottom orbital velocity characteristics. As seen in the figure, predictions of velocity height, U_{b*} , and T_c/T agree very well with the measured data while the model overpredicts u_{c*}/U_{b*} inside the surf zone. Since the agreement between measured and predicted u_{c*}/U_{b*} is quite good in the

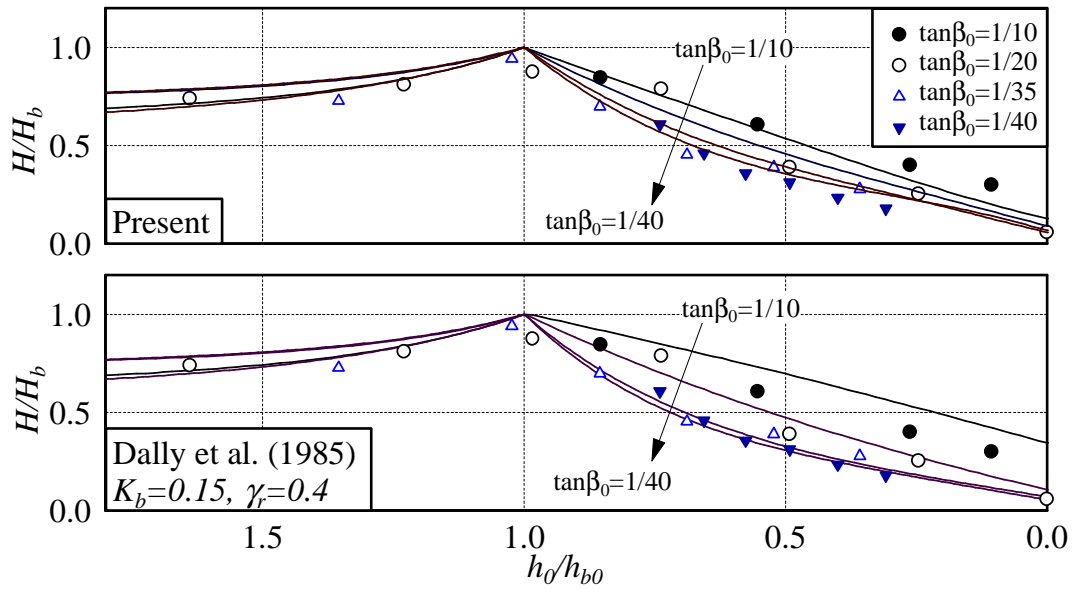


Figure 2-17: Comparisons of predicted (full line) and measured wave heights on uniform slopes. Measurements were reported by Mizuguchi et al. (1978), Okayasu and Katayama (1992), Cox and Kobayashi (1996), and Stive and Wind (1986) for $\tan \beta_0 = \partial h_0 / \partial x = 1/10, 1/20, 1/35$, and $1/40$.

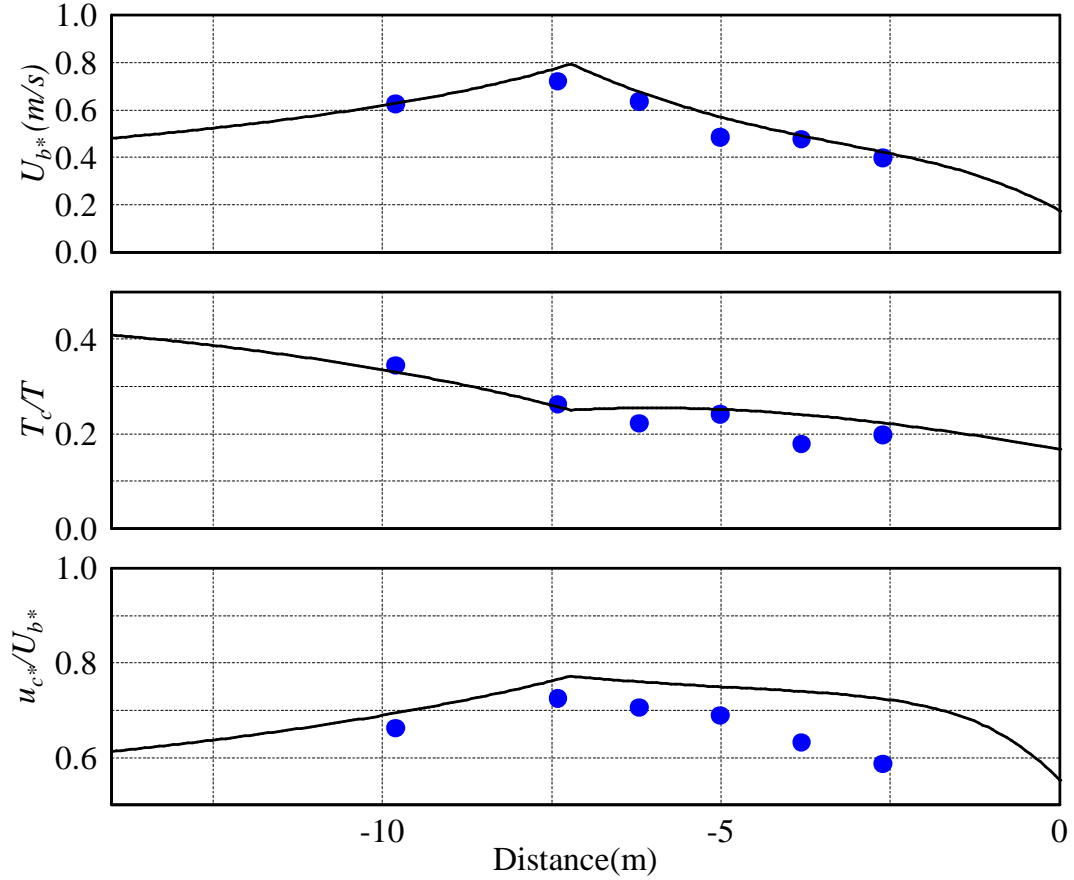


Figure 2-18: Measured and predicted non-linear wave characteristics of near-bottom orbital velocity profiles. (Cox and Kobayashi, 1996); measurements (circles) and predictions (full line)

vicinity of the break-point, this disagreement inside the surf zone suggests that other physical mechanisms should be accounted for inside the surf zone in order to improve predictions of near-bottom orbital velocity skewness.

Similarly, Figure 2-19 shows predictions of non-linear wave height, H_* , non-linear near-bottom wave velocity height, U_{b*} , and asymmetry and skewness parameters, T_c/T and u_{c*}/U_{b*} compared with measurements for periodic waves incident on a uniform slope (Test 6A-N reported by Hamilton and Ebersole, 2001). Here, T_c is the time between minimum and maximum near-bottom wave orbital velocity and u_{c*} is the maximum near-bottom orbital velocity. Hence $T_c/T = u_{c*}/U_{b*} = 0.5$

for linear sinusoidal waves. Measured values, shown as circles, were obtained by averaging 200 measured waves and the vertical lines represent the standard deviation of the measured data around the mean. As seen in Figure 2-19, excellent agreement is obtained between model predictions and measurements especially for U_{b*} , which plays an important role in the present hydrodynamic model's determination of the combined wave-current bottom shear stress. Whereas the model accurately predicts wave asymmetry, T_c/T , it tends to over-predict the skewness parameter, u_{c*}/U_{b*} inside the surf zone. Since the present non-linear wave model is based on Nwogu's (1993) modified Boussinesq equations, this comparison suggests that the Boussinesq equations may over-predict skewness of near-bottom wave orbital velocity inside the surf zone. Watanabe and Elnaggar (2000) pointed out that Boussinesq equation tends to overpredict u_{c*} inside the surf-zone from the comparisons of predicted and measured near-bottom wave orbital velocity profiles for periodic waves incident on a plane beach.

Figure 2-20 shows comparisons of predicted and measured wave heights and near-bottom wave orbital velocity heights for random waves incident on a uniform slope (Test 8A-E reported by Hamilton and Ebersole, 2001). The observed values for H_{rms} and U_{brms} shown as circles in Figure 2-20 were obtained from the measured time-series of surface elevation, $\eta(t)$, and near-bottom velocity, $u_b(t)$, through spectral analysis. Spectral contributions from frequencies above 4Hz and below 0.2Hz were omitted to remove high-frequency noise and surf-beats, which are not included in our steady state wave model. Noise-less time-series of $\eta(t)$ and $u_b(t)$ were then reconstructed from the these truncated spectral components and applied for individual wave analysis based on the zero-up-cross method. H_{rms} and U_{brms} obtained from individual wave analysis yielded near-identical values to those obtained from spectral analysis. Since the spectral analysis is based on linear theory and therefore yields linear rms-values, predicted H_{rms} and U_{brms} shown in the figure are based on linear theory. A measure of asymmetry, T_c/T , and skewness, u_{c*}/U_{b*} , for the random waves, compatible with our equivalent linear wave predictions, was obtained by individual wave analysis of the reconstructed time-series. Only waves with velocity heights, U_{b*} , larger than

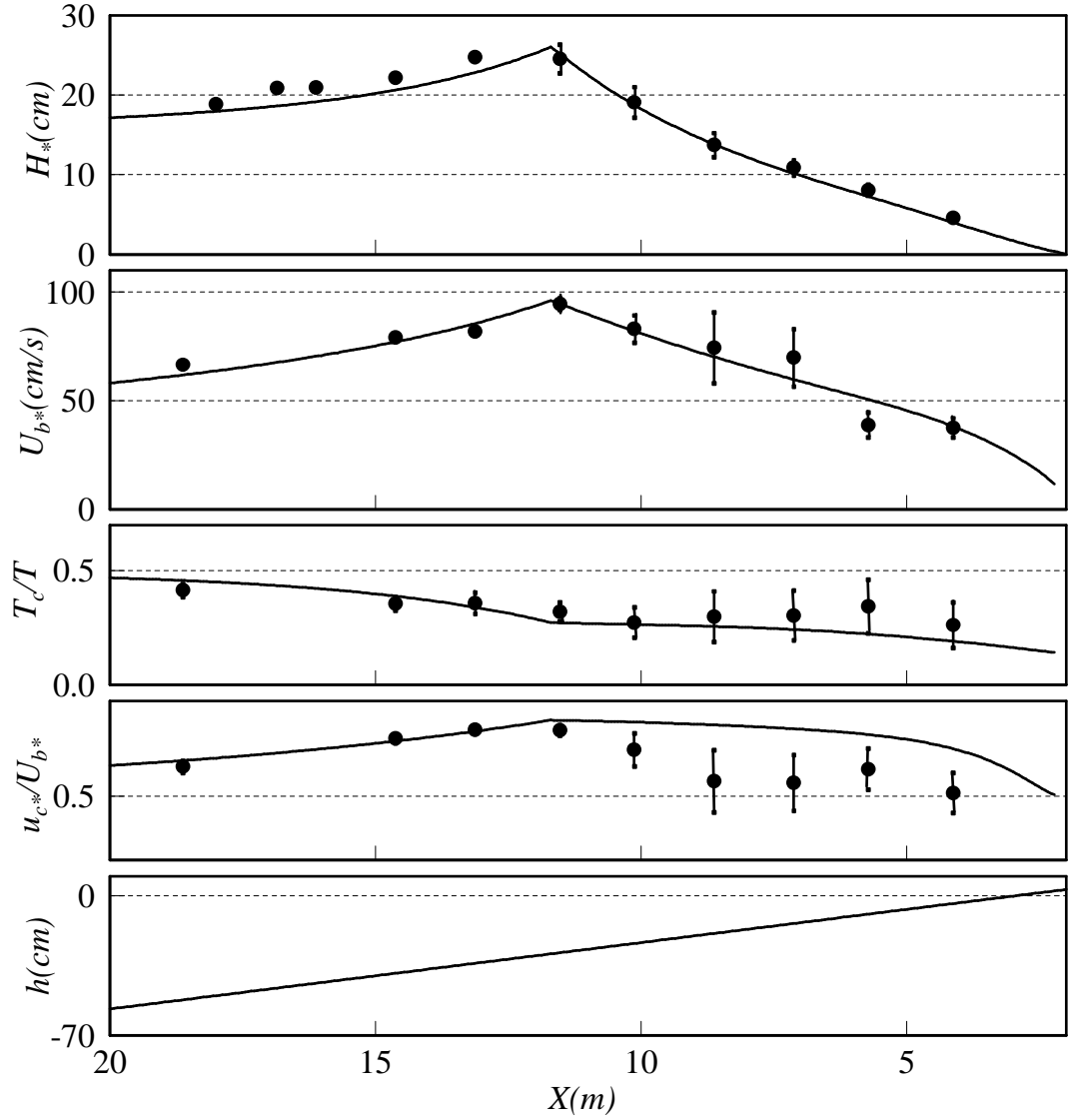


Figure 2-19: Comparisons of measured and predicted wave heights, H_* , near-bottom wave orbital velocity height, U_{b*} , asymmetry, T_c/T , and skewness, u_{c*}/U_{b*} , for periodic waves on plane 1 on 30 sloping beach. Measurements by Hamilton and Ebersole (2001): Test 6A-N

the median value of all individual waves were considered, and the resulting mean values of T_c/T and u_{c*}/U_{b*} are shown as full circles in Figure 2-20, with vertical lines representing the standard deviation around the mean.

Figures 2-21 and 2-22 show the same comparisons as Figure 2-20 but for random waves obliquely incident on movable bed beaches, respectively. Incident wave steepness for Figure 2-21 is smaller than that of Figure 2-22 and the waves in Figure 2-21 were spilling breakers and plunging breakers in Figure 2-22.

From comparisons in Figures 2-20, 2-21, and 2-22, the excellent predictive skills of the model are seen especially for predictions of H_{rms} and U_{brms} , which are of the most importance to determine bottom boundary conditions applied for the present near-shore mean current model. Good agreements shown in Figure 2-21 and 2-22 verify the model applicability to natural beach profiles in the field and arbitrary breaker types. Similar to the periodic wave case, Figure 2-19, predicted T_c/T and u_{c*}/U_{b*} agree well with measurements “outside” the surf zone but the model tends to overpredict u_{c*}/U_{b*} inside the surf zone. Equally good performances of the model for prediction of H_{rms} were presented by Tajima and Madsen (2002) and will be seen later when testing the near-shore mean current model in Chapter 4.

2.6.4 Non-Linear Near-Bottom Wave Orbital Velocity Profiles

Applicability of the non-linear near-bottom wave orbital velocity profile model is tested by comparing the model with experimental data obtained by Cox and Kobayashi (1996) and with Cnoidal Wave Theory (Isobe, 1979).

Besides wave heights and the wave set-up, Cox and Kobayashi (1996) also measured the time-series of the current velocity at multiple cross-shore locations and multiple elevations. Figures 2-23 and 2-24 show the comparisons of measured and predicted near-bottom wave orbital velocity profiles. In the figure, the measured “mean” velocity profiles were obtained by separately averaging the measured near-bottom velocities at the same wave phase. We then subtracted the net current velocities from

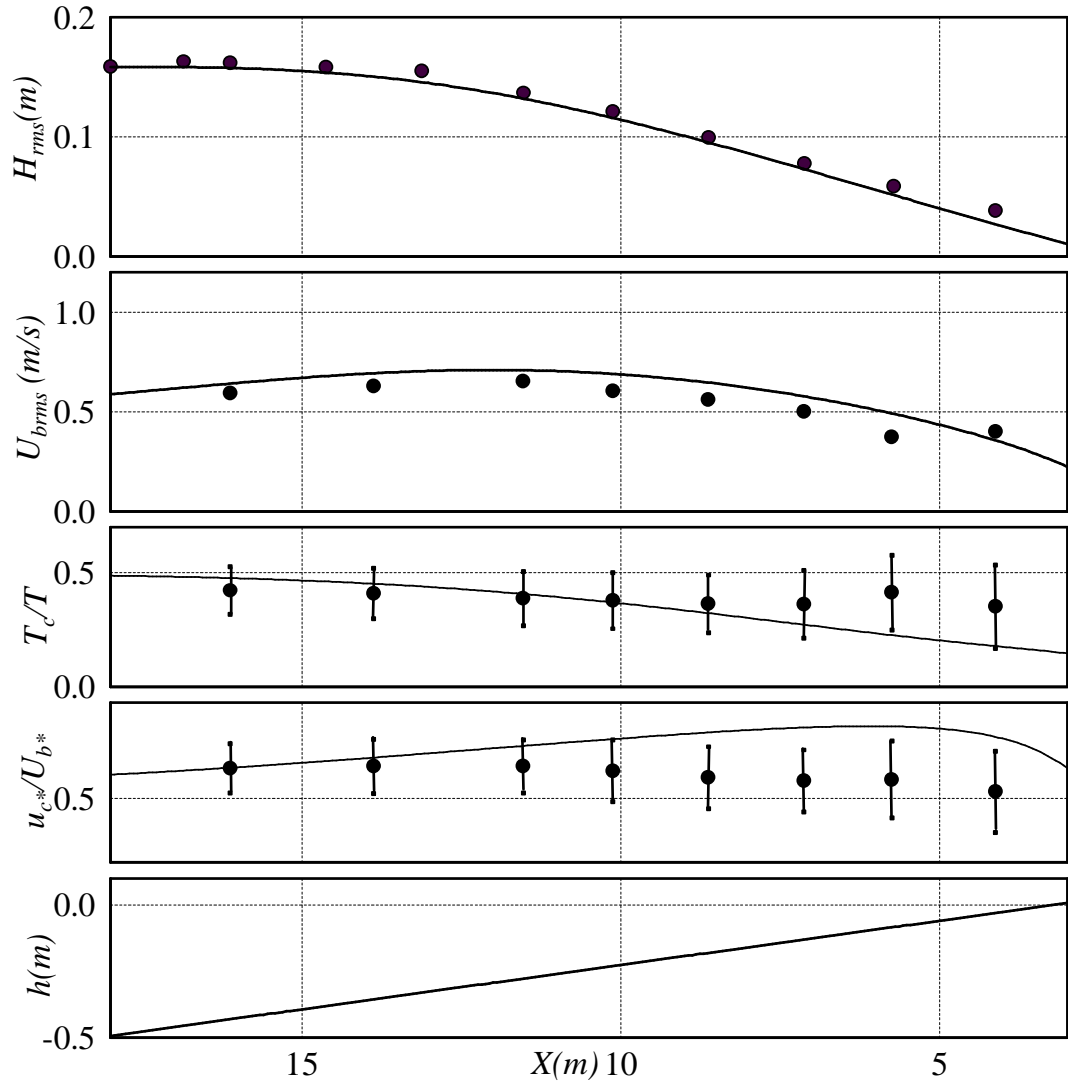


Figure 2-20: Comparisons of measured and predicted wave heights, H_* , near-bottom wave orbital velocity height, U_{b*} , asymmetry, T_c/T , and skewness, u_{c*}/U_{b*} , for random waves on plane 1 on 30 sloping beach. Measurements by Hamilton and Ebersole (2001): Test 8A-E

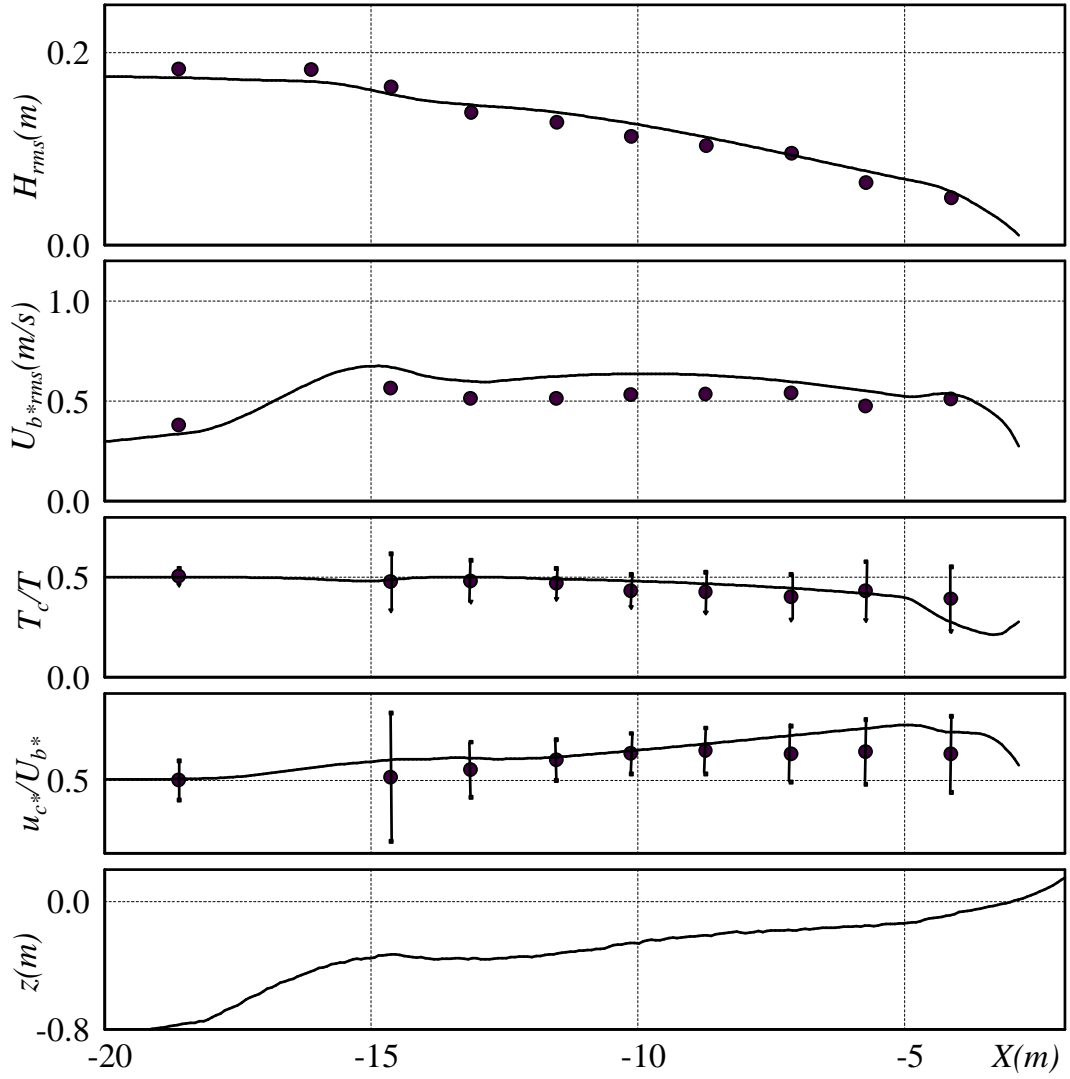


Figure 2-21: Comparisons of measured and predicted wave heights, H_* , near-bottom wave orbital velocity height, U_{b*} , asymmetry, T_c/T , and skewness, u_{c*}/U_{b*} , for random waves on movable bed beach. Measurements by Wang et al. (2002): Test 1, spilling breaker.

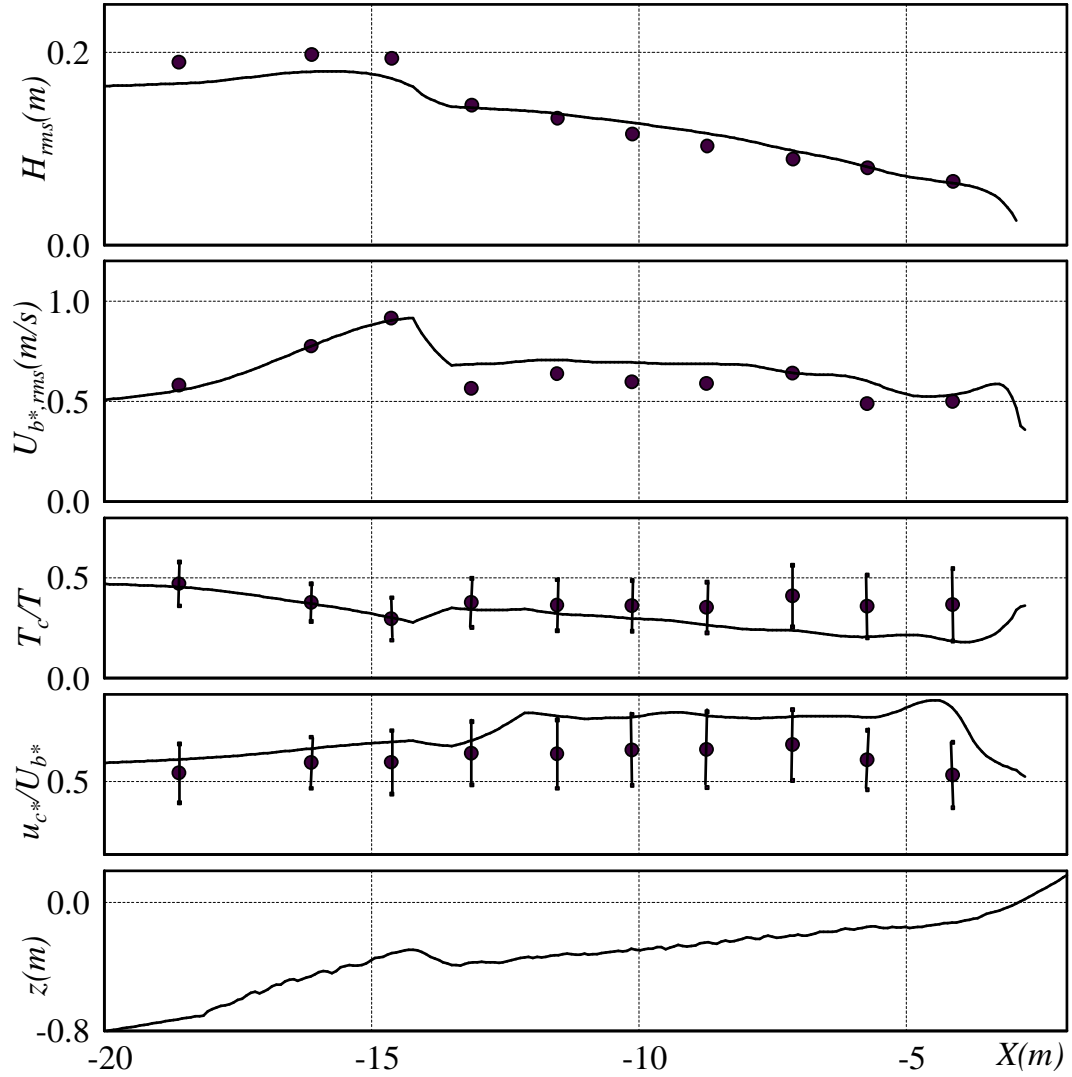


Figure 2-22: Comparisons of measured and predicted wave heights, H_* , near-bottom wave orbital velocity height, U_{b*} , asymmetry, T_c/T , and skewness, u_{c*}/U_{b*} , for random waves on movable bed beach. Measurements by Wang et al. (2002): Test 3, plunging breaker.

the obtained velocity profiles so that the component of mean return flow velocity is excluded. Development of a predictive model for the mean current velocities will be discussed later in Chapter 4. The non-linear wave parameters were predicted from the measured local wave heights at the same cross-shore location to avoid the predictive errors of our breaking and broken wave models. Methodologies for predicting non-linear wave parameters from known non-linear wave heights, H_* , are as discussed in Section 2.4.1. Cross-shore locations of each station shown in Figures 2-23 and 2-24 are identical to where the wave heights were measured (see Figure 2-13) and the station number in Figures 2-23 and 2-24 increases from deeper water toward the shoreline. As seen in Figure 2-13, station 1 is outside the surf zone, station 2 is in the vicinity of the breaking point, and stations 3 through 6 are inside the surf zone. Predicted approximation profiles agree well with measured data even inside the surf zone.

2.7 Summary and Conclusions

Numerical experiments with weakly non-linear periodic waves shoaling across a plane sloping bottom were used to establish simple expressions relating non-linear wave characteristics, x_* , to those obtained when the waves were shoaled according to linear wave theory, x . These relationships, (2.2) through (2.6), are of the form

$$x_* = xf(H_0/L_0, h/L_0, \tan\beta) \quad (2.28)$$

in which H_0/L_0 is the deep water (linear) wave steepness, h/L_0 is the local relative depth, $\tan\beta$ is the local bottom slope, and x is the prediction afforded by linear theory when the deep water wave is shoaled to the local depth, i.e., the equivalent linear wave conserves energy flux.

Using the relationships represented by (2.28) non-linear wave characteristics may be reconstructed from knowledge of the characteristics of their linear equivalent. To obtain this knowledge a model, based entirely on linear wave theory, was developed

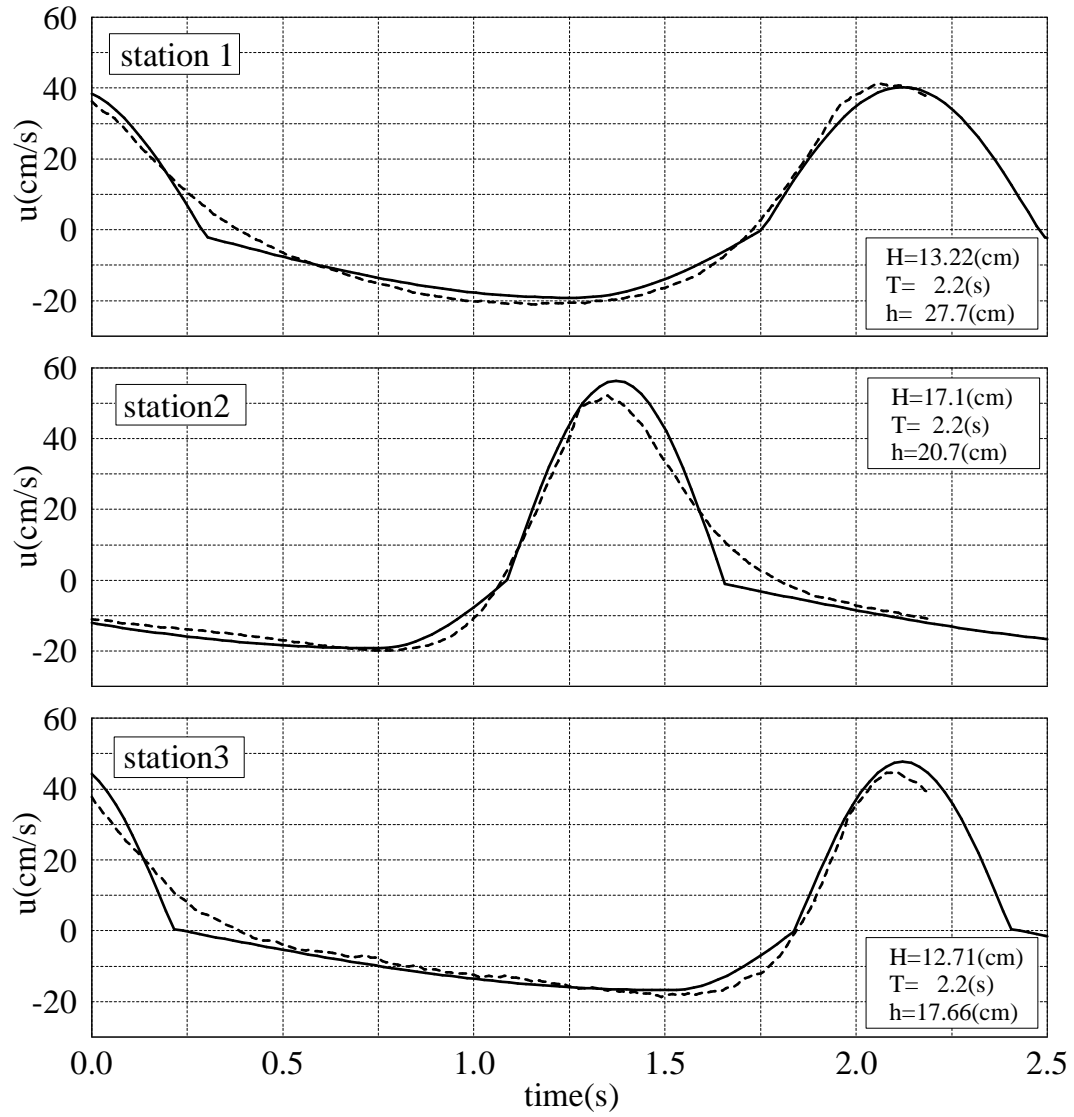


Figure 2-23: Comparisons of measured (dashed lines) and predicted (full lines) near-bottom wave orbital velocity profiles for periodic waves on plane 1 on 35 sloping beach. Measurements by Cox and Koabayshi (1996) (at stations 1, 2, and 3).

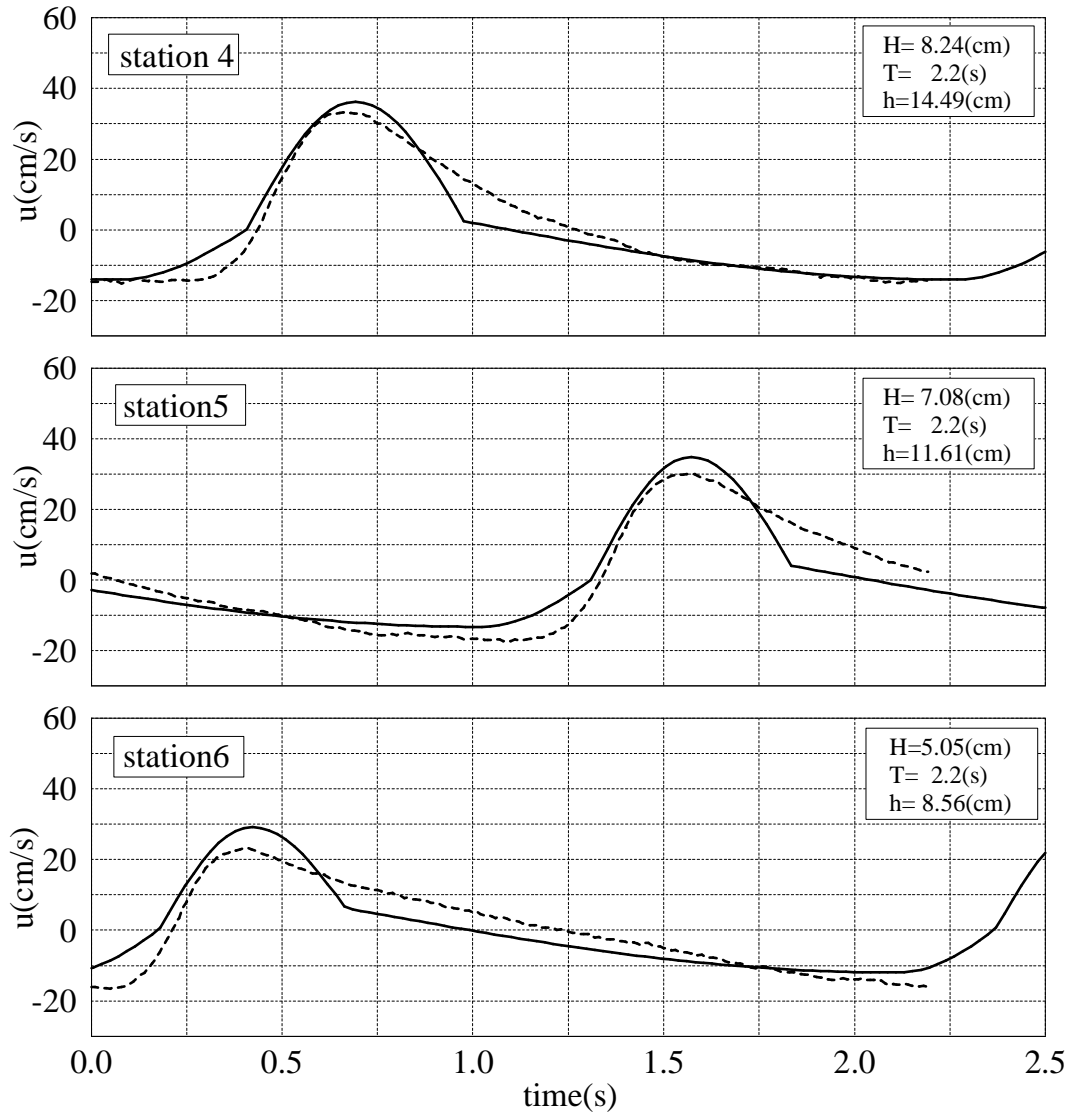


Figure 2-24: Comparisons of measured (dashed lines) and predicted (full lines) near-bottom wave orbital velocity profiles for periodic waves on plane 1 on 35 sloping beach. Measurements by Cox and Koabayshi (1996) (at stations 4, 5, and 6).

for the evolution of wave heights as periodic waves travel from deep water up to their breaking point and as broken waves on into the surf zone where they dissipate their energy. Since this model for shoaling, breaking, and broken periodic waves is based on linear theory, a simple extension to random narrow-banded spectral waves was presented.

The excellent predictive skills of the model, in terms of its prediction of measured, and therefore non-linear, wave heights in the vicinity of the breaking point and inside the surf zone are demonstrated for periodic waves normally incident on a plane beach, random waves normally incident on a barred concrete beach, and random waves of small oblique incidence on barred movable bed beach profiles. The model is also shown to be successful in predicting non-linear characteristics (magnitude, skewness and asymmetry) of the near-bottom wave orbital velocity around the breaking point and inside the surf zone.

The present model is simple to apply because it is based on linear wave theory and the concept of an equivalent linear wave. Since the equivalent linear wave conserves energy flux the present model should be particularly well suited for the evaluation of radiation stresses driving long-shore and cross-shore currents. This anticipation is supported by the demonstrated ability of the present model to accurately predict wave set-up for both periodic and random waves. Furthermore, the model's demonstrated ability to predict near-bottom orbital velocity features, which are of utmost importance in evaluation of flow resistance and sediment transport processes, suggests its suitability for adoption in models for hydrodynamic and sediment transport processes in the surf zone.

Chapter 3

Surface Roller Model

The present wave model, developed in Chapter 2, successfully predicts wave attenuation inside the surf zone and non-linear wave characteristics such as skewness and asymmetry of the near-bottom wave orbital velocity profiles. Predicted equivalent linear and non-linear wave characteristics may be applied in other models to predict wave-induced sediment transport rates as well as other near-shore hydrodynamic characteristics such as undertow, long-shore current and wave set-up. In order to explain the increase of the return flow velocity, which is observed inside the surf zone, however, we need to introduce the concept of surface rollers into the wave model.

Svendsen (1984) first introduced the surface roller model to explain the increase of the return flow velocity and the surface shear stress inside the inner surf zone. Since Svendsen's (1984) model is based on the experimental observations obtained in the inner surf zone, the model cannot evaluate the smooth evolution of the surface roller near the breaking point.

Okayasu et al. (1990) pointed out that Svendsen's (1984) model over-predicts the surface shear stress in the outer surf zone and proposed a new undertow model with the assumption that dissipated wave energy due to breaking is transferred to both the surface roller energy and turbulent energy. It is also assumed that dissipated wave energy at an arbitrary local point is evenly transferred to the turbulent energy through a certain distance, which is related to the local depth. The surface roller energy is then determined as an integration of the remaining dissipated wave energy, which

is caused by wave breaking but not yet transferred to turbulent energy. Although their model estimates total volume of the return flow throughout the surf-zone fairly well, their model still overestimates the surface shear stress near the breaking point. Since their shear stress model depends only on energy dissipation rate, their surface shear stress always acts in shoreward direction, which cannot explain the observation that the surface shear stress near the breaking point tends to act in the seaward direction. This feature is shown later by the experimental data. Moreover, because of the complexity of their model, it is difficult to apply this model to random wave conditions.

Dally and Brown (1995) pointed out the discontinuity of the surface roller evolution at the breaking point and introduced an energy balance equation for the surface roller to successfully explain the smooth transition of the surface roller evolution. Dally and Brown, moreover, calibrated the model against experimental data and an empirical coefficient, which determines the dissipation rate of the surface roller energy, was set to be constant. Since the calibration was done only for experimental cases for periodic incident waves on plane beaches, applicability of the model to various beach conditions is suspect. For example, Kurata and Hattori (2000) applied Dally and Brown's model to various experimental cases and pointed out that the optimum dissipation coefficient varies among various experimental conditions.

In this study, we follow a similar approach to Dally and Brown (1995) and develop the surface roller model which is consistent with the present wave model. Surface roller energy is first defined and relationships between surface roller energy and other surface roller characteristics are discussed. Using surface roller energy, an energy balance equation for the surface roller is developed and coupled with the present broken wave model. Model extensions to random waves are also developed. Finally, validity of the model is examined through comparison with some experimental results.

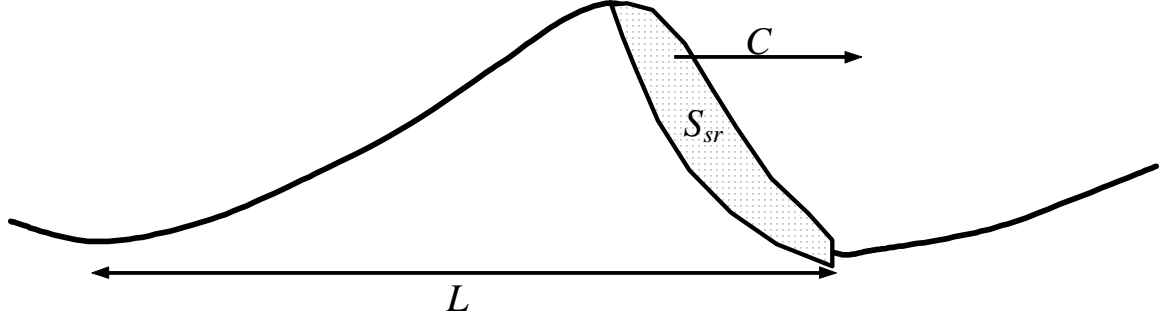


Figure 3-1: Sketch of the surface roller

3.1 Model Development

Figure 3-1 illustrates the dimensions of the surface roller. Similar to Dally and Brown (1995), we first characterize the surface roller in terms of its cross-section area, S_{sr} , and mean energy, E_{sr} . From observations, a surface roller is generated on the front of a broken wave crest and propagates with the broken wave. In this sense, it is reasonable to assume that the velocity characteristic of the water particles in the surface roller may be represented by the wave phase celerity, C . Under this assumption, kinetic energy of the surface roller per unit area, E_{sr} , may be defined as

$$E_{sr} = \frac{\rho S_{sr} C^2 / 2}{L} = \frac{\rho S_{sr} C}{2T} \quad (3.1)$$

where L is the local wave length and T is the wave period. Dally and Brown (1995) suggested that the actual surface roller energy should be proportional to E_{sr} with a proportionality constant greater than unity since water particle velocity in the roller may vary and be larger than the wave phase velocity, C . However, we simply take the total surface roller energy as E_{sr} for the time being because of our limited understanding of the physical mechanism of surface rollers. When deriving a surface roller energy balance equation, moreover, it is seen that this proportionality constant is implicitly accounted for in the other parameters.

3.1.1 Volume Flux and Depth-Averaged Return Flow Velocity

Volume flux per unit width, \vec{q}_{sr} , due to the surface roller is expressed as

$$\vec{q}_{sr} = \frac{S_{sr}}{T} \vec{n} = \frac{2E_{sr}}{\rho C} \vec{n} \quad (3.2)$$

where (3.1) was applied and $\vec{n} = (\cos \theta, \sin \theta)$ is the wave propagation direction with θ , an angle between the cross-shore and wave-propagation directions. Coupling with linear wave theory, total shoreward volume flux, Q_x , is then expressed as

$$q_x = \overline{\int_{-H/2}^{\eta} \tilde{u} dz} + q_{sr} = \frac{E + 2E_{sr}}{\rho C} \cos \theta \quad (3.3)$$

Under the assumption of long-straight beach, i.e. $\partial/\partial y = 0$, depth-averaged return flow velocity, \bar{U} , is then determined by requiring total volume flux in x -direction to be zero, i.e.

$$\bar{U} = -q_x/h \quad (3.4)$$

3.1.2 Momentum Flux

Similar to Svendsen's (1984) approach, contributions from the surface roller to the momentum balance are defined from the depth-integrated mean momentum equations in j -th horizontal direction ($j = 1, 2$).

$$\rho g (h_0 + \bar{\eta}) \frac{\partial \bar{\eta}}{\partial x_i} \delta_{ij} + \frac{\partial}{\partial x_i} S_{ij} + \frac{\partial}{\partial x_i} R_{sr,ij} + \tau_{bj} = 0 \quad (3.5)$$

where advection terms of the mean current are neglected. In the formula, $\bar{\eta}$ is an elevation of the mean water level, S_{ij} is the wave radiation stress tensor defined by (Mei, 1989)

$$S_{xx} = E \left[\frac{C_g}{C} (1 + \cos^2 \theta) - \frac{1}{2} \right] \quad (3.6)$$

$$S_{xy} = S_{yx} = \frac{E}{2} \frac{C_g}{C} \sin 2\theta \quad (3.7)$$

τ_{bj} , is the bottom shear stress and momentum flux due to the surface roller, $R_{sr,ij}$, is defined as

$$R_{sr,xx} = \frac{\rho S_{sr} C^2 \cos^2 \theta}{L} = 2E_{sr} \cos^2 \theta \quad (3.8)$$

$$R_{sr,xy} = R_{sr,yx} = \frac{\rho S_{sr} C^2 \cos \theta \sin \theta}{L} = E_{sr} \sin 2\theta \quad (3.9)$$

Especially for long straight beach condition, the wave set-up is determined by

$$\rho g (h_0 + \bar{\eta}) \frac{\partial \bar{\eta}}{\partial x} = -\frac{\partial}{\partial x} S_{xx} - \frac{\partial}{\partial x} R_{sr,xx} - \tau_{bx} \quad (3.10)$$

The volume flux and the wave set-up determined from (3.4) and (3.10) are compared with experiments to indirectly examine the validity of the present surface roller model.

3.1.3 Energy Balance Equation for Surface Roller

As seen from (3.2) and (3.8), all surface roller characteristics are defined in terms of its energy, E_{sr} . In order to determine the evolution of the surface roller energy, we construct an energy balance equation, which should be compatible with the present broken wave model expressed in the general two-dimensional form by

$$\nabla (EC_g \vec{n}) = -\frac{K_b}{h} C_g (E - E_r) \quad (3.11)$$

where $\nabla = (\partial/\partial x, \partial/\partial y)$ with x and y , cross-shore and along-shore axis and $E = \rho g H^2/8$ is the local wave energy and E_r is based on the recovery wave height, H_r , of the broken wave if it were to travel on in a constant depth equal to the local depth, h . To construct the surface roller energy evolution equations, we first assume the following features: (i) a part of the dissipated broken wave energy is provided into the surface roller and the rest of the broken wave dissipation energy is transferred to turbulent energy in the water column; (ii) surface roller energy is transported with wave phase velocity, C ; (iii) surface roller energy itself is also dissipated and

the dissipation rate is proportional to the local surface roller energy; (iv) surface roller vanishes when broken waves stop breaking and have recovered. Under these assumptions, the energy balance for the surface roller becomes

$$\alpha \nabla (EC_g \vec{n}) + \nabla (E_{sr} C \vec{n}) = -\frac{K_{sr}}{h} E_{sr} C \quad (3.12)$$

where α is the fraction of broken wave energy dissipation provided into the surface roller, i.e. $\alpha \leq 1$, and K_{sr} is a proportionality constant to be determined. Note that (3.12) becomes identical to Dally and Brown (1995) model if $\alpha = 1$ and long wave approximation, i.e. $C \simeq \sqrt{gh}$ is applied on the right hand side of (3.12). As seen in (3.12), the values of α and K_{sr} determine the relative importance of each term in (3.12) and therefore automatically absorb the effect of a proportionality constant applied to E_{sr} in Dally and Brown's model. α should be in the range $0 < \alpha \leq 1$ but exact estimation of the parameter is difficult because of the complexity of the feature. We assume that only the loss of potential energy of the broken waves, which is just a half of the total wave energy loss in linear theory, is contributed to the surface roller energy, E_{sr} , and therefore take $\alpha = 1/2$. This choice makes some sense since the surface roller is located above the water surface where potential wave energy resides, whereas most of the kinetic wave energy is distributed over the entire depth and not readily supplied to the surface roller energy. Finally, the complete energy balance equation is obtained by substitution of (3.11) in (3.12)

$$\nabla (E_{sr} C \vec{n}) = \frac{1}{h} \left(K_b C_g \frac{E - E_r}{2} - K_{sr} C E_{sr} \right) \quad (3.13)$$

As seen in (3.13), it should be pointed out that dissipation terms of waves and surface rollers, i.e. the terms in the right hand side of (3.11) and (3.12) are essentially identical because, “recovered energy” of the surface roller, $(E_{sr})_r$, should be zero when the broken wave recovers, i.e. reaches its recovery energy, E_r .

3.1.4 Determination of K_{sr} and Physical Implications

Similar to the present broken wave model, K_{sr} may be a function of the slope although Dally and Brown (1995) suggested K_{sr} to be constant, $K_{sr} = 0.2$. Since formulations of energy dissipation models for waves and surface rollers are identical, K_{sr} may also be related to K_b . Recalling our model assumption that half the broken wave energy dissipation is directly going into turbulence while the other half is going to the surface roller energy and subsequently into turbulence, it appears reasonable to assume that the mechanism by which the wave energy dissipation is transferred to turbulent energy should be similar for wave and surface roller and we therefore take $K_{sr} = K_b$ with K_b determined from (2.24) in Section 2.3,

$$K_b = \frac{5}{2} \frac{\gamma_s^2 \tan \beta}{\gamma_s^2 - \gamma_r^2} \quad (3.14)$$

Figure 3-2 shows the comparisons of the non-dimensional volume flux predicted by the present and Dally and Brown's (1995) models for the same experimental data shown in Figure 2.19, which compared slope-dependency of the broken wave attenuations on straight beaches with different bottom slopes. In the figure, h_0 is local still water depth and h_{b0} is the still water depth at the breaking point. The non-dimensional volume flux, q'_x , was obtained by dividing predicted volume flux, q_x , by $\sqrt{gh}h$ and normalized by the value at the breaking point. In the experiments, q_x was obtained by integrating the measured vertical profiles of U over the water depth. The volume flux predicted from (3.3) agrees well with measurements on various bottom slopes, $\tan \beta_0 = \partial h_0 / \partial x$. On the other hand, Dally and Brown's (1995) model over-predicts the volume flux especially in the outer surf zone. This over-prediction may be partially because of the over-predictions of the wave volume flux, q_{wx} , since the predicted volume flux at the breaking point, where the surface roller starts to contribute, is larger than the measured q'_x . Dally and Brown (1995) pointed out that q_{wx} is over-predicted if one were to apply linear theory based on the measured non-linear wave height and showed that the numerical application of the Stream Function Theory yields better predictions of q_{wx} . In the present comparison, however, we apply

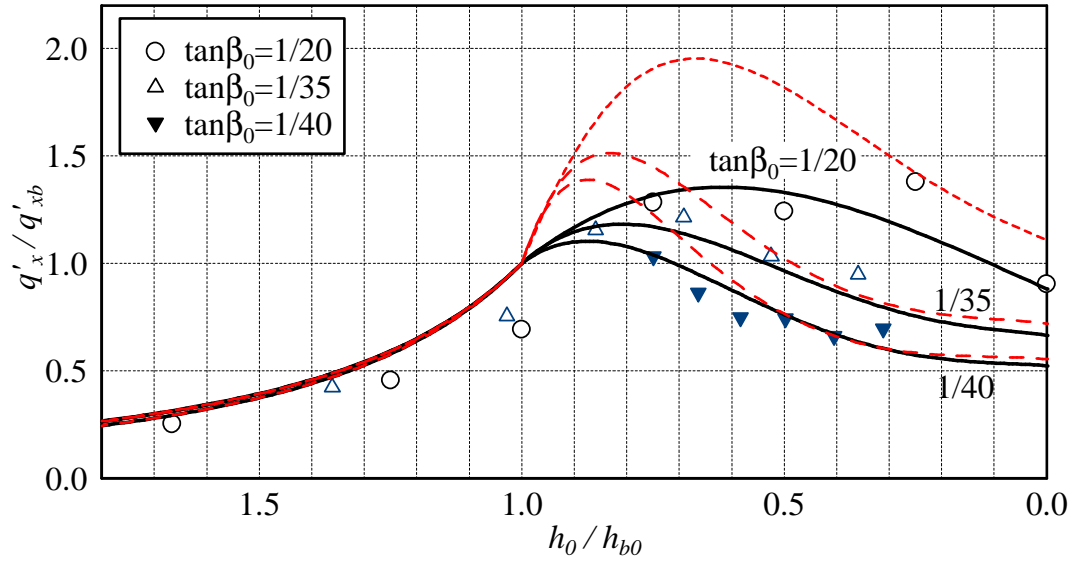


Figure 3-2: Comparisons of measured and predicted non-dimensional volume flux with periodic waves incident on uniform slopes. Resources of the experimental data were the same referred in Figure 2-17, i.e. by Mizuguchi et al. (1978), Okayasu and Katayama (1992), Cox and Kobayashi (1996), and Stive and Wind (1986) for $\tan \beta_0 = \partial h_0 / \partial x = 1/10, 1/20, 1/35$, and $1/40$; Present Model (full line) and Dally and Brown's Model (dashed line).

linear theory based on the predicted equivalent linear wave heights, which are smaller than non-linear wave heights, for both Dally and Brown's and our model. According to Tajima (2001), q_{wx} obtained in this manner agrees reasonably well with numerical predictions by Stream Function Theory except very near the breaking point where H_*/h is very large. In this sense, we can still expect reasonable predictions of q_{wx} in the surf zone where H_*/h is not as large as at the breaking point. It should also be noted that, in this comparison, Dally and Brown's energy balance equation was applied to the predicted equivalent linear wave conditions although their model was originally calibrated by using measured non-linear wave heights. If one were to use measured or predicted non-linear wave heights to evaluate the surface roller energy from Dally and Brown's model, the predicted surface roller energy and therefore q_x would be larger than shown in Figure 3-2, and the over-prediction by Dally and Brown's model would become even more pronounced. It is also seen in Figure 3-2 that the over-prediction of q_x by Dally and Brown's model increases as the bottom slope becomes larger. Similar to the comparisons of the broken wave heights in Figure 2-17, this observation verifies a slope-dependency of K_{sr} , as proposed in the present model.

3.2 Extension of the Model to Random Waves

Both wave and surface roller models are now complete for periodic wave conditions. Since both wave and surface roller models, (2.21) and (3.13), are governed by simple energy balance based on linear wave theory, the models are also readily extended to random wave conditions. As discussed in Section 2.5, the local mean wave energy for random waves is obtained from (2.27),

$$\nabla (EC_g \vec{n}) = -K_b \frac{C_g}{h} \exp(-\xi_b^2) \left[E(1 + \xi_b^2) - E_r \right] \quad (3.15)$$

The surface roller energy balance equation for random waves is identical to (3.13) but replacing the wave energy dissipation, seen in the first term of the right hand

side of (3.13), by the wave dissipation for random waves, i.e. the right hand side of (3.15):

$$\nabla (E_{sr} C \vec{n}) = \frac{K_b}{h} \left(\frac{C_g}{2} \exp(-\xi_b^2) [E(1 + \xi_b^2) - E_r] - C E_{sr} \right) \quad (3.16)$$

Here the surface roller energy is taken to be the average value. Since all other characteristics such as volume and momentum fluxes are determined in terms of the wave and surface roller energy, the same formulae, (3.2) and (3.8) are also applicable to random waves.

3.3 Numerical Application of the Model

From specified deep water wave conditions, i.e. the equivalent linear incident wave conditions are known, wave shoaling is computed by use of linear wave theory up to the breaking limit determined by (2.20). After the breaking point, (3.11) is discretized in a horizontal space grid and the shoreward unknown wave energy, E_{i+1} , is numerically solved from known variables such as E_i with i , shoreward grid number. Since $\bar{\eta}_{i+1}$ is also unknown, numerical iteration is required with initial condition, $\bar{\eta}_{i+1} = \bar{\eta}_i$. In the numerical iteration, $\bar{\eta}_{i+1}$ is determined from (3.10) with $E_{sr,i+1}$ obtained from (3.12). For random waves, (3.15) is applied instead of (3.11) in the entire computational region because a certain number of waves are always broken under the assumption of the Rayleigh distributed wave heights. Total volume flux and therefore the depth-averaged undertow velocity are then determined from (3.3) and (3.4).

3.4 Test of the Model

The predictive ability of the present model is examined through comparisons with experiments for periodic and random waves incident on uniform plane beaches and random waves incident on a barred beach.

Figure 3-3 shows the predicted wave heights, wave set-up, and depth-averaged undertow velocity compared with the experimental data for periodic waves normally incident on a plane beach presented by Cox and Kobayashi (1996). In the figure, full

lines and dashed lines denote predictions by the present model with and without the surface roller model, respectively. Wave set-up was computed from (3.10) but the bottom shear stress was neglected. It will be shown in Chapter 4 that the effect of the bottom shear stress on the wave set-up is negligibly small. Figure 3-4 shows the same comparisons as those in Figure 3-3 but for periodic waves obliquely incident on a plane beach with 1/20 slope. The experimental data shown in Figure 3-4 is reported by Hamilton and Ebersole (2001).

As seen in Figures 3-3 and 3-4, agreement between measured and predicted wave heights is excellent. From the comparison of wave set-up with and without the surface roller effects it is seen that the surface roller delays the sudden increase of the wave set-up right after the breaking point and it increases the wave set-up near the shore line. This surface roller effect clearly improves the predictive skills for the wave set-up. Similarly in the comparison of the undertow velocity, the surface roller significantly increases the undertow inside the surf zone and the peak is shifted shoreward from the breaking point. This feature cannot be explained solely from the wave volume flux because the cross-shore distribution of wave heights of periodic waves always has its peak at the breaking point. This observation also supports the necessity and validity of the present surface roller model.

Figure 3-5 shows comparisons of significant wave heights, wave set-up, and the depth-averaged undertow velocity for random waves normally incident on a plane uniformly sloping beach reported by Okayasu and Katayama (1992). Similarly, Figure 3-6 shows the same comparisons as those in Figure 3-4 but for random waves obliquely incident on a plane beach. The experimental data shown in Figure 3-6 are also reported by Hamilton and Ebersole (2001). Since random wave heights gradually attenuate, the effect of the surface roller on the wave set-up is relatively small comparing to the periodic waves shown in Figures 3-3 and 3-4. However, a similar effect of the surface roller observed in Figures 3-3 and 3-4 are also seen in Figures 3-5 and 3-6 and improves the predictions of the wave set-up. Similarly, the surface roller again increases dramatically the undertow predicted for waves alone, especially near the shoreline, and results in excellent predictions.

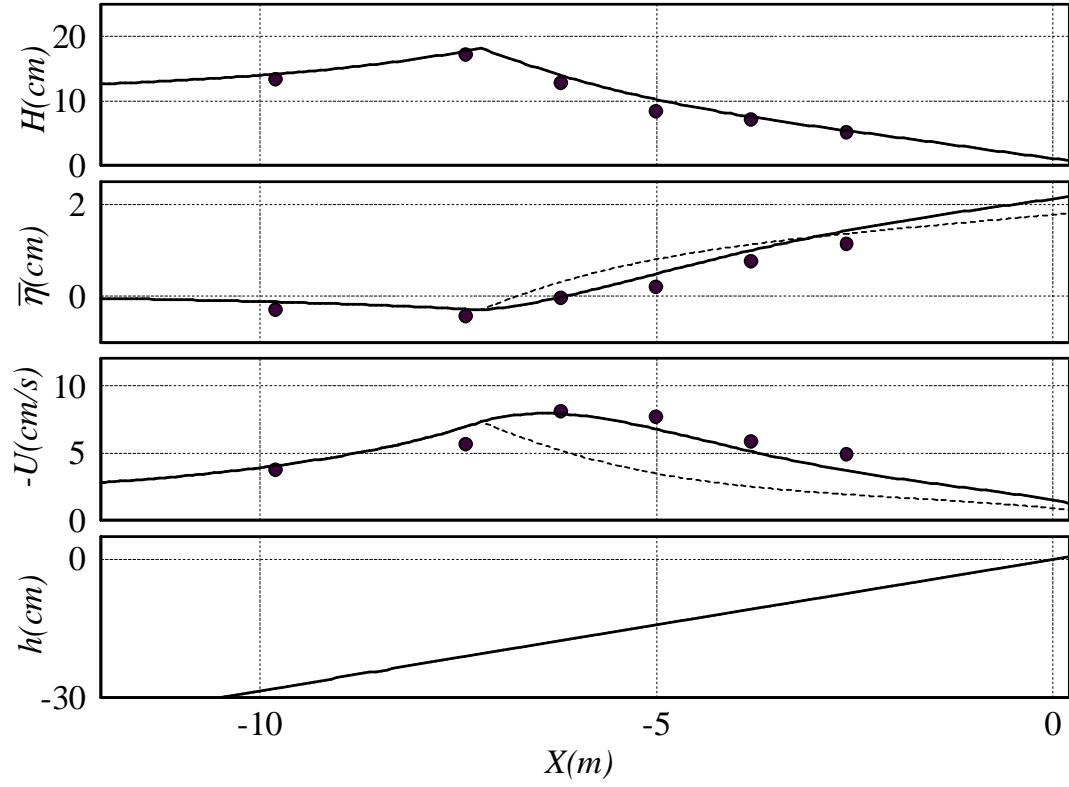


Figure 3-3: Comparisons of measured and predicted wave heights, wave set-up, and depth-averaged undertow velocity for periodic waves on plane 1 on 35 sloping beach. Measurements by Cox and Kobayashi (1996) (circles); Predictions with surface roller (full line) and without (dashed line).

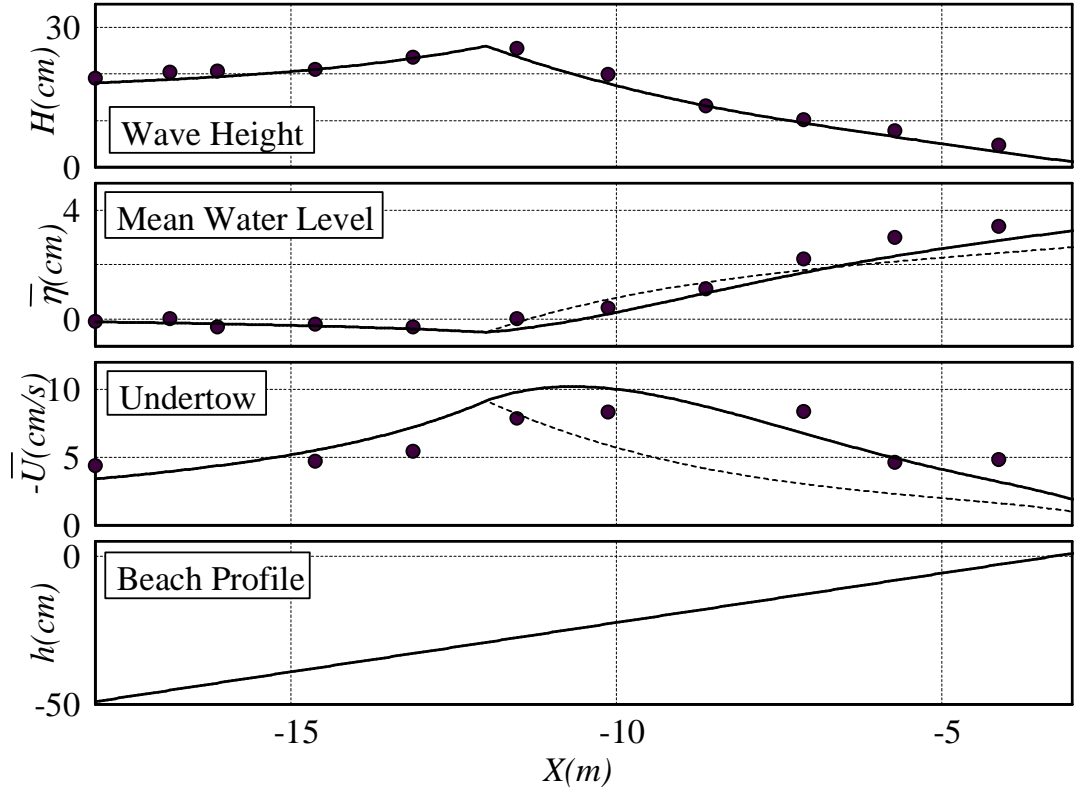


Figure 3-4: Comparisons of measured and predicted wave heights, H_* , wave set-up, $\bar{\eta}$, and depth-averaged return flow velocity, $-\bar{U}$, for periodic waves obliquely incident on plane 1 on 30 sloping beach. Measurements (Test 6A-N) Hamilton and Ebersole (2001) (circles); Predictions with surface roller (full line) and without (dashed line).

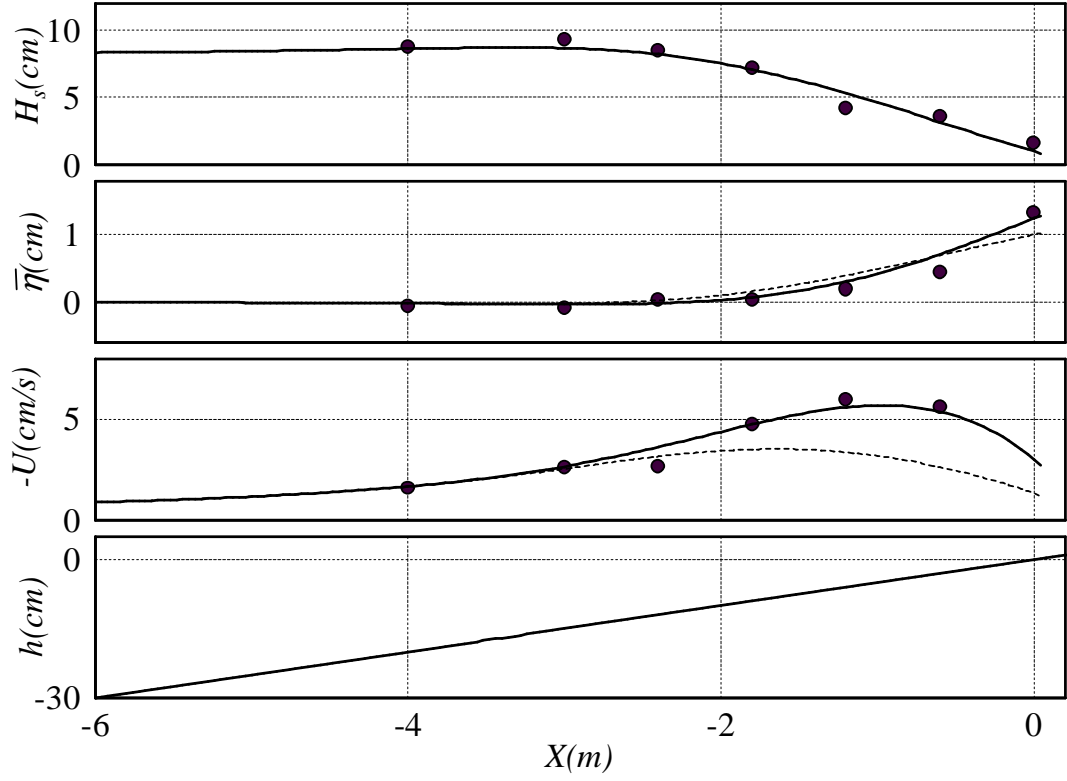


Figure 3-5: Comparisons of measured and predicted wave heights, wave set-up, and depth-averaged undertow velocity for random waves on plane 1 on 20 sloping beach. Measurements by Okayasu and Katayama (1992) (circles); Predictions with surface roller (full line) and without (dashed line).

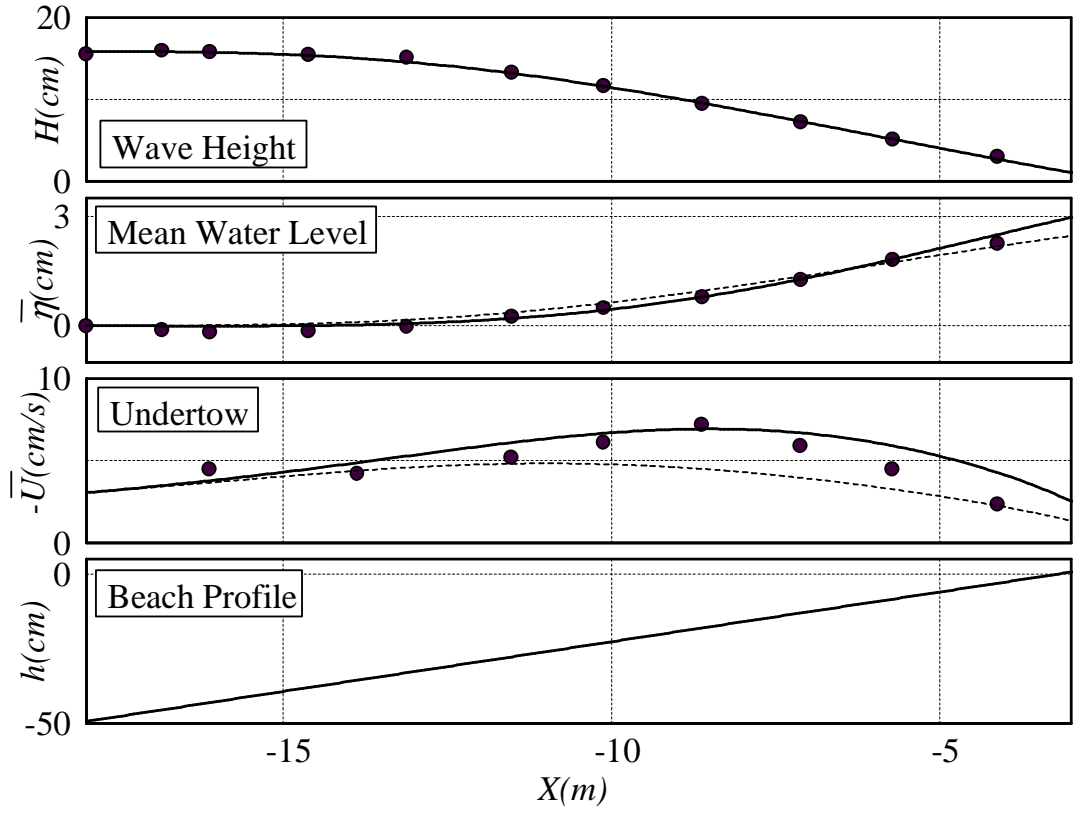


Figure 3-6: Comparisons of measured and predicted wave heights, H_{rms} , wave set-up, $\bar{\eta}$, and depth-averaged return flow velocity, $-\bar{U}$, for random waves obliquely incident on plane 1 on 30 sloping beach. Measurements (Test 8A-E) Hamilton and Ebersole (2001) (circles); Predictions with surface roller (full line) and without (dashed line).

Finally, Figure 3-7 shows the same comparisons as Figure 3-5 but for the experimental case when random waves are normally incident on a barred beach presented by Okayasu and Katayama (1992). Since the present model is valid only for $\beta \geq 0$, $\beta = 0$ was substituted in the numerical application where $\beta < 0$. It is seen from the figure that predicted significant wave heights agree very well with measurements even where the water depth is increasing, i.e. $\beta < 0$. Similar to previous observations, inclusion of surface roller effects overall improves predictions of the wave set-up and the undertow except predictions of the undertow around the bar crest. Since the model without the surface roller effect already over-predicts the undertow and the contribution of the surface roller is relatively small around the bar, this over-prediction may be mainly caused by the prediction of wave volume flux.

3.5 Summary and Further Implications

The wave model presented in Chapter 2 (Tajima and Madsen, 2002) was applied to predictions of the near-shore wave field. The concept of the surface roller was then introduced to improve predictions of depth-averaged undertow velocity and wave set-up. Physical characteristics of the surface roller were determined as functions of the surface roller energy, E_{sr} , and an energy balance equation, which is consistent with the present wave model, was developed to capture the spatial evolution of the surface roller energy. A simple extension of the model to random waves was also proposed.

The validity of the model was tested against experimental data for periodic and random waves incident on plane uniformly sloping beaches with various slopes and random waves incident on a barred beach. Through comparisons of the predicted wave heights, wave set-up and depth-averaged undertow, excellent agreement verified the predictive skills of the model. It should be emphasized that none of experimental data compared with the present model was applied to calibrate the model coefficients.

The present model may also be extended to predictions of longshore momentum forces and therefore longshore currents. For long straight beach conditions and assuming long linear wave theory, the momentum equation in the y -direction is deduced

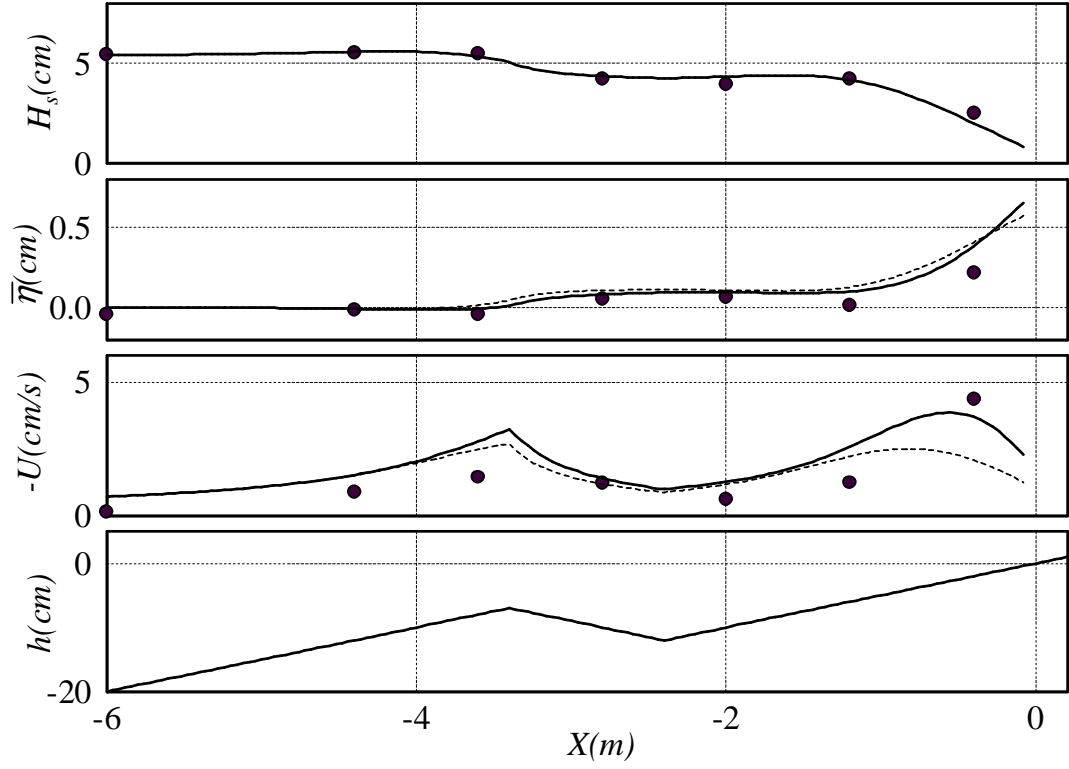


Figure 3-7: Comparisons of measured and predicted wave heights, wave set-up, and depth-averaged undertow velocity for random waves on barred beach profile. Measurements by Okayasu and Katayama (1992) (circles); Predictions with surface roller (full line) and without (dashed line).

from (3.5) to be

$$-\frac{\partial}{\partial x}E \cos \theta \sin \theta - 2\frac{\partial}{\partial x}E_{sr} \cos \theta \sin \theta \simeq \tau_{by} \quad (3.17)$$

where the first and the second terms of the left hand side of (3.17) are momentum forces due to the wave and the surface roller, respectively. At the breaking point for periodic waves, where the surface roller just starts to appear, the energy balance equation (3.12) implies $\partial E/\partial x \simeq -2\partial E_{sr}/\partial x$ for long waves. Therefore, the two terms on the left hand side of (3.17) cancel and the total longshore momentum force vanishes. This gives a continuous longshore current across the breaking point without the necessity of introducing lateral mixing to achieve this feature.

Some distance inside the surf zone, on the other hand, surface roller energy, E_{sr} , starts to decrease and both wave and surface roller terms in the left hand side of (3.17) becomes positive. Therefore, the surface roller increases the longshore momentum force inside the surf zone. This feature shifts the peak of the longshore current velocity shoreward. Ruessink et al. (2001) introduced the momentum force of the surface roller and showed this feature in their numerical model application.

Svendsen (1984), assumed that the shear stress at the mean water level in the shore-normal direction, τ_{sx} , is determined as a sum of the time-averaged wave pressure force and the surface roller momentum force,

$$\tau_{sx} = -\frac{1}{2}\frac{\partial}{\partial x}E - 2\frac{\partial}{\partial x}E_{sr} \quad (3.18)$$

This resulted in a shore-ward leaning undertow velocity profile well inside the surf zone, i.e. a positive gradient of the undertow velocity as mean water level is approached since both E and E_{sr} decrease in the wave propagation direction. In addition to this feature, our model is able to explain the sea-ward leaning undertow typically observed near the breaking point. Our energy balance equation again implies $\partial E/\partial x \simeq -2\partial E_{sr}/\partial x$ at the breaking point for periodic waves, and introducing this condition in (3.18) shows the surface roller momentum force, which acts in the sea-ward direction, to dominate. This results, therefore, in a sea-ward directed surface shear stress, τ_{sx} , acting at the mean water level and results in a sea-ward leaning

undertow velocity profile as the mean water level is approached. These features will be seen in the computational application of the present nearshore current model in Chapter 4.

Chapter 4

Nearshore current model

4.1 Introduction

The wave and surface roller models are now complete and readily applicable to the sediment transport model. The last hydrodynamic features we require for the development of the conceptual sediment transport model are the nearshore mean shear current induced by broken waves. From the knowledge of mean current and near-bottom wave orbital velocity, Madsen's (1994) combined wave-current bottom boundary layer model determines the bottom shear stress, which causes bedload sediment transport. The bottom shear stress also acts to entrain bottom sediments into the water column where turbulence dominated by wave breaking keeps a potentially large amount of sediments suspended and available for transport by the near-shore mean current in the seaward and longshore directions by the undertow and longshore current, respectively.

A two-dimensional horizontal (2DH) nearshore mean current models, based on the depth and time-averaged momentum equations (Longuett-Higgins, 1970; Phillips, 1977; Mei, 1989), are simple to apply and have therefore been widely used to evaluate the nearshore mean circulation such as longshore and rip currents (e.g. Noda et al., 1974; Ebersole and Darlymple, 1980; Wu and Liu, 1985). Under the long, straight beach assumption, 2DH equations can be reduced to the one-dimensional alongshore momentum equation (e.g. Longuett-Higgins, 1970; Thornton and Guza, 1986). The

primary forcing that induces the nearshore mean current is determined from the spatial variations of wave radiation stresses, which are separately obtained from a wave model. A number of authors have pointed out the significant effect of the surface roller momentum force that shifts the peak of the longshore current velocity on a long, straight beach toward inside the surf zone (e.g., Kuriyama, 1994; Okayasu et al., 1994; Lippmann, et al., 1995; Reniers et al., 1995; Osiecki and Dally, 1996; Reniers and Battjes, 1997; and Ruessink et al., 2001). Because of the simple application of the depth-averaged 2DH equations, however, the model can not appropriately evaluate the undertow velocity inside the surf zone. On the long, straight beach, for example, the mass conservation law requires the zero depth-integrated volume flux in the cross-shore direction while there exists strong seaward return flow (undertow) under the wave trough level that balances the wave-associated shoreward volume flux above the trough level. This feature also results in unrealistic evaluations of the mean current shear stress at the bottom because the 2DH model empirically determines the bottom current shear stress from depth-averaged current velocity while the near-bottom current velocity may differ significantly from depth-averaged current velocity.

In order to account for the vertical variation of the mean current velocity, the quasi-three dimensional (Q-3D) nearshore mean current models have been developed (De Vrind and Stive, 1987; Sanchez-Arcilla et al., 1990, 1992; Van Dongeren et al., 1994; Kuroiwa et al., 1998). All these models except Kuroiwa et al. (1998), who directly solved 3D Reynolds equations, are based on the depth and time-averaged 2DH momentum equations and the 1DV Reynolds equation is applied to determine the vertical profiles of the mean current velocity. To reduce the computational cost, all models assume certain explicit formulae to represent the velocity profiles. Putrevu and Svendsen (1992) and Svendsen and Putrevu (1994) suggested that the current-current and current-wave interactions play a significant role in characterizing the lateral mixing of nearshore mean current momentum. With the exception of Van Dongeren et al.'s (1994) model (SHORECIRC), however, most Q-3D models neglect these interactions and instead introduce empirical lateral dispersion terms first introduced by Bowen (1969) to explain lateral mixing. SHORECIRC (Van Don-

geren et al., 1994) accounted for the current-current and wave-current interactions in its 2DH depth-integrated momentum equations and applicability of the model has been tested by its developers (e.g. Svendsen et al., 1997; Van Dongren et al., 2003; Svendsen et al., 2003). In order to simplify the 2DH depth-integrated momentum equations, similar to the other models, SHORECIRC adopts quadratic velocity profiles, in which the vertical variations of the shear stress due to current-current and wave-current interactions are neglected. Although the vertical variations of the mean current velocity are determined, the model applies an empirical friction model based on depth-averaged mean current velocity to determine the bottom shear stress, which is critical in evaluation of the magnitude of the mean current velocity.

A number of numerical non-linear wave models such as Boussinesq-type models have been extended to the predictions of broken waves and wave-induced near-shore mean currents. Since the momentum equations in the Boussinesq-type models contain both wave and mean current velocity components, these models implicitly account for the current-current and wave-current interactions, whose importance was discussed in the previous paragraph. Most Boussinesq-type models, however, are based on potential flow assumptions and additional modeling is called for to evaluate the effects of turbulent fluctuations, which determine vertical profiles of near-shore mean shear currents. Turbulent fluctuations dominant around the surf zone are also essential to characterize the concentration distribution of suspended sediments. Watanabe and Elnaggar (2000) combined the fully non-linear Boussinesq equations and 1DV Reynolds momentum equations and developed a numerical scheme, which accounts for time-varying shear flows. In their model, vertical distributions of the turbulent intensity induced by wave breaking are determined by use of the k - ϵ equations. The model requires additional numerical iterations to solve the 1DV Reynolds and k - ϵ equations at every time step for which the Boussinesq equations are numerically solved.

Introducing the volume of fluid (VOF) method, originally developed by Hirt and Nichols (1981), further complex numerical models, which directly solve Reynolds equations for free-surface water flow, have been developed (e.g., RIPPLE, Kothe

et al., 1991; and CADMAS-SURF, Coastal Development Institute of Japan, 2001). Since the VOF method enables the model to treat arbitrary free surface conditions, numerical schemes in conjunction with the VOF method have been applied to more complicated problems, such as breaking waves with over-hanging surface profiles, swash zone hydrodynamics, and waves attacking breakwaters with complex shape, such as caissons with perforated-walls (e.g., Lin and Liu, 1998; Puleo et al., 2002; Takahashi et al., 2002). Lin and Liu (1998) modified RIPPLE, developed by Kothe et al., (1991), and introduced k - ϵ equations to solve for turbulent kinetic energy, k , and turbulence dissipation rate, ϵ , mainly caused by broken waves energy dissipation. Lin and Liu (1998) applied the model to the two-dimensional experiment for periodic waves normally incident on a plane beach and showed good agreements of predicted and measured free-surface elevations, velocity fields, and turbulent kinetic energy at arbitrary elevations. However, the massive computational load required by these complex models, may limit these models' utility for practical applications. For example, a practical model for predictions of beach topography changes must be efficient and flexible so that it can accommodate iterative computations for time-varying and hence arbitrary beach profiles.

In this study, therefore, we develop a 2DH-based Q-3D nearshore mean current model, which can be accommodated to the practical applications. We first summarize the external momentum forcing and volume fluxes obtained from our wave and surface roller models. These characteristics are introduced in the depth-integrated 2DH mean momentum equations to solve near-shore mean shear currents. Similar to Sanchez-Arcilla et al.'s (1990, 1992) approach, the water column is separated at the wave trough level and 2DH momentum equations are solved in two layers, one over the entire depth and the other above the trough level. Similar to Svendsen and Putrevu (1994), we account for the current-current and wave-current interaction effects in the 2DH momentum equations integrated over the entire depth. The present model, however, differs from Svendsen and Putrevu's (1994) model in that these interaction effects are also accounted for in the upper-layer 2DH momentum equations integrated above the trough level. A modified version of the wave-current bottom

boundary layer model presented by Madsen (1994) is then introduced to specify bottom boundary conditions for the near-shore mean current model. Simple expressions for the vertical distributions of the turbulent eddy viscosity allow us to obtain analytical solutions for vertical profiles of mean shear currents thereby enhancing model efficiency. The proposed turbulent eddy viscosity model may also be applied to evaluate the vertical concentration profiles of suspended sediments. Since the model deals with time-averaged variables and depth-integrated momentum equations, the entire model retains the computational efficiency and flexibility for practical applications. The waves may be periodic or random, the beach profile may be plane or barred, and the arbitrary bottom roughness must be specified. Finally, validity of the model is examined through comparison with a number of experimental results, which were not used for model calibrations.

4.2 Wave Model

We apply the wave model developed in Chapter 2. The present wave model first determines the equivalent linear wave characteristics through an energy balance equation from linear wave theory,

$$\begin{aligned}\nabla (EC_g \vec{n}) &= -D_b \\ &= -\frac{K_b}{h} C_g (E - E_r)\end{aligned}\tag{4.1}$$

as introduced in Section 2.3, (2.21). D_b is a dissipation rate of the broken wave energy, which will be applied to the turbulent eddy viscosity model. The proportionality constant for broken wave energy dissipation, K_b , is determined in (2.24) as

$$K_b = -\frac{5}{2} \frac{\gamma_s^2}{\gamma_s^2 - \gamma_r^2} \frac{\partial h}{\partial x} = \frac{5}{2} \frac{\gamma_s^2 \tan \beta}{\gamma_s^2 - \gamma_r^2}\tag{4.2}$$

with

$$\gamma_s = \gamma_r + A \tan \beta = 0.3 + 4 \tan \beta\tag{4.3}$$

from (2.25). Non-linear wave characteristics, such as near-bottom wave orbital velocity profiles, are then restored from the equivalent linear wave characteristics. The “height” of the non-linear near-bottom wave orbital velocity is applied in a combined wave-current bottom boundary layer model (Madsen, 1994) to predict bottom boundary conditions. For random waves, however, we use rms near-bottom velocity height based on linear theory to evaluate the bottom boundary conditions since Madsen’s (1994) model for random waves are based on spectral, i.e. linear wave theory. Excellent predictive skills of the model for the rms near-bottom wave orbital velocity height were shown in Figure 2-20. It should be pointed out that the present broken wave model was developed so that the predicted wave energy inside the surf zone is consistent with that of observed non-linear waves, while most existing models are calibrated in terms of measured broken wave heights. Since observed, i.e. non-linear, wave heights are usually larger than the equivalent linear wave heights, wave energy and energy flux may be over-predicted if one were to use observed non-linear wave heights in expressions based on linear wave theory. The over-prediction of wave energy and energy flux results in over-estimation of wave momentum forces, which may significantly affect predictions of wave-induced near-shore mean currents and wave set-up.

4.2.1 Volume Flux and Momentum Forcings

Wave volume flux and momentum forcings are defined based on the equivalent linear wave characteristics obtained from the present wave model. Components of the wave volume flux above the trough level, (q_{wx}, q_{wy}) are determined from linear theory by

$$(q_{wx}, q_{wy}) = \overline{\int_{h-H/2}^{h+\eta} (\tilde{u}, \tilde{v}) dz} = \frac{E}{\rho C} (\cos \theta, \sin \theta) \quad (4.4)$$

where \tilde{u} and \tilde{v} are wave orbital velocity components in x and y -directions, respectively. According to Tajima (2001), cross-shore volume flux due to waves, q_{wx} , obtained in this manner agrees reasonably well with numerical predictions by the Stream Function Theory, i.e. non-linear wave theory, except very near the breaking point where H/h

is very large.

Wave radiation stress tensors, S_{xx} and S_{xy} , are also expressed in terms of the wave energy, e.g. (Mei, 1989),

$$\begin{aligned} S_{xx} &= \overline{\int_0^{h+\eta} p + \rho \tilde{u}^2 dz} - \frac{\rho g}{2} h^2 \\ &= E \left[\frac{C_g}{C} (1 + \cos^2 \theta) - \frac{1}{2} \right] \end{aligned} \quad (4.5)$$

$$\begin{aligned} S_{xy} &= \overline{\int_0^{h+\eta} \rho \tilde{u} \tilde{v} dz} \\ &= \frac{E}{2} \frac{C_g}{C} \sin 2\theta \end{aligned} \quad (4.6)$$

Note that all these integrated wave characteristics are expressed in terms of wave energy. Since the broken wave model was developed so that the predicted wave energy flux inside the surf zone agrees with that of observed non-linear waves, predicted wave forcings and volume fluxes, all of which are expressed in terms of wave energy, may be considered to be consistent with actual non-linear waves.

4.2.2 Model Extension to Random Waves

Since the model is governed by a simple energy conservation equation based on linear wave theory, the model is readily extended to random wave conditions. Local mean wave energy, $E = \rho g H_{rms}^2 / 8$ is determined from energy balance equation for random waves, (2.27), and both volume fluxes and the momentum forcings are determined from (4.4), (4.5) and (4.6) by replacing H by H_{rms} for a random sea.

4.3 Surface Roller Model

In order to explain the increase of return flow velocity observed in the surf zone, relative to the value suggested by balancing the purely wave-associated volume flux given by (4.4), we developed a model for prediction of surface roller evolution in the surf zone in Chapter 3. The surface roller model is based on the energy balance equation that is consistent with the proposed broken wave energy dissipation model.

Validity of the model was indirectly examined by comparing predicted and measured volume fluxes as well as wave set-up, which is also affected by momentum forcings of the surface roller. It should be stressed that the surface roller model, just as the wave model, is based on simple energy balance equations that allow us to keep the model flexible and computationally efficient.

4.3.1 Volume Fluxes and Momentum Forcings

Under the assumption that the surface roller moves with the wave phase velocity, C , average surface roller energy per unit area, E_{sr} , is expressed as

$$E_{sr} = \frac{\frac{1}{2}\rho S_{sr} C^2}{L} = \frac{\rho S_{sr} C}{2T} \quad (4.7)$$

with S_{sr} denoting the area of the surface roller. Evolution of the surface roller energy is determined from energy balance equation (3.12),

$$\frac{1}{2}\nabla (EC_g\vec{n}) + \nabla (E_{sr}C\vec{n}) = -\frac{K_{sr}}{h}E_{sr}C \quad (4.8)$$

As discussed in Section 3.1.3, the present model differs from the Dally and Brown (1995) model in that we assume only the loss of potential energy, which is a half of the total wave energy loss in linear theory, is transferred from the broken waves to the surface roller. The proportionality constant, K_{sr} , is taken to be equal to K_b and, in contrast to Dally and Brown's (1995) model, K_{sr} is a function of the effective beach slope, β . Figure 3-2 demonstrated the improved predictive skills of the present model for evaluations of the slope-dependent return flow volume fluxes.

Based on the mean surface roller energy defined in (4.7), mean volume fluxes of the surface roller in x and y -directions, q_{srx} and q_{sry} , are expressed as

$$(q_{srx}, q_{sry}) = \frac{S_{sr}}{T} (\cos \theta, \sin \theta) = \frac{2E_{sr}}{\rho C} (\cos \theta, \sin \theta) \quad (4.9)$$

Similarly, average momentum fluxes due to the surface roller, R_{xx} and R_{xy} are ex-

pressed as

$$R_{xx} = \frac{\rho S_{sr} C^2 \cos^2 \theta}{L} = 2E_{sr} \cos^2 \theta \quad (4.10)$$

$$R_{xy} = \frac{\rho S_{sr} C^2 \cos \theta \sin \theta}{L} = E_{sr} \sin 2\theta \quad (4.11)$$

Under the long, straight beach assumption, in which total volume flux in the cross-shore direction is zero from mass conservation, the depth-averaged return flow velocity, \bar{U} , is determined by

$$\bar{U} = -\frac{q_{wx} + q_{srx}}{h} = -\frac{E + 2E_{sr}}{\rho C h} \cos \theta \quad (4.12)$$

and wave set-up due to broken waves and surface rollers is given by

$$\rho g h \frac{\partial \bar{\eta}}{\partial x} = -\frac{\partial}{\partial x} (S_{xx} + R_{xx}) - \tau_{cbx} \quad (4.13)$$

where the wave radiation stress, S_{xx} , is defined by (4.5) and τ_{cbx} is a mean bottom current shear stress. In general τ_{cbx} , which is determined later in the development of the near-shore mean current model, is of negligible importance in the mean force balance expressed by (4.13). Combining the energy balance equation (3.12) with the broken wave energy dissipation model for random waves, (2.27), the surface roller model is also readily extended to random waves. Mean surface roller energy determined in this manner is then applied to evaluate momentum and volume fluxes for use in the near-shore mean shear current model.

4.4 Near-Shore Mean Current Model

Wave and surface roller models are now available for the evaluation of external forcings in the near-shore mean current model. Figure 4-1 illustrates the present near-shore current model. To obtain the governing equations for the mean flow, we split the water column at the wave trough level and develop the mean shear current model for the region below the trough level, where we are within water at all times. In this

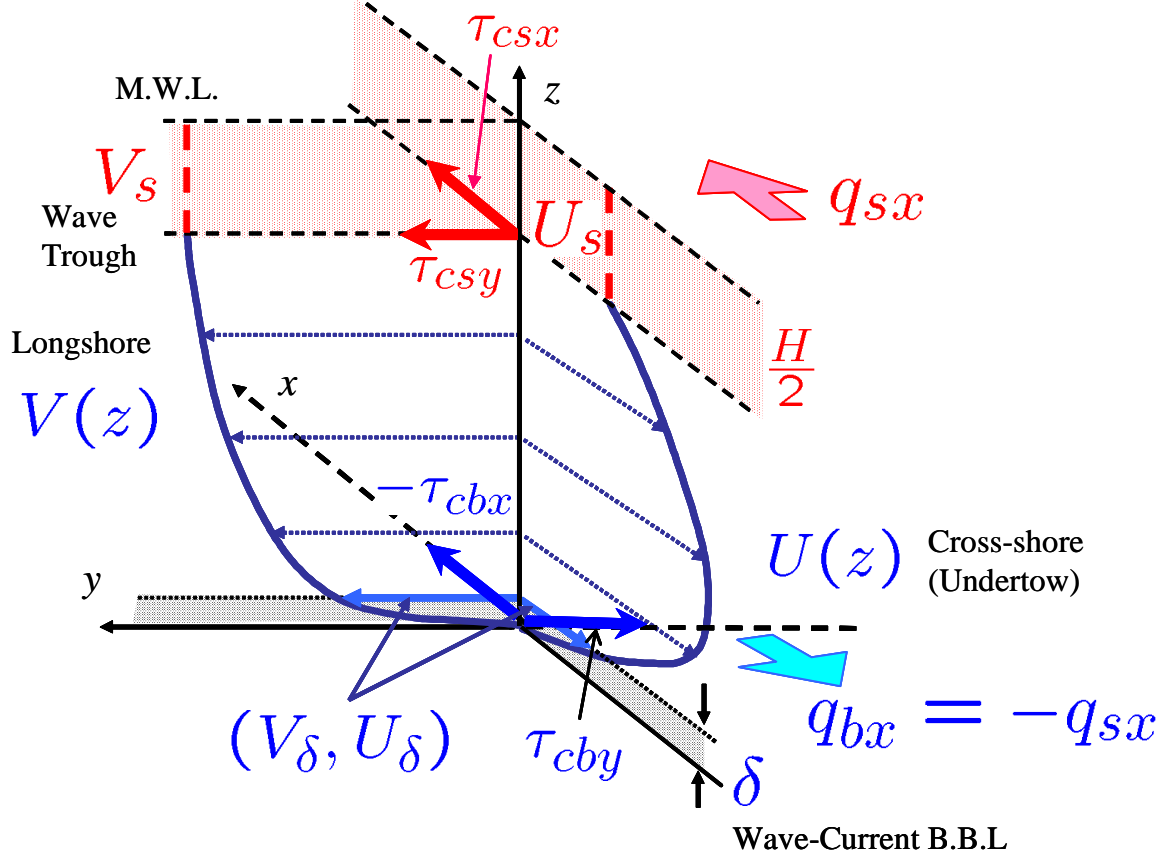


Figure 4-1: Illustration of the near-shore mean current model

manner, we can safely apply time-averaged Reynolds momentum equations for model construction. Above the trough level, we assume that the mean current velocity is vertically uniform and its magnitude is represented by the current velocity at the trough level determined from the mean current model below the trough level. Under this assumption, we define a mean shear stress acting at the trough level, which is applied as a forcing term in the governing momentum equation under the trough level.

4.4.1 Governing Equation

Below the trough level, vertical profiles of the near-shore mean shear currents are determined from

$$\rho \nu_t \frac{\partial \vec{U}}{\partial z} = \vec{\tau}_c \simeq \vec{\tau}_{cb} + \frac{\vec{\tau}_{cs} - \vec{\tau}_{cb}}{h_{tr}} z \quad (4.14)$$

where ν_t is a turbulent eddy viscosity, $\vec{U} = (U, V)$ is the mean current velocity, z is vertical coordinate-axis with $z = 0$ at the bottom, $\vec{\tau}_c = (\tau_{cx}, \tau_{cy})$ is the mean current shear stress vector, and $h_{tr} = h - H/2$ is a “trough water depth”, i.e. the elevation of the wave trough level above the bed with $h = h_0 + \bar{\eta}$ denoting the mean water depth. As seen in (4.14), we assume that $\vec{\tau}_c$ varies linearly in the vertical z -direction so that $\vec{\tau}_c$ may be simply expressed in terms of bottom and trough shear stress vectors, $\vec{\tau}_{cb} = (\tau_{cbx}, \tau_{cby})$ and $\vec{\tau}_{cs} = (\tau_{csx}, \tau_{csy})$, respectively (see Figure 4-1). Note that the vertical linear distribution of the shear stress is true for spatially slowly varying flows under the linear long-wave approximation and therefore is a reasonable assumption in the near-shore field. This linear-approximation of the shear stress and a simple turbulent eddy viscosity model enable us to obtain analytical expressions for the vertical profiles of the mean shear current. This feature contributes significantly to the computational efficiency of our model. Determination of the unknown variables in (4.14), ν_t , $\vec{\tau}_{cs}$ and $\vec{\tau}_{cb}$ is presented in the following sections.

4.4.2 Turbulent Eddy Viscosity Model

Figure 4-2 illustrates the feature of the present turbulent eddy viscosity model. For a simple shear current, in which a uniform shear stress is acting at the bottom boundary, a linear turbulent eddy viscosity is often applied in the vicinity of the bottom, i.e.

$$\nu_t = \kappa u_{*c} z \quad (4.15)$$

where $\kappa = 0.4$ is Von-Karman’s constant and $u_{*c} = \sqrt{|\vec{\tau}_{cb}|/\rho}$ is the shear velocity at the bottom. This eddy viscosity is shown by the thin line in Figure 4-2. For the present wave-induced near-shore shear current model, however, this simple linear eddy viscosity may not be sufficient because the current shear stress is assumed to vary in depth and the magnitude of the shear stress near the water surface may be much larger than that near the bottom because of broken waves and surface rollers. Besides, we should also expect significant excess turbulent fluctuations due to broken waves in the water column within the surf zone. In order to take these additional

turbulent fluctuations into account, we define the following turbulent eddy viscosity shown as a dotted line in Figure 4-2

$$\nu_t = \kappa u_{*s} z \sqrt{\frac{z}{h_{tr}}} \quad (4.16)$$

where u_{*s} is a surface shear velocity. Note that this expression is identical to (4.15) if one replaces the constant shear velocity u_{*c} by $u_{*s} \sqrt{z/h_{tr}}$, i.e. corresponding to a linearly increasing mean shear stress. This form of the eddy viscosity model is consistent with Deigaard et al.'s (1991) numerical solutions for broken waves, in which the k -equation was solved directly. We define the surface shear velocity, u_{*s} , as

$$u_{*s} = \sqrt{|\vec{\tau}_{cs}| / \rho + u_{*B}^2} \quad (4.17)$$

where $|\vec{\tau}_{cs}| = \sqrt{\tau_{csx}^2 + \tau_{csy}^2}$ is associated with the shear stress acting at the trough level and $u_{*B}^2 = M \left(\frac{D_b}{2\rho} \right)^{\frac{1}{3}}$ is the characteristic turbulent velocity due to the breaking wave energy dissipation, D_b , originally proposed by Battjes (1975), and here modified by a factor of 1/2 since only the kinetic wave energy dissipation is assumed to take place in the water column. The other 1/2 of dissipated wave energy, i.e. the dissipated potential wave energy, is assumed to be transferred into the surface roller as discussed in the context of surface roller modeling in Section 3.1.3. The empirical coefficient, M , is taken as $M = \kappa = 0.4$, which is within the range suggested by Battjes (1975). Finally, we define the complete turbulent eddy viscosity model as the maximum of (4.15) or (4.16),

$$\begin{aligned} \nu_t &= \max \left(\kappa u_{*c} z, \kappa u_{*s} z \sqrt{\frac{z}{h_{tr}}} \right) \\ &= \begin{cases} \kappa u_{*c} z & (\delta \leq z \leq z_m) \\ \kappa u_{*s} z \sqrt{\frac{z}{h_{tr}}} & (z_m \leq z \leq h_{tr}) \end{cases} \end{aligned} \quad (4.18)$$

as illustrated by a heavy line in Figure 4-2. In (4.18) $z_m = h_{tr} u_{*c}^2 / u_{*s}^2$ and δ is a wave bottom boundary layer thickness, which is determined from Madsen's (1994) modified wave-current bottom boundary layer model. Extensive studies to investigate

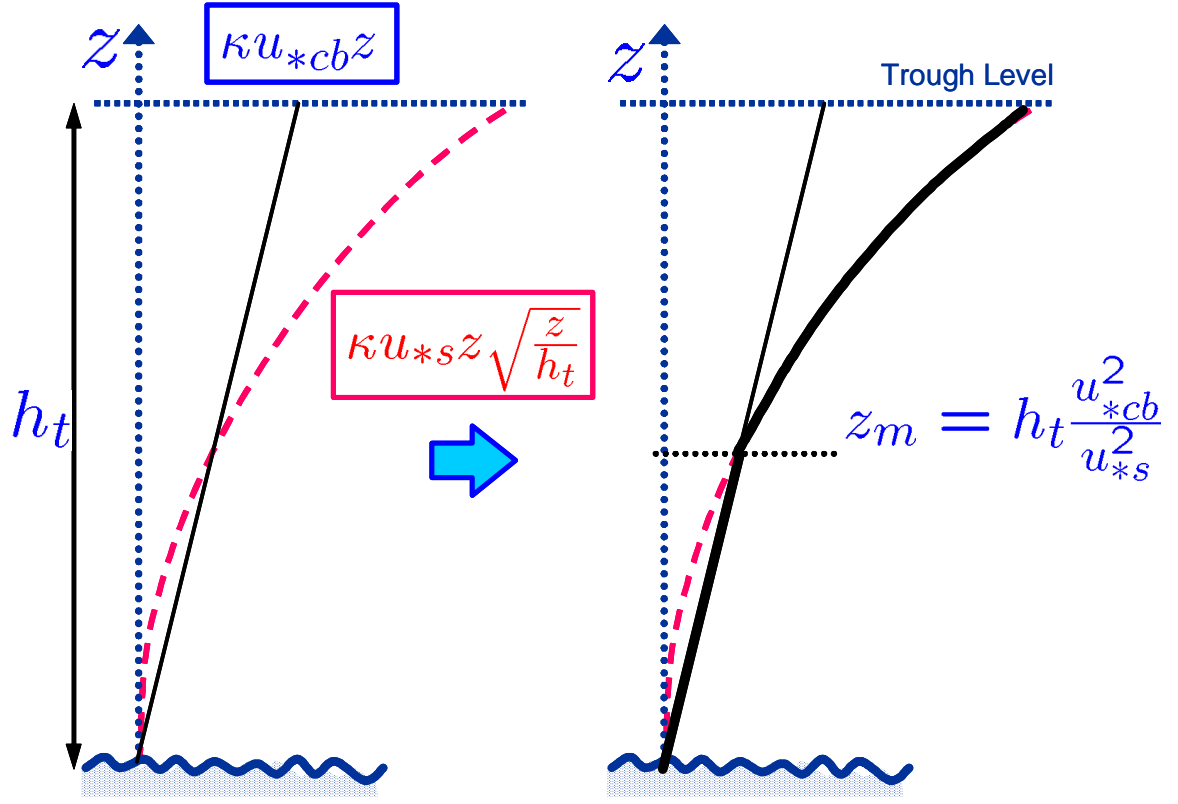


Figure 4-2: Turbulent Eddy Viscosity Model

the turbulence inside the surf zone are still ongoing and therefore the modeling of the turbulent eddy viscosity due to broken waves should be one of future modifications for the present model. For example, Lin and Liu (1998) applied VOF method (Hirt and Nichols, 1981) to treat the free-surface fluid boundary conditions for waves inside the surf zone and numerically solved 3D Reynolds equations and $k-\epsilon$ closures to predict surf zone hydrodynamic characteristics. They compared predicted turbulent eddy viscosity with experimental measurements obtained by Ting and Kirby (1996) and suggested that the vertical profile of the turbulent eddy viscosity well inside the surf zone may be represented by a parabolic curve ($\propto z^{1/4}$) and magnitude of the turbulent eddy viscosity may be scaled by a product of water depth and wave celerity, hC .

4.4.3 Bottom Boundary Condition

To obtain the complete solutions of (4.14), we need to specify the bottom boundary condition. Figure 4-3 illustrates the modified wave-current bottom boundary layer model proposed by Madsen (1994). As seen in Figure 4-3, Madsen's (1994) modified wave-current bottom boundary layer model determines the mean current velocity at the outer edge of the wave bottom boundary layer, $z = \delta$ as

$$\vec{U}_\delta = (U_\delta, V_\delta) = \frac{\vec{\tau}_{cb}}{\kappa \rho u_{*m}} \ln \left(\frac{\delta}{z_0} \right) \quad (4.19)$$

where $z_0 = k_N/30$ with k_N denoting the equivalent Nikuradse (1933) sand grain roughness of the bottom and u_{*m} is the maximum combined wave-current bottom shear velocity, defined by

$$u_{*m}^2 = \tau_m / \rho = C_\mu \tau_{wm} / \rho \quad (4.20)$$

with

$$C_\mu = \sqrt{1 + 2 |\cos \phi_{wc}| \frac{\tau_{cb}}{\tau_{wm}} + \left(\frac{\tau_{cb}}{\tau_{wm}} \right)^2} \quad (4.21)$$

$$\tau_{wm} = \frac{1}{2} \rho f_{cw} u_{bm}^2 \quad (4.22)$$

$$\tau_{cb} = \sqrt{\tau_{cbx}^2 + \tau_{cby}^2} \quad (4.23)$$

and ϕ_{wc} denoting the angle between wave and current bottom shear stress as see in Figure 4-3. The boundary layer thickness, δ , is determined from

$$\delta = A \frac{\kappa u_{*m}}{\omega} \quad (4.24)$$

with

$$A = \exp \left[2.96 (C_\mu A_{bm} / k_N)^{-0.071} - 1.45 \right] \quad (4.25)$$

It is noted here that A given by (4.25), which was obtained by Madsen and Salles (1998), represents the modification of Madsen's (1994) combined wave-current bottom boundary layer model, in which A was taken to be constant. In the expression for the

maximum wave bottom shear stress, (4.22), f_{cw} is the combined wave-current friction factor, u_{bm} is the amplitude of the near-bottom wave orbital velocity obtained from the wave model and $A_{bm} = u_{bm}/\omega$ is the corresponding bottom excursion amplitude. For periodic waves u_{bm} is determined from the predicted non-linear near bottom velocity height, i.e. $u_{bm} = U_{b*}/2$. For random waves, we apply the rms velocity height of the equivalent linear near-bottom wave velocity to determine u_{bm} , i.e. $u_{bm} = U_{b,rms}/2$. Excellent predictive skills of the present wave model for U_{b*} and $U_{b,rms}$ were seen in Figures 2-18 through 2-22. According to Madsen (1994), exact solutions of f_{cw} can be approximated by the following explicit formulae as a function of the dimensionless parameter, $X = C_\mu A_{bm}/k_N$.

$$f_{cw} = \max \begin{cases} C_\mu \exp(7.02X^{-0.078} - 8.82) & 0.2 < X < 10^2 \\ C_\mu \exp(5.61X^{-0.109} - 7.30) & 10^2 < X \end{cases} \quad (4.26)$$

The major advantage gained from the adoption of Madsen's (1994) bottom boundary layer model is that the bottom boundary condition is specified from the bottom roughness, k_N , which is a physically relevant quantity, e.g. comparable to the diameter of the bottom sand grains for fixed-bed conditions. The model is further applicable to movable bed conditions, such as rippled or sheet flow beds, by introducing the equivalent bottom roughness from empirically determined relationships for movable bed roughness.

4.4.4 Solution for Mean Current Profiles

Finally, complete analytical solutions for our mean current profiles are obtained by solving (4.14) with ν_t given by (4.18) and satisfying the bottom boundary conditions given by (4.19). The solution for the vertical profile of the mean current velocity

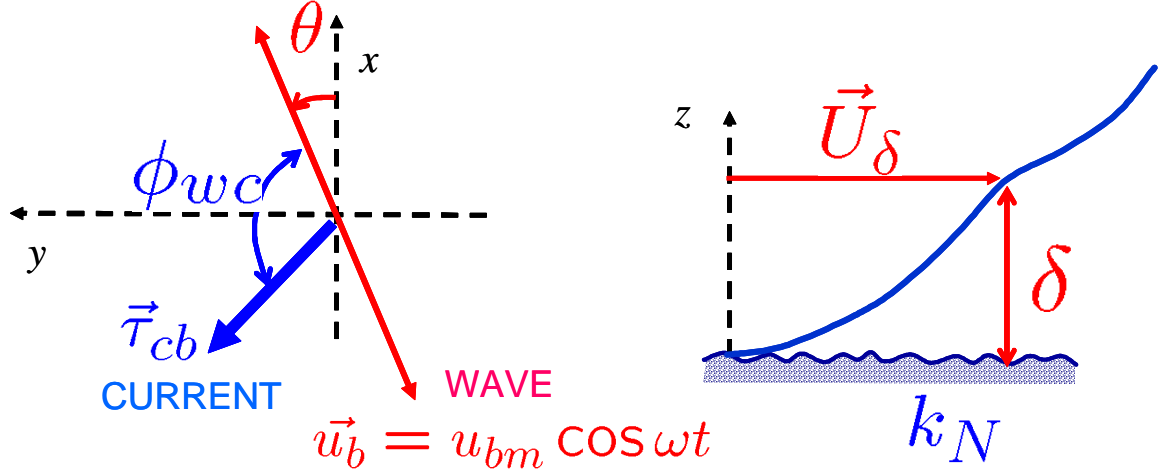


figure 4- Modified wave-current bottom boundary layer model proposed by Jensen (1994)

vector, \vec{U} , may be expressed as

$$\vec{U} = \begin{cases} A_1 \ln \frac{z}{z_0} & (z_0 \leq z \leq \delta) \\ \vec{U}_\delta + A_2 \ln \frac{z}{\delta} + A_3 \frac{z-\delta}{h_{tr}} & (\delta \leq z \leq z_m) \\ \vec{U}_{z_m} + A_4 (\sqrt{z} - \sqrt{z_m}) & (z_m \leq z \leq h_{tr}) \\ \vec{U}_s & (h_{tr} \leq z \leq h + \eta) \end{cases} \quad (4.27)$$

with

$$\begin{aligned} A_1 &= \frac{t}{\frac{cb}{*m}} \\ A_2 &= \frac{cb}{*c} \\ A_3 &= \frac{cs - cb}{*c} \\ A_4 &= \frac{2}{*s} \frac{cs - cb}{\sqrt{tr}} M \vec{r} \frac{r}{m} \end{aligned} \quad (4.28)$$

where \vec{U} , \vec{U}_m and \vec{U}_s are mean current velocity vectors at $z = \delta$ (given by (4.19)), $z = z_m$ and $z = h$, respectively.

Since the momentum force balances proposed in the following sections are expressed as depth-integrated momentum equations, we also integrate (4.27) to define relationships among $\vec{\tau}$, $\vec{\tau}$, and depth-integrated mean current velocities. Integration of (4.27) from the bottom to the trough level yields

$$\vec{\tau}_{cb} = \frac{\rho \kappa \vec{q}_b - C_1 \vec{\tau}_{cs}}{C_2} \quad (4.29)$$

with

$$C_1 = \frac{(z_m - \delta)(2h_{tr} - z_m - \delta)}{2h_{tr}u_{*cb}} + \frac{2h_{tr}}{3u_{*s}} \left(2 - 3\sqrt{\frac{z_m}{h_{tr}}} + \sqrt{\frac{z_m^3}{h_{tr}^3}} \right) \quad (4.30)$$

$$C_2 = \frac{1}{u_{*m}} \left(h_{tr} \ln \frac{\delta}{z_0} - \delta + z_0 \right) + \frac{1}{u_{*c}} \left(h_{tr} \ln \frac{z_m}{\delta} - (z_m - \delta) \left(2 - \frac{z_m + \delta}{2h_{tr}} \right) \right) + \frac{2h_{tr}}{3u_{*s}} \left(3\sqrt{\frac{h_{tr}}{z_m}} - 8 + 6\sqrt{\frac{z_m}{h_{tr}}} - \sqrt{\frac{z_m^3}{h_{tr}^3}} \right) \quad (4.31)$$

and

$$\vec{q}_b = (q_{bx}, q_{by}) = \int_0^{h_{tr}} \vec{U} dz = h_{tr} (U_0, V_0) \quad (4.32)$$

is the mean volume flux vector below the trough level with U_0 and V_0 representing the depth-averaged mean current velocity below the trough level in x and y directions, respectively.

For numerical application of the model, (4.29) is used to evaluate the bottom shear stress, $\vec{\tau}_{cb} = (\tau_{cbx}, \tau_{cby})$ as a function of $\vec{\tau}_{cs}$ and \vec{q}_b . Unknown variables, $\vec{\tau}_{cs}$ and \vec{q}_b , are determined through the following integrated momentum equations.

4.4.5 Integrated Momentum Equations

Integrated momentum equations above the trough level determine the relationship for mean trough shear stress, $\vec{\tau}_{cs}$, and mean current velocities above the trough level, \vec{U}_s . General relationships are derived in Appendix A. Under the long, straight beach condition, i.e. for $\partial/\partial y = 0$, momentum equations integrated above the trough level yield cross-shore (x) direction shear stress at trough level, $z = h_{tr}$

$$\tau_{csx} = F_{shpx} + F_{smx} + F_{swx} + F_{srx}$$

$$+F_{sumx} + F_{srmx} + F_{suwx} \quad (4.33)$$

where F_{shpx} , F_{smx} , F_{swx} , F_{srx} , F_{sumx} , F_{srmx} , and F_{suwx} are forces due to hydrostatic pressure, mean current components, waves, rollers, wave-current interactions, roller-current interactions, and the vertical mean momentum transfer, respectively. Neglecting atmospheric pressure and wind shear stress contributions, we have from (A.22)

$$F_{shpx} = -\rho g a \frac{\partial \bar{\eta}}{\partial x} \quad (4.34)$$

$$F_{smx} = -\rho a \frac{\partial U_s^2}{\partial x} - \rho U_s^2 \frac{\partial \bar{\eta}}{\partial x} \quad (4.35)$$

$$F_{swx} = -\frac{\partial}{\partial x} \left(\frac{E}{2} \right) - \frac{\rho a}{2} \frac{\partial (\hat{u}_s^2 - \hat{w}_s^2)}{\partial x} - \frac{\rho}{2} (\hat{u}_s^2 - \hat{w}_s^2) \frac{\partial \bar{\eta}}{\partial x} \quad (4.36)$$

$$F_{srx} = -\rho \frac{\partial}{\partial x} R_{xx} \quad (4.37)$$

$$F_{sumx} = -\rho \frac{\partial}{\partial x} (2q_{wx} U_s) \quad (4.38)$$

$$F_{srmx} = -\rho \frac{\partial}{\partial x} (q_{srx} U_s) \quad (4.39)$$

$$\begin{aligned} F_{suwx} &= \rho \overline{u_{tr} w_{tr}} \\ &= \rho \left(U_s \frac{\partial q_{sx}}{\partial x} + \hat{u}_s \frac{\partial q_{wx}}{\partial x} \right) \\ &\quad + \left(U_s^2 + \frac{\hat{u}_s^2}{2} \right) \frac{\partial (\bar{\eta} - a)}{\partial x} \end{aligned} \quad (4.40)$$

where $a = H/2$ is the amplitude of the equivalent linear wave, (\hat{u}_s, \hat{w}_s) is the wave orbital velocity amplitudes at the surface obtained from linear theory, $q_{sx} = q_{wx} + q_{srx} + aU_s$ is the total mean volume flux above the trough level. Similarly we have in the shore-parallel (y) direction, by use of (A.22) with $\partial/\partial y = 0$,

$$\begin{aligned} \tau_{csy} &= F_{smy} + F_{swy} + F_{sry} \\ &\quad + F_{sumy} + F_{srmx} + F_{svwy} + F_{svy} \end{aligned} \quad (4.41)$$

where

$$F_{smy} = -\rho a \frac{\partial U_s V_s}{\partial x} - \rho U_s V_s \frac{\partial \bar{\eta}}{\partial x} \quad (4.42)$$

$$F_{swy} = -\frac{\rho a}{2} \frac{\partial (\hat{u}_s \hat{v}_s)}{\partial x} - \frac{\rho \hat{u}_s \hat{v}_s}{2} \frac{\partial \bar{\eta}}{\partial x} \quad (4.43)$$

$$F_{sry} = -\rho \frac{\partial}{\partial x} R_{xy} \quad (4.44)$$

$$F_{swmy} = -\rho \frac{\partial}{\partial x} (q_{wx} V_s + q_{wy} U_s) \quad (4.45)$$

$$F_{sry} = -\rho \frac{\partial}{\partial x} (q_{srx} V_s) \quad (4.46)$$

$$\begin{aligned} F_{svwy} &= \rho \overline{v_{tr} w_{tr}} \\ &= \rho \left(V_s \frac{\partial q_{sx}}{\partial x} + \hat{v}_s \frac{\partial q_{wx}}{\partial x} \right) \\ &\quad + \left(U_s V_s + \frac{\hat{u}_s \hat{v}_s}{2} \right) \frac{\partial (\bar{\eta} - a)}{\partial y} \end{aligned} \quad (4.47)$$

$$\begin{aligned} F_{svy} &= a \frac{\partial \tau_{xy}}{\partial x} \\ &= \rho a \frac{\partial}{\partial x} \left(\nu_{ts} \frac{\partial V_s}{\partial x} \right) \end{aligned} \quad (4.48)$$

where the last term, F_{svy} , a turbulent viscous force, is expressed through use of (A.38). The mean momentum fluxes due to the surface roller, R_{xx} and R_{xy} in (4.37) and (4.44) were determined in (4.10) and (4.11), respectively.

Similarly, with reference to Appendix A for details, the integrated momentum equations over the entire depth (A.31), omitting atmospheric effects and taking $\partial/\partial y = 0$, result in

$$\tau_{cbx} = F_{bhpx} + F_{bmx} + F_{bwx} + F_{srx} + F_{swmx} + F_{srmx} \quad (4.49)$$

$$\begin{aligned} \tau_{cbx} &= F_{bmy} + F_{bwy} + F_{sry} + F_{swmy} + F_{srmx} \\ &\quad + F_{bvy} \end{aligned} \quad (4.50)$$

with

$$F_{bhpx} = -\rho g h \frac{\partial \bar{\eta}}{\partial x} \quad (4.51)$$

$$F_{bmx} = -\rho \frac{\partial}{\partial x} (aU_s^2 + q_{bx}U_0) \quad (4.52)$$

$$F_{bwx} = -\frac{\partial}{\partial x} S_{xx} \quad (4.53)$$

$$F_{bmy} = -\rho \frac{\partial}{\partial x} (aU_sV_s + q_{bx}V_0) \quad (4.54)$$

$$F_{bwy} = -\frac{\partial}{\partial x} S_{xy} \quad (4.55)$$

$$\begin{aligned} F_{bvy} &= \int_0^h \frac{\partial \tau_{xy}}{\partial x} dz \\ &= \rho a \frac{\partial}{\partial x} \left(\nu_{ts} \frac{\partial V_s}{\partial x} \right) + \rho h_{tr} \frac{\partial}{\partial x} \left(\nu_{t0} \frac{\partial V_0}{\partial x} \right) \end{aligned} \quad (4.56)$$

The wave radiation stress tensors, S_{xx} and S_{xy} in (4.53) and (4.55) are given by (4.5) and (4.6), respectively.

4.5 Model Test

Predictive performance of the near-shore current model is examined through comparisons of predicted and measured mean current velocity. We first examine the predictive skills for undertow velocity profiles by comparing model predictions with measurements for periodic or random waves normally incident on uniform plane or barred beaches. Predictions of the longshore current velocity profiles are then compared with measurements for periodic or random waves obliquely incident on plane straight beaches. Finally, applicability of the present bottom boundary layer model is also verified by comparing predicted depth-averaged longshore current velocity with experimental data, in which identical periodic waves are obliquely incident on a long, straight beach with different bottom roughness. Details on the numerical scheme used in the implementation of the theoretical model for near-shore currents are presented in Appendix B.

4.5.1 Undertow Velocity Profiles

Figure 4-4 shows the predicted wave height, mean water level and vertical profiles of the undertow velocity compared with the measurements reported by Cox and

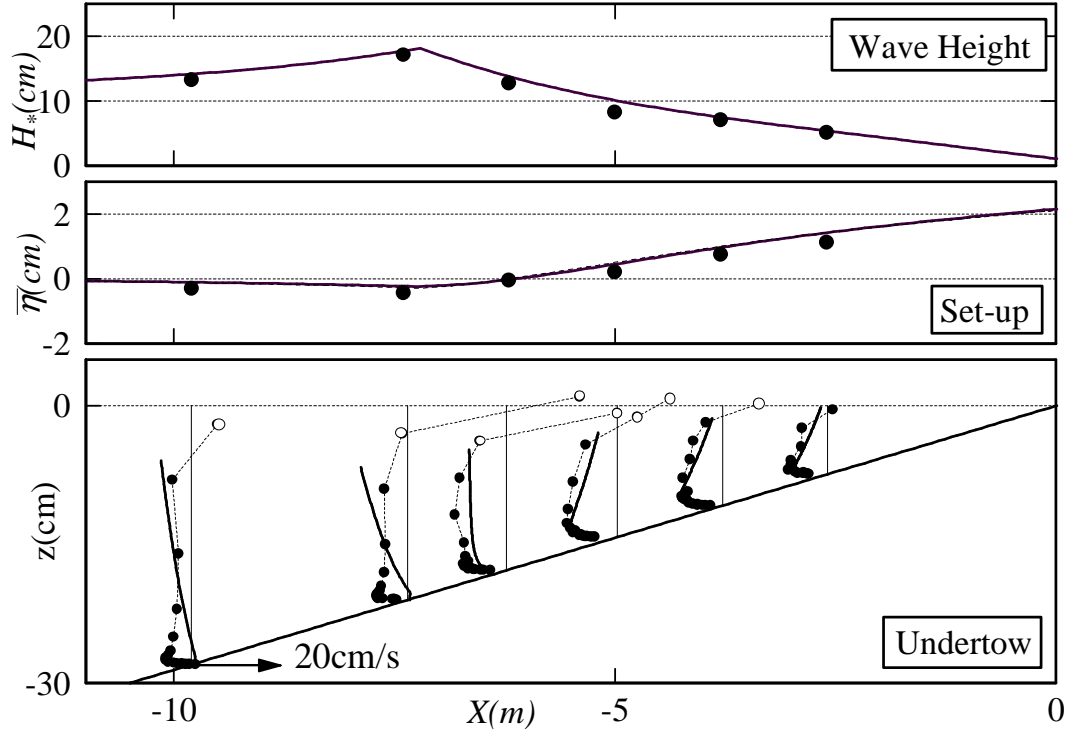


Figure 4-4: Comparison of measured and predicted wave heights, H_* , wave set-up, $\bar{\eta}$, and vertical profiles of undertow velocity for periodic waves on plane 1 on 35 sloping beach with bottom roughness $k_N = 1\text{mm}$. Measurements by Cox and Kobayashi (1996) (full circles indicate measurements below and open circles above trough level) and predictions (full line). Dotted line in set-up is the prediction neglecting the bottom shear stress and mean momentum forces.

Kobayashi (1996), in which periodic waves are normally incident on a uniform plane beach with $D = 1\text{mm}$ sand grains glued to the surface, i.e. k_N is taken to be $D = 1\text{mm}$. In the comparisons of wave set-up, the full line is the predicted wave set-up determined from the momentum equation (4.49) while the dashed line is the prediction obtained from (3.10) without τ_{cbx} . From the comparison of these two predictions, the effect of τ_{cbx} and current momentum forces in (4.49) are seen to be negligibly small. This suggests that excellent results for wave set-up may be obtained simply from the wave and surface roller model, (3.10), as shown in Figures 3-3, through 3-7, i.e. without having to solve the full set of equations.

This negligible effect of the bottom shear stress for prediction of the wave set-up is

more clearly illustrated in Figure 4-5, which compares the forcing terms of the cross-shore momentum equation for the entire depth, (4.49). Figure 4-5 (a) compares the wave radiation stress forcing, F_{bwx} (thin full line), the surface roller force, F_{srx} (thin dashed line), and the hydrostatic pressure forcing due to wave setup, F_{bhpx} (heavy dotted line). A heavy full line in the same figure indicates a sum of these three forcing terms. In these figures, the positive force (in N/m^2) acts in the shoreward direction while the negative force acts in the seaward direction. We hereafter refer to the forces due to waves and rollers as “external forces” because these forces, such as F_{bwx} and F_{srx} , are not associated with mean current velocity and are externally obtained from the wave and surface roller models developed in Chapters 2 and 3, respectively. As seen in Figure 4-5 (a), the hydrostatic pressure force, F_{bhpx} , counteracts the other two external forces, F_{bwx} and F_{srx} , and the sum of these three forces becomes very small compared to any of the three components. Figure 4-5 (b) shows “mean-current-associated” forcing terms due to the mean current advection, F_{bmx} (thin full line), the interaction of waves and mean currents, F_{swmx} (thin dotted line), and the interaction of surface rollers and mean currents, F_{srmx} (thin dashed line). Similar to Figure 4-5 (a), the heavy full line is a “net mean-current-associated force”, i.e. the sum of these three mean-current associated forcing terms. The magnitude of these mean-current associated forcing terms, which is at most $2(N/m^2)$, is smaller than the former external forcings, F_{bwx} , F_{srx} , and F_{bhpx} , some of which are larger than $10(N/m^2)$ near the breaking point. Similar to the external forcing and hydrostatic pressure terms, mean-current-associated forces also balance each other and the sum of these three forces becomes very small compared to either F_{bmx} , F_{swmx} , or F_{srmx} . Figure 4-5 (c) shows the sum of external forces and the hydrostatic pressure force, the net mean-current-associated force, and the sum of these two, i.e. the total cross-shore forcing that corresponds to the bottom shear stress, τ_{cbx} . Note that the force-scale of the last figure is much smaller than in the first figures and the magnitude of τ_{cbx} is about 50 times smaller than the hydrostatic pressure force, F_{bhpx} . This feature clearly supports the negligible effect of the bottom shear stress for prediction of wave set-up. Similar negligible effects of the bottom shear stress for prediction of wave setup will

be illustrated in subsequent comparisons for different experimental cases. Inside the surf zone, $-7 < X$ (m), the net mean-current-associated force, $F_{bmx} + F_{swmx} + F_{srmx}$, (thin full line) acts in the shoreward direction (positive force) and slightly reduces the seaward bottom shear stress, τ_{cbx} (heavy full line). However, the magnitude of the net mean-current-associated force is much smaller than the sum of external and hydrostatic pressure forces, $F_{bwx} + F_{srx} + F_{bpx}$ (thin dashed line) and τ_{cbx} becomes nearly equal to $F_{bwx} + F_{srx} + F_{bpx}$. This feature supports the negligible effect of the advective forces in the cross-shore momentum equations, which is assumed by a number of existing undertow velocity models, such as those by Svendsen (1984), Stive and Wind (1986), Okayasu et al. (1990), and Deigaard, et al. (1991).

Figure 4-6 compares the forcing terms of the cross-shore momentum equation above the wave trough level (4.33). Similar to Figure 4-5, Figure 4-6 (a) compares external forcings due to waves, F_{swx} , surface rollers, F_{srx} , and the hydrostatic pressure force, F_{shpx} , and (b) shows the mean-current-associated forcing terms, F_{smx} , F_{swmx} , F_{srmx} , and F_{suwx} . Heavy full lines in these figures denote the sum of the components in each figure. Figure 4-6 (c) compares the sum of external and hydrostatic pressure forces, the net mean-current-associated force, and the sum of these two, i.e. the total shear stress at the trough, τ_{csx} . Outside the surf zone, the wave energy increases as waves shoal up to the breaking point ($X \simeq -7$ (m)) and the increasing wave energy yields F_{swx} acting in the seaward direction, i.e. $F_{swx} < 0$ outside the surf zone as seen in Figure 4-6 (a). F_{srx} is zero outside the surf zone because no surface rollers are generated. F_{shpx} acts in the shoreward direction due to the wave set-down but is smaller than $|F_{swx}|$. The net mean-current-associated force above the trough also acts in the shoreward direction but the magnitude is relatively small compared to $|F_{swx}|$. As a result, seaward acting F_{swx} predominates the other forces and the total forcing, τ_{csx} , also acts in the seaward direction outside the surf zone (see the heavy line in Figure 4-6 (c)). The seaward-acting τ_{csx} yields a negative gradient of the undertow velocity as trough level is approached, i.e., the undertow becomes seaward-leaning near the surface. This feature is clearly observed in the two velocity profiles prior to breaking ($X < -7$ (m)) in Figure 4-4.

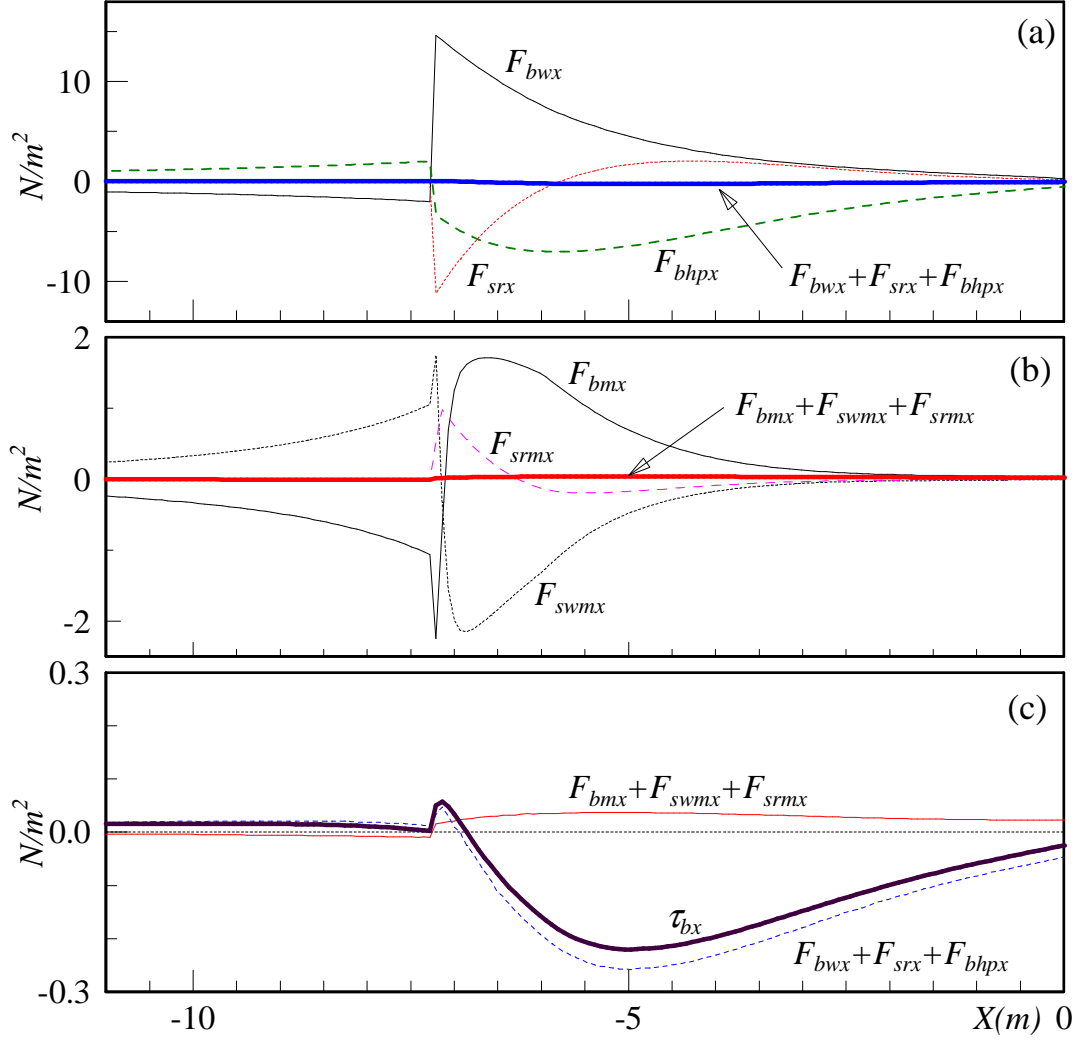


Figure 4-5: Comparisons of the cross-shore forcing terms in (4.49) for Cox and Kobayashi's (1996) experiment: (a) external forcings and hydrostatic pressure forces; (b) mean-current-associated forces; (c) total forces.

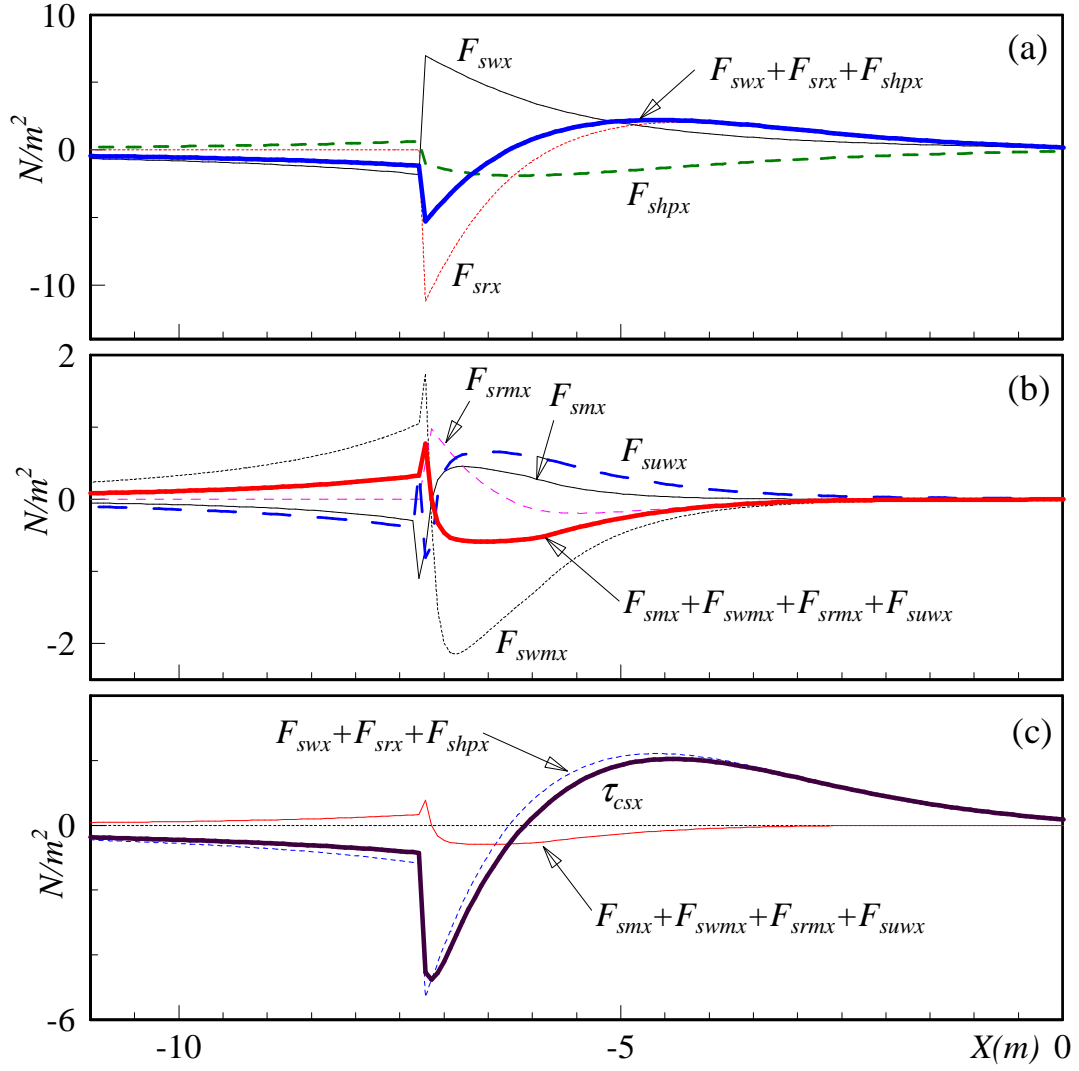


Figure 4-6: Comparisons of the cross-shore forcing terms in (4.33) for Cox and Kobayashi's (1996) experiment: (a) external forcings and hydrostatic pressure forces; (b) mean-current-associated forces; (c) total forces.

In the outer surf zone, abrupt decay of the wave energy after the breaking point causes a large F_{swx} and F_{bwx} acting in the shoreward direction while the growing surface roller yields the seaward acting F_{srx} . Because F_{bwx} is larger than the seaward acting F_{srx} just after the breaking point, as seen in Figure 4-5 (a), the mean water level rises towards the shore (wave set-up) and the resulting hydrostatic pressure forces, F_{bhpx} and F_{shpx} , act in the seaward direction to compensate the shoreward force due to F_{bwx} . Above the trough level, in contrast to the force balance for the entire depth, the sum of seaward acting F_{srx} and F_{shpx} is larger than the shoreward acting F_{swx} and the sum of these three forces, $F_{swx} + F_{srx} + F_{shpx}$, acts in the seaward direction. As broken waves propagate further inside the surf zone, the surface roller initially grows causing the dissipation of energy from the surface roller to gradually dominate the broken wave potential energy transferred to the surface roller. Thus, the seaward acting F_{srx} decreases and eventually starts to act in the shoreward direction. In this transition region, the seaward acting τ_{csx} also decreases and eventually turns to act in the shoreward direction. This feature is observed in the third undertow velocity profile in Figure 4-4, in which the undertow velocity is nearly uniform in the z -direction because τ_{csx} is relatively small in this vicinity ($X(m) \simeq -6$).

Well inside the surf zone, both F_{swx} and F_{srx} act in the shoreward direction and yield a relatively strong τ_{csx} acting in the shoreward direction. As seen in the last three velocity profiles near the shore line in Figure 4-4, undertow velocity profiles become shoreward-leaning near the surface. The model successfully explains these physical features and excellent agreement with measurements is obtained inside the surf zone. Similar to the comparisons in Figure 4-5, the mean-current-associated forces have little effect on τ_{csx} although it slightly smooths τ_{csx} (see Figure 4-6 (c)).

The model tends to over-predict the seaward-leaning undertow profile outside the surf zone. Since the total volume flux of the return flow is fixed, i.e. governed by the predetermined shoreward volume flux due to waves, the over-prediction of the seaward current velocity near the trough causes under-prediction of the seaward current velocity near the bottom. In the first two velocity profiles outside the surf zone, near-bottom mean current velocity even goes shoreward to compensate the over-predicted

seaward current velocity near the trough. This over-prediction of the seaward-leaning profiles is mainly because of the prediction of a very low turbulent eddy viscosity outside the surf zone since, for periodic waves, breaking does not contribute to any turbulence seaward of the breaking point. Thus, the model assumes zero wave breaking generated turbulence outside the surf zone although breaking wave turbulent energy, in reality, may be advected from within the surf zone beyond the breaking point by the undertow itself. As seen in Figures 4-5 and 4-6, dramatic changes of F_{smx} and F_{bmx} beyond the wave breaking point indicate that our assumption of the gently varying mean current velocity in the horizontal direction is violated. If the mean-current associated forces, such as F_{smx} or F_{bmx} , are comparable to other forces, the assumption of linearly varying shear stress in the vertical direction is also violated because vertically varying mean current velocity profiles do not yield linearly varying advection forces. For random waves, which are more important from a practical perspective, this over-prediction do not occur because a certain fraction of waves are always breaking under the model assumption and yield a certain amount of broken wave turbulence and hence increased eddy viscosity at all locations.

Figures 4-7, 4-8, and 4-9 show the same comparisons as those of Figures 4-4, 4-5, and 4-6, respectively, but for the experimental Case 2 reported by Okayasu and Katayama (1992), in which random waves are normally incident on a uniform plane 1 on 20 sloping smooth concrete beach (k_N is taken according to smooth turbulent flow, i.e. $k_N = 3.3\nu/u_{*m}$). Note that the breaking rms wave height ($H_{b,rms} \simeq 6cm$) in this experiment is smaller than half of the predicted equivalent linear breaking wave height in Cox and Kobayashi's (1996) experiment ($H_b \simeq 13cm$). Since the magnitude of the wave forcing is roughly proportional to H^2 , the predicted forcings in this experiment are therefore about four times smaller than those in Cox and Kobayashi's (1996) experiment. In contrast to the periodic wave case, shown in Figures 4-5 and 4-6, all the momentum forces vary gently in the cross-shore direction and, as discussed previously, excellent agreement of the undertow profiles are obtained even outside the surf zone. Similar to the periodic wave case, the mean-current-associated forces shown in Figures 4-8 and 4-9 are smaller than the external forces and have minor

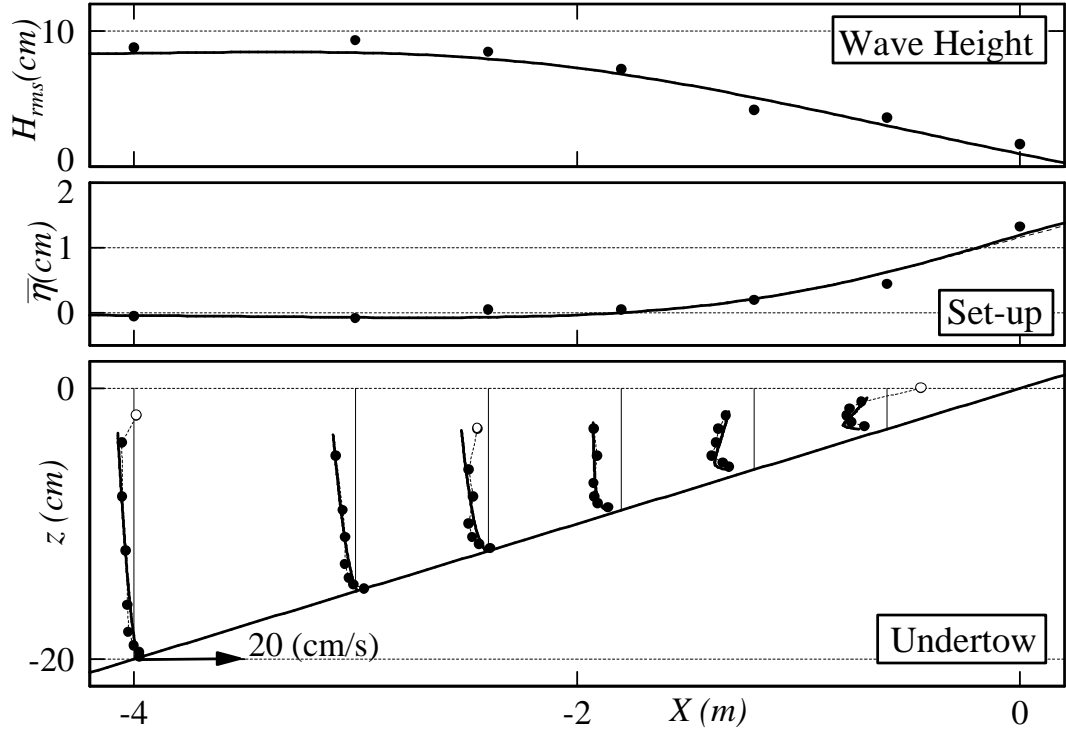


Figure 4-7: Comparison of measured and predicted wave heights, H_{rms} , wave set-up, $\bar{\eta}$, and vertical profiles of undertow velocity for random waves on plane 1 on 20 sloping beach with smooth concrete bed. Measurements(Case 2) by Okayasu and Katayama (1992) (full circles indicate measurements below and open circles above trough level) and predictions (full line). Dotted line in set-up is the prediction neglecting the bottom shear stress and mean momentum forces.

effects on the total shear stresses, τ_{csx} and τ_{cbx} .

Figure 4-10 shows the same comparisons as Figure 4-7 but for the experimental Case 3 presented by Okayasu and Katayama (1992), in which random waves are normally incident on a barred beach. As seen in the Figure, the wave model successfully predicts the following observational features: the first wave breaking in front of the bar-crest; wave recovery over the bar-trough; and the second wave breaking near the shore-line. Similar to other comparisons, excellent agreement of predicted and measured wave set-up verifies the total forcing balance in the cross-shore direction. Although the model slightly over-predicts the magnitude of the undertow velocity, characteristic features of the predicted undertow profiles, such as seaward and shore-

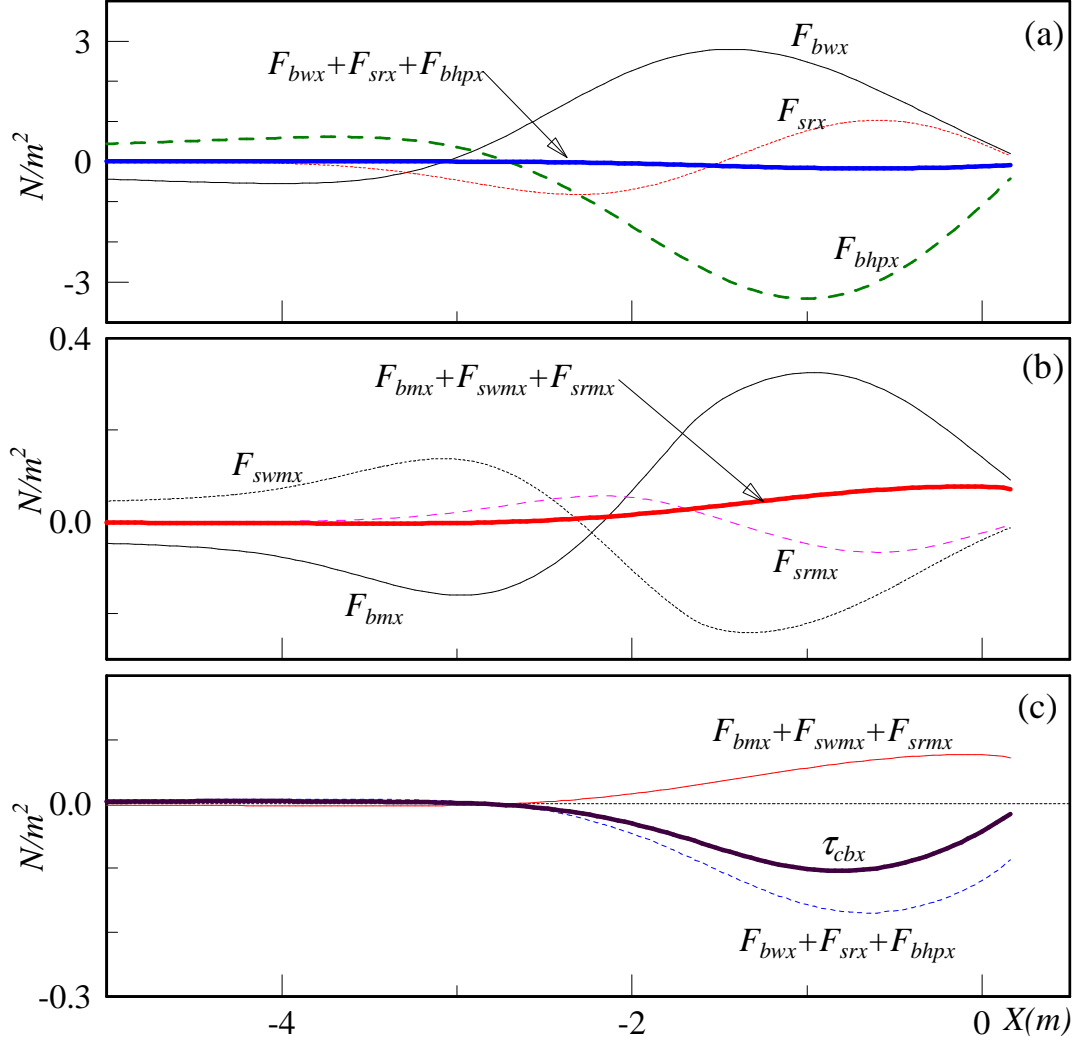


Figure 4-8: Comparisons of the cross-shore forcing terms in (4.49) for Okayasu and Katayama's (1992) experiment (Case 2): (a) external forcings and hydrostatic pressure forces; (b) mean-current-associated forces; (c) total forces.

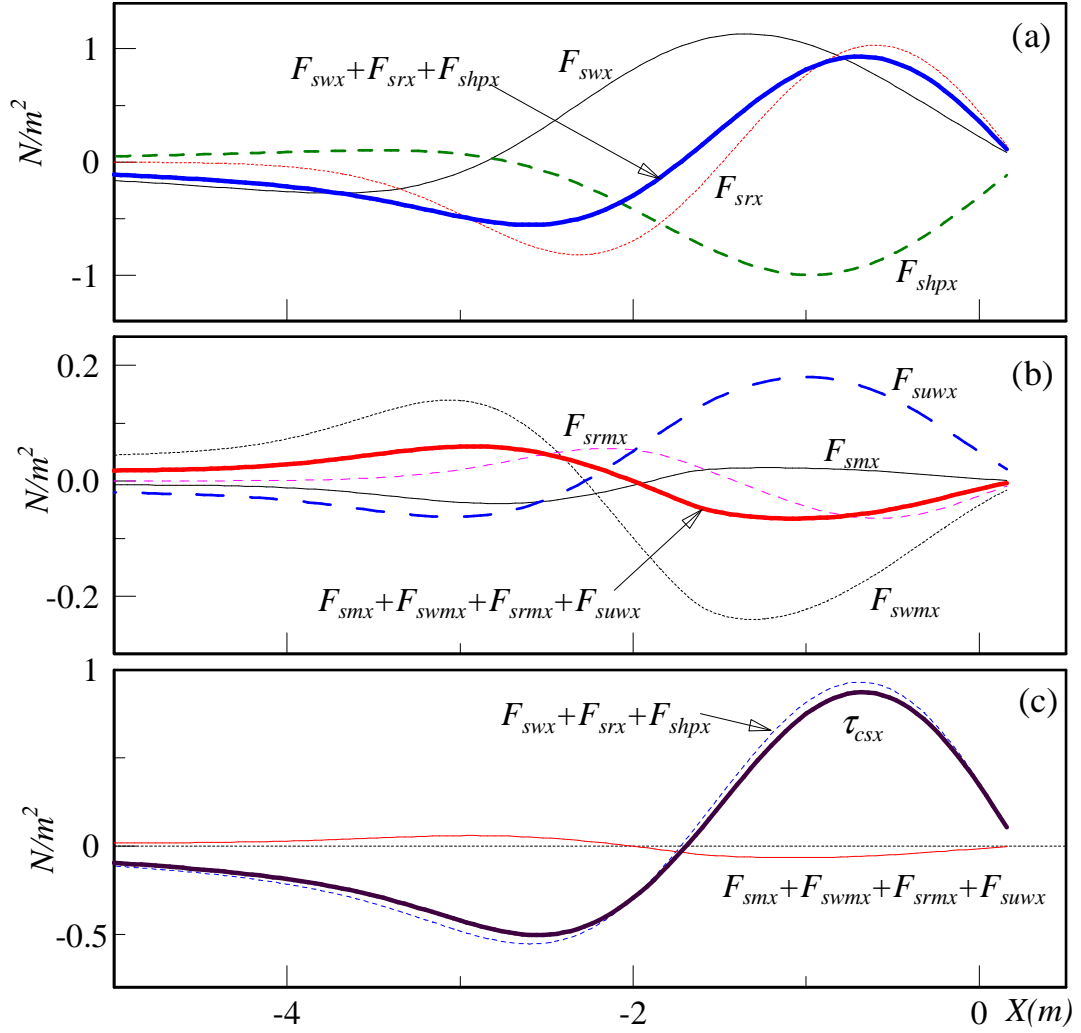


Figure 4-9: Comparisons of the cross-shore forcing terms in (4.33) for Okayasu and Katayama's (1992) experiment: (a) external forcings and hydrostatic pressure forces; (b) mean-current-associated forces; (c) total forces.

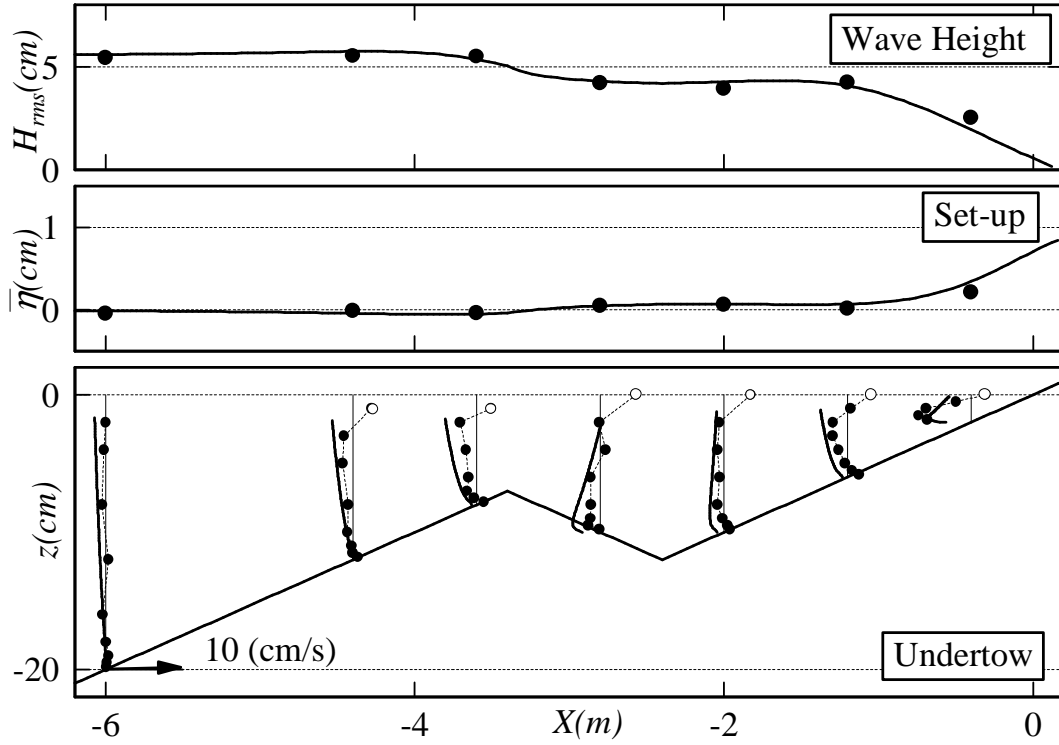


Figure 4-10: Comparison of measured and predicted wave heights, H_{rms} , wave set-up, $\bar{\eta}$, and vertical profiles of undertow velocity for random waves on barred beach with smooth concrete bed. Measurements(Case 3) by Okayasu and Katayama (1992) (full circles indicate measurements below and open circles above trough level) and predictions (full line). Dotted line in set-up is the prediction neglecting the bottom shear stress and mean momentum forces.

ward leanings, agree very well with measurements. This generally excellent agreement of predicted undertow velocity profiles with measurements supports the validity of the predicted shear stress distributions, i.e., the modeled momentum balance around the surf zone.

4.5.2 Longshore Current Profiles

Applicability of the model for prediction of longshore currents is first examined through comparison with the unique experimental data set obtained by the U.S. Army Corps of Engineers in their Longshore Sediment Transport Facility (LSTF). In

the LSTF, uniform longshore currents on a straight beach are achieved by multiple pumps installed at the end of the beach (Hamilton and Ebersole, 2001). Figure 4-11 shows the comparison of predicted and measured wave height, mean water level, vertical profiles of undertow and longshore current, and depth-averaged longshore current velocity for periodic waves obliquely incident on a long, straight plane 1 on 30 sloping beach (Test 6A-N). Since the plane beach was made of concrete, we assume a smooth turbulent bottom roughness condition for the model, i.e., the equivalent bottom roughness is determined from $k_N = 3.3\nu/u_{*m}$ with kinematic viscosity, $\nu = 10^{-6}(m^2/s)$. Agreement of predicted and measured wave heights, wave set-up, and undertow velocity profiles is equally as good as previous comparisons for normally incident waves. Similar to the comparisons of undertow velocity profiles for Cox and Kobayashi's (1996) periodic wave experiment, shown in Figure 4-4, the model over-predicts the seaward-leaning velocity profile near the breaking point, $X \simeq -11.5(m)$. However, inside the surf zone agreement between measured and predicted undertow velocity profiles is excellent. Predicted vertical profiles of the longshore current agree well with measurements with a tendency toward under-prediction of longshore currents very close to shore. In the comparison of depth-averaged longshore current velocity, \bar{V} , multiple full circles at the same x locations are the measurements from different longshore positions, from which one can see the uniformity and possible measurement variability of the measured longshore current velocity. As seen in the Figure, the model successfully captures the well-known observational feature that the cross-shore location of the peak longshore current velocity shifts shoreward from the breaking point.

Figure 4-12 shows the forcing terms in the momentum equation for the entire depth in the shore-parallel (y) direction, (4.50). Similar to Figure 4-5, Figure 4-12 (a) compares the external forces, (b) shows mean-current-associated forces, and (c) compares the net external forces, the net mean-current-associated forces, and the sum of these, i.e. the total bottom shear stress in the longshore y -direction, τ_{cby} . In these figures, the positive force is acting in the y -direction shown in Figure 4-1. As seen in Figure 4-12 (a), both wave radiation stress force, F_{bwy} , and the

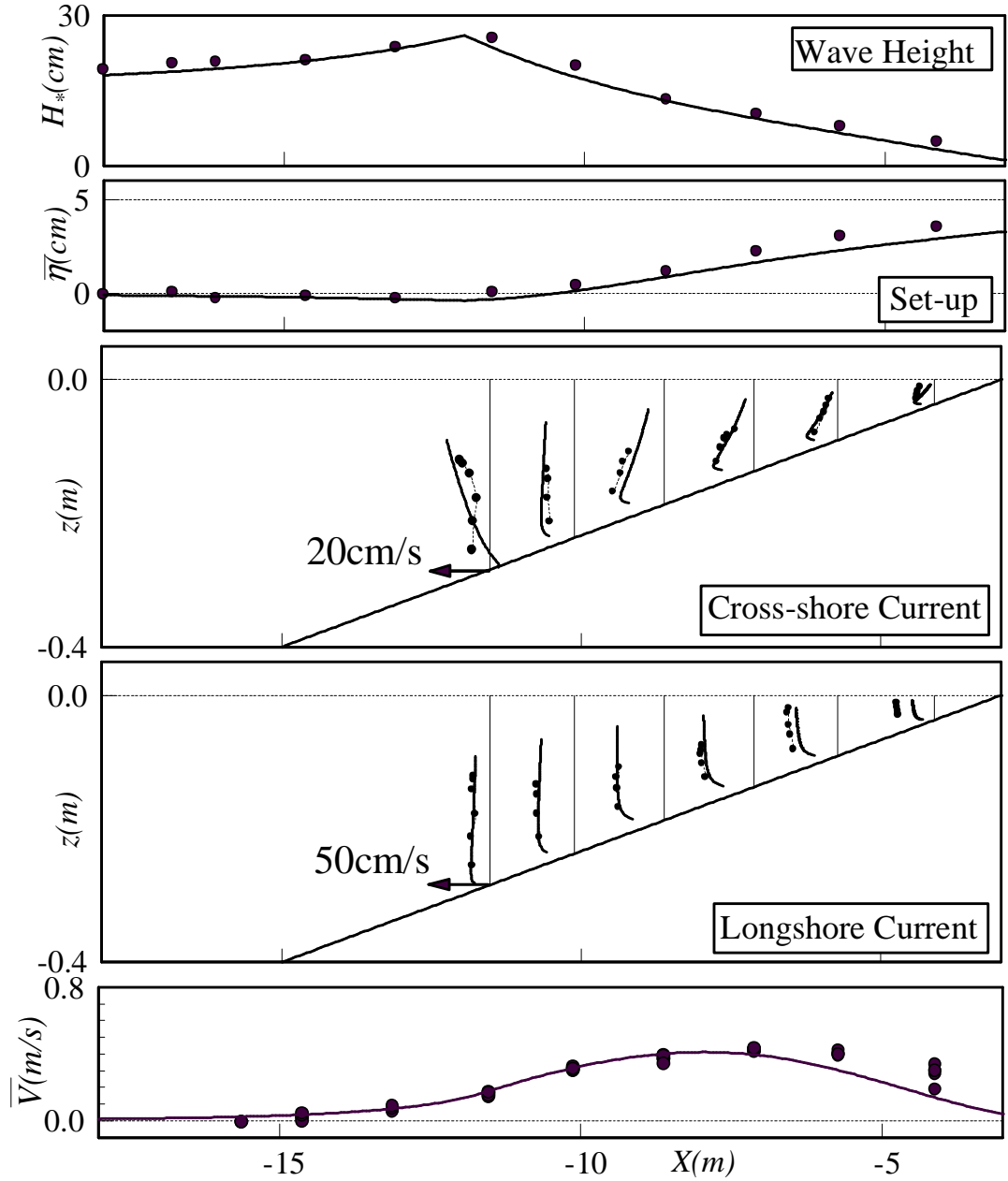


Figure 4-11: Comparisons of measured and predicted wave heights, H_* , wave set-up, $\bar{\eta}$, vertical profiles of undertow and longshore current velocity, and depth-averaged longshore current velocity, \bar{V} , for periodic waves on plane 1 on 30 sloping beach. Measurements (Test 6A-N) by Hamilton and Ebersole (2001) (full circles) and predictions (full line).

surface roller force, F_{sry} , are maximum and minimum, respectively, at the breaking point, $X \simeq -12 (m)$ where they counteract each other. Thus, the net external force, $F_{bwy} + F_{sry}$, becomes virtually zero at the breaking point. Zero-net external force at the breaking point allows the continuous transition of the net longshore external force beyond the breaking point. This feature, i.e. $F_{bwy} + F_{sry} \simeq 0$ at the breaking point, is obtained because the present surface roller model assumes only half of the broken wave energy dissipation to be transferred to the surface roller, i.e. $-\partial E/\partial x \simeq 2\partial E_{sr}/\partial x$ at the breaking point. If the model assumes more than half of the broken wave energy dissipation to be transferred to the surface roller, i.e. $-\partial E/\partial x < 2\partial E_{sr}/\partial x$, then $-F_{sry}$ dominates F_{bwy} and yields a negative net longshore external force at the breaking point. The negative net external force may result in predicting unrealistic negative longshore current velocity in the vicinity of the breaking point. As seen in Figure 4-12 (a), the cross-shore location of the peak external force is shifted from the breaking point toward inside the surf zone. This surface roller effect has been pointed out and introduced in one-dimensional longshore current models (e.g., Kuriyama, 1994; Okayasu et al., 1994; Reniers et al., 1995; Osiecki and Dally, 1996; Reniers and Battjes, 1997; and Ruessink et al., 2001).

In contrast to the force comparisons in the cross-shore (x) direction, shown in Figures 4-5 and 4-8, the magnitude of mean-current-associated forces, such as F_{bmy} and F_{swmy} , are comparable to the longshore external forces because external forces in the y -direction are not as large as those in x -direction when waves are near-normally incident on a long, straight beach. In this particular experiment case (Test 6A-N), for example, the angle between incident wave direction and x -axis is relatively small (10°) and the maximum wave radiation stress forces at the breaking point in x and y -directions are $F_{bwx} \simeq 23 (N/m^2)$ and $F_{bwy} \simeq 2 (N/m^2)$, respectively. In the shore-parallel (y) direction, therefore, the mean-current associated forces are of equal importance to longshore external forces. In Figure 4-12 (b) mean-current-associated forces, F_{bmy} , F_{swmy} , and F_{srmmy} , virtually balance each other and the net mean-current-associated force becomes much smaller than each of the three contributions. However, the magnitude of this net mean-current associated force is still comparable to the net

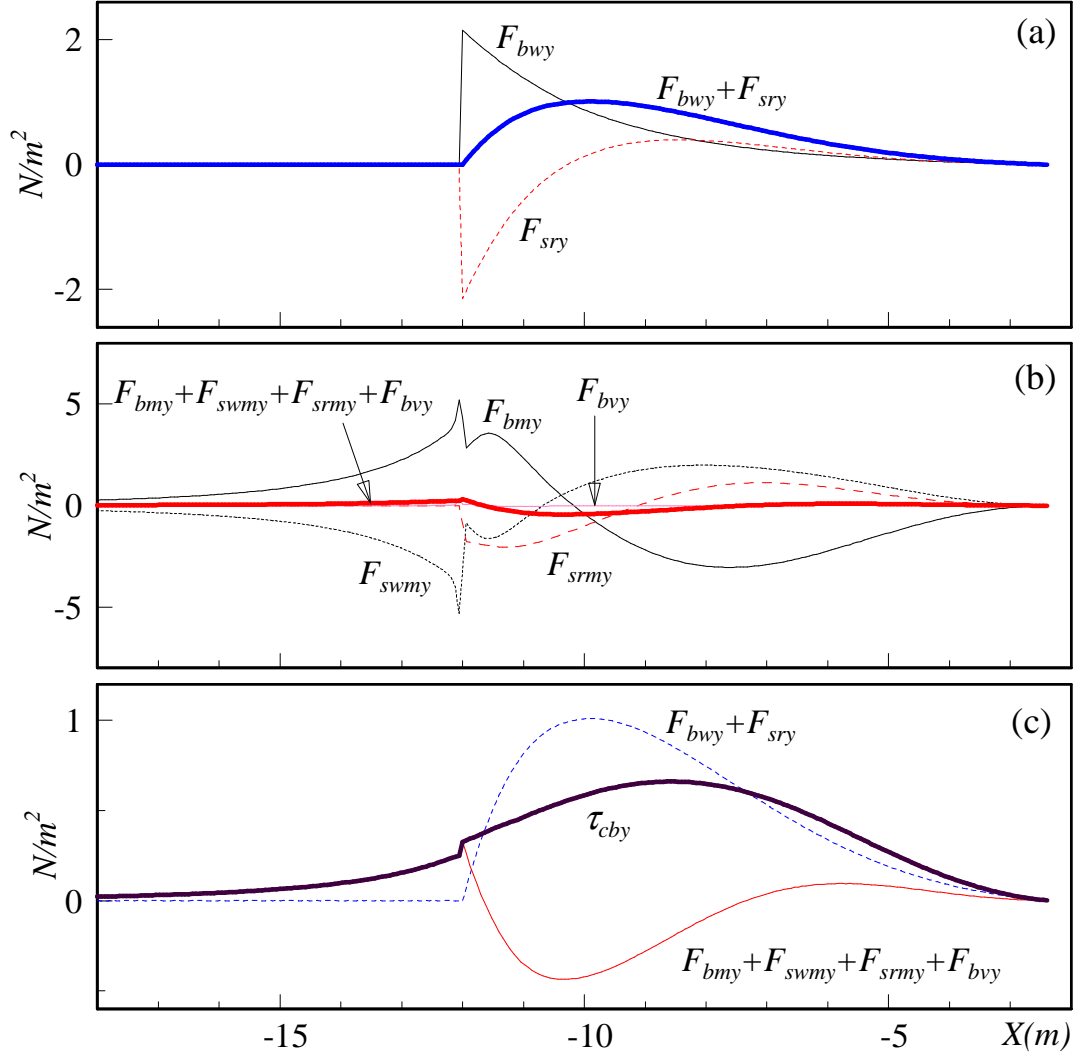


Figure 4-12: Comparisons of the longshore forcing terms in (4.50) for LSTF experiment (Test 6A-N): (a) external forcings and hydrostatic pressure forces; (b) mean-current-associated forces; (c) total forces.

external force (see Figure 4-12 (c)). The net mean-current-associated force increases the total longshore force, τ_{cby} , outside the surf zone ($X(m) < -12$) and near the shoreline ($X(m) > -7$) and it reduces τ_{cby} in the outer surf zone ($-12 < X(m) < -7$). As a result, the peak of τ_{cby} is shifted further inside the surf zone compared to the peak of net external force, $F_{bwy} + F_{sry}$, and the cross-shore profile of τ_{cby} becomes gentler than that of $F_{bwy} + F_{sry}$. Although Svendsen and Putrevu (1994) did not account for the surface roller, they also introduced the current-current and wave-current convective acceleration terms, F_{bmy} and F_{swmy} , and showed these forces smooth out the cross-shore profiles of the longshore current velocity and shift the peak longshore current velocity toward inside the surf zone. Svendsen and Putrevu (1994) also suggested, from their order-of-magnitude analysis, that this convective forcing works as a Bowen-type (Bowen, 1969) empirical lateral mixing but is about ten times larger than the lateral mixing due to turbulence. The present model shows the same feature in Figure 4-12 (b), in which the force due to the turbulent eddy viscosity, F_{bvy} , is negligibly small compared to the other three mean-current-associated forces, F_{bmy} , F_{swmy} , and F_{srmy} . It should also be pointed out that the current-current interaction terms, $\partial(UV)/\partial x$, need to account for the different mean current velocities, i.e. the one near the surface and the other averaged over the trough water depth, h_{tr} , otherwise the term $\partial(UV)/\partial x$ becomes zero under the long, straight beach assumption, where the total volume flux in the cross-shore direction must be zero.

SHORECIRC (Van Dongeren et al., 1994) is based on the concepts of Svendsen and Putrevu (1994) and accounts for the current-current and wave-current interactions in the integrated momentum equations over the entire depth. Besides the depth-integrated momentum equations, the present model solves the momentum equations integrated above the trough level, (4.33) and (4.41), and accounts not only for wave and surface roller effects but also for the mean-current-associated convective effects to evaluate the shear stress at the trough level, τ_{csy} . Figure 4-13 shows the forcing terms in the momentum equation above the trough level in the shore-parallel (y) direction, (4.41), for the same experiment. Similar to Figure 4-12, Figure 4-13 (a) compares longshore external forces, (b) shows the mean-current-associated forces,

and (c) illustrates the net external force, the net mean-current-associated force, and the sum of these, i.e. the total shear stress at the trough, τ_{csy} . Because the wave force above the trough, F_{swy} is smaller than the one for the entire depth, F_{bwy} , F_{sry} dominates near the breaking point and yields a negative net external force around the outer surf zone ($-12 < X(m) < -11$ in Figure 4-13 (a)). Well inside the surf zone, decreasing surface roller energy yields F_{sry} acting in the same direction as F_{swy} and increases the net external force. The mean-current-associated forces also counter act each other but the net mean-current-associated force is still relatively larger than the net longshore external force (see Figures 4-13 (b) and (c)). Finally, the net longshore mean-current-associated force significantly decreases τ_{csy} and yields negative τ_{csy} in $-8.5 > X(m)$ and increases τ_{csy} near the shoreline, $X(m) > -8.5$. The effect of τ_{csy} is seen in the comparisons of vertical profiles of the longshore current velocity shown in Figure 4-11. In the first two vertical profiles of the longshore current velocity from the deeper water, the negative τ_{csy} causes the longshore current velocity to be slightly “backward-leaning” as the trough level is approached. In the last three longshore current velocity profiles closer to the shoreline, the longshore current velocity becomes “forward-leaning” as the trough level is approached because τ_{csy} is positive in this region. Similar to Figure 4-12 (b), the lateral mixing force due to turbulence, F_{svy} , is negligibly small compared to the other mean-current associated forces.

The contributions of the various forcing terms to predictions of the longshore current velocity are more clearly illustrated in Figure 4-14 which compares predicted and measured depth-averaged mean longshore current velocity for this experiment. Full circles in the figure are the measurements and longshore current velocity profiles numbered from 1 to 5 are the predictions by the present model when the following terms are included: (1) only wave forces, F_{swy} and F_{bwy} ; (2) wave forces, F_{swy} and F_{bwy} , and the lateral mixing due to turbulence, F_{bvy} and F_{svy} ; (3) (1) plus surface roller forces, F_{srx} and F_{sry} ; (4) (2) plus surface roller forces, F_{srx} and F_{sry} ; (5) all terms except mean-current associated forcing terms, F_{smy} , F_{swmy} , and F_{srmy} , in the momentum equations integrated above the trough, (4.33) and (4.41); and (6) all terms. For all the cases, Madsen’s (1994) modified wave-current bottom boundary layer model was

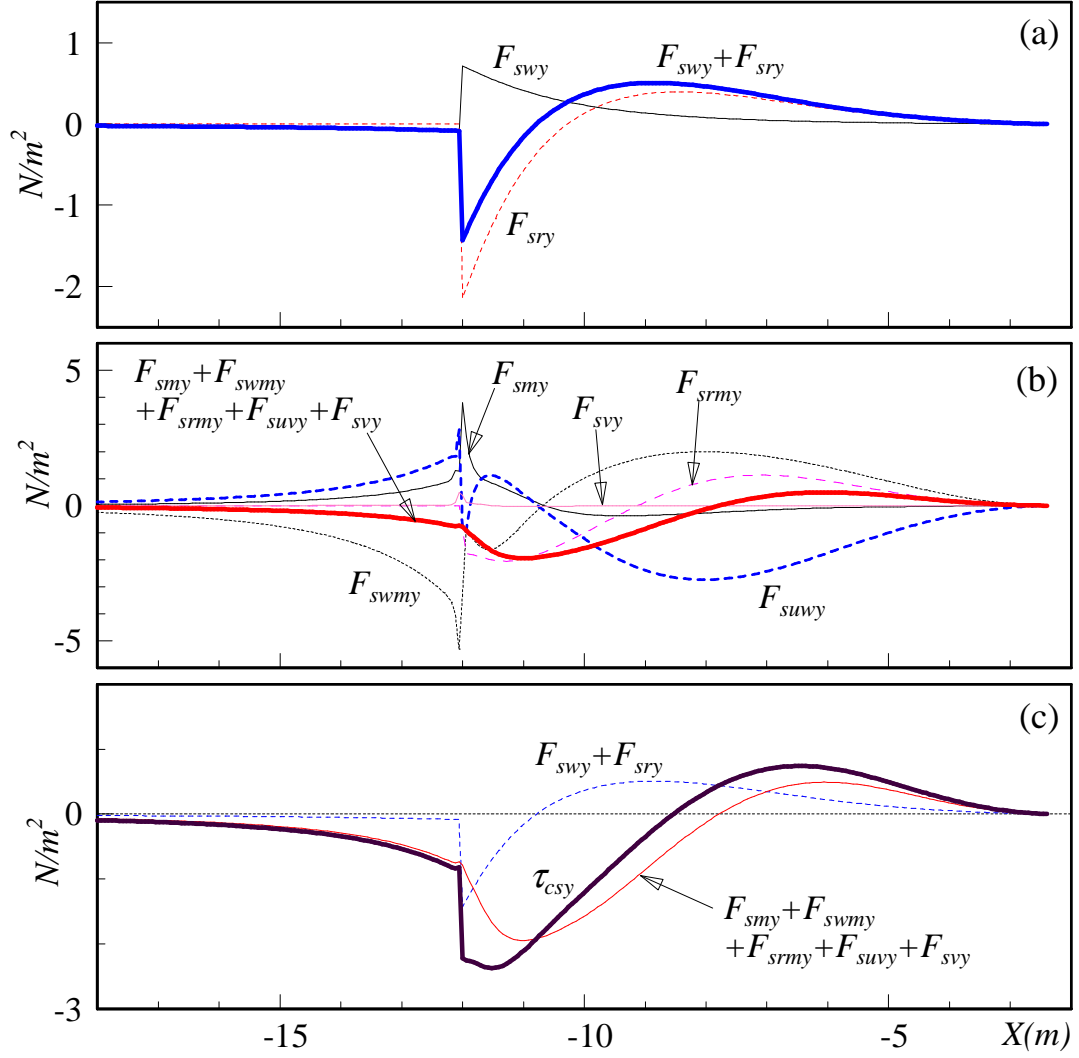


Figure 4-13: Comparisons of the longshore forcing terms in (4.41) for LSTF experiment (Test 6A-N): (a) external forcings and hydrostatic pressure forces; (b) mean-current-associated forces; (c) total forces.

applied to specify the bottom boundary condition, i.e. $\vec{\tau}_{cb}$. (1) corresponds to the Longuett-Higgins' (1970) original model without any lateral mixing terms and the predicted longshore current velocity profile (1) is similar to the cross-shore distributions of F_{bwy} . (2) accounts for the lateral mixing due to the turbulence and the predicted longshore current velocity is smoothed out comparing to (1). However, the peak of (2) is still near the breaking point and the model over-predicts the longshore current velocity near the breaking point and under-predicts the longshore current velocity well inside the surf zone. (3) adds the surface roller effect to (1). Similar to (1), the longshore current velocity profile (3) is similar to $F_{bwy} + F_{sry}$ shown in Figure 4-12 (a). The surface roller significantly shifts the peak longshore current velocity toward inside the surf zone and, as discussed in the force balance comparisons in Figure 4-12 (a), the model predicts virtually zero longshore current velocity at the breaking point and the predicted longshore current velocity (3) is continuous without introducing the lateral mixing term. Similar to the comparison between (1) and (2), lateral mixing term smooths (3) and yields (4). However, the model still over-predicts the longshore current velocity in the outer surf zone ($-12 < X(m) < -7$) and under-estimates near the shoreline ($X(m) > -7$). (5) includes the lateral convective terms for the entire depth but neglects the mean-current-associated force in the momentum equations above the trough, (4.33) and (4.41). In this manner, (5) is similar to SHORECIRC (Van Dongeren, 1994) although (5) also accounts for the surface roller effects and evaluates the bottom shear stress from Madsen's (1994) model. Comparing (5) and (4), the lateral convective forces spreads the longshore forcing near the breaking point toward outside the surf zone and well inside the surf zone and increases the longshore current velocity both outside and well-inside the surf zone. As seen in the figure, the peak of the longshore current velocity in (5) is shifted in the shoreward direction from the peak of (4). Finally, the complete model (6) adds the mean-current-associated forces in the momentum equations above the trough, (4.33) and (4.41). As discussed previously, the mean current associated forces in the longshore direction are relatively large compared to the longshore external forces and affects the predictions of longshore current velocity near the surface, V_s . Comparing (5) and (6) in Figure

4-14, the mean-current-associated forces above the trough further distributes and smooths the longshore current velocity by decreasing the longshore current velocity for $-10 < X(m) < -7$ and slightly increase it for $X(m) > -7$ and $-11 > X(m)$. Finally, Table 4.1 summarizes the root-mean-square errors, $\sigma(m)$, between measured and predicted depth-averaged longshore current velocities. As seen in the table, σ decreases, i.e. the predictive skill of the model improves as we progress from (1) to (6). In the complete model, σ is about 7cm, which is about 15% of the peak longshore current velocity.

Figures 4-15, 4-16 and 4-17 show the same comparisons as Figures 4-11, 4-12, and 4-13, respectively, but for random waves obliquely incident on the same LSTF concrete beach (Test 8A-E, reported by Hamilton and Ebersole, 2001). Similar to Figure 4-7, in which random waves are normally incident on a uniform plane beach, predicted undertow velocity profiles agree very well with measurements even outside the surf zone. Superb agreement of predicted and measured longshore current velocity is also seen in Figure 4-15. All the forcing terms in Figures 4-16 and 4-17 vary smoothly for random waves but show the similar characteristics to those seen in Figures 4-12 and 4-13. For example, both F_{sry} and mean-current-associated forces decrease τ_{cby} in the deeper water and increase τ_{cby} near the shore line. Above the trough, as seen in Figure 4-17 (c), the net mean-current-associated force dominates the net external force and is responsible for the decrease in τ_{csy} for $-8 > X(m)$ and the increase in τ_{csy} for $X(m) > -8$. Figure 4-18 shows the longshore current velocity comparisons in a similar manner as Figure 4-14, but for the random wave experiment (Test 8A-E). As seen in Figure 4-18, the near-identical velocity profiles for (1) and (2) or (3) and (4) indicate that the turbulent lateral mixing has a negligibly small effect on the prediction of the longshore current velocity because, as first suggested by Thornton and Guza (1981), the predicted longshore current velocity profile is already smooth for random waves. Comparing (4) with (3), the surface roller force dramatically decreases the longshore current velocity for $-11 > X(m)$ and increases it for $X(m) > -11$. The surface roller force clearly improves the predictive skills of the longshore current velocity shown in (4) although the longshore current velocity

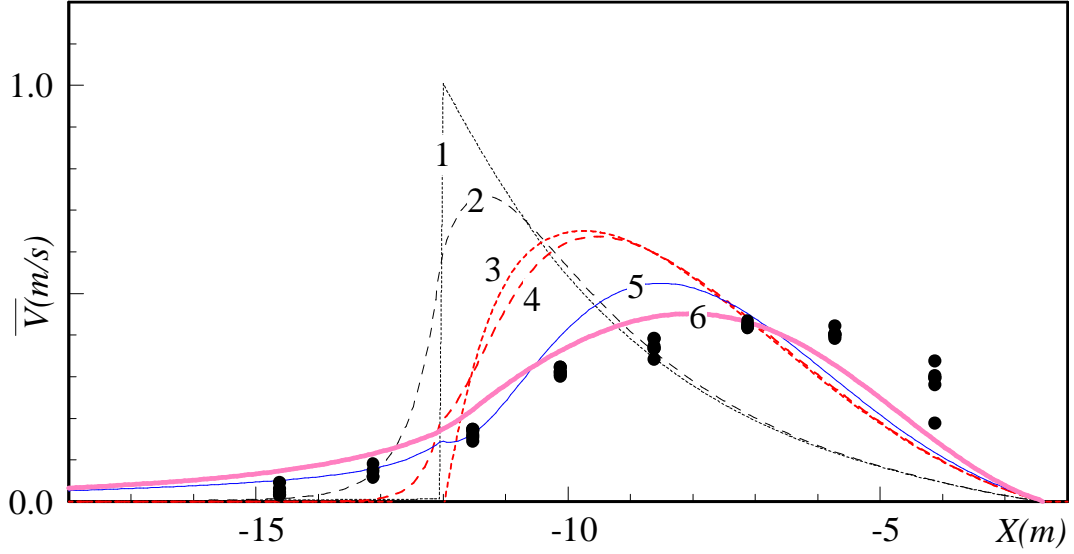


Figure 4-14: Comparisons of the depth-averaged longshore current velocity for LSTF experiment (Test 6A-N): measurements (full circles) and predictions by the present model when following terms are accounted: (1) only wave forces; (2) (1) plus the turbulent lateral mixing; (3) (1) plus surface roller forces; (4) (3) plus the turbulent lateral mixing; (5) all terms except mean-current associated forcing terms above the trough; and (6) all terms.

Table 4.1: Root-mean-square errors (m/s) between predicted and measured depth-averaged longshore current velocity (C6-N).

(1)	(2)	(3)	(4)	(5)	(6)
0.310	0.270	0.175	0.166	0.096	0.073

in $-7 > X(m)$ is still over-predicted by (4). Comparing (4), (5), and (6), inclusion of lateral convective forces for the entire depth and above the trough improves the prediction of the longshore current velocity and shifts the peak longshore current velocity toward the shoreline.

Finally, Table 4.2 summarizes the root-mean-square errors between measurements and predictions from (1) to (6). In the complete model (6), the root-mean-square error is less than 3cm, which is about 8% of the peak longshore current velocity.

Note that both predicted and measured vertical profiles of the longshore current velocity are nearly uniform above the bottom boundary layer in both Figures 4-11 and 4-15. This observation supports our assumption that variations of the local longshore current velocity over depth, V' , are sufficiently small compared with the depth-averaged current velocity, V_0 , to express the mean momentum forcing below the trough level in terms of depth-averaged currents. It should also be emphasized that the quantitative predictions of the longshore current velocity is highly dependent on the balance between the total longshore forcing and the bottom shear stress while the depth-averaged undertow velocity is already determined by requiring cross-shore total volume flux to be zero under the assumption of a long, straight beach. In this sense, the prediction of the longshore current velocity is more sensitive to the bottom boundary layer model. The excellent prediction of the longshore current velocity observed in Figures 4-11 and 4-15 therefore supports the applicability of the bottom boundary layer model for both periodic and random waves.

4.6 Effect of Bottom Roughness

Development of the nearshore mean current model was completed and tested against multiple experimental data. One of the significant improvements of the present nearshore current model is that the bottom roughness on fixed beds is explicitly specified by Nikuradse's (1933) grain size roughness without any calibration while most nearshore current models apply empirical friction coefficients, whose value has to be calibrated in each experiment. For example, Longuett-Higgins (1970) param-

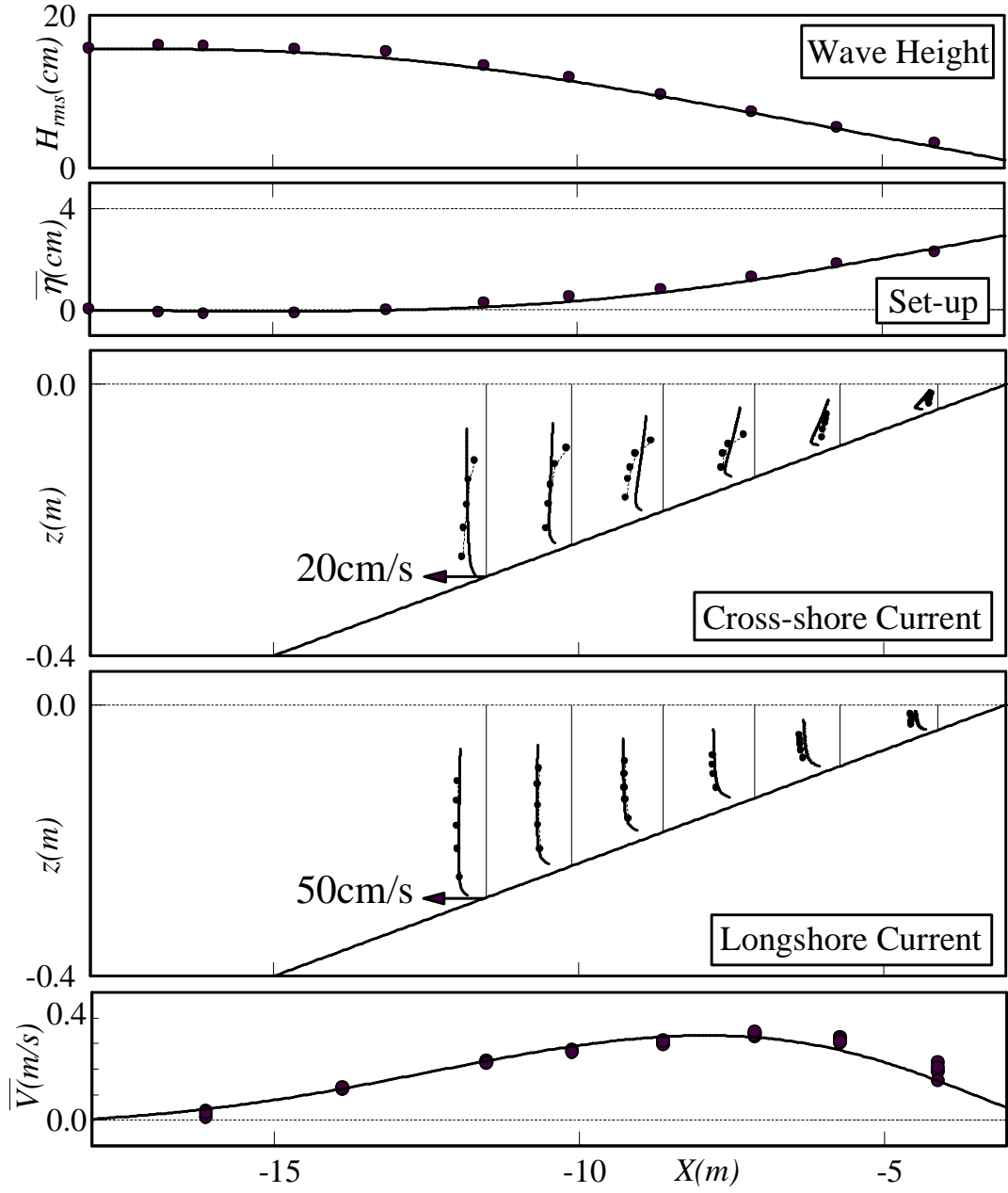


Figure 4-15: Comparisons of measured and predicted wave heights, H_{rms} , wave set-up, $\bar{\eta}$, vertical profiles of undertow and longshore current velocity, and depth-averaged longshore current velocity, \bar{V} , for random waves on plane 1 on 30 sloping beach. Measurements (Test 8A-E) by Hamilton and Ebersole (2001) (full circles) and predictions (full line).

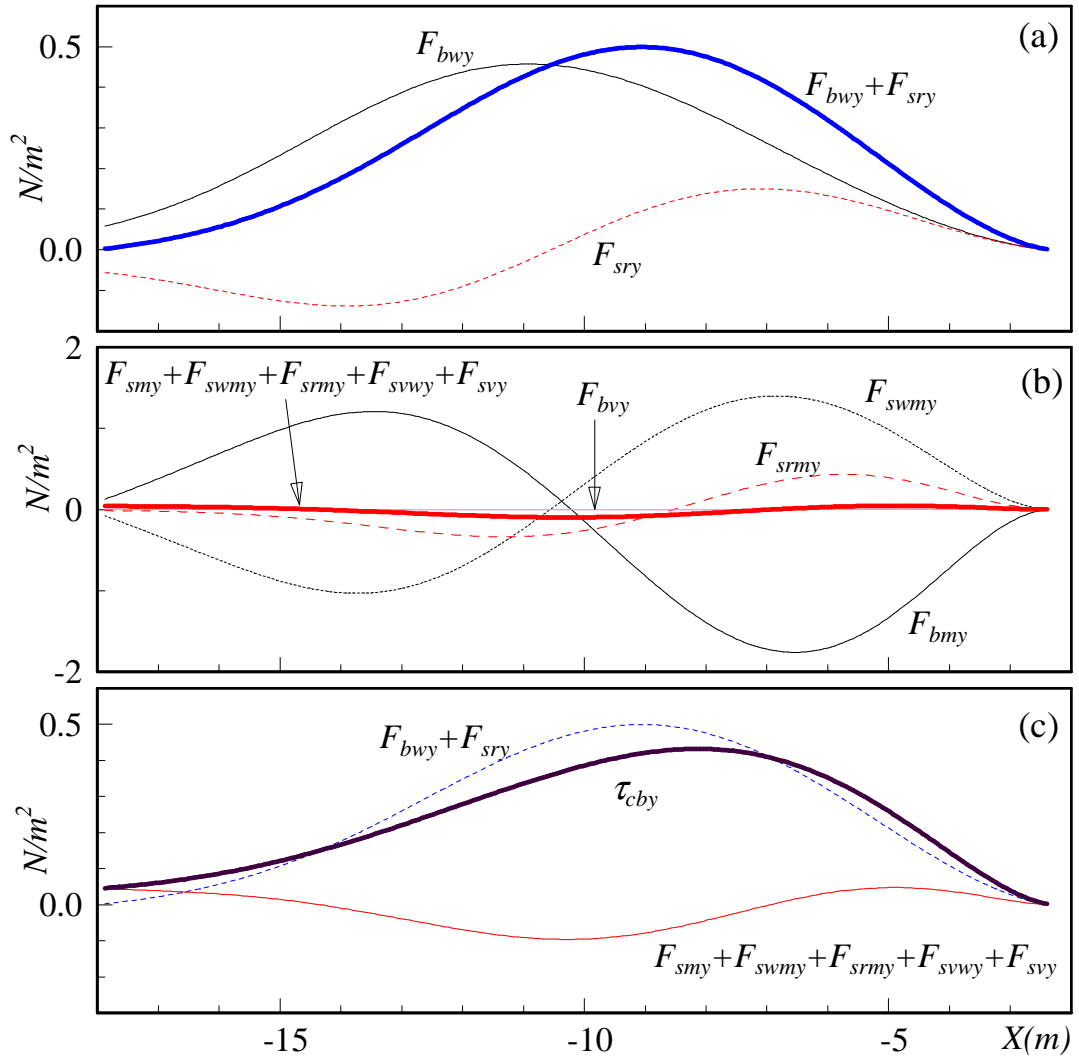


Figure 4-16: Comparisons of the longshore forcing terms in (4.50) for LSTF experiment (Test 8A-E): (a) external forcings and hydrostatic pressure forces; (b) mean-current-associated forces; (c) total forces.

Table 4.2: Root-mean-square errors (m/s) between predicted and measured depth-averaged longshore current velocity (C8-E).

(1)	(2)	(3)	(4)	(5)	(6)
0.121	0.118	0.073	0.070	0.046	0.029

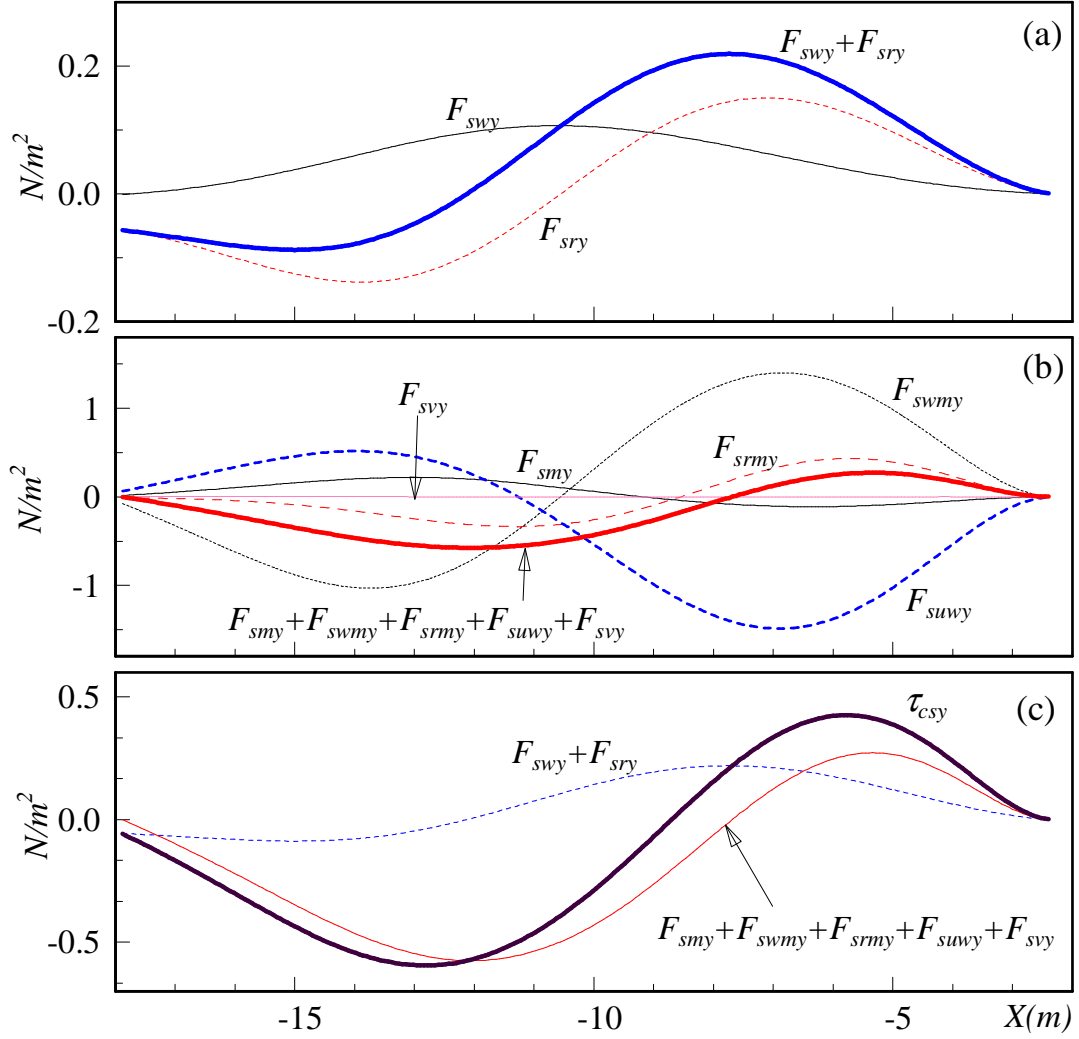


Figure 4-17: Comparisons of the longshore forcing terms in (4.41) for LSTF experiment (Test 8A-E): (a) external forcings and hydrostatic pressure forces; (b) mean-current-associated forces; (c) total forces.

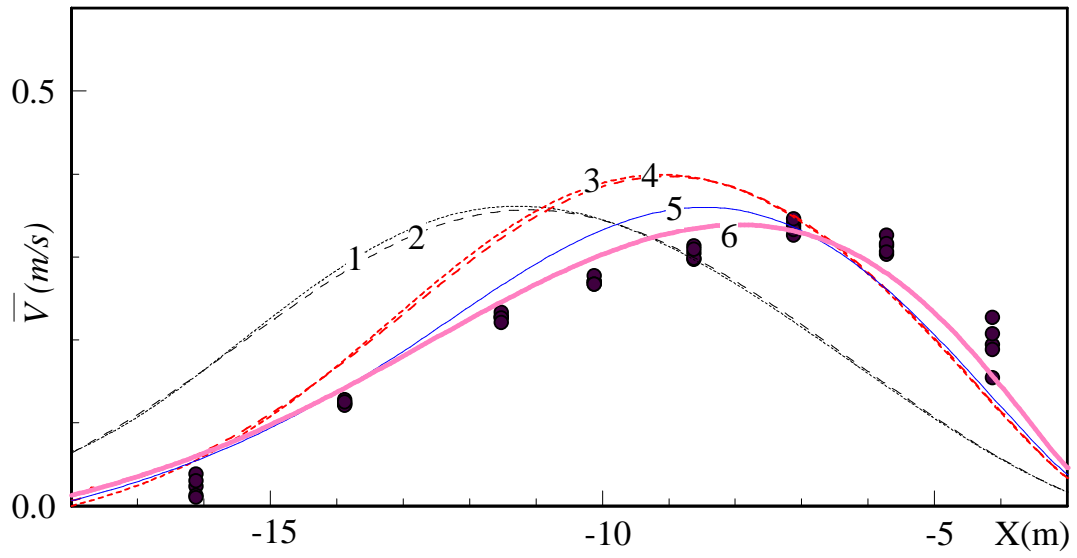


Figure 4-18: Comparisons of the depth-averaged longshore current velocity for LSTF experiment (Test 8A-E): measurements (full circles) and predictions by the present model when following terms are accounted: (1) only wave forces; (2) (1) plus the turbulent lateral mixing; (3) (1) plus surface roller forces; (4) (3) plus the turbulent lateral mixing; (5) all terms except mean-current associated forcing terms above the trough; and (6) all terms.

eterized the alongshore bottom stress by $\tau_{by} = \rho c_f < |\vec{U}_0 + \vec{u}_0| (V_0 + \tilde{v}_0) >$ where c_f is a drag coefficient to be calibrated and $< >$ represents the time-averaged of the depth-averaged velocity. Feddersen et al. (1998) pointed out that this quadratic form for the bottom stress has been used widely in steady channel flows but has not been verified directly in the surf zone and suggested the necessity to calibrate the “best-fit” c_f to apply this bottom stress model to predictions of the longshore current velocity.

In this section, we first apply the present model to Visser’s (1991) experiments in which periodic waves are obliquely incident on a plane beach with different fixed bed roughness that is explicitly determined from the diameter of the bottom sediment fixed to the bed. Through comparisons of predicted and measured velocity, we examine our model’s applicability to various “known” bottom roughness on the fixed bed.

On natural beaches with movable sand beds, however, the diameter of the sand grain may no longer represent the equivalent Nikuradse roughness. Once the flow intensity near the bed exceeds the threshold value and initiates sand motion, the sea bed may form ripples or sheet flow conditions and these bottom conditions may increase the equivalent bottom roughness above the value of the sand grain diameter.

In the second part of this section, we review some existing movable bed roughness models and compare them with measured data. We then introduce these movable bed roughness models into our nearshore current model and apply the model to LSTF movable bed experiments presented by Wang et al. (2002).

4.6.1 Fixed Bed (“Known” Roughness Case)

Ability of the model to accurately reproduce the effect of varying bottom roughness for fixed beds is examined through comparison with experiments reported by Visser (1991) who performed multiple experiments for identical periodic waves obliquely incident on a plane straight concrete beach with and without a cover-layer made of gravel. According to Visser (1991), the roughness of the concrete bed was estimated as $D_{90}=0.6\text{mm}$, while in the gravel bed experiment the bottom was covered by 5 to 10 mm gravel with $D_{90}=8\text{mm}$. Given the smoothing effect of the cement when sand

is incorporated in a concrete mix, we expect the equivalent Nikuradse roughness for the concrete bed to be less than D_{50} of the sand mix. So, for the concrete bed, k_N is expected to fall in the lower sand diameter range, say around 0.3mm. For the gravel beach, D_{50} is estimated from the information available to be 6 to 7 mm. Based on these considerations we assumed a range of bottom roughness in the application of the modified Madsen (1994) bottom boundary layer model, which assumes $k_N = D_{50}$ for flat sand bed, and took $k_N = 0.1, 0.3$, and 0.5 mm for the concrete bed and $k_N = 5, 6$, and 7 mm for the gravel bed. For $D_{50} = 0.1$ mm, the bed condition became smooth turbulent flow, i.e., locally computed smooth turbulent k_N -values were slightly larger than 0.1mm in this particular experimental case.

Figure 4-19 shows the comparison of predicted and measured depth-averaged longshore current velocity for experimental Cases 4 and 5 (concrete beach) and 7 and 8 (gravel-covered beach) presented by Visser (1991). The primary difference of the incident wave conditions between Cases 4 and 7 and Cases 5 and 8 are the wave periods, i.e. $T = 1.02$ s for Cases 4 and 7 and $T = 1.85$ s for Cases 5 and 8, respectively. Under the identical incident wave conditions, peak depth-averaged longshore current velocity for the gravel bed Cases 7 and 8 are slightly less than half of those for the "smooth" concrete bed Cases 4 and 5. As seen in the figure, our model captures this decrease of the longshore current velocity. It is also observed from the figure that the predicted longshore current velocity decreases about 25 percent when k_N is changed from 0.1 mm to 0.5 mm while the decreases of the longshore current velocity is about 20 percent when k_N is changed from 5 mm to 7 mm. This observation suggests that the prediction of the longshore current velocity is sensitive to the value of the bottom roughness, k_N , if this is varied by an order of magnitude or more. Our model accurately predicts this sensitivity to bottom roughness through its adoption of the modified Madsen (1994) bottom boundary layer model to evaluate the bottom friction experienced by the wave-induced mean shear currents.

The depth-averaged return current, i.e. the undertow, in the long, straight beach case ($\partial/\partial y = 0$) is constrained by having to balance the shoreward volume flux above the trough level, which is dominated by wave and surface roller contributions

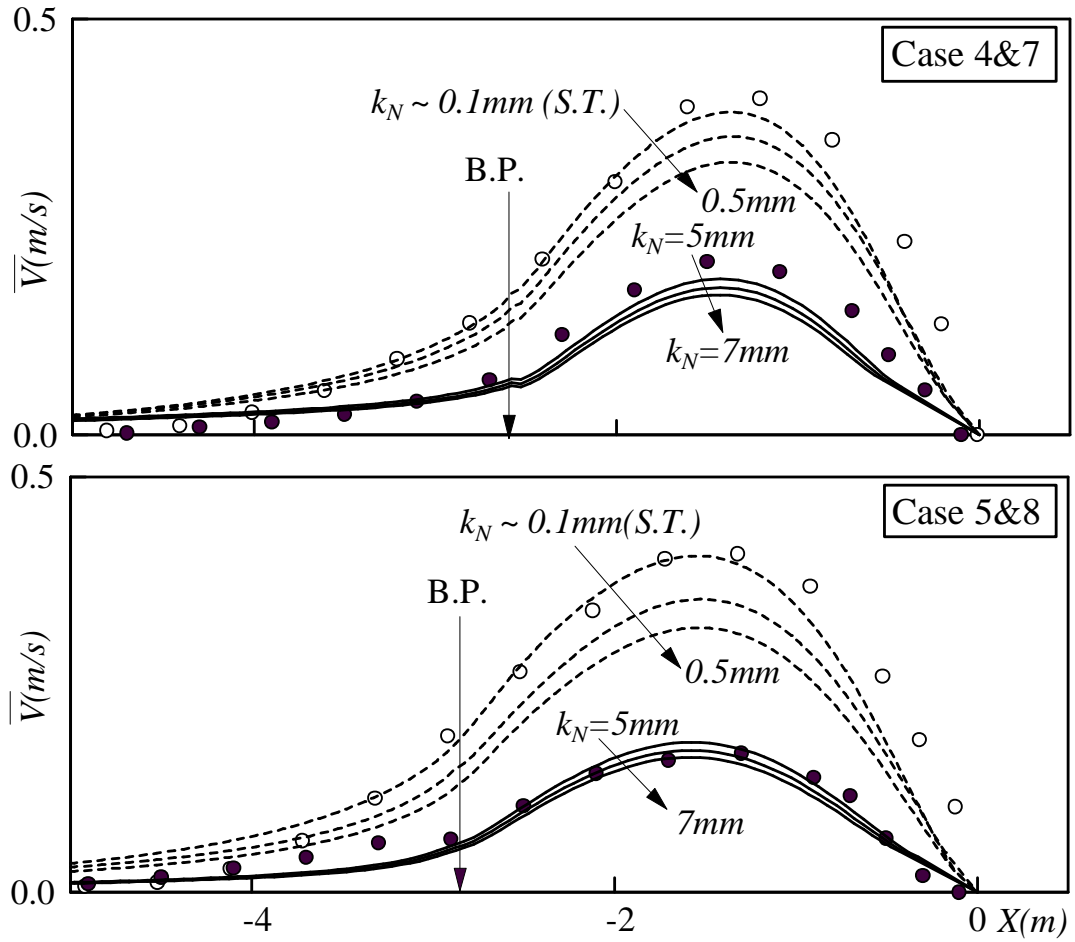


Figure 4-19: Comparisons of measured and predicted depth-averaged longshore current velocity, \bar{V} , for periodic waves on plane 1 on 20 sloping beach with different bottom roughness. Measurements (Cases 4 and 7 above and Cases 5 and 8 below) by Visser (1991) (Concrete bed (Cases 4 and 5) by open circles and gravel bed (Case 7 and 8) by full circles) and predictions (Concrete bed (Cases 4 and 5) by dashed line and gravel bed (Case 7 and 8) by full line).

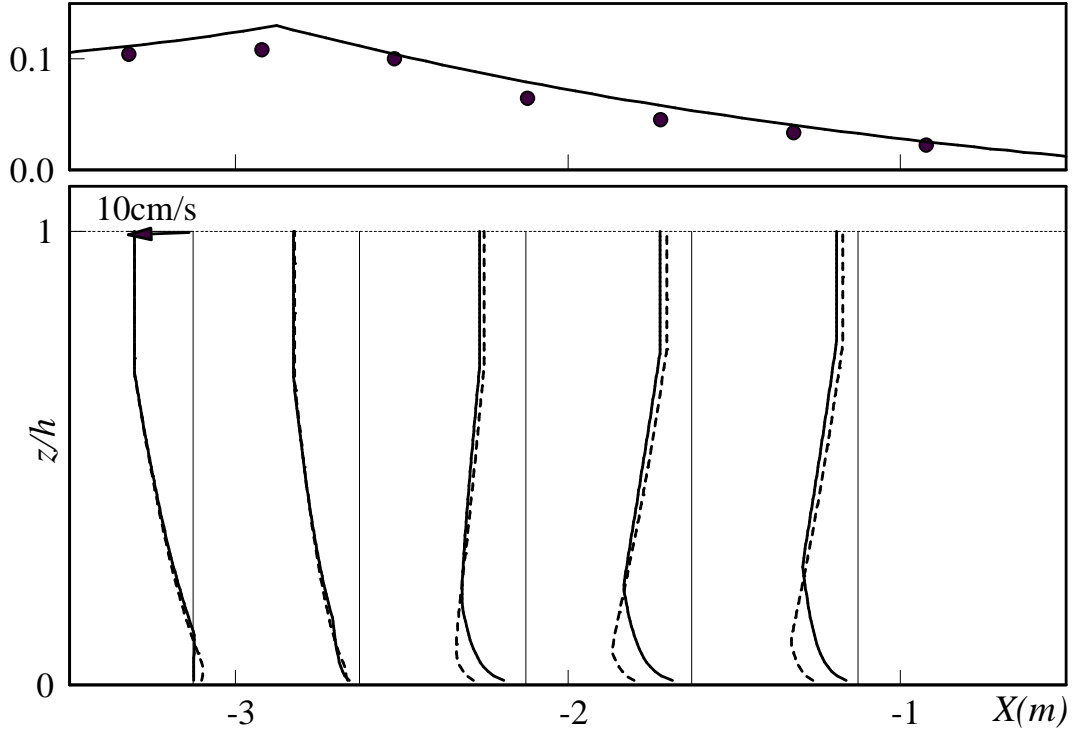


Figure 4-20: Comparison of predicted undertow velocity profiles with different bottom roughness for periodic waves on plane 1 on 20 sloping beach (Corresponding to experimental Case 4 and 7 by Visser, 1991). $k_N=0.1\text{mm}$ (dashed line) and $k_N=6\text{mm}$ (full line).

that are independent of bottom roughness. For this reason undertow predictions are insensitive to the specification of the bottom roughness, k_N . This conclusion, which is limited to uniform beach conditions, i.e. $\partial/\partial y = 0$, is supported in Figure 4-20 by the undertow velocities predicted by our model corresponding to Visser's experiments for smooth ($k_N = 0.1\text{mm}$) and rough ($k_N = 6\text{mm}$) beaches (Cases 4 and 7).

4.6.2 Comparison with Longuet-Higgins' (1970) Model

In this section, we compare the present model with classical Longuet-Higgins' (1970) longshore current model (referred to as LH model hereafter), which predicts the depth-averaged longshore current velocity for periodic waves incident on a long, straight beach with uniform slope. While developments of the present model relied on experi-

mental data only for the wave breaking criteria, $\gamma_b = H_b/h_b$ in (2.20) and the broken wave dissipation coefficient, K_b in (2.24), Longuet-Higgins' (1970) model requires empirical coefficients for lateral dispersion coefficient, N , and the bottom friction coefficient, C_f in addition to the breaking criteria, γ_b . The LH model does not contain broken wave dissipation coefficient because Longuet-Higgins (1970) assumes the broken wave height in the surf zone is simply determined by $H_b = \gamma_b h_b$ without solving wave energy dissipation. Introducing a parameter, $P = \pi N \tan \beta / (\gamma_b C_f)$, relative importance of the lateral dispersion force to the bottom friction force, the normalized depth-averaged longshore current velocity, $\bar{V}^* = \bar{V}/\bar{V}_B$, is expressed as follows.

When $P \neq 2/5$:

$$\bar{V}^* = \begin{cases} B_1 (X/X_B)^{P_1} + A (X/X_B) & \text{for } 0 \leq X \leq X_B \\ B_2 (X/X_B)^{P_2} & \text{for } X_B \leq X \end{cases} \quad (4.57)$$

and when $P = 2/5$:

$$\bar{V}^* = \begin{cases} \frac{10}{49} (X/X_B) - \frac{5}{7} (X/X_B) \ln (X/X_B) & \text{for } 0 \leq X \leq X_B \\ \frac{10}{49} (X/X_B)^{-5/2} & \text{for } X_B \leq X \end{cases} \quad (4.58)$$

with

$$P_1 = -\frac{3}{4} + \sqrt{\frac{9}{16} + \frac{1}{P}} \quad (4.59)$$

$$P_2 = -\frac{3}{4} - \sqrt{\frac{9}{16} + \frac{1}{P}} \quad (4.60)$$

$$A = \left(1 - \frac{5}{2}P\right)^{-1} \quad (4.61)$$

$$B_1 = \frac{1}{P(1 - P_1)(P_1 - P_2)} \quad (4.62)$$

$$B_2 = \frac{1}{P(1 - P_2)(P_1 - P_2)} \quad (4.63)$$

$$\bar{V}_B = \frac{5\pi}{16} \frac{\gamma_b}{C_f} \sqrt{gh_b} \tan \beta \sin \theta_b \quad (4.64)$$

Here X is the sea-ward distance from the shore-line, X_B is a width of the surf zone,

i.e. the distance between shore-line and wave breaking point, and θ_b is an angle between cross-shore direction and wave propagation direction at the breaking point. Although Longuet-Higgins (1970) originally applied a single breaking criteria, $\gamma_b = 0.78$, we apply our wave breaking model, whose excellent agreement with measured data was confirmed in Chapter 2, to specify the breaking point and corresponding wave characteristics at the breaking point, γ_b and θ_b . In order to obtain more accurate predictions for the LH model, we also introduced the mean water shore-line location predicted by the present wave and surface roller model. If one were to neglect the wave set-up and apply the still water shore-line, the LH model yields zero longshore current velocity at the still water shore-line and therefore underpredicts the longshore current velocity near the shore-line. Based on these variables provided from the present wave model, we calibrated the empirical coefficients, P and C_f , so that the root-mean-square (rms) error of predicted and measured longshore current velocity is minimized.

Similar to Figure 4-19, Figure 4-21 shows the predicted and measured depth-averaged longshore current velocity for Visser's (1991) experiments, Cases 4 and 7, and Cases 5 and 8, respectively. In Figure 4-21, heavy dashed and heavy full lines are the predictions by the present model with equivalent bottom roughness, $k_N = 0.1\text{mm}$ and $k_N = 5\text{mm}$, respectively, and thin dashed and thin full lines are predictions by the best-fit LH model. As seen in Figure 4-21, the best-fit LH model tends to over-predict \bar{V} outside the surf zone and under-predict the peak longshore current velocity. Table 4.3 compares the rms errors both for the LH model and the present model. The Table also shows the best-fit coefficients, P and C_f , and the corresponding lateral dispersion coefficient, N for the LH model. In Table 4.3, the same comparisons are also shown for the LSTF experimental cases, Test 6A-N and 8A-E, reported by Hamilton and Ebersole (2001). For the random wave case, Test 8A-E, we applied either rms or significant incident wave heights as if these waves were regular waves to determine the unique breaking point and the corresponding breaking wave conditions. These breaking wave characteristics are then applied to the LH model because the LH model is limited to periodic wave conditions. As seen in the Table, rms errors of the present

model against the measured data are comparable to those for the best-fit LH model although the present model contains no fitting parameters that are derived from the experimental data. From the Table, the dispersion coefficient, N , falls in an order of 10^{-2} as originally suggested by Longuet-Higgins (1970). However, the best-fit N -value is nearly doubled from Case 5 ($N = 0.006$) to Case 8 ($N = 0.011$) while the only difference between Cases 5 and 8 is the bottom roughness. This feature indicates the difficulty in developing a methodology for the determination of an optimum dispersion coefficient. For Visser's (1991) experiments, best-fit friction factors, C_f , are consistent with the bed roughness, i.e. C_f is relatively small for concrete bed ($C_f \simeq 0.006$ for both Cases 4 and 5) and large for gravel bed ($C_f \simeq 0.015$ for both Cases 7 and 8). On the similar concrete smooth bed condition, however, C_f -value for Test 6A-N ($C_f = 0.0035$) becomes much smaller than those for Cases 4 and 5. This feature also suggests the uncertainty associated with establishment of an empirical definition of C_f . Considering all these facts, it is one of the essential improvements of the present model that the model does not contain any of these empirical coefficients and still rivals the predictive skills of the best-fit classical LH model.

4.6.3 Movable Bed Bottom Roughness

On natural beaches with movable sand grain beds, the diameter of the sand grain may no longer represent the equivalent Nikuradse grain roughness. Once the flow intensity near the bed exceeds the threshold value and initiates sand motion, the sea bed may form ripples or sheet flow conditions and these bottom bed forms may increase the equivalent bottom roughness.

The equivalent bottom roughness on a movable sandy bed, k_N , may be decomposed into three components: k_{ND} , grain roughness scaled by a grain size, D multiplied by a constant with a value ranging $1 \sim 2.5$; k_{NR} , "ripple roughness," an extra form drag due to ripple geometry; and k_{NM} , a roughness due to the sediment motion (e.g., Smith and McLean, 1977; Grant and Madsen, 1982; and Xu and Wright, 1986). Total equivalent bottom roughness on the movable bed is often expressed as a sum

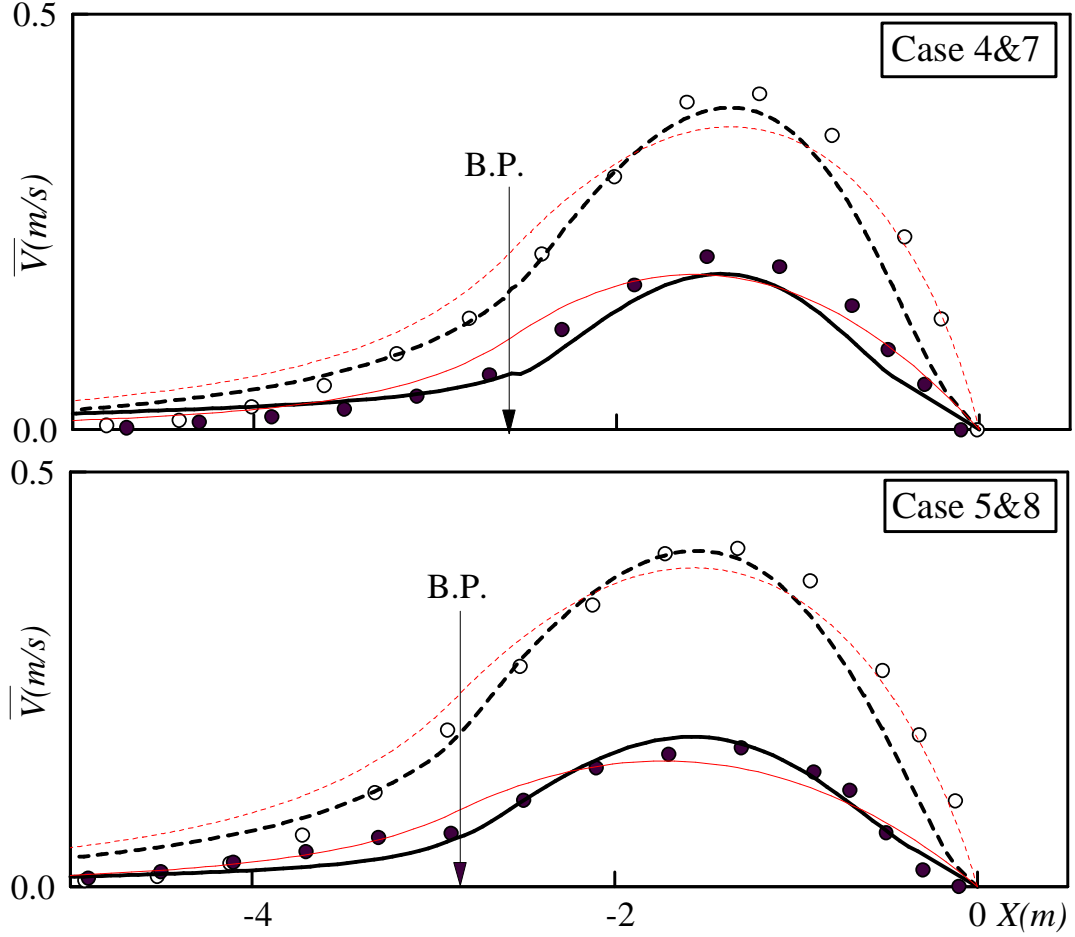


Figure 4-21: Comparisons of measured and predicted depth-averaged longshore current velocity, \bar{V} , for periodic waves on plane 1 on 20 sloping beach with different bottom roughness. Measurements (Cases 4 and 7 above and Cases 5 and 8 below) by Visser (1991) (Concrete bed (Cases 4 and 5) by open circles and gravel bed (Case 7 and 8) by full circles) and predictions (Concrete bed (Cases 4 and 5) by dashed line and gravel bed (Case 7 and 8) by full line). Heavy lines are the predictions by the present model with $k_N = 5\text{mm}$ (full) and $k_N = 0.1\text{mm}$ (dashed) and thin lines are the predictions by the best-fit LH model.

of these components (e.g., Smith and McLean, 1977; Grant and Madsen, 1982).

$$k_N = k_{ND} + k_{NR} + k_{NM} \quad (4.65)$$

Although there is no physical justifications for simply adding up these components to yield the total equivalent bottom roughness, (4.65) seems to be a reasonable representation because one of these three roughness values usually dominates the others depending on bed conditions and (4.65) is therefore equivalent to taking a maximum of these three roughness.

Relative importance of these three components is often classified in terms of the Shields Parameter based on a sediment diameter:

$$\psi'_{wm} = \frac{\tau'_{wm}}{(s-1)\rho g D} = \frac{\frac{1}{2}f'_{cw}u_{bm}^2}{(s-1)\rho g D} \quad (4.66)$$

where $s = \rho_s/\rho$ with ρ_s and ρ , density of the sediment and water, respectively, f'_{cw} is a skin friction factor (Madsen, 1994) determined from (4.26) by replacing equivalent bottom roughness k_N by the bottom sediment diameter, D .

No Sediments in Motion

If the maximum skin friction Shields Parameter, ψ'_{wm} , is smaller than the critical Shields parameter, ψ_{cr} , no ripples are generated and there is no sediment transport, i.e. $k_{NR} = k_{NM} = 0$. The critical Shields Parameter, ψ_{cr} , is determined from Madsen and Grant's (1976) modified Shields diagram, in which the critical Shields Parameter is expressed as a function of the sediment-fluid parameter,

$$S_* = \frac{D}{4\nu} \sqrt{(s-1)gD} \quad (4.67)$$

with kinematic viscosity, $\nu \simeq 1.0 \times 10^{-6}(\text{m}^2/\text{s})$. Explicit approximation formulae of this diagram are proposed by Soulsby and Whitehouse (1997) as

$$\psi_{cr} = \begin{cases} 0.085 S_*^{-2/7} & S_* < 1.53 \\ 0.095 S_*^{-2/3} + 0.056 \left(1 - \exp \left(-\frac{S_*^{3/4}}{20} \right) \right) & 1.53 \leq S_* \end{cases} \quad (4.68)$$

Rippled Bed

When ψ'_{wm} exceeds ψ_{cr} , sand grains are put in motion and form ripples that produce ripple roughness, k_{NR} , which dominates in (4.65). Geometrical characteristics of sand ripples generated under waves have been studied both in laboratory experiments and field measurements (e.g., Inman, 1957; Keneddy and Falcon, 1965; Carstens et al., 1969; Mogridge and Kamphuis, 1972; Dingler, 1974; Miller and Komar, 1980; Nielsen, 1981; Madsen and Rosengaus, 1988; Sato and Horikawa, 1988; Traykovski et al., 1999; Li et al., 1998; Styles and Glenn, 2002). Based on these observations, a number of predictive models for rippled bed geometry have been proposed (e.g., Nielsen, 1981; Grant and Madsen, 1982; Wikramanayake and Madsen, 1991; Mogridge et al., 1994; Wiberg and Harris, 1994; Li et al., 1996; Traykovski et al., 1999; Styles and Glenn, 2002). These observations and models indicate that, as ψ'_{wm} increases and exceeds ψ_{cr} , ripple geometry immediately reaches its “equilibrium” stage where the ripple steepness, η_r/λ , with ripple height, η_r , and length, λ , becomes a maximum and stays roughly constant independent of ψ'_{wm} . Grant and Madsen (1982) suggested that the ripple roughness, k_{NR} , for equilibrium ripples is expressed by $k_{NR} = 27.7\eta_r (\eta_r/\lambda)$ based on experiments with periodic waves. Nielsen (1983) also obtained a similar expression but a smaller roughness,

$$k_{NR} = 8\eta_r (\eta_r/\lambda) \quad (4.69)$$

for equilibrium ripples under oscillatory flows. Because η_r/λ for equilibrium ripples is nearly constant, Wikramanayake and Madsen (1991) suggested that k_{NR} may be

uniquely determined by the ripple height,

$$k_{NR} = 4\eta_r \quad (4.70)$$

This simple expression was also verified by Rankin and Hires (2000) in their laboratory studies of oscillatory flow over equilibrium ripples.

As ψ'_{wm} further increases, the bed form enters a “breakoff” range where the ripple steepness, η_r/λ , decreases and eventually all ripples vanish as “sheet” flow conditions are approached. Grant and Madsen (1982), based on laboratory experiments with periodic waves, expressed the breakoff limit for ripples in terms of Shields Parameter,

$$\psi'_B = 1.8S_*^{0.6}\psi_{cr} \quad (4.71)$$

Here the bed form enters the breakoff range when $\psi'_{wm} \geq \psi'_B$. Styles and Glenn (2002) suggested a smaller breakoff limit based on random wave measurements collected both in field and laboratory. In the breakoff range, k_{NR} should also fade out as ripples are washed out and the bed enters sheet flow conditions. Due to the lack of data, however, solid determination for k_{NR} in the breakoff range is not yet available.

In the vicinity of the surf zone, where significant sediment transport is expected, extensive turbulence due to broken waves and wave induced nearshore currents may affect geometric characteristics of ripples. Li and Amos (1998) pointed out that most existing models are based on pure wave conditions and showed, from field observations, the significant influence of the mean shear current on ripple geometry. This feature is also observed in Appendix C where existing ripple geometry models are compared with LSTF movable bed experiments. We leave this problem for future modifications because we focus on predictions of extensive sediment transport rates around the surf zone in the field for which sheet flow conditions are expected.

Sheet Flow

As ψ'_{wm} further increases, all ripples are washed out and the bed enters sheet flow conditions. The initiation limit of sheet flow conditions have also been characterized in terms of the Shields Parameter (e.g. Dingle and Inman, 1976; Smith and McLean, 1977; Soulsby, 1997; Li and Amos, 1999). According to Li and Amos (1999), for example, the critical Shields Parameter for sheet flow, ψ'_{up} , is expressed as a simple function of sand grain size

$$\psi'_{up} = 0.172D^{-0.376} \quad (4.72)$$

with diameter, D , in cm. Note that ψ'_{up} is based on the skin friction Shields Parameter and ψ'_{up} for random waves is calibrated with the measured maximum Shields Parameter represented by significant waves, which is about twice the Shields Parameter obtained from the root-mean-square wave height adopted as the representative wave here, i.e. $\psi'_{wm,s} \simeq 2\psi'_{wm,rms}$. Gallagher et al. (2003) compared existing models and showed that the Li and Amos (1999) model agrees fairly well with field data.

For sheet flow conditions, k_{NR} becomes zero as ripples vanish, but a near-bottom sheet flow layer of intensive sediment transport calls for extra roughness due to sediment motion, k_{NM} . Because k_{NM} should be related to bedload sediment transport, most models express k_{NM} as a function of the sediment diameter, D , and Shields Parameters, ψ'_{wm} and ψ_{cr} , determined by (4.66) and (4.68), respectively (e.g., Smith and McLean, 1977; Grant and Madsen, 1982; Nielsen, 1983; and Madsen et al., 1993, Xu and Wright, 1995). Based on the field measurements obtained off the coast of Duck, NC, USA, Madsen et al. (1993) suggested $k_N = 15D$. Since these field data yielded $\psi'_{wm} \simeq 1$ and because it is physically reasonable to assume that the movable bed roughness for sheet flow conditions depends on the flow intensity over the bed, which in turn is related to ψ'_{wm} , Madsen (Coastal Engineering Manual, 2001) suggests k_N for sheet flow to be

$$k_N = 15\psi'_{wm}D \quad (4.73)$$

Xu and Wright (1995) applied existing roughness models to predict vertical profiles of the horizontal mean current velocity based on Madsen and Wikramanayake's (1991)

wave-current bottom boundary layer model and compared them with the same field observations presented by Madsen et al. (1993). From these comparisons, Xu and Wright pointed out Smith and McLean (1977), Grant and Madsen (1982), and Nielsen (1981) models over-predict k_N and proposed

$$k_N = D + 5D (\psi'_{wm} - \psi_{cr}) \quad (4.74)$$

In contrast to the above models that are based on a skin friction shear stress, with roughness of a grain diameter, D , Wilson (1989) showed that k_N is correlated fairly well with Shields Parameter based on the total shear stress, ψ , and proposed,

$$k_N = 5D\psi \quad (4.75)$$

From the experimental results for high-stress steady flow over a sheet flow bed (Wilson, 1965, 1966), Wilson (1987) also showed that the well-known Meyer-Peter-Muller (1948) bedload sediment transport formula agrees well with experimental data if the Shields Parameter, ψ , based on the total shear stress, i.e. based on the sheet flow movable bed roughness, is used instead of a skin friction Shields Parameter, ψ' . This observation supports the use of the Shields Parameter based on total bottom shear stress for determination of k_{NM} , because k_{NM} should be strongly related to the bedload sediment transport.

Herrmann (2004) expressed the equivalent bottom roughness as a function of the Shields Parameter, ψ , critical shear stress, ψ_{cr} , and sediment diameter, D . From a number of experimental data sets for steady flow over a sheet flow bed (Brooks, 1954; Einstein and Chien, 1955; Barton and Lin, 1955; Nomicos, 1956; Lyn, 1986) Herrmann obtained

$$\begin{aligned} k_N &= k_{ND} + k_{NM} \\ &= 2D + 4.5D (\psi - \psi_{cr}) \end{aligned} \quad (4.76)$$

Here, $k_{ND} = 2D$ may be interpreted as the roughness of an immobile bed ($\psi' < \psi_{cr}$),

and $k_{NM} = 4.5D(\psi - \psi_{cr})$ yields a movable bed roughness value close to Wilson's (1989) model, (4.75). According to Herrmann (2004), the root-mean-square relative error of (4.76) from the measured optimum roughness was around 0.35.

In order to extend Herrmann's (2004) model to the wave-current combined flow, we assume that the local Shields Parameter, ψ , is represented by the maximum Shields Parameter, ψ_m ,

$$k_N = 2D + 4.5D(\psi_m - \psi_{cr}) \quad (4.77)$$

Since the Shields Parameter is roughly proportional to u_{bm}^2 , ψ_m for random waves should be represented by root-mean-square wave characteristics.

In order to examine the validity of these equivalent bottom roughness models, we compare (4.73), (4.74), (4.75), and (4.77) with field measurements presented by Madsen et al. (1993) [Table 4.4]. In Table 4.4, current shear velocity, u_{*c} , and the apparent bottom roughness, $k_{Na} = 30z_{0a}$, were determined so that the logarithmic mean current velocity profile,

$$u_c(z) = \frac{u_{*c}}{\kappa} \ln \frac{z}{z_{0a}} \quad (4.78)$$

best fits the mean current velocities measured at various elevations. From the measured data summarized in Table 4.5, Madsen et al. (1993) adopted Grant and Madsen (1986) wave-current bottom boundary layer model and evaluated the equivalent bottom roughness, k_N , by requiring the predicted mean current velocity at the outer edge of the wave-current bottom boundary layer, $z = \delta$, to be equal to the measured mean current (4.78). In this study we followed the same procedure as Madsen et al. (1993) and re-evaluated k_N by applying the Madsen's (1994) modified wave-current bottom boundary layer model. Table 4.5 summarizes the "measured" equivalent bottom roughness obtained in this manner and the predicted k_N obtained from (4.73), (4.74), (4.75), and (4.77). In Table 4.5, the equivalent bottom roughness is normalized by the sediment diameter, k_N/D , and the mean relative errors, μ , and variances, σ , are based on $\ln k_N$ because the predictions of the nearshore mean current depends on $\ln k_N$, as seen in (4.78), rather than on k_N . The relative error of the predicted equivalent bot-

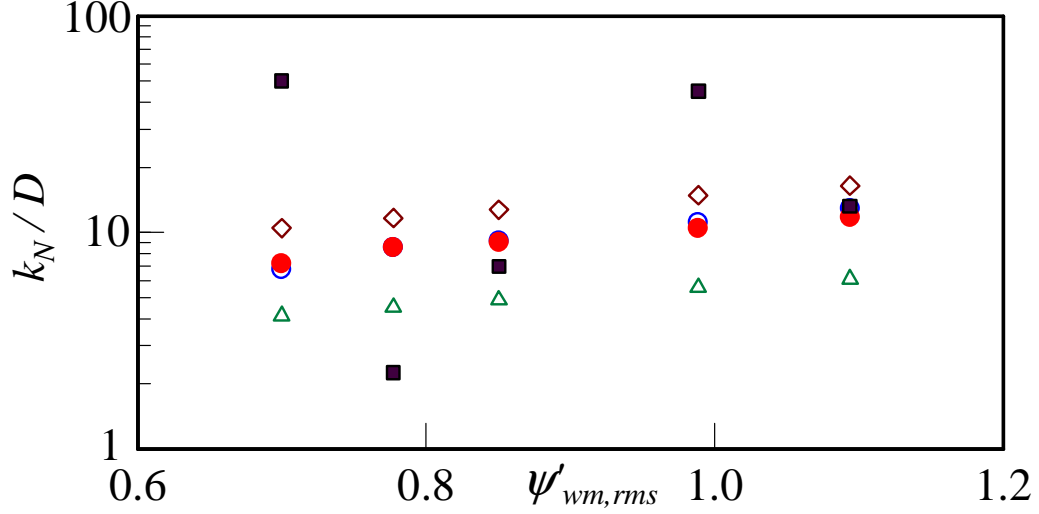


Figure 4-22: Relative equivalent bottom roughness, k_N/D vs. $\psi'_{w,rms}$. Measurements (full rectangles) presented by Madsen et al. (1993) and models by Herrmann (2004) (full circles); Wilson (1989) (open circles); Xu and Wright (1995) (triangles); and Coastal Engineering Manual (2002) (diamonds).

tom roughness, μ , is therefore determined by $\mu = \langle (\ln k_{N,pred} - \ln k_{N,meas}) / \ln k_{N,pred} \rangle$ with $\langle \rangle$ denoting the average.

Figure 4-22 compares the predicted and measured k_N/D as functions of $\psi'_{wm,rms}$ shown in Table 4.5. As illustrated in Figure 4-22, the measured relative roughness, shown as full rectangles, exhibit significant scatter. Note that (4.73), which gives the smallest error and variance, was originally calibrated from the same field data shown in Figure 4-22 while (4.75) and (4.77) were obtained from dramatically different experiments involving steady flow conditions. In this study, we apply (4.77) to predict the equivalent bottom roughness for sheet flow conditions. Sensitivity of the predictions of the mean current velocity to bottom roughness is investigated in the following section where our nearshore current model is applied to movable bed LSTF experiments (Wang et al., 2002).

Table 4.3: Root-mean-square errors of the present model and the best-fit LH model, and best-fit empirical coefficients for the LH model for experiments (Cases 4, 7, 5, and 8) presented by Visser (1991) and LSTF experiments (Tests 6A-N and 8A-E) reported by Hamilton and Ebersole (2001). Predictions for the present model are based on $k_N = 0.1\text{mm}$ (Cases 4 and 5) and $k_N = 5\text{mm}$ (Cases 7 and 8). For the random wave case (Test 8A-E), breaking characteristics of the equivalent periodic wave, applied to the LH model, are determined from: (A) rms; and (B) significant incident wave heights, respectively.

Cases	rms error (cm/s)		γ_b	best fit parameters (LH)			
	LH	Present		P	C_f	N	γ_b/C_f
Case 4	3.2	3.9	0.74	0.28	0.0061	0.008	120.2
Case 7	1.8	2.5		0.15	0.0144	0.010	51.2
Case 5	3.5	3.6	0.69	0.26	0.0056	0.006	123.9
Case 8	1.5	1.4		0.16	0.0160	0.011	43.0
6A-N	6.5	7.4	0.65	0.40	0.0035	0.009	184.1
8A-E (A)	3.1	3.0	0.67	0.18	0.0048	0.006	140.9
8A-E (B)	3.9		0.69	0.40	0.0058	0.015	118.3

Table 4.4: Apparent roughness, k_{Na} , obtained from field data (Madsen, et al., 1993)

No.	$u_{bm}(\text{cm/s})$	$T(\text{s})$	$\phi_{wc}(^\circ)$	$u_{*c}(\text{cm/s})$	$k_{Na}(\text{cm})$
1	73.4	10.1	88	2.44	28.14
2	78.8	11.1	69	2.37	2.19
3	82.9	11.1	81	2.71	4.53
4	90.9	11.8	86	3.35	20.67
5	96.2	11.8	79	3.14	8.85

4.6.4 Model Application to LSTF Movable Bed Experiments

To examine the model's applicability for movable bed conditions, we apply the present model to LSTF movable bed experiments (Wang et al., 2002). As summarized in Table 1.1, Test 1 introduced shorter waves and had spilling breakers while Test 3 had longer incident waves and plunging breakers. The median sieve diameter of the bed sediments is 0.15mm that corresponds to the nominal median diameter, $D_{n50} \simeq 0.167\text{mm}$. From the depth data, which were recorded along cross-shore transects at intervals of 5mm, both Test 1 and Test 3 had ripples on the bed whose heights ranged from zero up to 1cm.

Appendix C shows the observed ripple geometry in Test 1 and Test 3 and compares observations with some of the existing predictive models for ripple geometry. According to personal communications (Mr. Ernest Smith of ERDC, USACE, Vicksburg, MS), directions of these ripples were randomly distributed and ripple crests were rounded off and short in length. The local skin friction wave Shields Parameters, $\psi'_{wm,s} = 2\psi'_{wm,rms}$, obtained from the predicted near-bottom wave orbital velocity were greater than the Grant and Madsen (1982) breakoff limit, ψ'_B ($\simeq 0.35$, determined by (4.71) with $D_{n50} = 0.167\text{mm}$), at all the cross-shore locations. Especially in Test 3, predicted $\psi'_{wm,s}$ were even larger than the sheet flow limit, ψ'_{up} ($\simeq 0.84$, determined by Li and Amos (1996), (4.72), with $D_{n50} = 0.167\text{mm}$), around the bar crest where measured ripple heights were nearly zero. Note that excellent predictive skills for near-bottom wave orbital velocity heights, which were already confirmed in Chapter 2, supports the validity of the above analysis. According to Nielsen (1981) and Wikramanayake and Madsen (1991), the random waves tend to generate ripples with smaller steepness and rounder crests compared with those generated by periodic waves. Moreover, the extensive turbulence due to breaking waves could also cause a reduction of the ripple heights and steepness. Based on these discussions, the ripple roughness, k_{NR} , should be much smaller than those introduced in (4.69) or (4.70) because both of these were originally obtained from laboratory experiments with equilibrium ripples. From the observational fact that actual ripple crests in the LSTF

experiments, Test 1 and Test 3, were rounded off and short, the ripple roughness may be reasonably assumed to have been negligibly small in these experiments.

Figure 4-23 (a) compares the cross-shore distributions of observed depth-averaged longshore current velocities in Test 1 with predicted longshore currents when the local equivalent roughness is represented by (i) the present sheet flow roughness model, (4.77); (ii) the sheet flow roughness by Madsen (Chapter 6 in Coastal Engineering Manual, 2001), (4.73); and (iii) the roughness scaled by a local ripple height, $k_N = \eta_r$, Figure 4-23 (b) shows the cross-shore distributions of measured individual ripple heights (full circles) and spatially averaged ripple heights (dashed line), which were directly applied to compute the longshore current velocity with $k_N = \eta_r$. Comparison of (4.77) and (4.73) is shown in Figure 4-23 (c) and by comparison with (b) it is seen that the sheet flow movable bed roughness k_N is less than $k_{NR} = \eta_r$ by more than an order of magnitude.

Figures 4-24 (a) – (d) show the same comparisons as Figure 4-23 but for the experimental case, Test 3. Tables 4.6 and 4.7 show the mean errors (μ) of predicted \bar{V} (cm/s) at each cross-shore location for Test 1 and 3, respectively. Since multiple measured longshore current velocities are available at the same cross-shore location from the different alongshore (y) locations, the mean error at each cross-shore location is determined as an average of the difference between measurements and predictions, $\mu = \langle x \rangle$ with $x = \bar{V}_{pred.} - \bar{V}_{meas.}$ and Tables 4.6 and 4.7 show the standard deviation of measured longshore current velocity to see the potential variance of the measurements. As seen in both Figures and Tables, the model over-predicts the longshore current velocity when sheet flow roughness, (4.77) or (4.73) is applied, i.e. when the ripple roughness is neglected. However, the model under-predicts the longshore current velocity if $k_N = k_{NR} = \eta_r$ is applied. We can deduce from this observation that the optimum roughness to yield the best-fit longshore current velocity predictions should be larger than the roughness corresponding to the pure sheet flow conditions but smaller than the roughness scaled by the ripple heights. In Test 3, as seen in Table 4.7, $k_N = \eta_r$ appears to yield the minimum mean error for predictions of the longshore current velocity. As seen in Figure 4-24, however, the model with $k_N = \eta_r$ under-

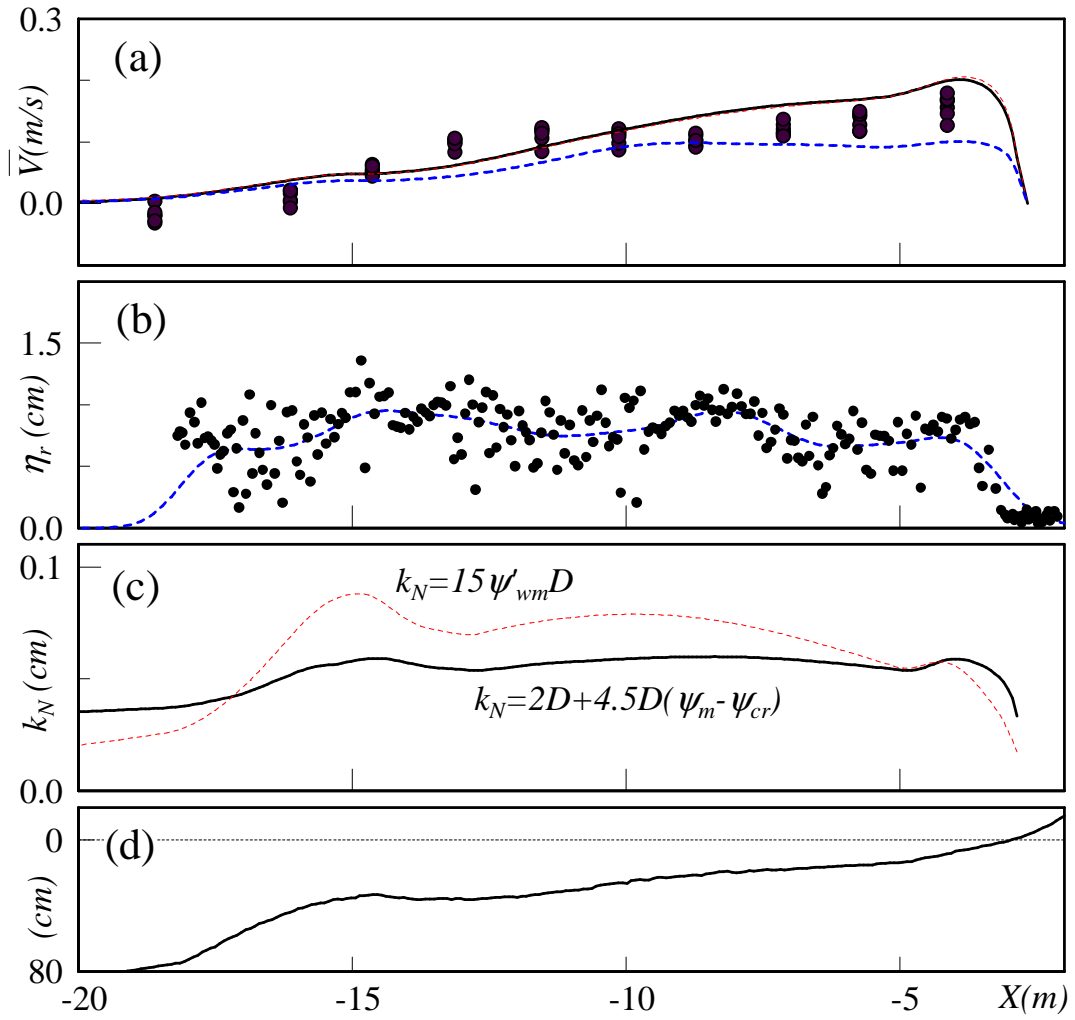


Figure 4-23: Cross-shore distributions of (a) depth-averaged longshore current velocity, (b) ripple heights, (c) equivalent bottom roughness, and (d) water depth; Experiments (full circles) presented by Wang et al. (2002) (Test 1) and predictions with roughness represented by Herrmann's (2004) (full line); Madsen(2001) (thin dashed line); and $k_N = \eta_r$ (heavy dashed line).

predicts the longshore current velocity inside the surf zone where we the relatively large sediment transports are expected. Considering the significant uncertainty in the sheet flow roughness, observed in the Figure 4-22, the present nearshore current model predicts reasonably accurate longshore current velocities when based on Herrmann's (2004) sheet flow roughness model, (4.77).

Finally, Figures 4-25 and 4-26 show the comparisons of measured and predicted wave heights, setup, vertical profiles of cross-shore and longshore current velocities for Test 1 and Test 3, respectively, when Herrmann's (2004) sheet flow bottom roughness, (4.77), was used to specify the movable bed roughness. Although the model slightly over-predicts the longshore current velocity, as discussed in the previous comparisons, the predicted vertical profiles of the cross-shore and longshore current velocity agree reasonably well with measured velocity profiles.

4.7 Summary and Conclusions

The near-shore mean current fields are determined from 2DH momentum equations integrated above the trough level and over the entire depth, respectively. Vertical profiles of the mean shear currents are analytically determined from a simple turbulent eddy viscosity model and a linearly varying mean shear stress obtained from the trough-level and the bottom shear stresses. Closed form solutions for the mean current velocity profiles are obtained and integrated to yield explicit expressions for forcings needed in the integrated momentum equations. This feature dramatically reduces the computational load for numerical applications of the model. The present near-shore current model is also applicable to random waves by using external forcings and volume fluxes for waves and surface rollers determined from our wave and surface roller models for random wave applications. Although we here limited the model application to the long, straight beach conditions, the model concepts can be extended to arbitrary beach profiles including along-shore variability.

In the cross-shore (x) direction, the forces, due to the hydrostatic pressure, wave radiation stress, and the surface roller, dominate the other forces such as bottom

Table 4.5: Equivalent roughness, k_N/D , obtained from field data (Madsen et al., 1993)

		k_N/D				
No.	$\psi'_{wm,rms}$	Meas.	(4.77)	(4.75)	(4.74)	4.73
1	0.70	50.16	7.18	6.77	4.12	10.50
2	0.78	2.25	8.54	8.56	4.51	11.66
3	0.85	6.96	9.00	9.18	4.88	12.76
4	0.99	44.97	10.49	11.15	5.57	14.83
5	1.09	13.20	11.80	12.90	6.09	16.41
μ			-0.182	-0.178	-0.635	-0.018
σ			0.593	0.605	1.004	0.474

Table 4.6: Mean errors of predicted and standard deviations of measured longshore current velocity (Test 1: spilling breaker). Predictions are (1) Herrmann (2004), (2) Madsen (2001), and (3) $k_N = \eta_r$

X(m)	$\mu(\text{cm/s})$			meas.
	(1)	(2)	(3)	$\sigma(\text{cm/s})$
-4.13	3.97	4.19	-5.95	1.85
-5.73	3.82	3.67	-3.83	1.40
-7.13	4.13	3.85	-2.32	0.97
-8.73	4.00	3.71	-0.35	0.80
-10.13	1.08	0.84	-1.67	1.19
-11.53	-1.80	-1.97	-4.31	1.30
-13.13	-3.57	-3.69	-5.33	0.75
-14.63	-0.65	-0.66	-1.81	0.74
-16.13	2.65	2.74	1.95	1.16
Average	1.52	1.41	-2.62	1.13

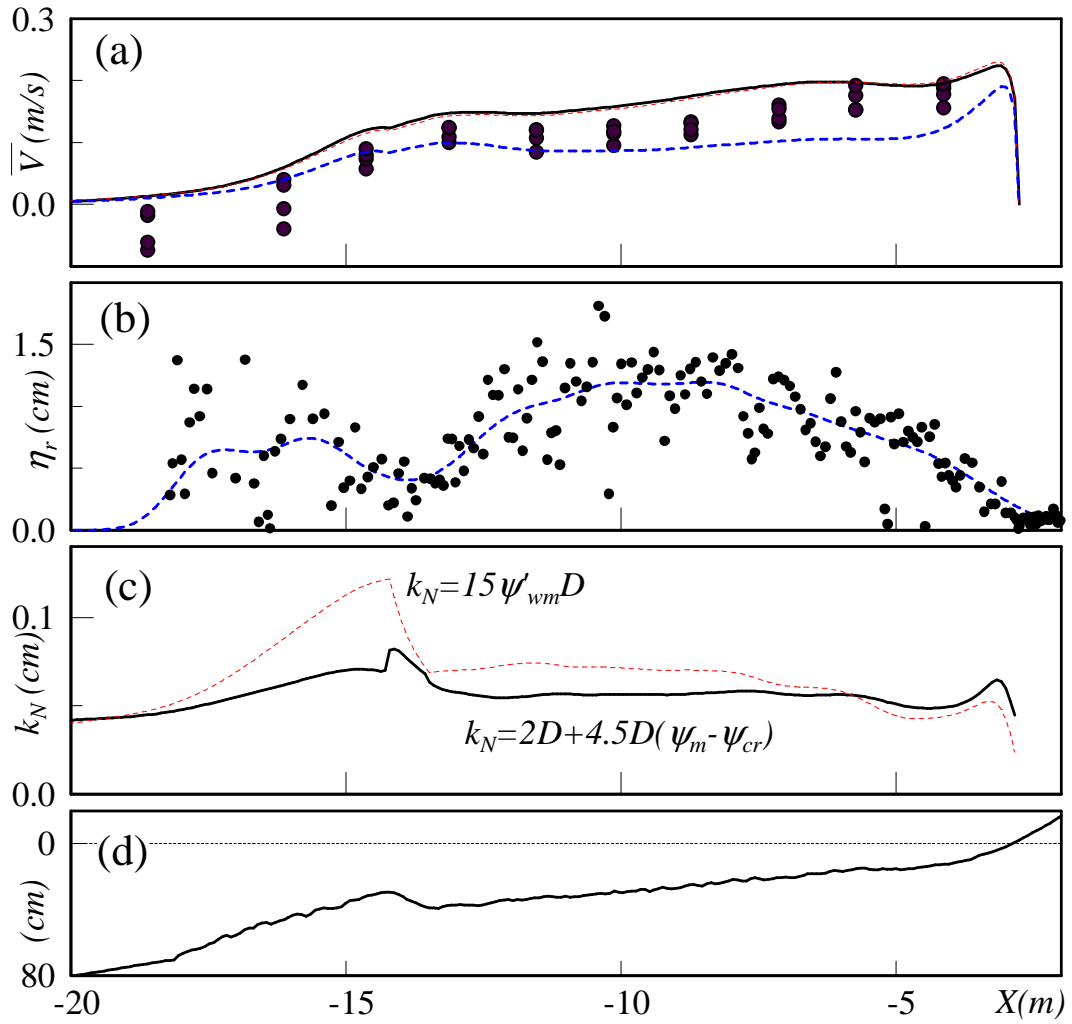


Figure 4-24: Cross-shore distributions of (a) depth-averaged longshore current velocity, (b) ripple heights, (c) equivalent bottom roughness, and (d) water depth; Experiments (full circles) presented by Wang et al. (2002) (Test 3) and predictions with roughness represented by Herrmann's (2004) (full line); Madsen(2001) (thin dashed line); and $k_N = \eta_r$ (heavy dashed line).

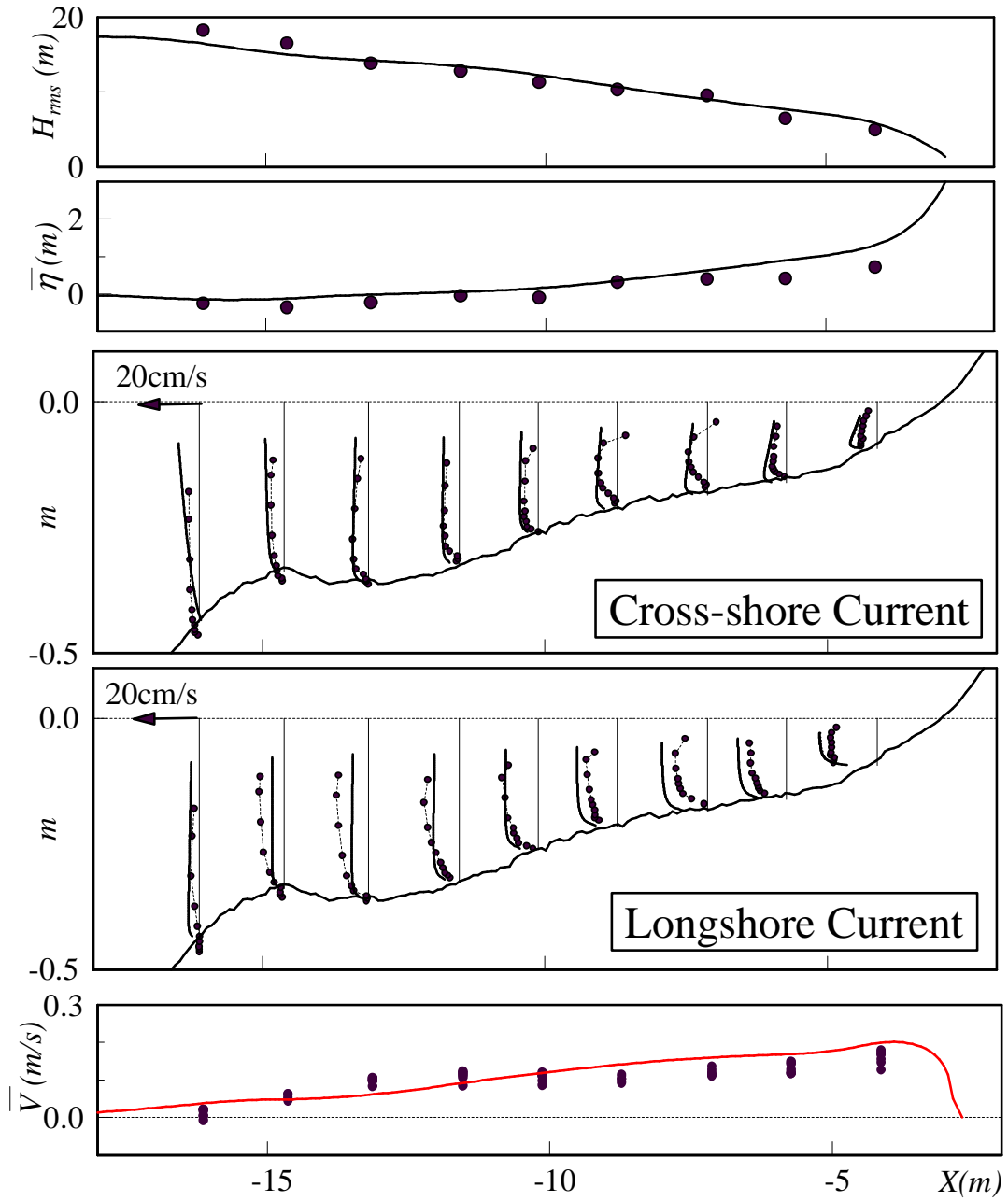


Figure 4-25: Comparisons of measured and predicted wave heights, H_{rms} , wave set-up, $\bar{\eta}$, vertical profiles of undertow and longshore current velocity, and depth-averaged longshore current velocity, \bar{V} , for random waves barred beach with movable sand bed. Measurements (Test 1: spilling breaker) by Wang et al. (2002) (full circles) and predictions (full line).

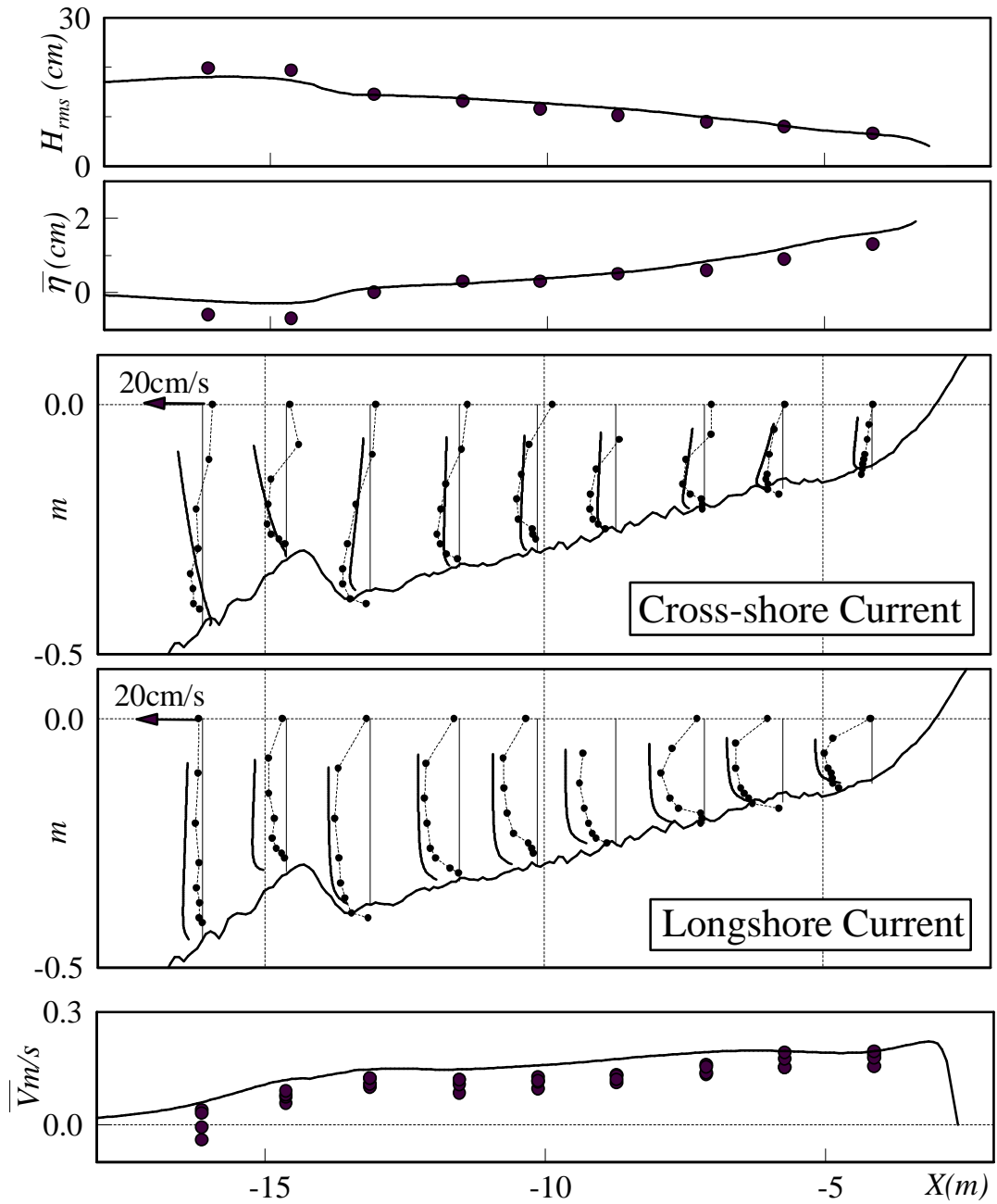


Figure 4-26: Comparisons of measured and predicted wave heights, H_{rms} , wave set-up, $\bar{\eta}$, vertical profiles of undertow and longshore current velocity, and depth-averaged longshore current velocity, \bar{V} , for random waves barred beach with movable sand bed. Measurements (Test 3: plunging breaker) by Wang et al. (2002) (full circles) and predictions (full line).

Table 4.7: Mean errors of predicted and standard deviations of measured longshore current velocity (Test 3: plunging breaker). Predictions are (1) Herrmann (2004), (2) Madsen (2001), and (3) $k_N = \eta_r$

X(m)	$\mu(\text{cm/s})$			meas.
	(1)	(2)	(3)	$\sigma(\text{cm/s})$
-4.13	1.70	2.10	-5.59	1.71
-5.73	2.88	2.93	-6.22	1.93
-7.13	4.74	4.46	-4.41	1.24
-8.73	5.12	4.70	-3.20	0.96
-10.13	4.47	4.05	-2.66	1.32
-11.53	3.96	3.58	-2.04	1.69
-13.13	3.35	2.89	-1.48	1.17
-14.63	4.58	4.09	1.00	1.37
-16.13	5.45	5.15	3.46	3.67
Average	4.03	3.77	-2.35	1.67

friction shear stress and mean-current-associated convective acceleration forces. Reasonable predictions of the wave set-up and set-down are therefore obtained from the force balance equations without bottom shear stress.

In the shore-parallel (y) direction, in contrast, mean-current-associated convective acceleration forces were comparable to the wave and the surface roller forces. In the depth-integrated momentum equations, similar to Svendsen and Putrevu's (1994) model, the mean-current-associated forces, such as the current-current, wave-current and surface roller-current interactions, had significant effects to disperse the longshore current velocity and, coupled with the surface roller model, to shift the peak of the longshore current velocity toward the shoreline. These mean-current-associated forces dominate the lateral mixing due to turbulence and allow us to avoid an empirical lateral mixing to obtain smoothly varying near-shore current fields. The present model also accounted for the mean-current associated forces in the momentum equations above the trough level and the trough shear stress obtained in this manner shifted the peak of the longshore current velocity further inside the surf zone and improved the predictive skills of the longshore current velocity profiles on the plane beach.

The modified Madsen (1994) wave-current bottom boundary layer model was adopted to specify the bottom boundary conditions for the near-shore current model.

The application of Madsen's (1994) bottom boundary layer model reduces the specification necessary to evaluate the bottom shear stress term in the momentum equations to a specification of the bottom roughness. This bottom roughness may be known, e.g. in laboratory experiments with fixed-bed roughness, or it may be estimated for movable bed conditions, such as rippled or sheet flow beds, by introducing the equivalent bottom roughness through empirically determined relationships as functions of bottom sediment and flow characteristics. Some of these equivalent bottom roughness models were reviewed and adopted for computations.

Predictive skills of the near-shore current model were examined through comparisons with experimental data for periodic or random waves normally or obliquely incident on uniform plane and barred beaches. The validity of the adoption of the modified Madsen (1994) wave-current bottom boundary layer model was confirmed by comparing predicted depth-averaged longshore current velocity with experimental data by Visser (1991), in which both smooth concrete and gravel beaches were subjected to identical periodic incident wave conditions. The model successfully explains the decrease of the longshore current velocity due to the increase in bottom roughness. From the model comparison with Visser's (1991) experiments, we observed that the longshore current velocity is sensitive to the value of the bottom roughness, k_N , if this is varied by an order of magnitude or more. Therefore, we can expect reasonable predictions of the longshore current velocity if we know the bottom roughness within an order of magnitude accuracy.

The model was also applied to the LSTF experiments with movable sand bed, in which the bed conditions are in a "break-off" range. The model with the sheet flow roughness slightly over-predicted the longshore current velocity while it underestimated with $k_N = k_{NR} \simeq \eta_r$, which is about an order of magnitude larger than the sheet flow roughness.

It should be stressed that no parameter was fitted against any near-shore mean current data. In the entire nearshore hydrodynamics models, the parameters empirically fitted against the experimental data were (i) the breaking criteria, $(u_c/C)_b$, (ii) proportionality constant for broken wave dissipation, K_b , and (iii) the equivalent

bottom roughness on the movable bed, k_N (Herrmann, 2004). For the fixed bed plane beach condition, predictive skills of the present model are still comparable to those of the best-fit classical Longuet-Higgins' (1970) longshore current model, in which the optimum empirical coefficients for the lateral dispersion, N , and the bottom friction, C_f , are calibrated. For the movable bed condition, the movable bed roughness was separately obtained from steady flow experiments and none of the LSTF experimental data was used to calibrate the movable bed roughness. Considering these facts, quantitative predictive skills of the longshore current model for the movable bed condition, whose mean prediction error of the depth-averaged longshore current velocity was $O(10\%)$, are also overall good.

Chapter 5

Sediment Transport Model

5.1 Introduction

Nearshore hydrodynamic characteristics are readily obtained from the hydrodynamics model presented in Chapter 4. In this chapter, we apply these nearshore hydrodynamic characteristics to construct a process-based predictive model for the local sediment transport rates on a long, straight beach. The basic idea underlying the sediment transport model is to apply methodologies developed for flow conditions outside the surf zone by Madsen (2001) with appropriate modifications dictated by the new environment. The sediment transport consists of two different modes, (1) Bedload and (2) Suspended Sediment transports. The effect of the surf zone hydrodynamics, such as wave breaking and surface rollers, are taken into account through the increased turbulent diffusivity due to wave breaking and mean trough shear stress in addition to the mean current bottom shear stress.

In this Chapter, we first summarize the conceptual bedload and suspended load sediment transport models (Madsen, 2001) and extend these models to the surf zone. Applicability of the present model is then tested against the LSTF experiments (Wang et al., 2002). It should be emphasized that no empirical coefficient is introduced in the present model, except for the resuspension parameter in the reference concentration model. This parameter is obtained from steady flow experiments, i.e. independently determined from the LSTF experiments against which the model's predictive skills

are being tested.

5.2 Bedload Sediment Transport

According to Madsen (1991), the conceptual model for the instantaneous bedload sediment transport rate is expressed as

$$\begin{aligned}\vec{q}_{sB}(t) &= q(t) \frac{\vec{\tau}_{bs}(t)}{|\vec{\tau}_{bs}(t)|} \\ &= \frac{8}{(s-1)\rho g} \max[0, |\vec{\tau}_{bs}(t)| - \tau_{cr,\beta'}] \\ &\quad \frac{(\sqrt{|\vec{\tau}_{bs}(t)|/\rho} - \alpha_{\beta'} \sqrt{\tau_{cr,\beta'}/\rho})}{\cos \beta' (\tan \phi_m + \tan \beta')} \frac{\vec{\tau}_{bs}(t)}{|\vec{\tau}_{bs}(t)|}\end{aligned}\quad (5.1)$$

with

$$\tan \beta' = -\frac{\partial h_0}{\partial x} \cos \theta_\tau(t) = \tan \beta_0 \cos \theta_\tau(t) \quad (5.2)$$

$$\tau_{cr,\beta'} = \tau_{cr} \cos \beta' \left(1 + \frac{\tan \beta'}{\tan \phi_s}\right) \quad (5.3)$$

$$\alpha_{\beta'} = \sqrt{\frac{\tan \phi_m + \tan \beta'}{\tan \phi_s + \tan \beta'}} \quad (5.4)$$

where $s = \rho_s/\rho$ with ρ_s and ρ the density of the sediment and the fluid, respectively, $\tau_{cr,0}$ is the critical bottom shear stress when $\beta' = 0$, $\tan \beta_0 = -\partial h_0/\partial x$ is the bottom slope. $\theta_\tau(t)$ is the instantaneous direction of the time-varying “sediment transport” shear stress, $\vec{\tau}_{bs}(t)$, which is defined in the following section. $\phi_s \simeq 50^\circ$ and $\phi_m \simeq 30^\circ$ are the angles of static and moving friction, respectively, as recommended by Madsen (2001) from comparison of (5.1) to experimental findings by King (1991) and Luque and Beek (1976). Note that β' , the local bottom slope in the direction of the bottom shear stress, also varies with time because the direction of the bottom shear stress, $\vec{\tau}_{bs}(t)$, is a function of time. As seen in (5.1), the bedload sediment transport rate becomes zero if the magnitude of the bottom shear stress is smaller than the critical shear stress, i.e. $|\vec{\tau}_{bs}(t)| < \tau_{cr,\beta'}$. The critical shear stress on a plane bed, $\tau_{cr,0}$, is

determined by $\tau_{cr,0} = \psi_{cr} \rho (s - 1) g D$ with the critical Shields parameter ψ_{cr} given by (4.68) in Section 4.6.3.

5.2.1 Sediment Transport Roughness and Shear Stress

The sediment transport shear stress for bedload sediment transport, $\vec{\tau}_{bs}$, is based on an equivalent sediment transport roughness, k_{Ns} , and represents the component of the total bottom shear stress that induces sediment transport. On a rippled bed, for example, the shear stress component due to the ripple form drag does not directly induce sediment motion and therefore should not be accounted for as a component of the shear stress for the computation of sediment transport, $\vec{\tau}_{bs}$. On a sheet flow bed, as discussed in Section 4.6.3, Wilson (1987) pointed out that the Meyer-Peter-Muller (1948) bedload sediment transport formula agreed well with experimental data if the total shear stress based on the movable bed roughness was introduced as the sediment transporting force. Madsen's (1991) conceptual bedload sediment transport model yields nearly the same bedload sediment transport characteristics as the Meyer-Peter-Muller formula under the plane no-sloping bed condition. In this sense, $\vec{\tau}_{bs}$ on a sheet flow bed should be equivalent to the total shear stress and the corresponding roughness, k_{Ns} , should be represented by the sheet flow roughness,

$$k_{Ns} = k_N = [2 + 4.5 (\psi_{ms} - \psi_{cr})] D \quad (5.5)$$

as introduced in (4.77) (Herrmann, 2004). On a rippled bed, a number of studies have suggested that the skin friction shear stress should be based on the roughness scaled by the sediment diameter, e.g. $k_{Ns} = D$ (Madsen, 1991 and 2001), which yields the ordinary suggested skin friction shear stress, τ'_b , based on $k'_N = D$ and the corresponding skin friction wave Shields Parameter, ψ'_{wm} , introduced in (4.66) in Section 4.6.3. In this study, we distinguish ψ' based on $k'_N = D$ and ψ_s based on k_{Ns} because k_{Ns} is not always equal to the sediment diameter and we still need to evaluate ψ'_{wm} to determine the movable bed conditions by comparing ψ'_{wm} with the critical Shields Parameters for sediment motion, ψ_{cr} , break-off, ψ'_B , and sheet flow,

ψ'_{up} , introduced in (4.68), (4.71), and (4.72), respectively. We thus refer to $\vec{\tau}_{bs}$ as the sediment transport shear stress and correspondingly, to k_{Ns} as the sediment transport roughness.

When the sediment transport roughness, k_{Ns} , is smaller than the “total” movable bed roughness, k_N , Madsen’s (1994) modified wave-current bottom boundary layer model requires additional computations to evaluate the sediment transport shear stress from the knowledge of the total shear stress and the ambient flow conditions. Appendix D summarizes the numerical scheme for evaluation of the sediment transport shear stress for $k_N > k_{Ns}$ based on Madsen’s (1994) modified wave-current bottom boundary layer model, all of which are presented in the *Coastal Engineering Manual* (2001). On rippled beds, adoption of $k_{Ns} = D$ may be reasonable if the flow intensity is relatively small and the sand grains individually roll over the bed. As the flow intensity increases and starts to wash out the ripples, however, moving sand grains on the bed start to form a “sheet flow layer” and the sediment transport roughness should increase and eventually reach the sheet flow roughness. In this sense, a smooth transition of the sediment transport roughness is assured for the transition from rippled bed to sheet flow if the sediment transport roughness is determined from (5.5) regardless of whether the bed is rippled or not. In this study, however, we focus on sheet flow conditions, which are predominant in the field near and inside the surf zone, and therefore have $k_N = k_{Ns}$.

The time-varying sediment transport shear stress, $\vec{\tau}_{bs}(t)$, is decomposed into wave and mean current sediment transport shear stresses

$$\vec{\tau}_{bs}(t) = (\tau_{bsx}(t), \tau_{bsy}(t)) = (\tau_{ws}(t) \cos \theta + \tau_{cbsx}, \tau_{ws}(t) \sin \theta + \tau_{cbsy}) \quad (5.6)$$

Following Madsen’s (1994) modified wave-current bottom boundary layer model, which is based on linear wave theory and assumption of time-independent turbulent eddy viscosity, ν_T , the instantaneous wave shear stress, $\tau_{ws}(t)$, is determined by

$$\tau_{ws}(t) = -\rho\nu_T \frac{\partial u_{bw}(t)}{\partial z} = \frac{1}{2} \rho f_{cws} u_{bm}^2 \cos(\omega t + \varphi) \quad (5.7)$$

where u_{bm} is the amplitude of the near-bottom wave orbital velocity, f_{cws} is a friction factor for the sediment transport shear stress determined from (4.26) with $k_N = k_{Ns}$, and φ is the phase difference between near-bottom wave orbital velocity, $u_{bm} \cos(\omega t)$, and the wave-associated bottom shear stress, $\tau_{ws}(t)$. In the near-shore region, however, relatively strong non-linear wave effects are expected and resulting skewness and asymmetry of the near-bottom wave orbital velocity profile may significantly affect the net sediment transport rate in the wave-propagation direction, i.e. in the shore-normal (x) direction. In this study, we first account for the non-linear wave effects by

$$\tau_{ws}(t - \varphi/\omega) = \frac{1}{2} \rho f_{cws} u_{bm} u_{bw}(t) \quad (5.8)$$

where the non-linear near-bottom wave orbital velocity, $u_{bw}(t)$, is determined by (2.7) introduced in Section 2.1.3. Note that (5.8) is equivalent to (5.7) if $u_{bw}(t)$ has a linear sinusoidal profile. Alternatively, assuming time-varying turbulent eddy viscosity (Trowbridge and Madsen, 1984), the non-linear wave shear stress may be expressed by

$$\tau_{ws}(t - \varphi/\omega) = \frac{1}{2} \rho f_{cws} |u_{bw}(t)| u_{bw}(t) \quad (5.9)$$

In Section 5.6, we respectively apply (5.7), (5.8), and (5.9) to evaluate the wave-associated shear stress and compare the predicted sediment transport rates with LSTF experimental data and examine the non-linear wave effects on the sediment transport characteristics.

The phase difference between u_{bw} and τ_{ws} may also yield a phase difference between instantaneous suspended sediment concentrations and the wave orbital velocity because the near-bottom sediment concentration should be strongly related to the time-varying bedload sediment transport rate. Thus the phase difference may affect the mean wave-associated suspended sediment transport in the wave direction and therefore influence the balance of the total shore-normal sediment transport rate. In the shore-parallel (y) direction, however, the wave-associated sediment transport is generally negligibly small because of the near-normal incidence of the waves. Therefore, the phase difference as well as wave non-linearity should have little influence

on the mean longshore sediment transport rate (LSST). This feature will also be discussed in Section 5.6.

5.2.2 Net Bedload Sediment Transport Rate

Substituting (5.6) into (5.1) and averaging it over a wave period, the net bedload sediment transport components in the cross-shore (x) and the shore-parallel (y) directions are

$$\bar{q}_{SBx} = \frac{1}{T} \int_0^T q_{SB}(t) \frac{\tau_{bsx}(t)}{|\vec{\tau}_{bs}(t)|} dt \quad (5.10)$$

$$\bar{q}_{SB y} = \frac{1}{T} \int_0^T q_{SB}(t) \frac{\tau_{bsy}(t)}{|\vec{\tau}_{bs}(t)|} dt \quad (5.11)$$

We numerically evaluate the integrations in (5.10) and (5.11) to obtain the components of bedload sediment transport rate.

5.3 Suspended Sediment Transport

The suspended sediment transport rate, \vec{q}_{SS} , is generally defined by

$$\vec{q}_{SS}(t) = \int_{z_r}^{h+\eta} c(z, t) \vec{u}(z, t) dz \quad (5.12)$$

where z is the vertical axis with $z = 0$ at the bed, z_r is the elevation where bedload sediment transport rate switches to suspended sediment transport rate, $c(z, t)$ is the vertical distribution of suspended sediment concentration, and $\vec{u}(z, t) = (u(z, t), v(z, t))$ is the horizontal velocity components. Both velocity and concentration are respectively decomposed into mean and wave components,

$$c(z, t) = C(z) + c_w(z, t) \quad (5.13)$$

$$\vec{u}(z, t) = \vec{U}(z) + \vec{u}_w(z, t) \quad (5.14)$$

where (C, \vec{U}) denote the mean and (c_w, \vec{u}_w) are the wave-associated-fluctuations around the mean. Substituting (5.13) and (5.14) into (5.12) and time-averaging over a wave period yields the mean suspended sediment transport,

$$\begin{aligned}\vec{q}_{ss} &= \int_{z_r}^h C \vec{U} dz + \overline{\int_{z_r}^h c_w \vec{u}_w dz} + \overline{\int_h^{h+\eta} c_w \vec{U} dz} + \overline{\int_h^{h+\eta} C \vec{u}_w dz} \\ &\simeq \int_{z_r}^h C \vec{U} dz + \overline{\int_{z_r}^h c_w \vec{u}_w dz}\end{aligned}\quad (5.15)$$

The first term in (5.15) is the contribution due to product of the mean current and the mean suspended sediment concentration and therefore referred to as “mean suspended load.” The second term in (5.15) is the component due to the wave-associated-fluctuating velocity and sediment concentration and is therefore referred to as “mean wave-associated suspended load.” As discussed in Section 5.2.1, the phase difference between bottom shear stress and wave orbital velocities must be accounted for if this mean wave-associated suspended load were to be evaluated. The integrations near the surface, i.e. the third and the forth terms in (5.15), may be assumed negligible because the suspended sediment concentrations near the surface is considerably smaller than near the bed.

5.3.1 Further Simplifications

On a long, straight beach we assume that the incident waves are obliquely propagating toward the shore line at a small angle of incidence. In this case, the wave-associated sediment transport components in the longshore direction may be assumed negligible. The total LSST is therefore simplified by

$$q_y \simeq \bar{q}_{SB_y} + \int_{z_r}^h C V dz \quad (5.16)$$

Similarly, the effect of non-linear asymmetric and skewed near-bottom velocity profiles, which appear in (5.7) and may be accounted for in (5.11), are also expected to be negligible in the evaluation of the longshore sediment transport rate by (5.16). Non-linear wave velocities may significantly affect the sediment transport balance in

the direction of wave propagation, i.e. in the cross-shore direction. This feature will be discussed later in the evaluation of the cross-shore sediment transport rate.

5.4 Mean Concentration Distribution

Assuming that the system is slowly changing in the horizontal direction and neglecting the cross-shore diffusive and advective sediment fluxes, the time-averaged mass conservation law in the vertical (z) direction requires

$$-w_f C = \nu_s \frac{\partial C}{\partial z} \quad (5.17)$$

where ν_s is the turbulent eddy diffusivity. According to Jimenez and Madsen (2003), the fall velocity of natural sediment, w_f , is determined by

$$w_f = \frac{\sqrt{(s-1)gD_n}}{0.954 + 5.12/S_{*n}} \quad (5.18)$$

where D_n is a nominal sediment diameter ($\simeq D_s/0.9$ with sieve diameter, D_s) and S_{*n} is the fluid-sediment parameter based on $D = D_n$ determined from (4.67).

5.4.1 Turbulent Eddy Diffusivity.

A number of field observations have been performed to indirectly investigate the vertical distributions of the turbulent eddy diffusivity by requiring ν_s to satisfy (5.17) with measured vertical distributions of sediment concentrations and sediment fall velocity (e.g. Vincent and Downing, 1994; Sheng and Hay, 1995; Vincent and Osborne, 1995; Lee et al., 2002; and Lee et al., 2003). These studies suggest that the turbulent eddy diffusivity near the bed increases linearly with elevation from the bottom, z . According to Lee et al., (2003), the magnitude of the turbulent eddy diffusivity is scaled by the maximum of wave-current or mean current shear velocities depending on their relative intensity. In this study, we assume $\nu_s = \nu_T$ (e.g. Rouse, 1938; Kalinske and

Pien, 1943; Dobbins, 1944; Hunt, 1954) and take

$$\nu_s = \nu_T = \begin{cases} \kappa u_{*m} z & (z \leq \delta) \\ \kappa u_{*c} z & (\delta \leq z \leq z_m) \\ \kappa u_{*s} z \sqrt{\frac{z}{h_{tr}}} & (z_m \leq z \leq h_{tr}) \end{cases} \quad (5.19)$$

as is introduced in (4.18), with $z_m = h_{tr} u_{*c}^2 / u_{*s}^2$ being the elevation where $\kappa u_{*c} z = \kappa u_{*s} z \sqrt{z/h_{tr}}$ is satisfied. All of these variables are already obtained in the nearshore hydrodynamics models presented in Chapter 4.

5.4.2 Bottom Boundary Condition

We now need a bottom boundary condition in order to solve (5.17) with the present eddy diffusivity (5.19) and to obtain the vertical profile of the sediment concentration. There are two approaches to determine the bottom boundary condition, either specifying the upward volume flux of the sediment near the bed, the so-called “pickup function,” or specifying the reference concentration at a certain elevation above the bottom.

If one were to solve the unsteady advection-diffusion equations for the sediment concentration, the pickup function may be preferred. For example, Kobayashi and Johnson (2001) determined the depth-averaged sediment concentration, \bar{C} , from the depth-integrated unsteady mass balance equation in the cross-shore direction (CBREAK),

$$\frac{\partial}{\partial t} (h\bar{C}) + \frac{\partial}{\partial x} (h\bar{C}\bar{u}) = p - w_f \bar{C} \quad (5.20)$$

with pick up function, p , determined by

$$p = \frac{e_B D_B + e_f D_f}{(s-1) \rho g h} \quad (5.21)$$

where the depth-averaged shoreward velocity, $\bar{u}(t)$, is obtained from a separate hydrodynamic model, D_B is an energy dissipation rate due to wave breaking, D_f is an energy dissipation rate due to bottom friction, and e_B and e_f , are empirical co-

efficients of suspension efficiency for D_B and D_f , respectively. In their model, the bottom sediments are accumulated if settling volume flux, $w_f \bar{C}$, dominates the upward volume flux, p , and the bottom sediments are eroded if vice versa. Because their model applied \bar{C} to determine the settling volume flux, which should be a product of w_f and the near-bottom sediment concentration, the model may not be applicable to the system in which the vertical variations of the sediment concentration is not negligible. Qin et al. (2002) applied the unsteady 1DV advection-diffusion equation to determine the vertical distributions of the suspended sediment concentration with bottom boundary condition specified by Van Rijn's (1984) pick up function. Although they accounted for the vertical variation of the suspended sediment, advective and diffusive horizontal volume fluxes were neglected.

In the equilibrium state, i.e. when the upward and downward sediment fluxes balance each other as seen in (5.17), the relationship between upward entrainment rate (pickup function), p , and the reference concentration at a certain height above the bottom, C_r , can be found from the vertical mass balance equation (5.17) (Nielsen, 1992):

$$p = w_f C_r \quad \text{at } z = z_r \quad (5.22)$$

Hence, either approach, pickup function or reference concentration, can be equivalently applied under the assumption of the equilibrium state, (5.17). Since we focus on the predictions of the time-averaged sediment concentration, we simply adopt a reference concentration approach.

Einstein (1950) first suggested that the reference concentration should be strongly related to the bedload sediment transport rate and the saltating load layer thickness. He also suggested that the reference elevation above the bed, z_r , should be related to the thickness of the bedload transport layer and took $z_r = 2D$. Yalin (1963) proposed that the sediment concentration near the bed in unidirectional flow is proportional to the normalized excess skin friction shear stress:

$$S' = \frac{\tau' - \tau_{cr}}{\tau_{cr}} \quad (5.23)$$

Following Yalin (1963), Smith and McLean (1977) determined the reference concentration for unidirectional flow as a function of S' :

$$C_r(z_0) = C_b \frac{\gamma_0 S'}{1 + \gamma_0 S'} \quad (5.24)$$

where z_0 is the roughness height in the boundary layer, C_b ($\simeq 0.65$) is the volumetric bed concentration and γ_0 is the resuspension parameter to be calibrated. Smith and McLean (1977) introduced the factor $(1 + \gamma_0 S')^{-1}$ to ensure that the maximum of (5.24) should not exceed the volumetric bed concentration, C_b . For $\gamma_0 S' \ll 1$, (5.24) is nearly proportional to S' as suggested by Yalin (1963), i.e.

$$C_r(z_0) = C_b \gamma_0 S' \quad (5.25)$$

This approach has been widely used for both unidirectional flow in rivers and estuaries and for combined waves and currents in the coastal environment (e.g., Madsen et al., 1994; Webb and Vincent, 1999; Green et al., 2000; Rose and Thorne, 2001). However, the values of the resuspension parameter, γ_0 , reported by various authors vary from 10^{-5} to 10^{-2} (Hill et al., 1988; Webb and Vincent, 1999). Empirical fitting formulae of γ_0 have also been proposed, based on field data, in which γ_0 decreases with increasing skin friction shear velocity (e.g. Vincent and Downing, 1994; Vincent and Osborne, 1995; Lee et al., 2002). These significant variations of γ_0 -values may be largely because of the uncertainty of the roughness height, z_0 . For example, Webb and Vincent (1999) predicted z_0 from an equivalent bottom roughness, $z_0 = k_N/30$. As shown in Figure 4-22, the measured movable bottom roughness for sheet flow conditions exhibit significant scatter and the existing predictive models also differ from each other by about an order of magnitude. Similar scatter of the ripple heights, which are believed to characterize the ripple roughness, k_{NR} , are also seen in Figures C-3 and C-4 in Appendix C for both existing models and measurements. Because the sediment concentration varies dramatically near the bottom, the definition of the reference elevation, z_r , is critical to obtain a widely applicable reference concentration model. While some studies have arbitrarily set a reference elevation for the reference

concentrations (e.g., $z_r = 2\text{cm}$ by Vincent and Osborne, 1994; and $z_r = 1\text{cm}$ by Lee et al., 2003), McLean (1992) followed Einstein's concept and applied the bedload layer thickness, δ_B to be z_r . He pointed out that $z_r = z_0$ is typically much smaller than the bedload layer thickness, δ_B , below which grain-grain collisions can be important and sediment velocity differs from ambient fluid velocity. Van Rijn (1984) suggested the reference level, z_r , to be related to the bed form height,

$$z_r = 0.5\eta_r \text{ or } k_N \text{ (with } z_{r,min} = 0.01h) \quad (5.26)$$

and expressed the reference concentration based on field measurements in unidirectional flow:

$$C_r = 0.011 \frac{D_{50}}{z_r} \frac{S'^{1.5}}{S_*^{0.2}} \quad (5.27)$$

Note that (5.27) is a function of z_r , which is much larger than z_0 (cf. $z_0 = k_N/30$ for rough turbulent boundary layer). The validity of (5.27) was confirmed by Rose and Thorne (2001) who compared the model with field data collected in the river Taw estuary, UK, over a sandy rippled bed. However, z_r is a function of η_r or k_N , which may contain considerable uncertainty as discussed previously. Wikramanayake and Madsen (1994) simply adopted $z_r = 7D$ and proposed the resuspension parameter in (5.25), to be of the order 10^{-3} . Herrmann (2004) followed Wikramanayake and Madsen (1994) and adopted $z_r = 7D$ to determine the reference concentration based on a number of sheet flow experiments for unidirectional flow:

$$C_r = 0.0022 \left(\frac{\tau_{bs}}{\tau_{cr}} - 1 \right) \quad (5.28)$$

Herrmann's (2004) model, (5.28), is based on the same concept as Yalin-type (1963) models, (5.25), but differs in that (5.28) applies τ_{bs} , the sediment transport shear stress based on the sheet flow bottom roughness while other models apply τ'_b , the skin friction shear stress based on the roughness scaled by a sediment diameter. As discussed in Section 4.6.3, we deduced, from observations presented by Wilson (1665, 1667, and 1687), that the bedload sediment transport on a sheet flow bed should be

determined by τ_{bs} and not τ'_b . Since the reference concentration is strongly related to the bedload sediment transport C_r should, for the sheet flow conditions, also be determined by τ_{bs} . The magnitude C_r obtained in (5.28) is consistent with Wiberg et al.'s (1994) model, who suggested $\gamma_0 \simeq 0.002$ based on a large amount of field observations. In this study, we apply Herrmann's (2004) model both for the reference concentration, (5.28), and for the movable bed roughness, (4.77).

Because Herrmann's (2004) reference concentration formula (5.28) is based on unidirectional flow, we need to extend the model for combined wave-current flow conditions. Grant and Madsen (1982) demonstrated that the response time of the rolling grains on the bed is much smaller than the wave period. Based on this feature, Glenn and Grant (1987) applied Smith and McLean's (1977) reference concentration formula for uni-directional flow as an instantaneous reference concentration and simply averaged it over wave period to obtain the mean reference concentration. Following the same procedure and introducing (5.6) into (5.28), the mean reference concentration for combined wave-current flow is determined by

$$C_r = \frac{0.0022}{T} \int_0^T \max \left(0, \frac{|\vec{\tau}_{bs}(t)|}{\tau_{cr,\beta'}} - 1 \right) dt \quad (5.29)$$

Note that $\tau_{bs}(t)$, defined in (5.6), is the time-varying shear stress based on the sheet flow roughness, (4.77), and the instantaneous reference concentration becomes zero if $|\tau_{bs}(t)| < \tau_{cr,\beta'}$. The critical shear stress on the slope, $\tau_{cr,\beta'}$, also changes with time depending on the flow directions.

It should be pointed out that Herrmann's model (5.28) is based on experimental data for sheet flow bed conditions. Characteristics of C_r may significantly differ between rippled bed and flat bed conditions. This feature was observed by Webb and Vincent (1999), who plotted C_r at $z_r = z_0$ as a function of skin friction Shields Parameter and showed the dramatic decrease of C_r at the limit between equilibrium and breakoff ripples. When sharp-crested ripples are generated by regular waves, laboratory results indicate that vertical advections associated with large vortices around the ripple crests dominate the turbulent eddy diffusivity near the bed (e.g. Sleath,

1982; and Ribberink and Al-Salem, 1994). The detailed modeling of C_r for equilibrium ripple beds and smooth transition of C_r in the breakoff ripple region may be required for the establishment of a complete suspended sediment transport model. Here, however, we deal with sheet flow conditions and thus avoid this challenging problem.

5.4.3 Mean Concentration Profiles

Solving (5.17) with turbulent eddy diffusivity (5.19) and bottom boundary condition (5.29), vertical profiles of the mean concentration are explicitly obtained as

$$C = \begin{cases} C_r \left(\frac{z}{z_r} \right)^{-\frac{w_f}{\kappa u_{*m}}} & (z_r \leq z \leq \delta) \\ C_\delta \left(\frac{z}{\delta} \right)^{-\frac{w_f}{\kappa u_{*c}}} & (\delta \leq z \leq z_m) \\ C_{z_m} \exp \left(\frac{2w_f}{\kappa u_{*s}} \left(\sqrt{\frac{h_{tr}}{z}} - \sqrt{\frac{h_{tr}}{z_m}} \right) \right) & (z_m \leq z \leq h_{tr}) \end{cases} \quad (5.30)$$

with

$$C_\delta = C_r \left(\frac{\delta}{z_r} \right)^{-\frac{w_f}{\kappa u_{*m}}} \quad (5.31)$$

$$C_{z_m} = C_\delta \left(\frac{z_m}{\delta} \right)^{-\frac{w_f}{\kappa u_{*c}}} \quad (5.32)$$

5.4.4 Mean Longshore Suspended Sediment Transport

As introduced in (4.27), the longshore current profiles are expressed as

$$V = \begin{cases} A_{1y} \ln \frac{z}{z_0} & z_0 \leq z \leq \delta \\ V_\delta + A_{2y} \ln \frac{z}{\delta} + A_{3y} \frac{z-\delta}{h_{tr}} & (\delta \leq z \leq z_m) \\ V_{z_m} + A_{4y} \left(\sqrt{z} - \sqrt{z_m} \right) & (z_m \leq z \leq h_{tr}) \\ V_s & (h_{tr} \leq z \leq h + \eta) \end{cases} \quad (5.33)$$

with

$$\begin{pmatrix} A_{1y} \\ A_{2y} \\ A_{3y} \\ A_{4y} \end{pmatrix} = \begin{pmatrix} \frac{\tau_{cby}}{\rho K u_{*m}} \\ \frac{\tau_{cby}}{\rho K u_{*c}} \\ \frac{\tau_{csy} - \tau_{cby}}{\rho K u_{*c}} \\ \frac{2}{\rho K u_{*s}} \left(\frac{\tau_{csy} - \tau_{cby}}{\sqrt{h_{tr}}} + \tau_{cby} \sqrt{\frac{h_{tr}}{zz_m}} \right) \end{pmatrix} \quad (5.34)$$

where V_δ , V_{z_m} and V_s are mean longshore current velocity at $z = \delta$, $z = z_m$ and $z = h_{tr}$ given by (5.33), respectively. Note that the mean current velocity determined by (5.33) is valid only where $z \geq z_0$ whereas the vertical integration for suspended load (5.16) requires the velocity above z_r . We thus call for special treatments if $z_r < z_0$. On a sheet flow bed, z_0 is determined from (4.77) as

$$z_0 = \frac{k_{Ns}}{30} = \left(\frac{2 + 4.5(\psi_m - \psi_{cr})}{30} \right) D \quad (5.35)$$

which exceeds $z_r = 7D$ when $\psi_m > \psi_{cr} + 46$. Since the magnitude of ψ_m is at most of order 1, $z_r < z_0$ does not happen on a sheet flow bed. On a rippled bed, z_0 based on the ripple roughness, k_{NR} , can be larger than $z_r = 7D$. Below the outer edge of the bottom boundary layer thickness based on the total roughness, k_N , however, Madsen's (1994) modified wave-current bottom boundary layer model is repeatedly applied to determine the mean current velocity profile based on the sediment transport roughness, k_{Ns} . Since the magnitude of k_{Ns} is scaled by D , similar to the sheet flow bed, z_{0s} based on k_{Ns} is assured to be smaller than $z_r = 7D$. Therefore, we can always expect realistic mean current velocities for the integration of (5.16). As discussed in Section 5.2.1, the numerical scheme for prediction of the velocity profile below the outer edge of the bottom boundary layer when $k_N > k_{Ns}$ is presented in Appendix D. Combining the mean concentration profile (5.30) and the mean longshore current velocity (5.33), the integrations in (5.16) below z_m can be analytically determined and the total suspended LSST is represented by

$$q_{SSy} = q_{SS1y} + q_{SS2y} + \int_{z_m}^h CV dz \quad (5.36)$$

where

$$\begin{aligned}
q_{SS1y} &= \int_{z_r}^{\delta} CV dz \\
&= C_r A_{1y} z_r \ln \frac{\delta}{z_r} \left(\frac{1}{2} \ln \frac{\delta}{z_r} + \ln \frac{z_r}{z_0} \right) \quad \text{for } m_1 = 1 \\
&= C_r A_{1y} \frac{1}{1 - m_1} \left\{ \delta \left(\frac{\delta}{z_r} \right)^{-m_1} \left(\ln \frac{\delta}{z_0} - \frac{1}{1 - m_1} \right) \right. \\
&\quad \left. + z_r \left(\frac{1}{1 - m_1} - \ln \frac{z_r}{z_0} \right) \right\} \quad \text{for } m_1 \neq 1
\end{aligned} \tag{5.37}$$

with

$$m_1 = \frac{w_f}{\kappa u_{*m}} \tag{5.38}$$

and

$$q_{SS2y} = \int_{\delta}^{z_m} CV dz = q_{SS21,y} + q_{SS22,y} + q_{SS23,y} \tag{5.39}$$

where if $m_2 = 1$:

$$q_{SS21,y} = V_{\delta} C_{\delta} \delta \ln \frac{z_m}{\delta} \tag{5.40}$$

$$q_{SS22,y} = C_{\delta} A_{2y} \frac{\delta}{2} \left(\ln \frac{z_m}{\delta} \right)^2 \tag{5.41}$$

$$q_{SS23,y} = \frac{A_{3y} C_{\delta} \delta^2}{h_{tr}} \left(\frac{z_m}{\delta} - \ln \frac{z_m}{\delta} - 1 \right) \tag{5.42}$$

otherwise ($m_2 \neq 1$):

$$q_{SS21,y} = V_{\delta} C_{\delta} \frac{\delta}{1 - m_2} \left[\left(\frac{z_m}{\delta} \right)^{1 - m_2} - 1 \right] \tag{5.43}$$

$$\begin{aligned}
q_{SS22,y} &= C_{\delta} A_{2y} \frac{1}{1 - m_2} \\
&\quad \times \left\{ z_m \left(\frac{z_m}{\delta} \right)^{-m_2} \left(\ln \frac{z_m}{\delta} - \frac{1}{1 - m_2} \right) + \frac{\delta}{1 - m_2} \right\}
\end{aligned} \tag{5.44}$$

$$\begin{aligned}
q_{SS23,y} &= \frac{A_{3y} C_{\delta}}{h_{tr}} \left\{ z_m \left(\frac{z_m}{\delta} \right)^{-m_2} \left(\frac{z_m}{2 - m_2} - \frac{\delta}{1 - m_2} \right) \right. \\
&\quad \left. + \frac{\delta^2}{(1 - m_2)(2 - m_2)} \right\} \quad \text{for } m_2 \neq 2
\end{aligned} \tag{5.45}$$

$$q_{SS23,y} = \frac{A_{3y}C_\delta\delta^2}{h_{tr}} \left(\ln \frac{z_m}{\delta} + \frac{1}{3} \left(\frac{z_m^3}{\delta^3} - 1 \right) \right) \quad \text{for } m_2 = 2 \quad (5.46)$$

with

$$m_2 = \frac{w_f}{\kappa u_{*c}} \quad (5.47)$$

The integration above $z = z_m$ in (5.36) is numerically evaluated by applying Simpson's 1/3 rule (Hoffman, 1992) with an interval of $\Delta z = h/100$. Since the suspended sediment concentration above $z = z_m$ is relatively small compared to the concentration near the bed, numerical errors in the integration do not affect the total suspended sediment transport rate significantly.

5.5 Grain Size Effect on Suspended Sediment

In the field, the bottom sediments may consist of a mixture of different grain sizes. In the hydrodynamic model, the characteristics of the mixed-size grains are often represented by the median sand diameter, D_{50} , to determine the equivalent movable bed bottom roughness and corresponding bottom shear stresses. As seen in (5.1), the bedload sediment transport formula does not contain explicit effects of the sediment diameter, although the sediment transport shear stress, $\vec{\tau}_{bs}$, and the critical shear stress may be slightly affected by grain size.

In contrast to the bedload sediment transport rate, mixed grain sizes may affect the suspended sediment concentrations in the water column and therefore affect the suspended sediment transport (e.g., Lee and Hanes, 1996; Lee et al., 2002). As seen in (5.30), the magnitude of the suspended sediment concentration in the water column is determined from the balance of upward sediment flux due to turbulent eddy diffusivity and the downward flux due to gravitational sediment settlement. For instance, the concentration in the range $\delta \leq z \leq z_m$ decreases with the elevation from the bottom, z , to the power of $m_2 = w_f/\kappa u_{*c}$. If the fall velocity of the sand grains exceeds the upward sediment flux due to turbulence, represented by κu_{*c} , the suspended sediment concentration dramatically decreases as the elevation from the bottom increases and

the resulting suspended sediment transport rate also substantially decreases. The prediction of the suspended sediment transport is therefore very sensitive to the settling velocity, i.e. the sediment grain size. In this study, we account for the effect of different grain sizes in evaluation of the suspended sediment transport rate.

We first separate the mixed-size grains into a number of size-classes and find the weight fractions, f_b , of each class through a sieve analysis. Assuming that the bedload sediment transport rate and the reference concentrations are independent of the sand grain size, the equivalent i -th sand concentration profile, $C_i(z)$, is determined from (5.30) by replacing w_f with the i -th class sand of diameter D_i and corresponding fall velocity, $w_{f,i}$. Here C_r is determined based on D_{50} and specified at $z_r = 7D_{50}$. The concentration component of the i -th size-class sediment is then determined by $f_{b,i}C_i(z) / (\sum_{i=1}^N f_{b,i})$. Finally, integrating all the components of each concentration fraction, the mean concentration profiles of the mixed sand grains, $C(z)$, are determined by

$$C(z) = \sum_{i=1}^N f_{b,i}C_i(z) / \sum_{i=1}^N f_{b,i} \quad (5.48)$$

In order to reduce the computational load in a numerical application of the model, several size-classes may be selected to represent all size-classes. In the following section, we examine the impact of the different settling velocities and selections of representative size-classes on predictions of suspended sediment concentrations.

5.6 Model Application to LSTF Experiments

To examine the predictive skills of the present sediment transport model, we apply the model to the LSTF experiments reported by Wang et al. (2002). In the LSTF experiments, vertical distributions of the sediment concentrations were measured at seven cross-shore locations along cross-shore transects at various shore-parallel (y) locations. These seven cross-shore locations correspond to one of nine cross-shore stations at which current velocity profiles were also measured. In order to indicate the cross-shore locations of these nine stations, Figures 5-1 and 5-2 show the same longshore mean current velocity profiles as Figure 4-25 and 4-26 for Test 1 (spilling

breakers) and Test 3 (plunging breakers), respectively. In the figures, stations are numbered from 1 to 9 and profiles of mean concentration of suspended sediment were measured at stations from 2 through 8.

5.6.1 Sediment Characteristics

Figure 5-3 shows the cumulative distribution of the sieved grain sizes of the sampled bottom sediments used in the LSTF experiment. As seen in the figure, most sand diameters are within the range of $0.07\text{mm} < D < 0.3\text{mm}$. The median sieve diameter of the sampled sands is $D_{50} = 0.15(\text{mm})$. In the present model, as discussed in Section 4.6.3, we apply the equivalent nominal median diameter, $D_{n50} \simeq D_{50}/0.9 = 0.167(\text{mm})$ to represent the sand characteristics. As a complete application of the model, we first account for all twenty six diameter classes to evaluate the suspended sediment concentrations. To simplify the computation we alternatively select several diameter classes out of all twenty six classes to represent the characteristics of the bottom sediments. Figure 5-4 shows the weight fractions of each class and the open circles in the figure denote the six classes with highest weight fractions which were used to represent the bottom sediment characteristics. The sediments classified in these six classes accounts for 87% of the entire sediment sample and therefore we can expect these six classes to reasonably represent the characteristics of the bottom sediments. Table 5.1 summarizes the sediment characteristics of the twelve finest diameter classes. In the complete model, we also account for the rest of fourteen classes but the total weight fraction of these coarser diameter classes are about 0.36% and their contributions to the sediment transport should be negligibly small. In Table 5.1, settling velocities for each sand diameter were determined from Jimenez and Madsen (2003) model (5.18) and the high-lighted diameter classes, D_4 to D_9 , are the dominant six classes shown as open circles in Figure 5-4.

In the LSTF experiments, the local longshore sediment transport rates (LSST) were obtained at 20 cross-shore locations from the volumes collected in each of twenty sand-traps, which are installed adjacent to each other at the downstream end of the straight beach (Wang et al., 2002). We can also obtain the “measured” suspended

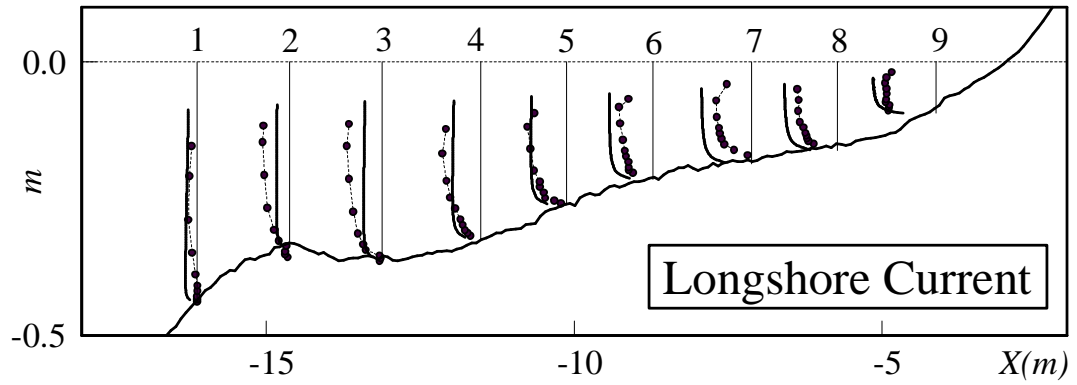


Figure 5-1: Cross-shore locations of measured longshore current velocity profiles; LSTF experiments by Wang et al. (2002) (Test 1)

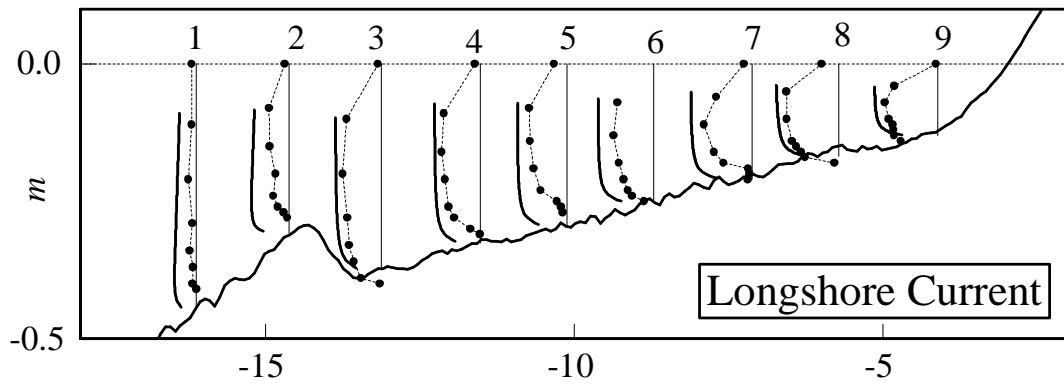


Figure 5-2: Cross-shore locations of measured longshore current velocity profiles; LSTF experiments by Wang et al. (2002) (Test 3)

Table 5.1: Characteristics of bottom sediments in each grain size class

	Sieve Size (mm)		D_s (mm)	D_n (mm)	w_f (cm/s)	f_b (%)
	min	max				
D_1	0.053	0.063	0.058	0.064	0.30	0.14
D_2	0.063	0.074	0.069	0.076	0.41	1.11
D_3	0.074	0.088	0.081	0.090	0.55	3.69
D_4	0.088	0.105	0.097	0.107	0.75	9.39
D_5	0.105	0.125	0.115	0.128	1.01	18.55
D_6	0.125	0.149	0.137	0.152	1.35	16.86
D_7	0.149	0.177	0.163	0.181	1.78	19.94
D_8	0.177	0.210	0.194	0.215	2.29	12.35
D_9	0.210	0.250	0.230	0.256	2.92	9.83
D_{10}	0.250	0.297	0.274	0.304	3.66	5.56
D_{11}	0.297	0.354	0.326	0.362	4.51	1.84
D_{12}	0.354	0.420	0.387	0.430	5.47	0.40
	0.420	4.757				0.36

sediment transport rates at Stations 2 to 8, shown in Figures 5-1 and 5-2, by vertically integrating the products of measured sediment concentrations and current velocities. From these data, one can indirectly obtain “measured” longshore bedload sediment transport rates by subtracting the measured suspended sediment transport rate from the LSST. Note however that these estimations of bedload and suspended load transport rates are very rough because the vertical resolutions of the measured sediment concentrations and current velocities are not high enough. It should also be pointed out that the measured suspended sediment concentration itself may contain certain errors because the measured concentrations were obtained from optical backscatter sensors (OBS) with OBS response calibrated for a single diameter grain size although the strong size-dependency of the OBS response is suggested (e.g., Ludwig and Hanes, 1990). Following the discussions in Section 4.6.3, we assume that the bed is reasonably represented by a sheet flow bed both for Test 1 and Test 3.

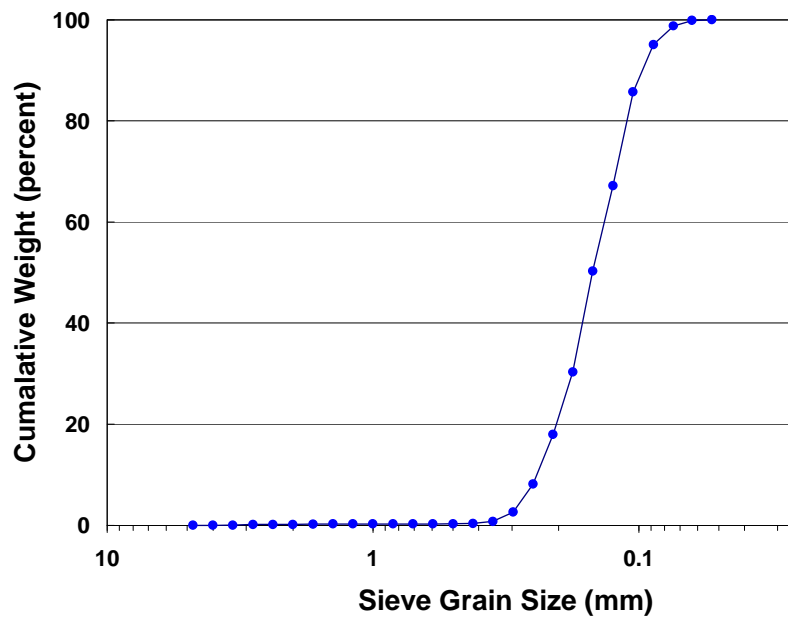


Figure 5-3: Cumulative distributions of sampled sand used in LSTF experiment (Wang et al., 2002)

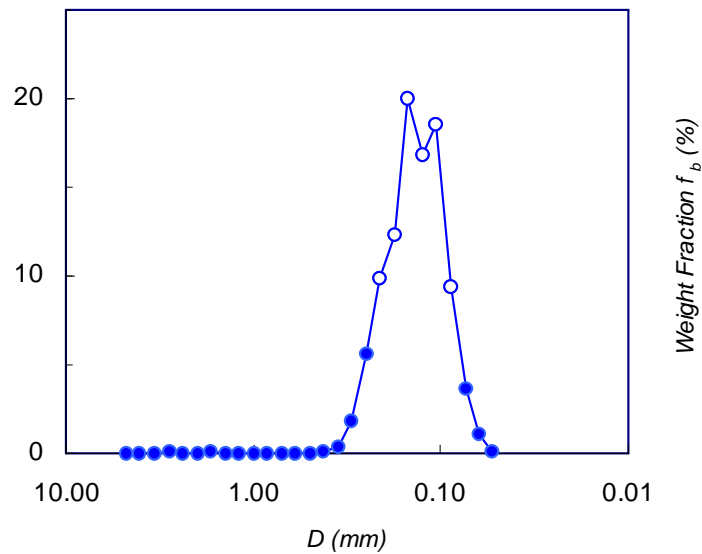


Figure 5-4: Weight fractions of each diameter class. Open circles are the dominant six classes applied to represent the sediment characteristics.

Table 5.2: Predicted hydrodynamic characteristics at Station 4 for Test 1 and Test 3.

	H_{rms} (m)	T (s)	$U_{b,rms}$ (m/s)	τ_{cbs} (N/m ²)	$\tau_{cr,0}$ (N/m ²)	$T_{c'}/T$	T_c/T	u_{c*}/U_{b*}	$\tan \beta$
Test 1	0.14	1.5	0.62	0.15	0.17	0.45	0.49	0.58	0.033
Test 3	0.14	3.0	0.71	0.21	0.17	0.28	0.32	0.72	0.024

5.6.2 Bedload Sediment Transport

Instantaneous bedload transport

In order to investigate the characteristics of the instantaneous bedload sediment transport rates, we first compare the predicted time-varying bedload sediment rates for Test 1 and Test 3 at Station 4 shown in Figures 5-1 and 5-2, respectively. Table 5.2 summarizes the predicted hydrodynamic characteristics at Station 4. At Station 4, the still water depth ($h_0 \simeq 32\text{cm}$) and the predicted wave heights ($H_{rms} \simeq 14\text{cm}$) are about the same for both Test 1 and Test 3. However, Test 1 has a shorter wave period than Test 3 and therefore the relative water depth, h/L_0 , for Test 1 is larger than for Test 3. Thus, as discussed in Section 2.1.3, wave non-linearity effects are weaker in Test 1 than in Test 3 and the predicted skewness parameter of the near-bottom wave orbital velocity, u_{c*}/U_{b*} , becomes smaller in Test 1 than in Test 3. As discussed in Section 5.2.1, we examine the wave non-linearity effects by comparing the bedload sediment characteristics when the bottom wave shear stresses are determined by: (A) linear wave assumption (5.7); (B) non-linear wave with time-independent turbulent eddy viscosity (5.8); and (C) non-linear wave with time-varying turbulent eddy viscosity (5.9).

(A) Linear Sinusoidal Velocity Profile Figures 5-5 (Test 1) and 5-6 (Test 3) show the predictions of (a) time varying sinusoidal near-bottom wave orbital velocity, $u_{bw}(t) = u_{bm} \cos(\omega t)$, (b) corresponding absolute value of the sediment transport shear stress, $|\tau_{bs}(t)|$ with wave shear stress determined from (5.7), and (c) and (d) bedload sediment transport rates in the cross-shore (x) and the shore-parallel (y) directions, $q_{SBx}(t)$ and $q_{SB y}(t)$, respectively. All the variables shown in the figures

are those predicted for Station 4. In Figures (a) and (c), positive values are in the shore-ward direction. As seen in Figures 5-5 and 5-6, all the profiles are symmetrical in t/T . However, the peak of $|\tau_{bs}|$ at $t/T = 0$ is larger than the other peak at $t/T = 0.5$ because the sea-ward acting mean current shear stress, τ_{cbx} , increases the total shear stress when the wave shear stress, $\vec{\tau}_{ws}(t)$, is acting in the sea-ward direction while τ_{cbx} decreases the total shear stress when it counteracts $\vec{\tau}_{ws}(t)$ (see Figures 5-5 and 5-6 (b)).

In (b), the dashed straight line indicates the critical shear stress on the non-sloping bed, $\tau_{cr,0}$, and the full straight line denotes the mean current sediment transport shear stress, $|\vec{\tau}_{cbx}| = \sqrt{\tau_{cbx}^2 + \tau_{cbx}^2}$. In Test 1, as seen in Table 5.2 and Figure 5-5 (b), $|\vec{\tau}_{cbx}|$ is slightly smaller than $\tau_{cr,0}$ and the predicted total sediment transport shear stress, $|\tau_{bs}|$, falls below $\tau_{cr,0}$ in the ranges $0.25 < t/T < 0.28$ and $0.73 < t/T < 0.75$ when the wave shear stress is near zero. When $|\tau_{bs}| < \tau_{cr,0}$, the bedload sediment transport components in x and y directions become zero as seen in Figures 5-5 (c) and (d). For Test 3, in contrast to Test 1, $|\vec{\tau}_{cbx}|$ is always larger than $\tau_{cr,0}$ and the predicted $|\tau_{bs}|$ does not fall below $\tau_{cr,0}$ (see Figure 5-6 (b)).

In (c) and (d) of Figures 5-5 and 5-6, the full line denotes the prediction by the complete model (5.1) and the dashed line is the predictions when the bottom slope effect is neglected, i.e. $\beta_0 = 0$ is substituted in (5.1). The full straight lines in these figures are the net bedload sediment transport rates. Although the bottom slope effect is relatively small, as seen in Figure 5-5 (c), the bottom slope ($\tan \beta_0 = -\partial h_0 / \partial x \simeq 0.033$ at Station 4 in Test 1) decreases the shore-ward sediment transport near the crests of the near-bottom wave orbital velocity ($0.4 < t/T < 0.6$, $t/T < 0.1$, and $0.9 < t/T$). The bottom slope effect is hardly seen when the wave shear stress is small ($0.1 < t/T < 0.4$ and $0.6 < t/T < 0.9$). In these intervals, the mean current shear stress in the shore-parallel (y) direction dominates and the time-varying “transport bottom slope,” $\tan \beta'$ in (5.2) becomes negligibly small. The bottom slope effect on net sediment transport rate predictions will be shown later. Although the bottom slope in the shore-parallel (y) direction is zero under the long, straight beach assumption, the cross-shore bottom slope also decreases $q_{SB,y}(t)$ near the crest of the

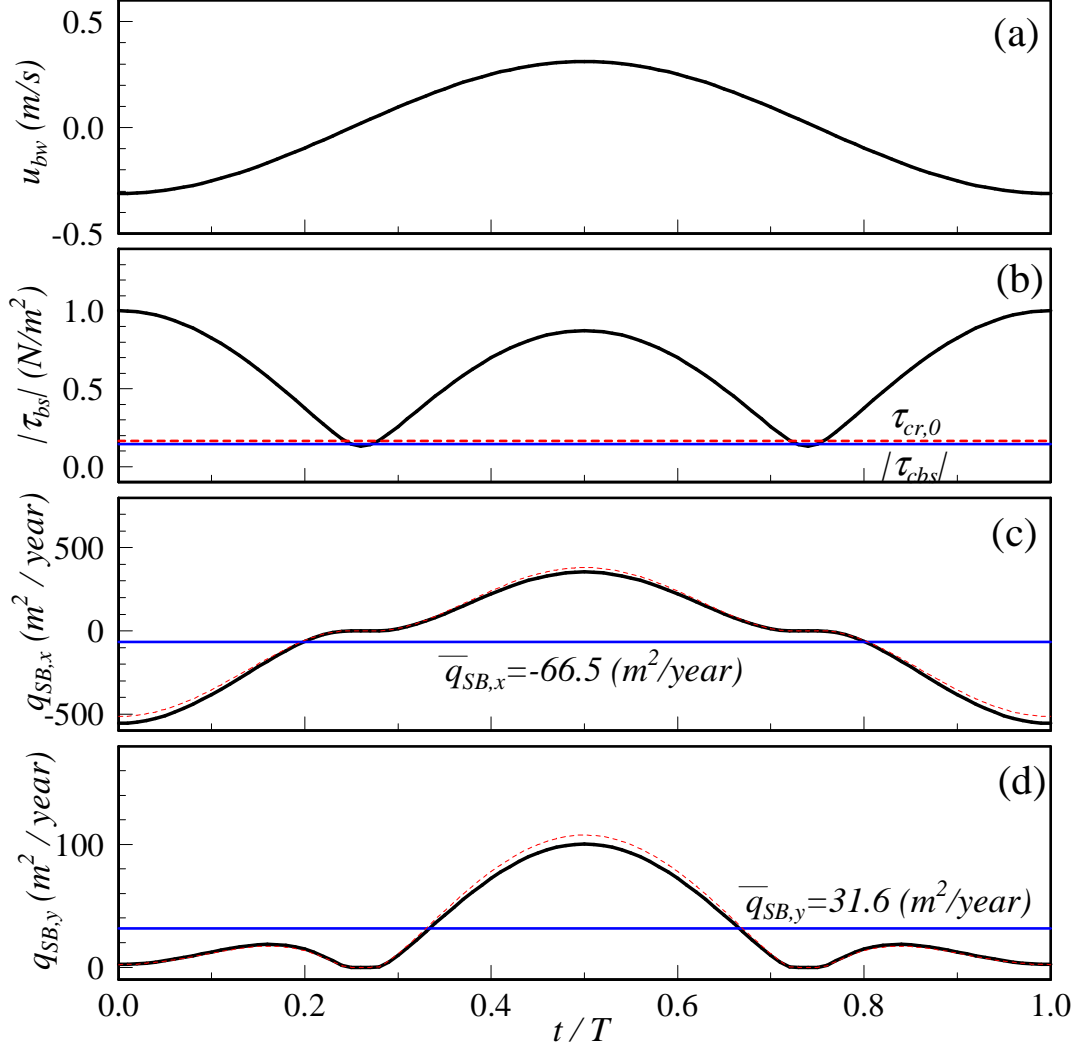


Figure 5-5: Time-varying profiles of (a) linear sinusoidal near-bottom wave orbital velocity and corresponding profiles of (b) sediment transport shear stress, (c) cross-shore (x) and (d) longshore (y) bedload sediment transport rates at Station 4 in Test 1 of LSTF experiments. Full and dashed lines in (c) and (d) are when the bottom slope effect is accounted for and neglected, respectively. (case (A), $\tau_{ws}(t) \sim u_{bm} \cos(\omega t - \pi)$)

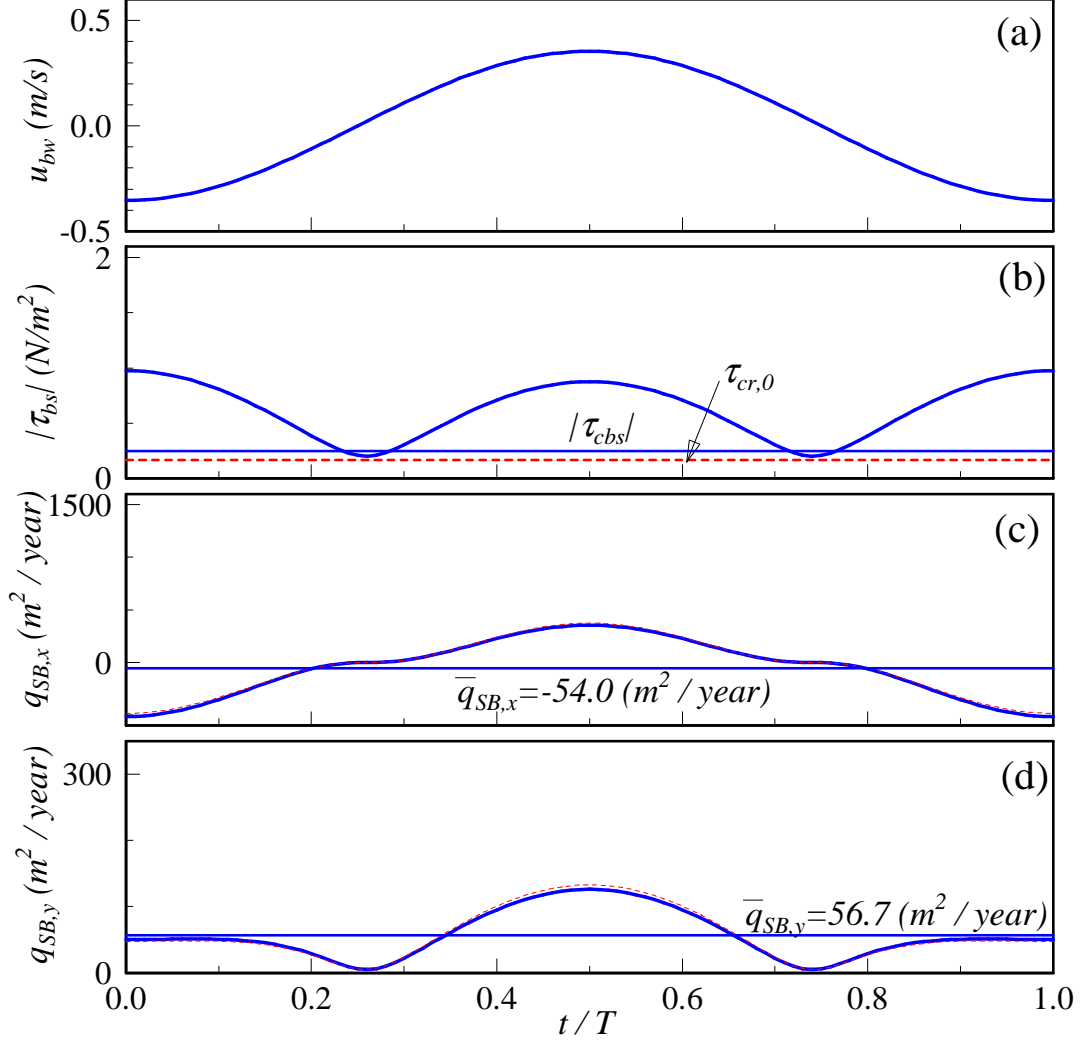


Figure 5-6: Time-varying profiles of (a) linear sinusoidal near-bottom wave orbital velocity and corresponding profiles of (b) sediment transport shear stress, (c) cross-shore (x) and (d) longshore (y) bedload sediment transport rates at Station 4 in Test 3 of LSTF experiments. Full and dashed lines in (c) and (d) are when the bottom slope effect is accounted for and neglected, respectively. (case (A), $\tau_{ws}(t) \sim u_{bm} \cos(\omega t - \pi)$)

shore-ward $u_{wb}(t)$, $0.4 < t/T < 0.6$, in Figure 5-5 (d). This feature is because the “intensity” of the bedload sediment transport, $q(t)$, defined in (5.1) decreases when the shear stress acts in the up-slope direction.

It is also interesting to note that the longshore bedload transport, $q_{SB,y}(t)$, does not yield a minimum value as the near-bottom orbital velocity approaches its minimum, $t/T \rightarrow 1$ whereas the cross-shore bedload transport, $q_{SB,x}(t)$, becomes minimum at $t/T = 1$ (see Figures 5-5 and 5-6 (c) and (d)). In Test 3, $q_{SB,y}(t)$ yields the local maximum at $t/T = 1$ (Figure 5-6 (d)). In the vicinity of $t/T = 1$, the wave shear stress acts opposite to the wave-propagation direction and therefore the wave shear stress in the longshore (y) direction, τ_{wsy} , counteracts the current shear stress in the longshore (y) direction, τ_{cbsy} , and yields a minimum longshore component of the total shear stress, $\tau_{bsy}(t)$. However, because the wave component in the y -direction is very small, the mean current shear stress τ_{cbsy} dominates $\tau_{wsy}(t)$ and the total shear stress, $\tau_{sby}(t) = \tau_{cbsy} + \tau_{wsy}(t)$, still acts in the longshore current direction ($y > 0$). Because $|\tau_{bs}|$ is maximum at $t/T = 1$, the “intensity” of the bedload sediment transport, $q(t)$, in (5.1) is also maximum at $t/T = 1$. Thus the increase of $q(t)$ dominates the decrease of $\tau_{sby}(t)$ near $t/T = 1$ and the product of the two components, $q_{SB,y}$, yield relatively large bedload sediment transport in the longshore current direction.

(B) Non-linear Wave Shear Stress Determined by (5.8) Figures 5-7 (Test 1) and 5-8 (Test 3) show the same comparisons as Figures 5-5 and 5-6 but the wave non-linearity is accounted for by determining the wave shear stress from (5.8). Figures 5-7 and 5-8 (a) show the time varying non-linear near-bottom wave orbital velocity, $u_{bw}(t)$. Because the wave non-linearity is relatively weak in Test 1, the near-bottom wave orbital velocity profile is nearly sinusoidal in Test 1 and Figure 5-7 shows near-identical profiles to Figure 5-5 while the velocity profile in Test 3 is skewed and asymmetrical (see Figure 5-8 (a)).

Comparing Figures 5-6 and 5-8 (c), the non-linear wave velocity profile significantly increases the predictions of maximum and minimum cross-shore bedload sediment transport rates ($q_{SB,x,\max}, q_{SB,x,\min}$) from (352 (m²/year), -512 (m²/year)) to

(736 (m²/year), -175 (m²/year)) and also increases the net cross-shore sediment transport rate, $\bar{q}_{SB,x}$, from -54 (m²/year) to 28 (m²/year). In the shore-parallel (y) direction (Figures 5-6 and 5-8 (d)), the wave non-linearity raises $q_{SB,y,\max}$ from 203 (m²/year) to 126 (m²/year). However, the predicted net bedload sediment transport rates, $\bar{q}_{SB,y}$, are nearly identical in both non-linear and linear wave orbital velocity profiles. This feature is more clearly observed in the following paragraph, in which we compare the net bedload sediment transport rates.

(C) Non-linear Wave Shear Stress Determined by (5.9) Similarly, Figures 5-9 and 5-10 show the same predictions as Figures 5-5 and 5-6 but the wave shear stress, τ_{ws} , was determined by (5.9). Crests of the wave shear stresses for (C) (Figures 5-9 and 5-10 (b)) become steeper than those for (B) (Figures 5-7 and 5-8 (b)) and the peaks of $q_{SB,x}$ and $q_{SB,y}$ in (C) are much larger than those in (B). As a result, the net cross-shore bedload transport, $\bar{q}_{SB,x}$, significantly increases from (B) to (C). In Test 3, for example, $\bar{q}_{SB,x}$ increases from 28(m²/year) to 135(m²/year). In the shore-parallel (y) direction, however, the net longshore bedload transport, $\bar{q}_{SB,y}$, are nearly identical in (B) and (C). In Test 3, $\bar{q}_{SB,y}$ slightly decreases from (B) to (C) because $q_{SB,y}$ in (C) is smaller than the one in (B) around the the wave crest ($t/T < 0.2$ and $0.4 < t/T$) and this decrease of $q_{SB,y}$ dominates the increase of $q_{SB,y}$ near the peak ($t/T \sim 0.3$) when integrating $q_{SB,y}$ to obtain the net longshore bedload transport, $\bar{q}_{SB,y}$. Comparisons of the cross-shore distributions of net bedload transport rates among cases (A), (B) and (C) are shown in the following section.

Net bedload transport

Figures 5-11 and 5-12 compare the predicted net bedload sediment transport rate components in the cross-shore (x) and the shore-parallel (y) directions for Test 1 and Test 3, respectively. The four lines shown in Figures 5-11 and 5-12 are the predictions when: (A) (5.7) was applied to determine wave shear stress for sinusoidal velocity profile (thin dashed line), (B) wave non-linearity was counted by (5.8) (thin full line), (C) wave non-linearity is accounted for by (5.9) (heavy full line), and (D) same as

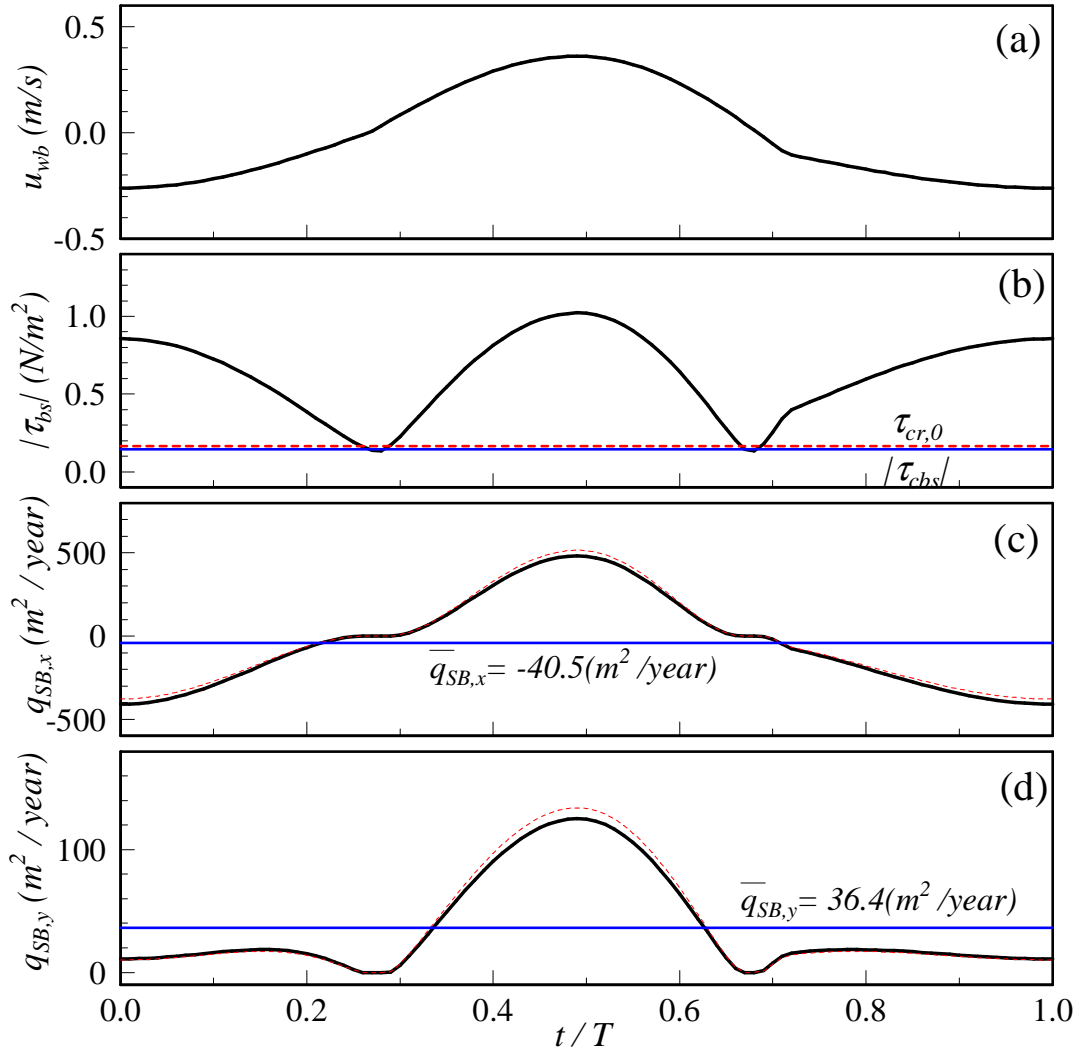


Figure 5-7: Time-varying profiles of (a) non-linear near-bottom wave orbital velocity and corresponding profiles of (b) sediment transport shear stress, (c) cross-shore (x) and (d) longshore (y) bedload sediment transport rates at Station 4 in Test 1 of LSTF experiments. Full and dashed lines in (c) and (d) are when the bottom slope effect is accounted for and neglected, respectively. (case (B), $\tau_{ws}(t) \sim u_{bw}(t)$)

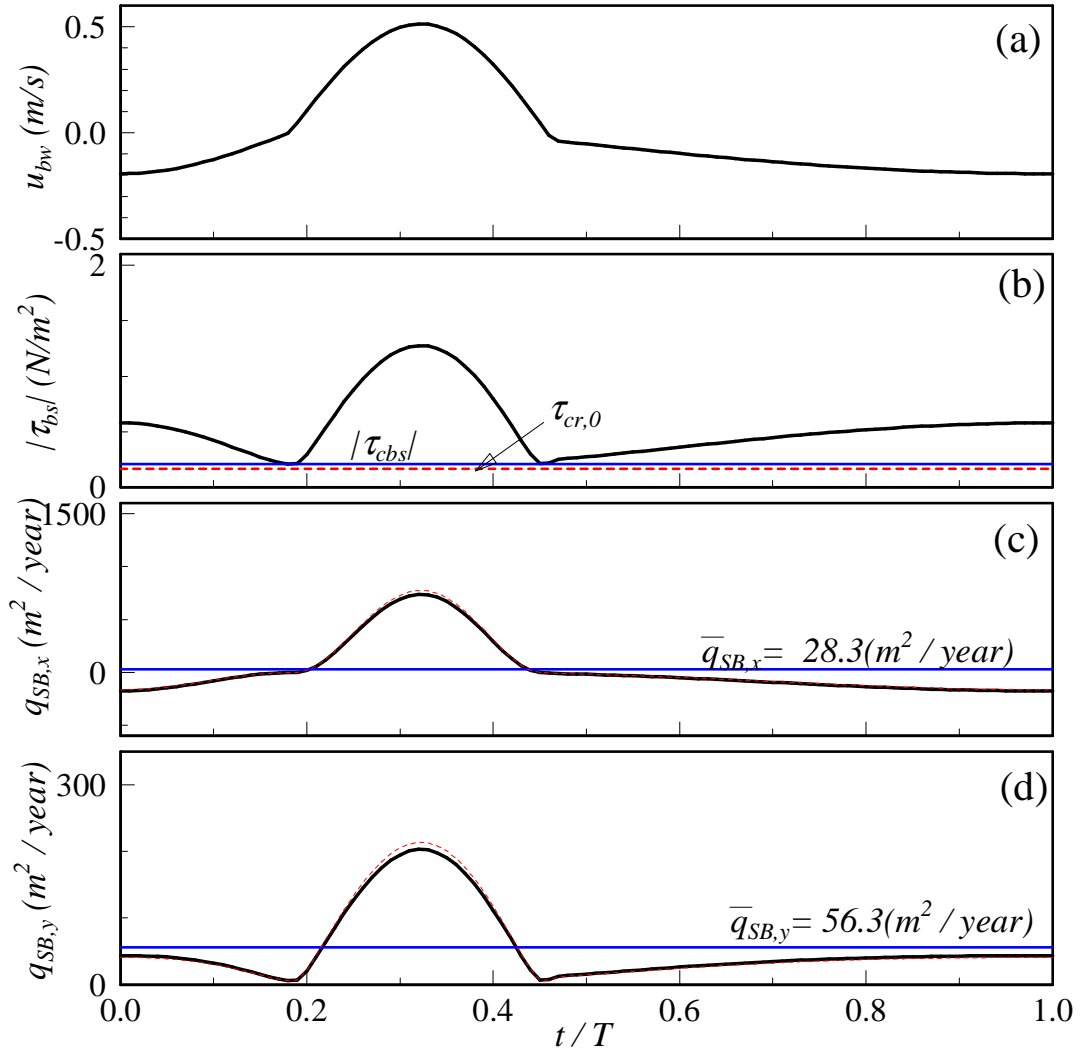


Figure 5-8: Time-varying profiles of (a) non-linear near-bottom wave orbital velocity and corresponding profiles of (b) sediment transport shear stress, (c) cross-shore (x) and (d) longshore (y) bedload sediment transport rates at Station 4 in Test 3 of LSTF experiments. Full and dashed lines in (c) and (d) are when the bottom slope effect is accounted for and neglected, respectively. (case (B), $\tau_{ws}(t) \sim u_{bw}(t)$)

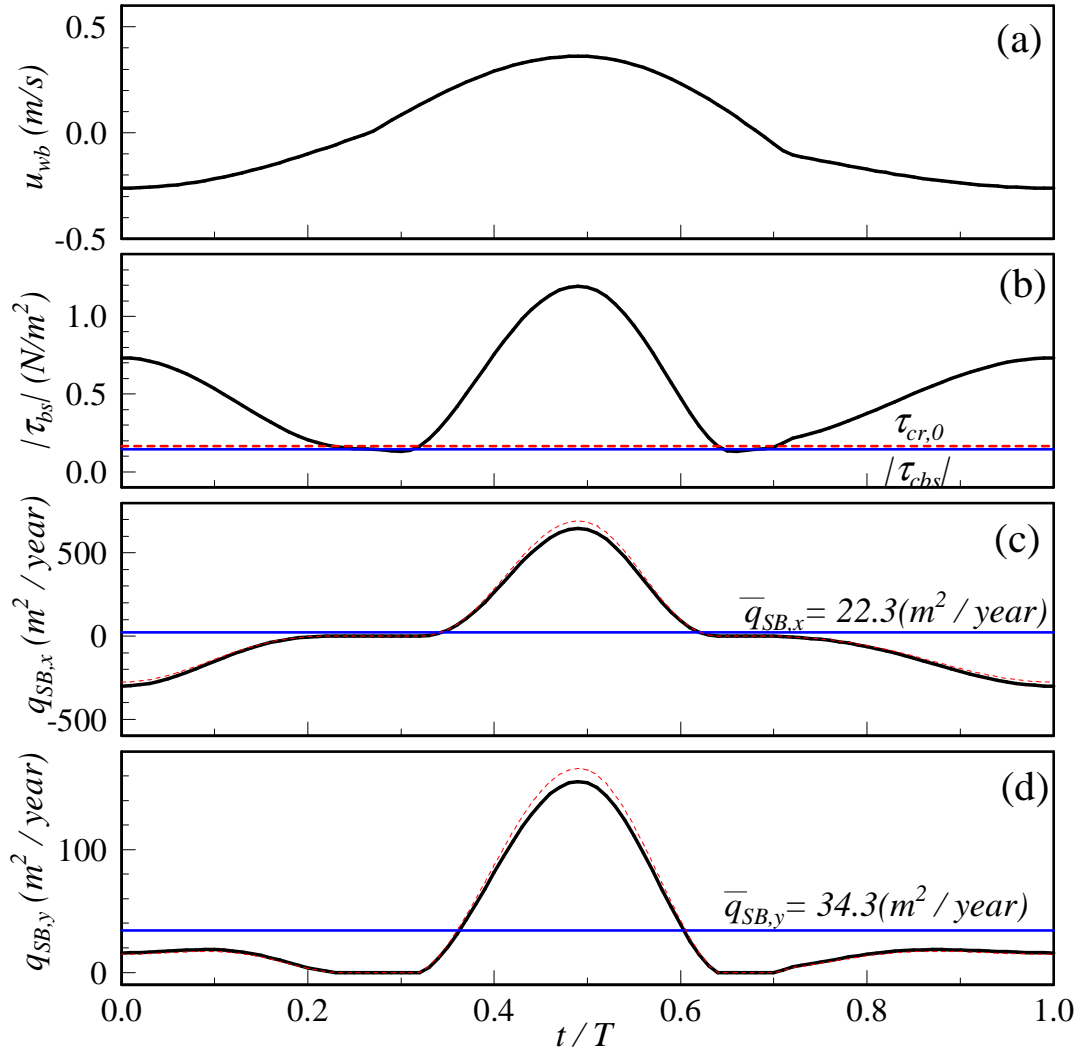


Figure 5-9: Time-varying profiles of (a) non-linear near-bottom wave orbital velocity and corresponding profiles of (b) sediment transport shear stress, (c) cross-shore (x) and (d) longshore (y) bedload sediment transport rates at Station 4 in Test 1 of LSTF experiments. Full and dashed lines in (c) and (d) are when the bottom slope effect is accounted for and neglected, respectively. (case (C), $\tau_{ws}(t) \sim |u_{bw}(t)| u_{bw}(t)$)

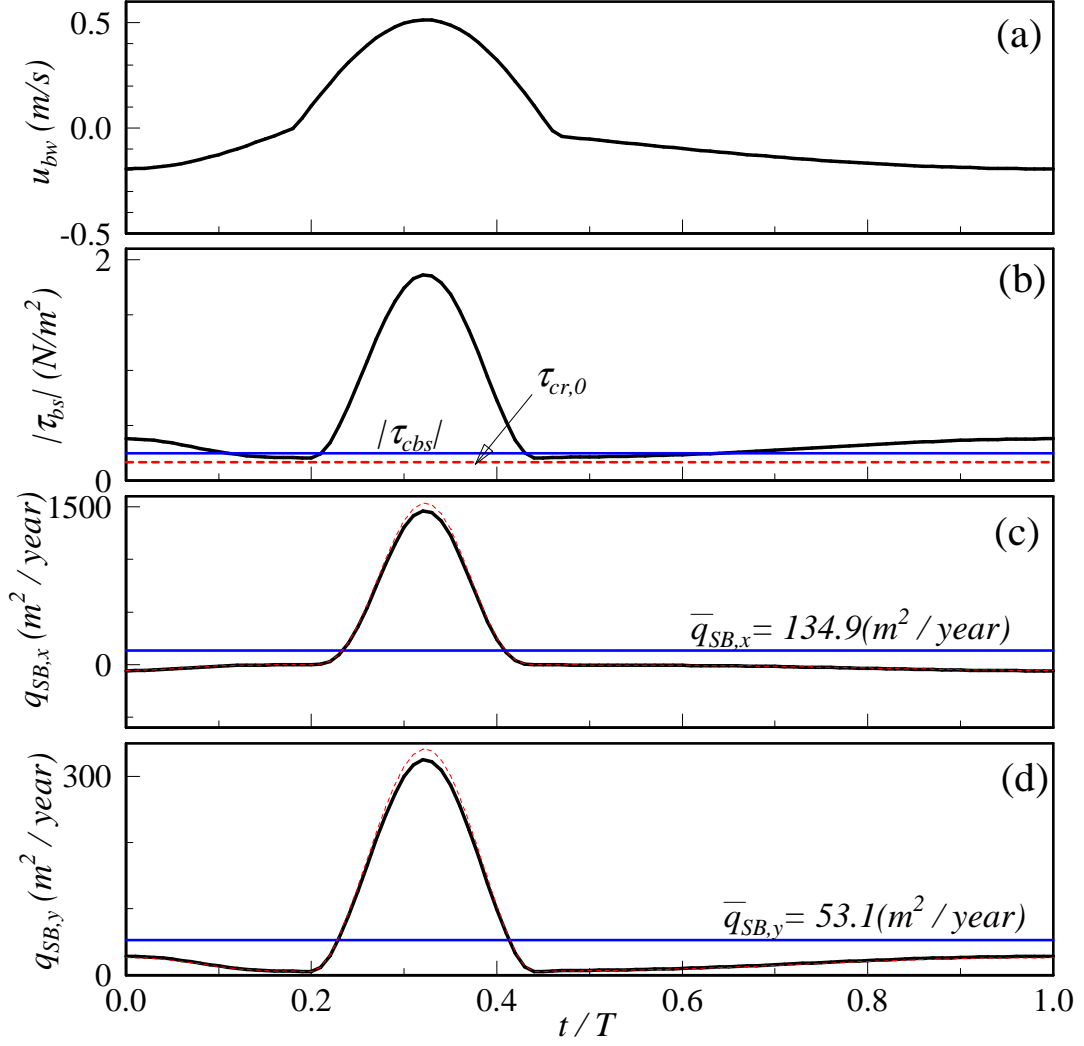


Figure 5-10: Time-varying profiles of (a) non-linear near-bottom wave orbital velocity and corresponding profiles of (b) sediment transport shear stress, (c) cross-shore (x) and (d) longshore (y) bedload sediment transport rates at Station 4 in Test 3 of LSTF experiments. Full and dashed lines in (c) and (d) are when the bottom slope effect is accounted for and neglected, respectively. (case (C), $\tau_{ws}(t) \sim |u_{bw}(t)| u_{bw}(t)$)

(C) but the bottom slope effect was neglected. In the comparisons of the net long-shore bedload transport rates, full circles are the “measured” bedload transport rate obtained by subtracting suspended load transport rates from the total LSST. Open circles denote the cross-shore locations where “measured” suspended load transport rates exceeded the measured LSST and yielded unrealistic negative “measured” bedload transport rates.

In the cross-shore (x) direction, both bottom slope and wave non-linearity significantly affect the predictions of net bedload sediment transport rate, $\bar{q}_{SB,x}$. In the cross-shore range of $-18 < X(m) < -15$ in Figure 5-11, for example, the cross-shore net bedload sediment transport rate, $\bar{q}_{SB,x}$, decreases by about $30(\text{m}^2/\text{year})$ from (D) (heavy dashed line) to (C) (heavy full line) due to the bottom slope effect. Because the bottom slope on the sea-ward side of the bar crest ($\tan \beta_0 \simeq 0.15$ in $-18 < X(m) < -15$) is larger than the bottom slope inside the surf zone ($\tan \beta_0 \simeq 0.03$), the decrease of $\bar{q}_{SB,x}$ due to the bottom slope is more pronounced in this area ($-18 < X(m) < -15$). Between the bar crest and trough in Test 3 ($-13.3 < X(m) < -14.3$ in Figure 5-12), the water depth increases from the bar crest toward the bar trough and the resulting large negative bottom slope significantly increases $\bar{q}_{SB,x}$ from (D) to (C). Comparing predictions by (A) and (B) in Figures 5-11 and 5-12, the non-linear wave profile also significantly increases the shore-ward $\bar{q}_{SB,x}$. Because the wave-non-linearity is stronger in Test 3 than in Test 1, as discussed previously, the increase of the shore-ward $\bar{q}_{SB,x}$ is larger in Test 3 than in Test 1. Comparing (B) and (C), the definitions of wave shear stress due to the non-linear wave velocity, i.e. (5.8) and (5.9) significantly affect the predictions of net bedload transport rates in the cross-shore directions. Thus, it should be stressed that the quantitative evaluations of the non-linear wave effect on the shoreward bedload sediment transport rate still contains significant uncertainty. Because Madsen’s (1994) bottom boundary layer model is based on the linear wave assumption, for example, use of the friction factor obtained in this manner may not be appropriate for the non-linear near-bottom wave orbital velocity profiles.

In the shore-parallel (y) direction, in contrast to the cross-shore (x) direction, nei-

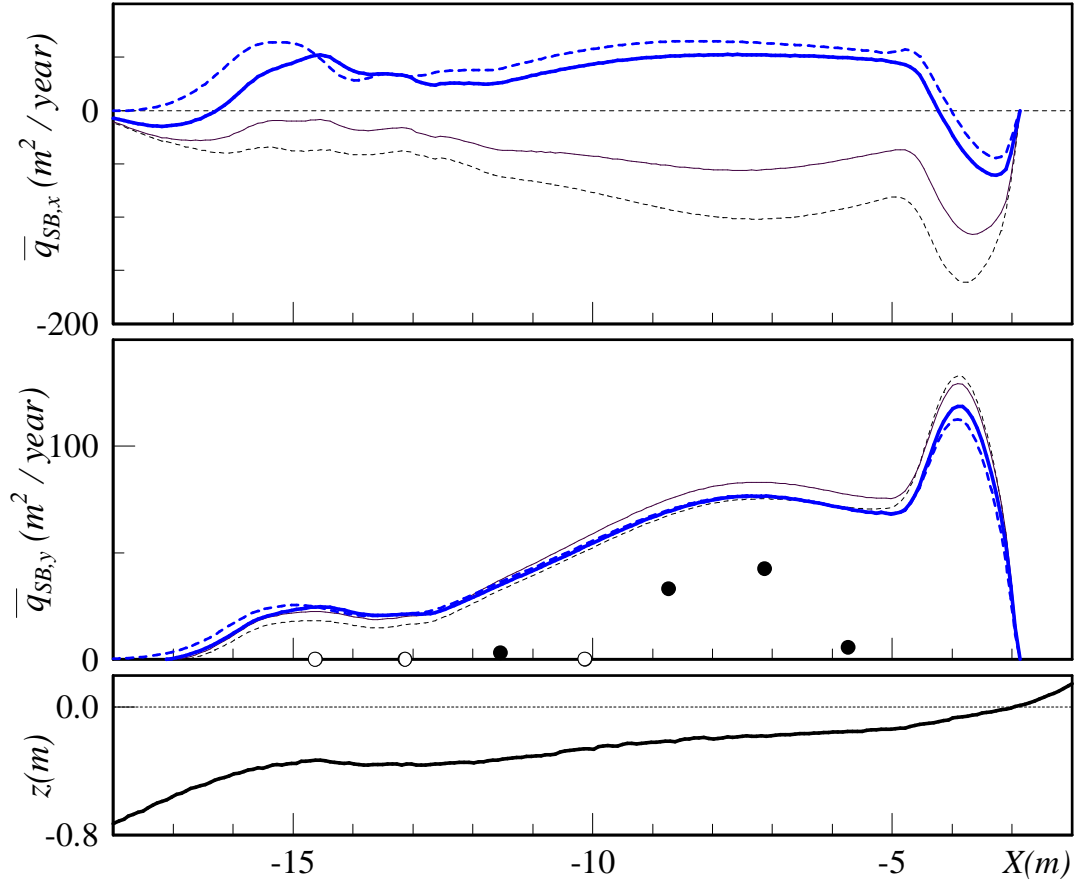


Figure 5-11: Cross-shore distributions of the net bedload sediment transport rates in the cross-shore (x) and the shore-parallel (y) directions (Test 1). Predictions are based on: (A) $\tau_{ws}(t) \sim u_{bm} \cos(\omega t)$ (thin dashed line); (B) $\tau_{ws}(t) \sim u_{bw}(t)$ (thin full line); (C) $\tau_{ws}(t) \sim |u_{bw}(t)| u_{bw}(t)$ (heavy full line); and (D) same as (C) without bottom slope effects (heavy dashed line). Full circles are the longshore bedload sediment transport rates obtained from the measurements and open circles denote the cross-shore locations where measured suspended sediment transport rates exceed the measured total LSST.

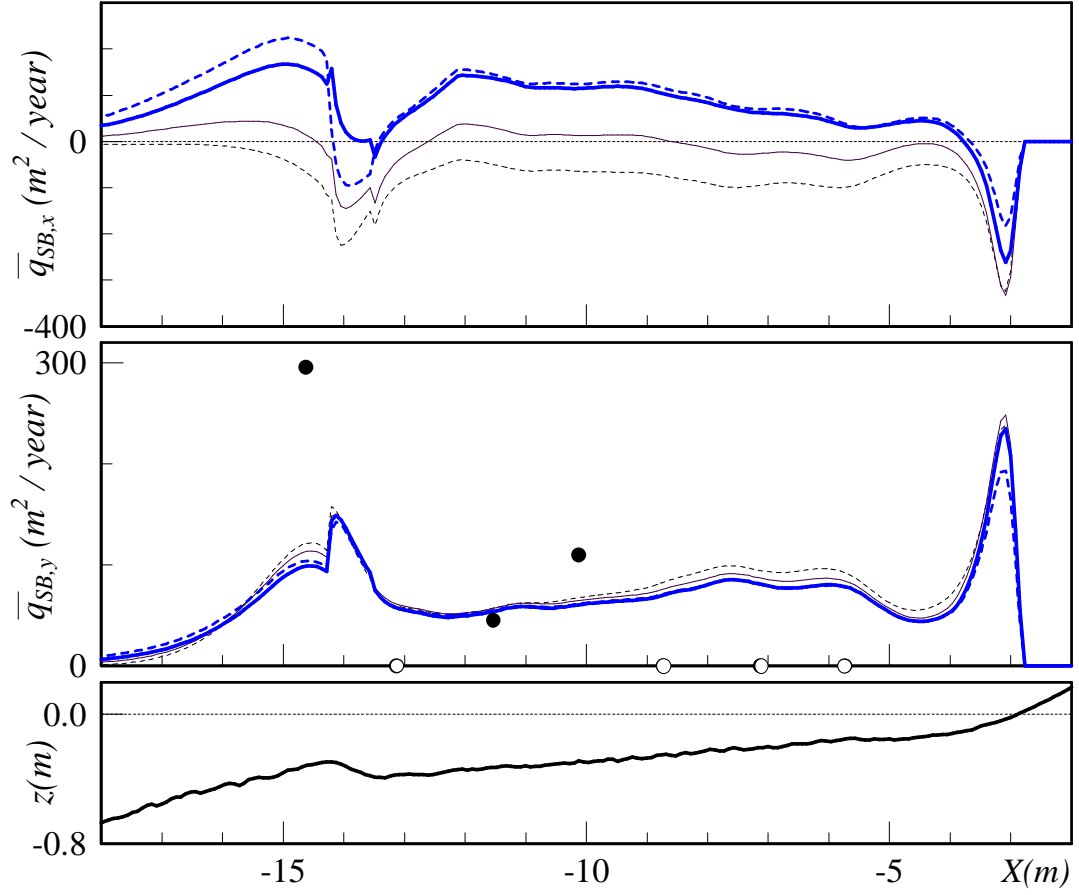


Figure 5-12: Cross-shore distributions of the net bedload sediment transport rates in the cross-shore (x) and the shore-parallel (y) directions (Test 3). Predictions are based on: (A) $\tau_{ws}(t) \sim u_{bm} \cos(\omega t)$ (thin dashed line); (B) $\tau_{ws}(t) \sim u_{bw}(t)$ (thin full line); (C) $\tau_{ws}(t) \sim |u_{bw}(t)| u_{bw}(t)$ (heavy full line); and (D) same as (C) without bottom slope effects (heavy dashed line). Full circles are the longshore bedload sediment transport rates obtained from the measurements and open circles denote the cross-shore locations where measured suspended sediment transport rates exceed the measured total LSST.

ther bottom slope nor wave non-linearity have a significant effect on the net longshore bedload sediment transport rate, $q_{SB,y}$. For instance, the difference among predictions of (A), (B), (C) and (D) are at most 20(m²/year) for Test 3 near the bar crest and this difference is a mere 15% of the net longshore bedload transport rate.

In comparisons of the longshore bedload sediment transport rates, full circles denote the “measured” bedload sediment transport rates, obtained by subtracting “measured” suspended sediment transport from the measured total LSST. Open circles are the cross-shore (x) locations where the “measured” suspended sediment transport rates exceed the total LSST and yield unrealistic negative bedload sediment transport rates. As seen in both Test 1 and Test 3 (Figures 5-11 and 5-12), three and four points out of seven measured stations yield negative bedload sediment transport rates. This feature indicates not only the uncertainty of the “measured” bedload sediment transport rates but also the relatively small contributions of the bedload sediment transport to the total LSST in these particular experimental cases.

5.6.3 Suspended Sediment Transport

Reference Concentration

Similar to Figures 5-5 to 5-10, Figures 5-13 and 5-14 show the linear sinusoidal near-bottom wave orbital velocity, corresponding sediment transport bottom shear stress, $|\vec{\tau}_{bs}(t)|$, determined from (5.7), and the reference concentration, $C_r(t)$, determined from (5.29) at Station 4 for Test 1 and Test 3, respectively. Because C_r is linearly related to $|\vec{\tau}_{bs}(t)|$ in (5.29), the predicted time-varying reference concentration is nearly identical to the sediment transport shear stress. Thin dashed curves in Figures 5-13 to 5-16 are the predicted reference concentrations when the bottom slope effect is neglected. As seen in the comparisons between the full and dashed lines, the effect of the bottom slope is negligibly small.

Figures 5-15 and 5-16, show the same comparisons as Figures 5-13 and 5-14 but when accounting for non-linear wave orbital velocity, $u_{bw}(t)$. In the Figure, the profiles with heavy dashed line are predictions when $\tau_{ws}(t)$ was determined from (5.8)

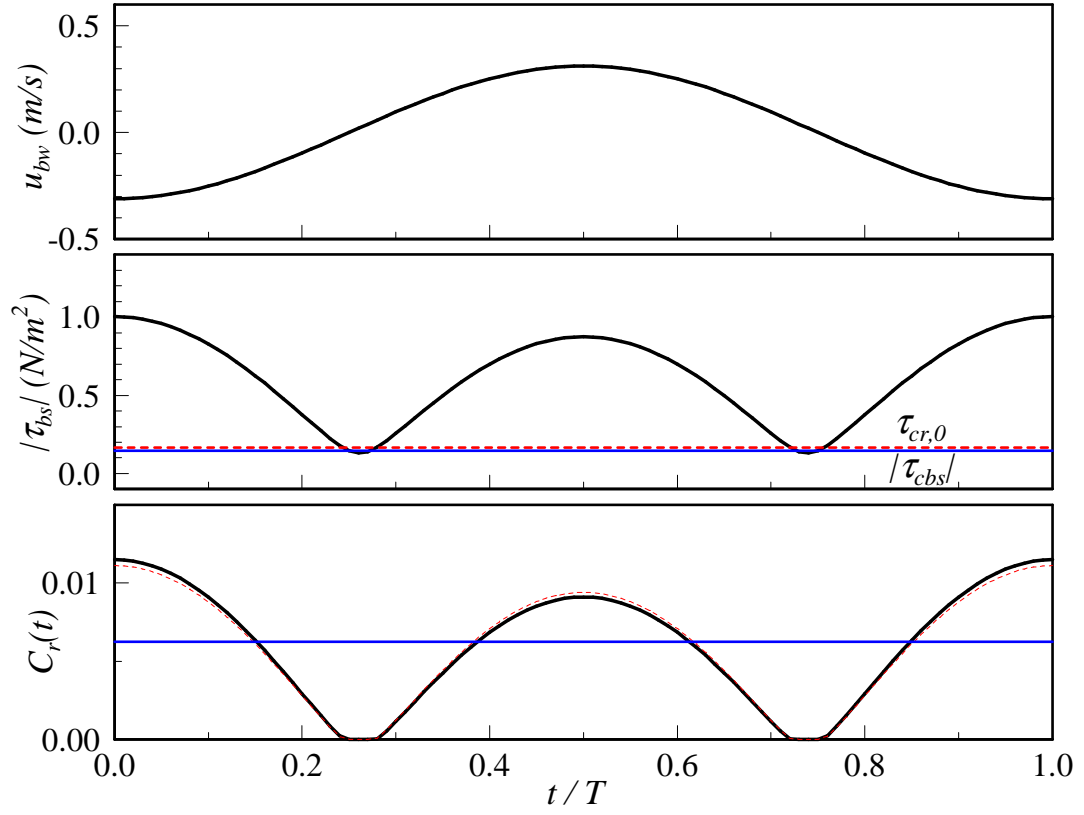


Figure 5-13: Time-varying profiles of linear sinusoidal near-bottom wave orbital velocity and corresponding profiles of sediment transport shear stress and reference concentrations at Station 4 in Test 1. Full and dashed lines in the reference concentration are when the bottom slope effect is accounted for and neglected, respectively.

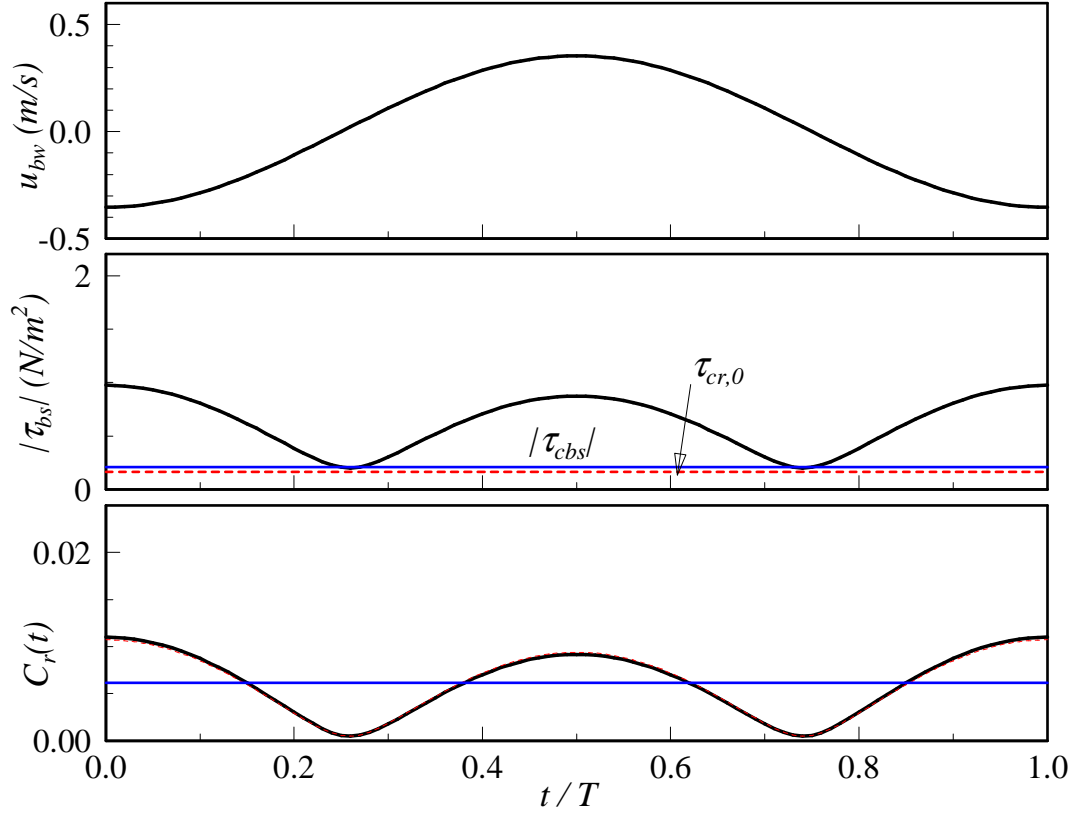


Figure 5-14: Time-varying profiles of linear sinusoidal near-bottom wave orbital velocity and corresponding profiles of sediment transport shear stress and reference concentrations at Station 4 in Test 3. Full and dashed lines in the reference concentration are when the bottom slope effect is accounted for and neglected, respectively.

(case B) and full line profiles are predictions when $\tau_{ws}(t)$ was determined from (5.9) (case C). Thin dashed curves are the same as case (C) but the bottom slope effects were neglected. Straight dashed and full lines in the comparisons of reference concentrations are the mean reference concentrations for (B) and (C), respectively. Similar to comparisons of the net longshore bedload transport rates, the mean reference concentrations in (C) (full line) tends to be smaller than those in (B) (dashed line) because, for example in Test 3 (Figure 5-16), the decrease of $C_r(t)$ from (B) to (C) near the wave trough ($t/T < 0.2$ and $0.4 < t/T$) dominates the increase of $C_r(t)$ from (B) to (C) near the wave crest ($0.2 < t/T < 0.4$).

Figures 5-17 and 5-18 show the cross-shore distributions of the mean reference concentration for Test 1 and Test 3, respectively. Similar to the comparisons in Figures 5-11 and 5-12, four lines denote the predictions when: (A) wave non-linearity was neglected (thin dashed line); (B) non-linearity was accounted for by (5.8) (thin full line); (C) wave non-linearity was counted by (5.9) (heavy full line); and (D) same as (C) but the bottom slope effects were neglected (heavy dashed line). Comparing (C) (heavy full line) and (D) (heavy dashed line), bottom slope effects on predictions of mean reference concentration are very small both for Test 1 and Test 3. The non-linear wave effect determined by (B) is also negligibly small for Test 1 and amounts to a difference between (A) (thin dashed line) and (B) (thin full line) in Test 3 of at most 20%. Non-linear wave effect determined by (C) tends to decrease the mean reference concentration by roughly 20% from the one in case (B). However, as will be seen in the following sections, these differences are relatively small compared to the error due to the selections of representative sediment diameters for mixed sand grains. In subsequent model applications, we show the predictions based on case (C) to compare with measurements. However, the difference of non-linear wave effects among cases (A), (B), and (C) will be quantitatively compared with the measured LSST and suspended sediment transport rates.

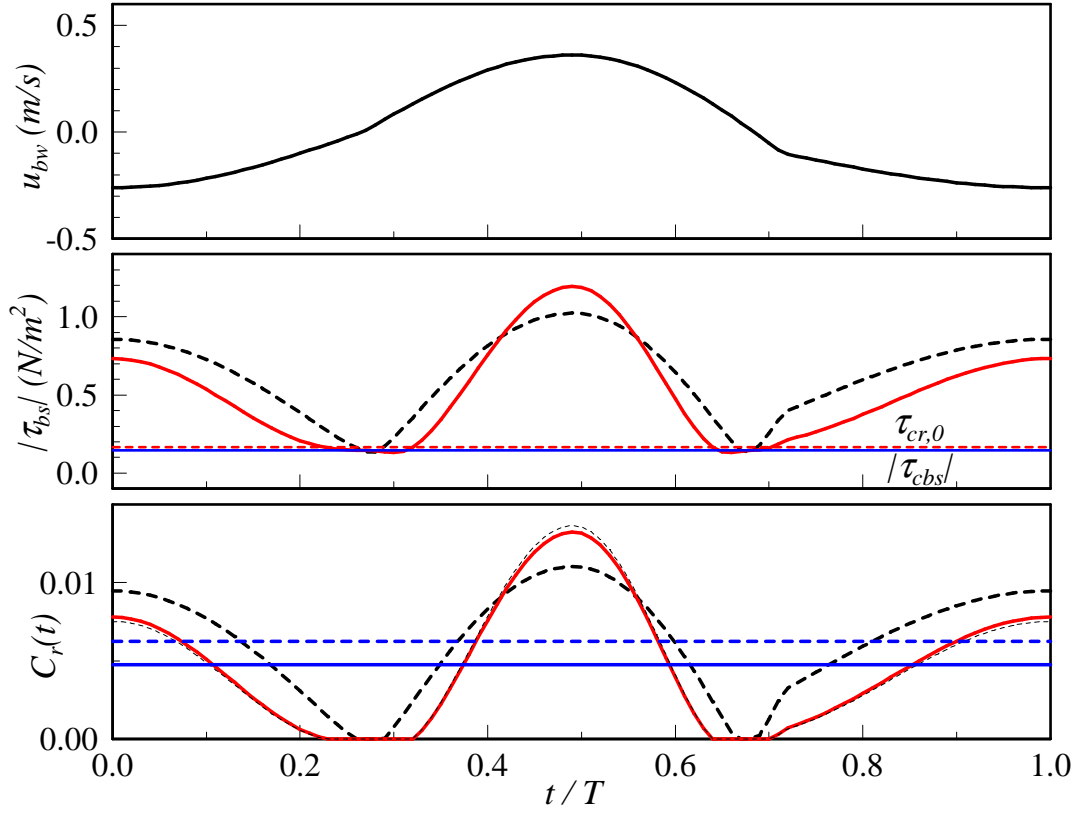


Figure 5-15: Time-varying profiles of non-linear near-bottom wave orbital velocity and corresponding profiles of sediment transport shear stress and reference concentrations at Station 4 in Test 1. Profiles are (B) (heavy dashed line), (C) (heavy full line), and (C) without bottom slope effects (thin dashed line). Straight dashed and full lines in the reference concentrations are the mean reference concentrations for (B) and (C), respectively.

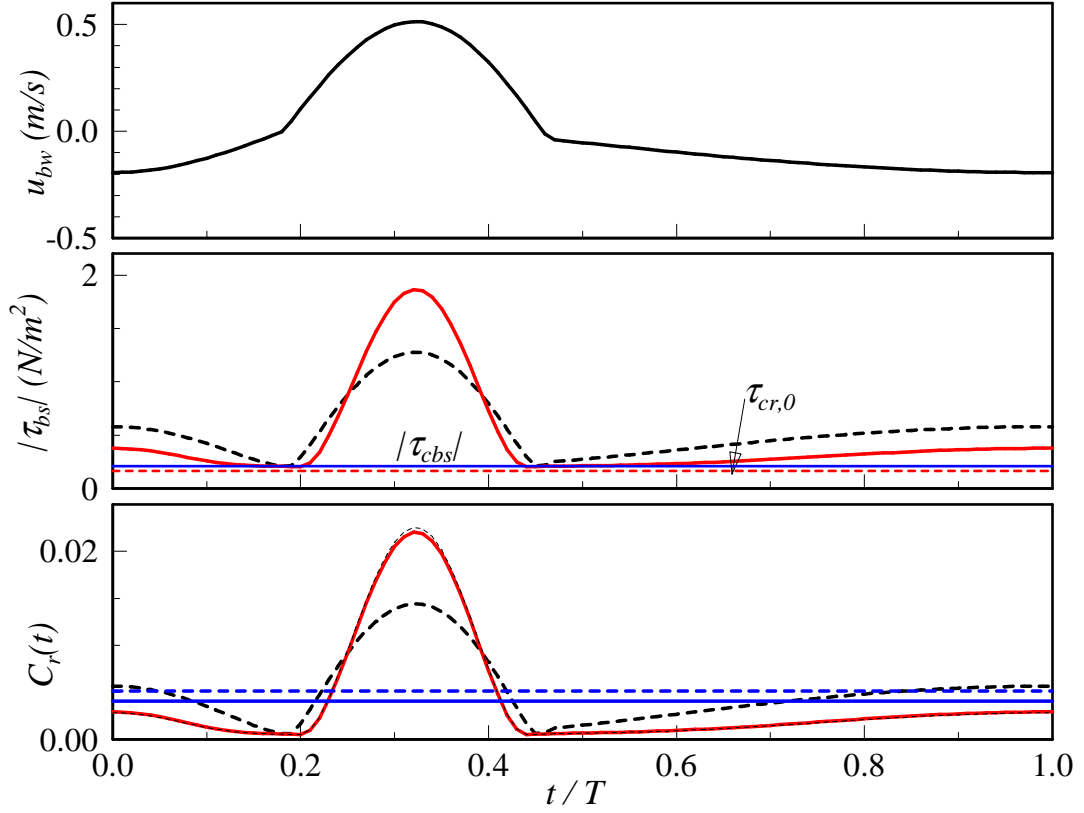


Figure 5-16: Time-varying profiles of non-linear near-bottom wave orbital velocity and corresponding profiles of sediment transport shear stress and reference concentrations at Station 4 in Test 3. Profiles are (B) (heavy dashed line), (C) (heavy full line), and (C) without bottom slope effects (thin dashed line). Straight dashed and full lines in the reference concentrations are the mean reference concentrations for (B) and (C), respectively.

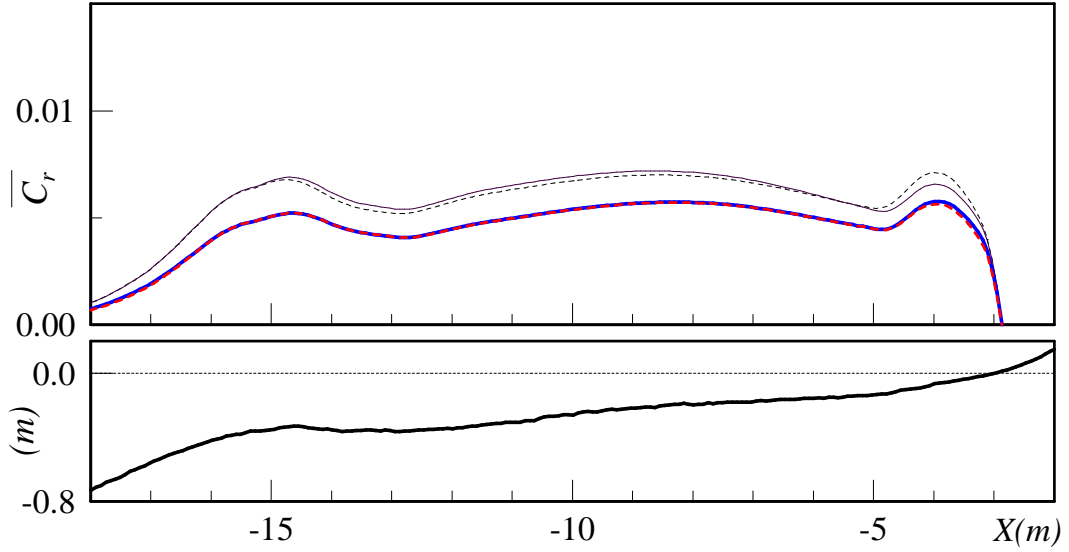


Figure 5-17: Cross-shore distributions of the mean reference concentration (Test 1). Predictions are based on: (A) $\tau_{ws}(t) \sim u_{bm} \cos(\omega t)$ (thin dashed line); (B) non-linear profile with $\tau_{ws}(t) \sim u_{bw}(t)$ (thin full line); (C) $\tau_{ws}(t) \sim |u_{bw}(t)| u_{bw}(t)$ (heavy full line); and (D) same as (C) without bottom slope effects (heavy dashed line).

Mean Concentration Profiles

Based on the mean reference concentrations obtained by case (C) in the previous section, we compare the predicted and measured suspended sediment concentrations. As discussed in Section 5.5, we account for multiple grain sizes to evaluate the different sediment settling velocities and resulting different concentration profiles. Figure 5-19 shows the measured (full circles) and predicted (full lines) concentration profiles at seven cross-shore Stations from 2 through 8 indicated in Figure 5-1 for Test 1. Similar to the comparisons of longshore depth-averaged current velocity, such as Figures 4-23 and 4-24, the multiple full circles at the same elevations are measurements at the same cross-shore (x) location but from the different along-shore (y) locations, from which one can see the uniformity and potential measurement variability of the measured concentration distributions. At each station, six full lines are the predicted concentration profiles when each of six sediment diameters, D_4 to D_9 , shown in Table 5.1, were applied to determine the concentration profile in (5.30). As discussed in Section

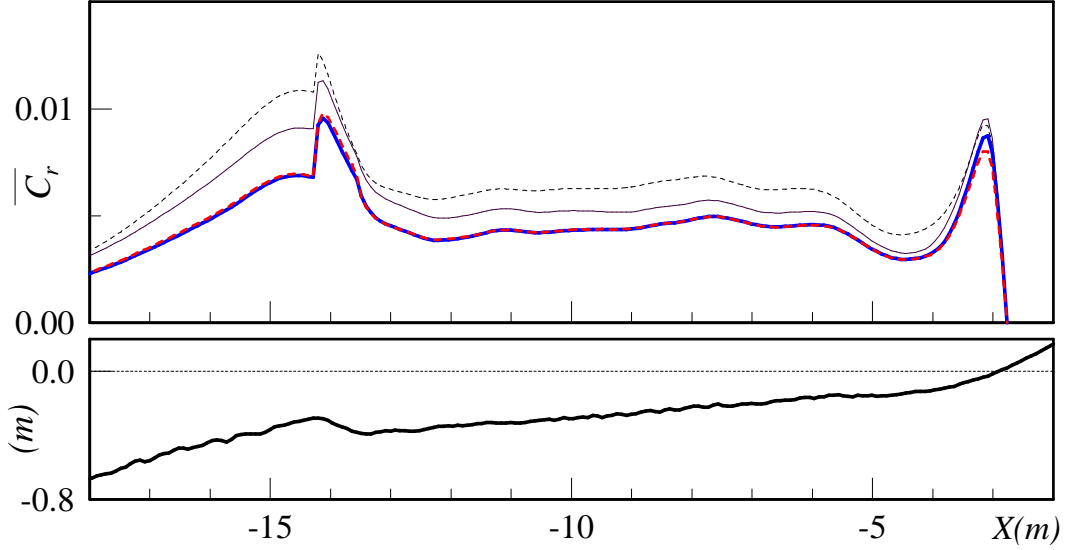


Figure 5-18: Cross-shore distributions of the mean reference concentration (Test 3). Predictions are based on: (A) $\tau_{ws}(t) \sim u_{bm} \cos(\omega t)$ (thin dashed line); (B) non-linear profile with $\tau_{ws}(t) \sim u_{bw}(t)$ (thin full line); (C) $\tau_{ws}(t) \sim |u_{bw}(t)| u_{bw}(t)$ (heavy full line); and (D) same as (C) without bottom slope effects (heavy dashed line).

5.5, we applied an identical reference concentration, C_r , based on D_{n50} to predict concentration profiles corresponding to each size-class. Therefore, the only difference among these concentration profiles at the same cross-shore location is the settling velocity, whose value varies with sediment diameter as seen in Table 5.1. Among six concentration profiles shown in each figure, the highest concentration profile is the predictions for the finest size-class, i.e. $D = D_4$, and the lowest concentration profile is when $D = D_9$ is applied. As seen in Figure 5-19, predicted concentration profiles are very sensitive to the sediment diameters, i.e. the settling velocities. At Station 2 in Figure 5-19, for example, when the sediment diameter is increased about 1.5 times from $D_4 = 0.11\text{mm}$ to $D_6 = 0.15\text{mm}$, the corresponding settling velocity becomes about 1.8 times larger (from $w_{f4} = 0.75\text{cm/s}$ to $w_{f6} = 1.35\text{cm/s}$) and the near-surface concentration, $C_s = C(z = h_{tr})$, decreases about 20 times, from $C_{s4} = 1.5 \times 10^{-4}$ to $C_{s6} = 7 \times 10^{-6}$.

We now examine the sensitivity of the mean concentration profile predictions to

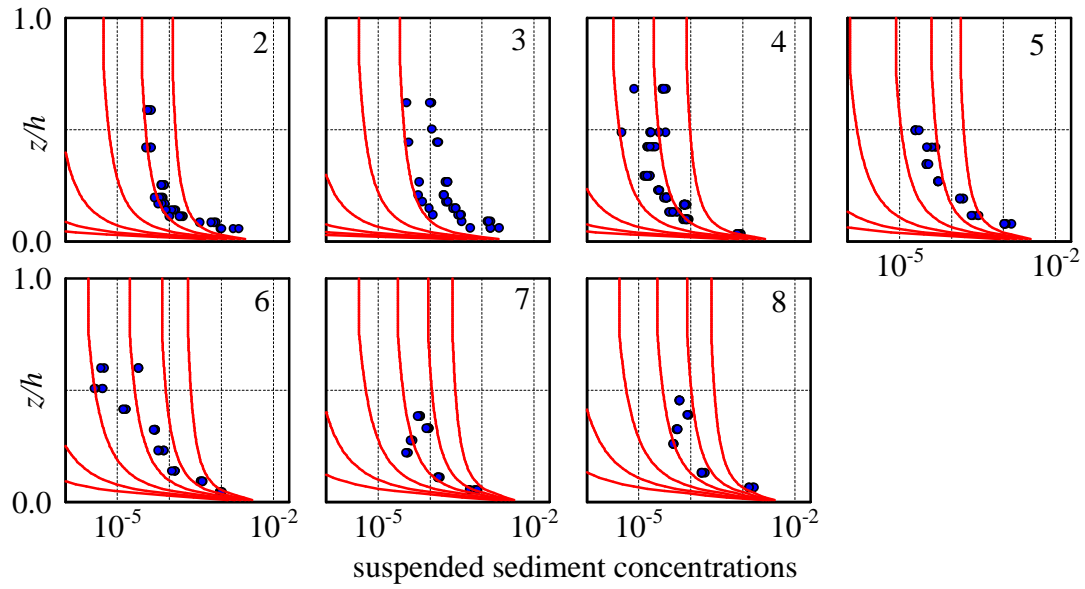


Figure 5-19: Comparisons of the predicted and measured mean suspended sediment concentrations. Measurements (circles) are obtained by Wang et al., (2002) (Test 1) and predictions (six full lines in each figure) are when D_4 to D_9 were applied respectively. The highest concentrations in each figure is when the finest diameter, $D = D_4$, is applied and the predicted concentration lowers as D changes from D_4 to D_9 .

the selection of size-classes to represent the mixed-size bottom sediments. Figure 5-20 compares the measured concentrations (full circles) for Test 1 with predictions afforded by (5.48) when: (i) only a median diameter, $D_{n50} = 0.167\text{mm}$, is applied (thin dashed line); (ii) only three diameters of highest weight fractions, D_5 , D_6 , and D_7 , are applied (thin full line); (iii) six diameters, D_4 to D_9 are applied (thick dashed line); and (iv) all twenty six diameter classes were accounted for (heavy full line). In the numerical application, the only difference among case (ii) through (iv) is the number of size-classes counted in (5.48). In (ii), for example, we applied three size-classes and evaluated the mean concentration profile of the three reference concentrations by (5.48). Figure 5-20 clearly shows that the predicted near-surface concentrations for the single median diameter, case (i), are about an order of magnitude smaller than those for cases (ii) to (iv), in which multiple grain sizes are taken into account. This feature makes sense because, as discussed previously, the sediment concentration exponentially increases with decreasing sediment diameter and the resulting mean concentration is predominantly determined by the large concentrations due to finer sediments. Accounting for three diameters, D_5 , D_6 , and D_7 , which covers about 55% of the entire mixture grains, improves the prediction of the mean concentration significantly compared to case (i). Taking the other three diameter classes into account (case (iii)), which cover an additional 32% of the bottom sediments, the predicted mean concentration becomes slightly larger. The difference between case (ii) and (iii) is at most 50% (at Station 3) and is considerably less than the difference between (i) and (ii). Accounting for the last 13% of diameter sizes (case (iv)), the predicted concentration further increases although the differences between (iii) and (iv) are considerably smaller than the difference between (i) and (ii). As seen in Table 5.1, the total weight fraction of the additional finer diameter classes, D_1 through D_3 , is less than 5% but these finer classes still have some effects and increase the mean concentrations slightly.

At Station 3, the model under-predicts the measured mean concentrations and the predicted concentrations at Station 3 are lower than those at the neighboring Stations 2 and 4. As seen in Figure 5-1, Station 3 is located at the bar trough

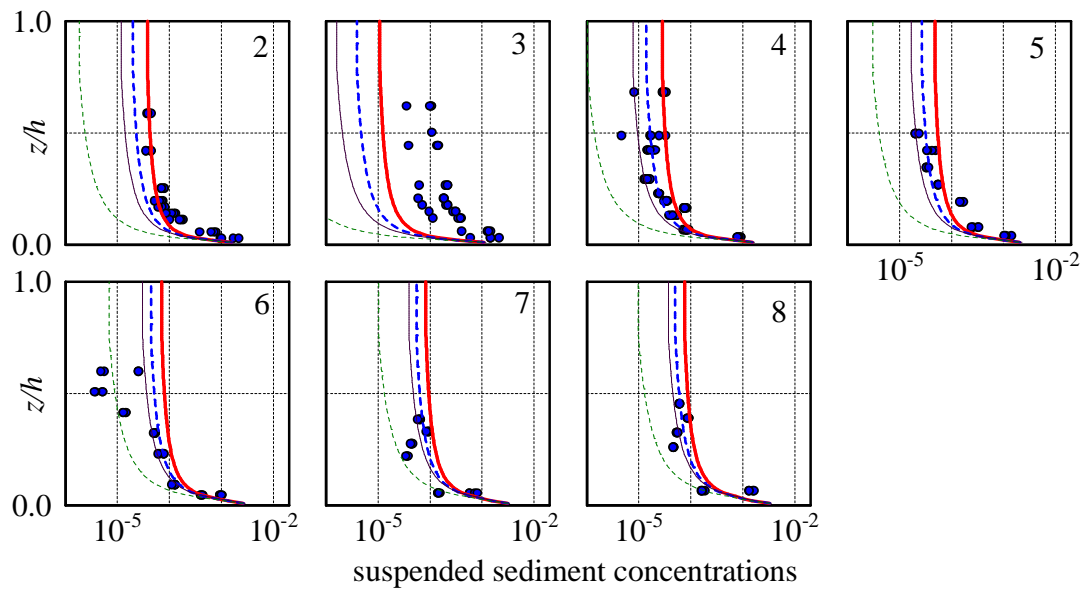


Figure 5-20: Comparisons of the predicted and measured mean suspended sediment concentrations. Measurements (circles) are obtained by Wang et al., (2002) (Test 1) and predictions are when following diameters were applied: D_{n50} (thin dashed line); D_5 , D_6 , and D_7 (thin full line); D_4 to D_9 (heavy dashed line); and all diameter classes (heavy full line).

and the water depth at Station 3 is slightly larger than the depth at Stations 2 and 4. The deeper water at Station 3 yields smaller near-bottom wave orbital velocity and bottom shear stress, which yields a smaller reference concentration, \bar{C}_r , than at Stations 2 and 4 (see Figure 5-17). Because relatively large concentrations are predicted and observed at the adjacent Stations 2 and 4, concentrations at Station 3 may be increased if the lateral fluxes of the suspended sediment due to dispersion and advections are taken into account. A similar underestimation of the concentration at the bar-trough is observed in Test 3 (Figure 5-2). However, it should also be noted that the uncertainty of the measured concentrations at Station 3 appears relatively large. This feature will be observed later when the total longshore sediment transport rate and the suspended sediment transport rate are compared. In these comparisons, it will be seen that the measured longshore suspended sediment transport rate, $q_{SS,y}$, exceeds the total measured LSST, q_y at Station 3 in Test 1 (Figure 5-28), which clearly casts doubts on the accuracy of the measurement at Station 3.

Figure 5-21 compares the measured and predicted mean concentration profiles at each cross-shore location for Test 3. Similar to Figure 5-20, a thin dashed line, thin full line, heavy dashed line, and heavy full line denote the predictions when (i) only D_{n50} is applied; (ii) D_5 , D_6 , and D_7 , are applied; and (iii) six diameters, D_4 to D_9 are applied and (iv) all diameter classes are applied, respectively. Similar to comparisons for Test 1, the use of the single median diameter, case (i), underpredicts the mean concentrations by about an order of magnitude. Predictions when (ii) three, (iii) six or (iv) all diameter classes are accounted for are nearly identical although the predictions of (iv) are larger than predictions afforded by (ii) or (iii). The mean concentrations at Station 2 are about an order of magnitude larger than those at the other Stations. Station 2 is located just sea-ward of the bar crest and most waves start to break around Station 2 (see Figures 5-2 and 2-22). Breaking waves yield a large turbulent eddy diffusivity and therefore keep larger amounts of sediment suspended in the water column. The present model appears to capture this feature and the predicted concentration profile at Station 2 agree quite well with measurements. Similar to the concentration comparisons in Test 1 (Figure 5-20), the

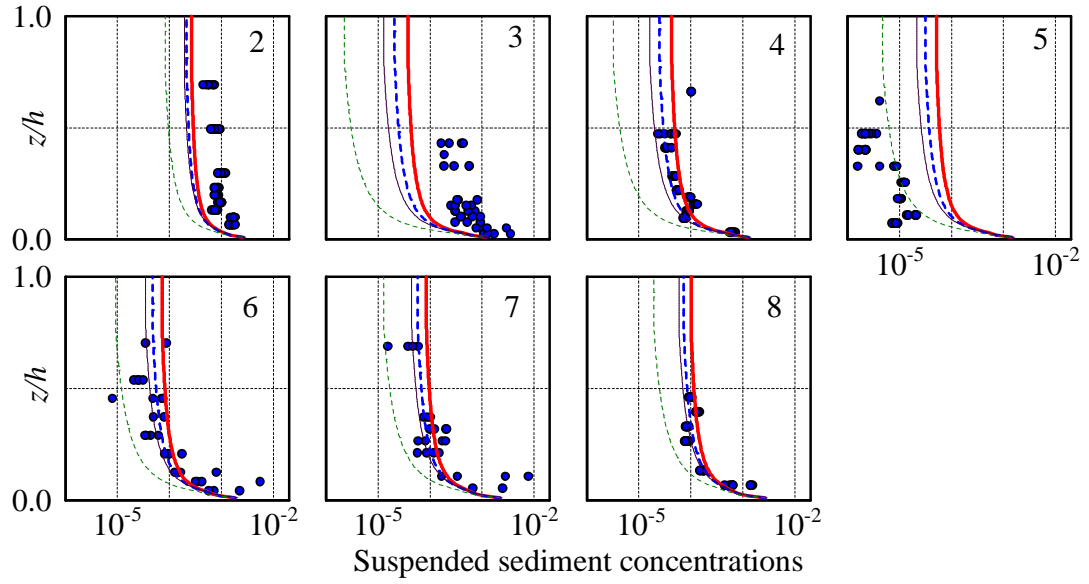


Figure 5-21: Comparisons of the predicted and measured mean suspended sediment concentrations. Measurements (circles) are obtained by Wang et al., (2002) (Test 3) and predictions are when following diameters were applied: D_{n50} (thin dashed line); D_5 , D_6 , and D_7 (thin full line); D_4 to D_9 (heavy dashed line); and all diameter classes (heavy full line).

model under-predicts the mean concentration at the bar-trough, Station 3 (see Figure 5-2).

Mean Suspended Sediment Transport Rate

Figures 5-22 and 5-23 show the cross-shore distributions of predicted and measured suspended sediment transport rates for Test 1 and Test 3, respectively. The measured suspended sediment transport rates (circles) are obtained by vertically integrating the products of measured concentrations and measured current velocity components in the cross-shore (x) and the shore-parallel (y) directions. Similar to Figures 5-20 and 5-21, predictions are when: (i) only D_{n50} is applied (thin dashed line); (ii) D_5 , D_6 , and D_7 , are applied (thin full line); (iii) six diameters, D_4 to D_9 are applied (heavy dashed line); and (iv) all diameter classes are applied (heavy full line). As seen in the figures, predictions with all diameter classes (iv) yields the largest suspended sediment

transport rates although the difference of predictions between the cases with multi diameter classes, (ii), (iii), and (iv) are relatively small compared to the differences from the predictions with the single diameter case (i). Overall, the predicted suspended sediment transport rates (iv) agree well with measurements except at Station 3 ($X \simeq -13\text{m}$). As noted in the previous section, the large “measured” suspended sediment transport rates at Station 3 are due to the large sediment concentrations. As noted in the comparisons of bedload transport rates, the measured suspended load at Station 3 was larger than the total LSST by a significant amount. We will discuss the uncertainty of the measured suspended sediment at Station 3 in the following section. Tables 5.3 and 5.4 compare measured and predicted cross-shore and longshore suspended sediment transport rates (m^2/year) and compare their relative errors at each of seven Stations for Test 1 and Test 3, respectively. The relative errors, μ , are normalized by each predicted value, i.e. determined by $\mu = 1 - q_{SS,meas}/q_{SS,pred}$. In Tables 5.3 and 5.4, we compare the predictions based on: (A) $\tau_{ws}(t) \sim \cos \omega t$; (B) $\tau_{ws}(t) \sim u_{bw}(t)$; and (C) $\tau_{ws}(t) \sim |u_{bw}(t)| u_{bw}(t)$. In case (C), we also compare the predictions with different choices of diameter classes (i) to (iv) while only case (iv), i.e. the case of all diameter size classes, is accounted for in cases (A) and (B). Because of the uncertainty of the measured suspended sediment transport rates at Station 3, average errors in suspended sediment transport rates shown in the tables are obtained from the values at six stations excluding Station 3. From Tables 5.3 and 5.4, it is seen that the predicted average suspended sediment transport rates in (C)+(iv) are within a relative error of at most 42% both in the cross-shore and shore-parallel directions and for Test 1 and Test 3. Out of seven stations including Station 3, the number of Stations, whose predicted $\bar{q}_{SS,x}$ and $\bar{q}_{SS,y}$ in case (C)+(iv) fall within 50% from measurements, are four and five for Test 1 and three and five for Test 3, respectively. In the cross-shore (x) direction, the case (i) tends to underestimate the sea-ward suspended sediment transport rates while (ii), (iii), and (iv) yield better predictions for $q_{SS,x}$. It is also seen that the predictions are more sensitive to the choice of diameter classes, (i) to (iv), than to the determinations of the wave shear stress (A), (B) and (C). For example, average longshore suspended sediment transport rate for Test 1

Table 5.3: Comparisons of measured and predicted suspended load transport rates in the cross-shore and longshore directions at seven Stations and their relative errors (Test 1, spilling breakers). Predictions (A) and (B) are only for case (iv) and the values at Station 3 ($X = -13.1\text{m}$) are excluded for the average values.

	X(m)	meas. (m ² /year)	Predictions (m ² /year)						relative error (μ)					
			(A)	(B)	(C)				(A)	(B)	(C)			
					(i)	(ii)	(iii)	(iv)			(i)	(ii)	(iii)	(iv)
\bar{q}_{ssx}	-5.7	-37.3	-62.2	-62.4	-24.9	-40.7	-43.1	-51.6	0.40	0.40	-0.49	0.08	0.14	0.28
	-7.1	-20.2	-80.1	-81.7	-29.6	-50.3	-54.3	-66.4	0.75	0.75	0.32	0.60	0.63	0.70
	-8.7	-34.2	-78.2	-80.4	-25.1	-44.7	-50.0	-63.9	0.56	0.57	-0.36	0.24	0.32	0.47
	-10.1	-37.2	-59.3	-61.1	-16.6	-30.3	-35.2	-47.4	0.37	0.39	-1.24	-0.23	-0.06	0.21
	-11.5	-25.8	-40.0	-41.2	-10.7	-18.7	-22.2	-31.3	0.36	0.38	-1.40	-0.38	-0.16	0.18
	-13.1	-79.7	-22.3	-23.3	-7.2	-10.9	-12.4	-17.7	-2.58	-2.43	-10.02	-6.34	-5.44	-3.51
	-14.6	-27.7	-55.1	-56.2	-10.6	-22.8	-28.8	-42.6	0.50	0.51	-1.61	-0.21	0.04	0.35
	Avg.	-30.4	-62.5	-63.9	-19.6	-34.6	-38.9	-50.5	0.51	0.52	-0.55	0.12	0.22	0.40
\bar{q}_{ssy}	-5.7	97.4	136.2	136.7	44.8	81.3	90.0	113.0	0.28	0.29	-1.17	-0.20	-0.08	0.14
	-7.1	49.0	163.2	166.5	51.0	94.9	106.3	135.3	0.70	0.71	0.04	0.48	0.54	0.64
	-8.7	63.8	150.6	154.7	43.5	81.9	93.8	122.9	0.58	0.59	-0.47	0.22	0.32	0.48
	-10.1	89.4	106.2	109.4	28.7	53.1	62.3	84.9	0.16	0.18	-2.12	-0.68	-0.44	-0.05
	-11.5	52.0	60.8	62.7	16.1	28.3	33.6	47.7	0.14	0.17	-2.22	-0.84	-0.55	-0.09
	-13.1	172.4	22.6	23.6	6.9	10.6	12.3	18.0	-6.62	-6.30	-23.82	-15.27	-13.06	-8.60
	-14.6	58.5	42.7	43.6	10.2	19.6	23.5	33.0	-0.37	-0.34	-4.71	-1.99	-1.49	-0.77
	Avg.	68.3	109.9	112.3	32.4	59.8	68.2	89.5	0.38	0.39	-1.11	-0.14	0.00	0.24

predicted by the case (C)+(iv) is about 20% smaller than the one predicted by (A) while it is about three times larger than the one predicted by (C)+(i) (Table 5.3). This feature suggests that appropriate knowledge of bottom sediment characteristics is essential to ensure the accurate prediction of the suspended sediment transport rate. The model tends to over-predict $q_{ss,y}$ but this over-prediction is partially due to the over-predictions of the longshore current velocity as seen in Section 4.6.3. However, the ability of the model to predict the mean suspended sediment transport rate is overall good, considering the fact that the reference concentration model, (5.29), was obtained from separate experiments for unidirectional steady flow and that the non-linear wave effects may vary the prediction of C_r by some 20% as observed in Figure 5-18.

Comparing Figures 5-22 and 5-23, the suspended sediment transport rate for the plunging breaker case (Test 3) has a strong peak near the bar crest ($X \simeq -14\text{m}$) where rms wave heights abruptly start to dissipate while the spilling breaker case

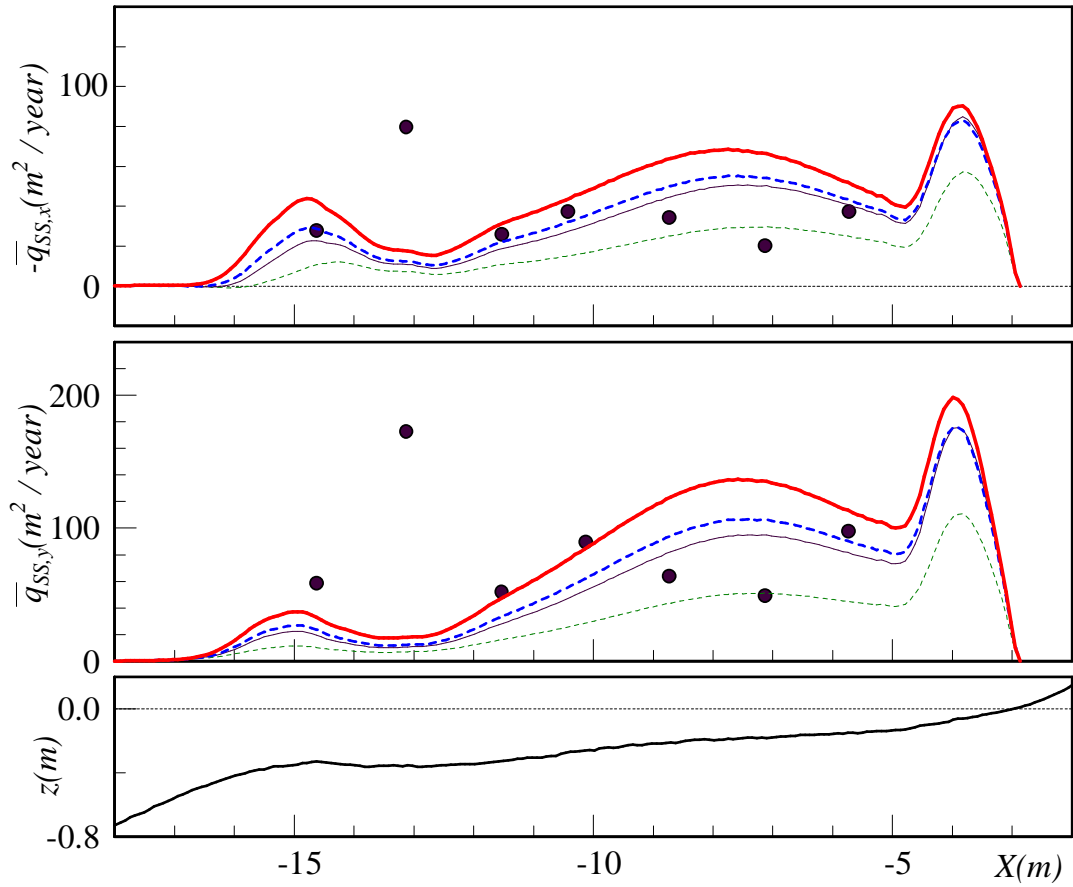


Figure 5-22: Cross-shore distributions of the net cross-shore, $\bar{q}_{SS,x}$, and longshore, $\bar{q}_{SS,y}$, suspended sediment transport rates for LSTF experiments (Test 1). Measurements (circles) and predictions are when following sediment size-classes are accounted for: (i) D_{n50} (thin dashed line); (ii) D_5 , D_6 , and D_7 (thin full line); (iii) D_4 through D_9 (havy dashed line); and (iv) all diameter classes (heavy full line).

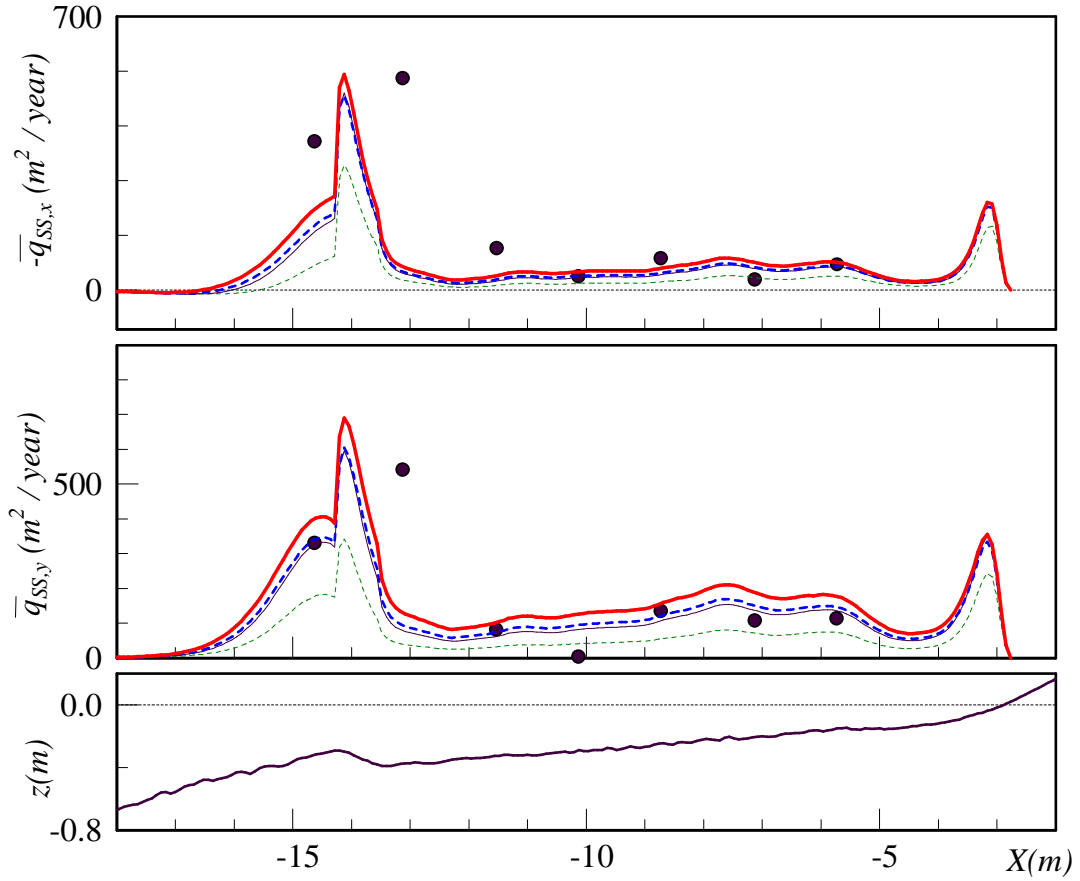


Figure 5-23: Cross-shore distributions of the net cross-shore, $\bar{q}_{SS,x}$, and longshore, $\bar{q}_{SS,y}$, suspended sediment tranport rates for LSTF experiments (Test 3). Measurements (circles) and predictions are when following sediment size-classes are accounted for: (i) D_{n50} (thin dashed line); (ii) D_5 , D_6 , and D_7 (thin full line); (iii) D_4 through D_9 (havy dashed line); and (iv) all diameter classes (heavy full line).

Table 5.4: Comparisons of measured and predicted suspended load transport rates in the cross-shore and longshore directions at seven Stations and their relative errors (Test 3, plunging breakers). Predictions (A) and (B) are only for case (iv) and the values at Station 3 ($X = -13.1\text{m}$) are excluded for the average values.

	X(m)	meas. (m ² /year)	Predictions (m ² /year)						relative error (μ)					
			(A)	(B)	(C)				(A)	(B)	(C)			
					(i)	(ii)	(iii)	(iv)			(i)	(ii)	(iii)	(iv)
\bar{q}_{ssx}	-5.7	-65.5	-94.7	-80.1	-35.6	-58.9	-61.0	-70.9	0.31	0.18	-0.84	-0.11	-0.07	0.08
	-7.1	-27.0	-95.9	-80.6	-32.0	-55.2	-58.7	-70.5	0.72	0.67	0.16	0.51	0.54	0.62
	-8.7	-81.0	-80.7	-66.0	-21.1	-39.5	-44.1	-56.0	0.00	-0.23	-2.84	-1.05	-0.84	-0.44
	-10.1	-34.5	-68.6	-57.3	-17.1	-32.0	-36.3	-47.2	0.50	0.40	-1.02	-0.08	0.05	0.27
	-11.5	-107.4	-55.0	-46.2	-12.1	-23.3	-27.3	-37.1	-0.95	-1.32	-7.86	-3.61	-2.93	-1.89
	-13.1	-541.2	-80.5	-74.2	-25.7	-43.3	-47.3	-59.3	-5.72	-6.29	-20.09	-11.50	-10.44	-8.12
	-14.6	-380.2	-326.1	-273.6	-63.4	-149.2	-165.7	-207.3	-0.17	-0.39	-5.00	-1.55	-1.29	-0.83
	Avg.	-115.9	-120.2	-100.6	-30.2	-59.7	-65.5	-81.5	0.04	-0.15	-2.84	-0.94	-0.77	-0.42
\bar{q}_{ssy}	-5.7	113.0	236.4	199.9	73.1	135.1	145.6	177.0	0.52	0.43	-0.55	0.16	0.22	0.36
	-7.1	106.7	256.4	215.7	71.4	136.4	150.7	188.6	0.58	0.51	-0.49	0.22	0.29	0.43
	-8.7	134.9	226.0	184.8	54.9	107.0	121.4	156.9	0.40	0.27	-1.46	-0.26	-0.11	0.14
	-10.1	3.4	184.4	154.1	41.4	81.8	95.0	126.8	0.98	0.98	0.92	0.96	0.96	0.97
	-11.5	81.5	151.6	127.4	31.9	62.8	74.3	102.2	0.46	0.36	-1.56	-0.30	-0.10	0.20
	-13.1	540.6	176.8	162.9	39.6	79.0	94.1	130.3	-2.06	-2.32	-12.65	-5.84	-4.74	-3.15
	-14.6	330.8	630.0	528.6	177.3	326.3	340.7	400.6	0.48	0.37	-0.87	-0.01	0.03	0.17
	Avg.	128.4	280.8	235.0	75.0	141.6	154.6	192.0	0.54	0.45	-0.71	0.09	0.17	0.33

(Test 1) does not have such a prominent peak around the bar-crest. The present model captures this feature reasonably well. This feature, i.e. the difference between plunging and spilling breakers will be discussed in the following Section.

5.6.4 Total Sediment Transport

In this Section, we compare the bedload and suspended sediment transport and discuss the relative contributions of these components to the total sediment transport. Effect of the breaker type, i.e. plunging or spilling, on the sediment transport rate is also discussed in the comparisons of the longshore sediment transport rates.

Cross-Shore Sediment Transport (CSST)

Figures 5-24 and 5-25 show the cross-shore distributions of bedload (thin full line), suspended load (dashed line) and the total sediment transport rates (heavy full line) in the cross-shore directions for Test 1 and Test 3, respectively. In the figures, predictions are based on case (B), in which the wave shear stress, $\tau_{ws}(t)$, is determined by (5.8), i.e. $\tau_{ws}(t) \sim u_{bw}(t)$, and the shore-ward sediment transport rates are taken positive. As seen in the figures, both bedload and suspended load transports are in the sea-ward direction and the resulting total sediment transport is therefore away from the shore. Since the beach profiles of both Test 1 and Test3 reached an “equilibrium” state in the experiments, the net cross-shore sediment transport should be close to zero. An equilibrium state requires the model’s predictions to have a shore-ward sediment transport that balances the sea-ward sediment transport. One of the primary components that contribute to balancing the sea-ward sediment transport may be the “mean wave-associated suspended load” discussed in Section 5.3, which we are not currently considering in our model. For example, Kobayashi and Tega (2002) showed in their experiments that the mean wave-associated suspended sediment transport in the shore-ward direction balances the mean suspended sediment transport rate in the sea-ward direction.

As seen in Figures 5-11 and 5-12, accounting for skewness of the non-linear near-

bottom wave orbital velocity produces a significant contribution to a shore-ward bedload sediment transport. In this sense, evaluation of non-linear wave effects may significantly affect the cross-shore balance of the sediment transport rate. Figures 5-26 and 5-27 show the same comparisons as those in Figures 5-24 and 5-25 but the predictions are based on case (C), in which the wave shear stress is obtained by (5.9), i.e. $\tau_{ws}(t) \sim |u_{bw}(t)| u_{bw}(t)$. As seen in the Figures 5-26 and 5-27, the non-linearity effects significantly increase the shore-ward net bedload transport and the resulting total cross-shore sediment transport rate approaches zero both in Test 1 and Test 3 over the major part of the surf zone except near the shoreline for both Test 1 and Test 3 and near the bar-crest for Test 3.

For the plunging breaker case (Test 3), since H_{rms}/h becomes largest near the bar-crest, relatively strong skewness and the asymmetry of the non-linear near-bottom wave orbital velocity are expected. Asymmetry, i.e. rapid rise of the shore-ward wave orbital velocity is associated with the acceleration momentum forcings. Effect of acceleration on bedload transport has recently been considered (Drake and Calatoni, 2001; Hoefel and Elgar, 2003) and would lead to a shoreward transport contribution where the wave asymmetry is the most pronounced. As seen in Figure 2-22, measured and predicted T_c/T is locally smallest near the bar-trough ($X \simeq -14\text{m}$). The small T_c causes the rapid rise of the shore-ward wave orbital velocity and therefore yields the strong wave asymmetry. We do not account for this effect in our bedload transport model. In fact, given the negligible effect of fluid acceleration on bedload transport inferred from Madsen's (1991) analysis of the mechanics of bedload transport, we do not believe that accounting for fluid accelerations would greatly improve the predictions of a seaward net bedload transport around the bar-crest. However, given the short time of the rise in velocity prior to maximum orbital velocity would result in a thinner bottom boundary layer thickness as maximum u_{bw} is reached and this effect would vary the friction factor, f_{cw} , although our model employs a constant f_{cw} based on a periodic wave of period T . If one were to account for the different time scales for accelerations, i.e. T_c when u_{bw} rises from $u_{b\min}$ to $u_{b\max}$, and $T - T_c$ when u_{bw} decreases from $u_{b\max}$ to $u_{b\min}$, one would then expect larger friction factors and

therefore the larger bottom shear stress when τ_{bws} is shore-ward and the smaller shear stress when τ_{bws} is sea-ward. This effect would produce an increase in shore-ward net bedload transport.

The major sea-ward transport contribution near the bar-crest in Figure 5-25 is the suspended sediment transport due to considerably larger sediment concentrations. Since the suspended sediment concentration is large, we could also expect the large shoreward transport contributions due to wave-associated mean suspended load transport.

Both for spilling and plunging waves (Test 1 and Test 3) a net seaward transport is predicted in the swash zone, i.e. immediately before the shore line (Figures 5-24 and 5-25). As seen in Figures 2-21 and 2-22, predicted and measured non-linear wave parameters, u_{*c}/U_{b*} and T_c/T show relatively weak non-linear wave effects. Therefore, the lack of shore-ward sediment transport may be due to the other mechanisms. For example, our model does not account for the swash zone hydrodynamics while the swash zone hydrodynamics such as wave run-ups and the varying mean water level due to surf beats could have considerable effects on the cross-shore sediment transport processes.

Further modifications of and additions to the model for evaluations of non-linear wave, wave-associated suspended sediment transport and hydrodynamics and sediment transport processes in the swash zone, are therefore called for in order to accurately evaluate the cross-shore balance of sediment transport rates on an equilibrium beach.

Long-Shore Sediment Transport (LSST)

In contrast to the cross-shore sediment transport, we showed in the preceding sections that the longshore sediment transport is predominantly determined from the mean current component both in the bedload and suspended load and the effect of the wave-associated transport components are negligibly small in the longshore direction due to the small angle of wave incidence. Figures 5-28 and 5-29 show the cross-shore distributions of the predicted bedload (thin full line), suspended load (dashed

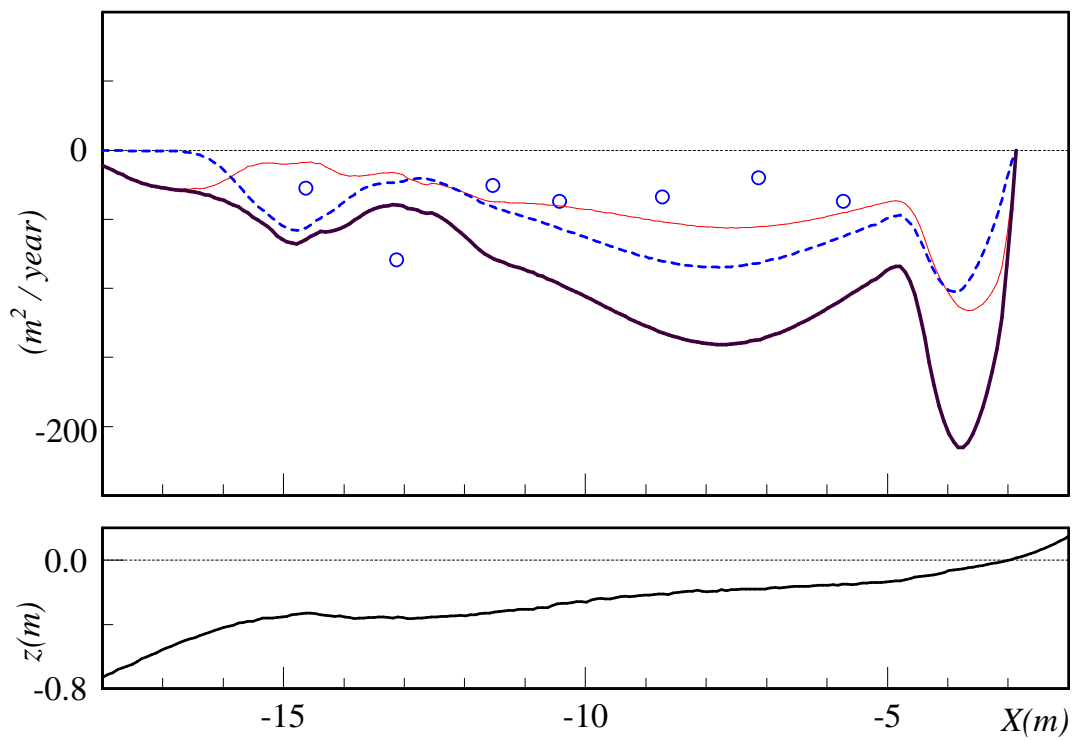


Figure 5-24: Cross-shore distributions of the measured cross-shore suspended sediment transport rates (open circles) and the predicted bedload (thin full line), suspended load (dashed line), and the total sediment transport rate (heavy full line) in the cross-shore direction for Test 1. (prediction case (B) $\tau_{ws}(t) \sim u_{bw}(t)$)

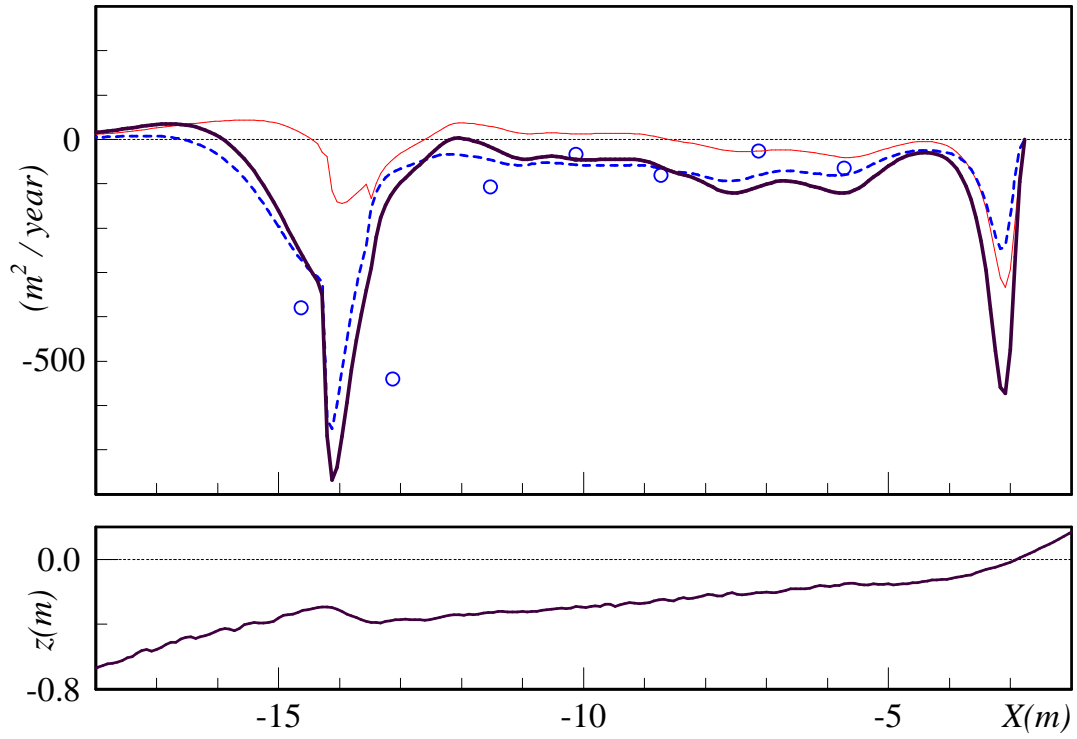


Figure 5-25: Cross-shore distributions of the measured cross-shore suspended sediment transport rates (open circles) and the predicted bedload (thin full line), suspended load (dashed line), and the total sediment transport rate (heavy full line) in the cross-shore direction for Test 3. (prediction case (B), $\tau_{ws}(t) \sim u_{bw}(t)$)

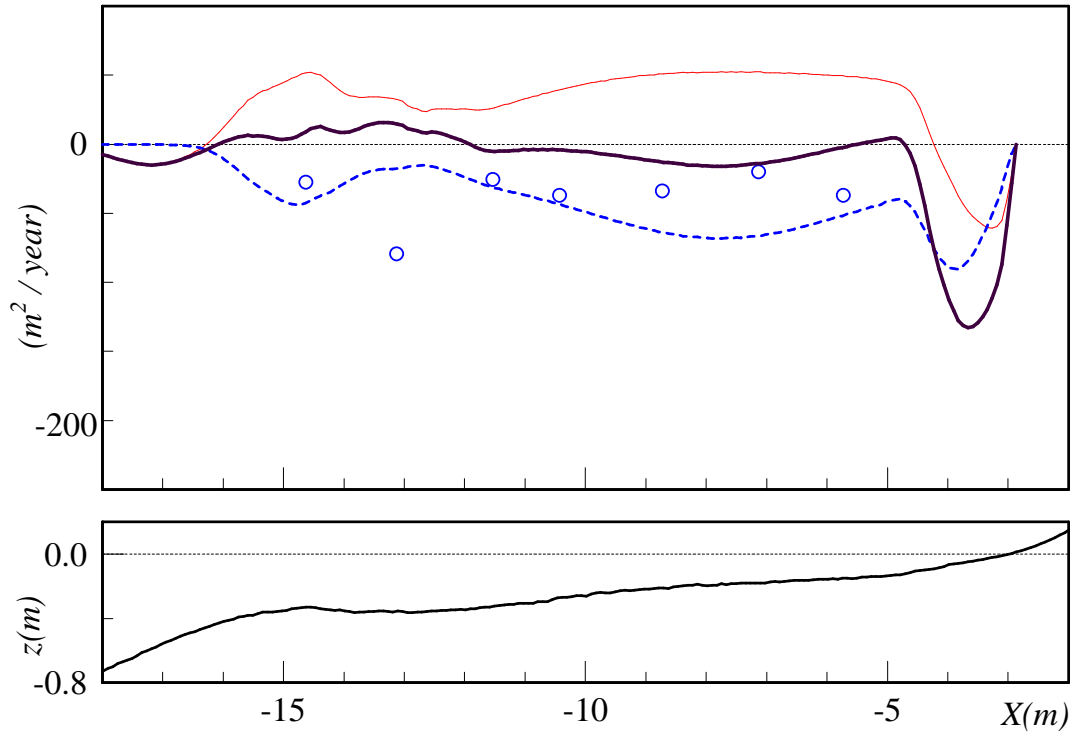


Figure 5-26: Cross-shore distributions of the measured cross-shore suspended sediment transport rates (open circles) and the predicted bedload (thin full line), suspended load (dashed line), and the total sediment transport rate (heavy full line) in the cross-shore direction for Test 1. (prediction case (C), $\tau_{ws}(t) \sim |u_{bw}(t)| u_{bw}(t)$)

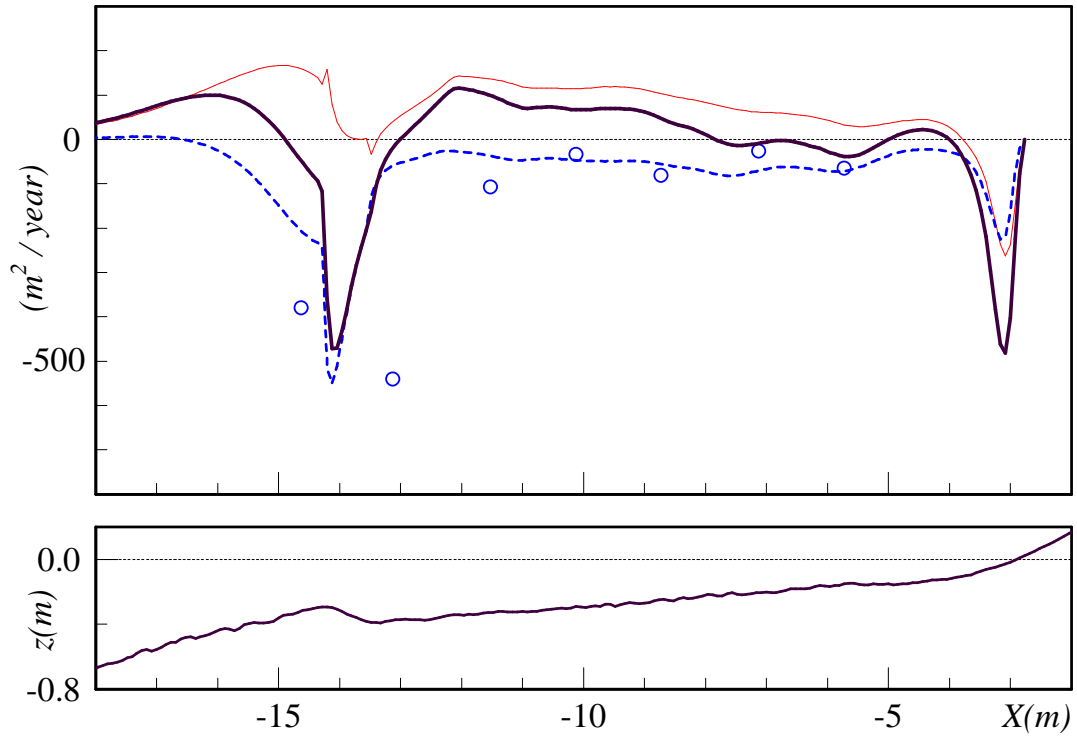


Figure 5-27: Cross-shore distributions of the measured cross-shore suspended sediment transport rates (open circles) and the predicted bedload (thin full line), suspended load (dashed line), and the total sediment transport rate (heavy full line) in the cross-shore direction for Test 3. (prediction case (C), $\tau_{ws}(t) \sim |u_{bw}(t)| u_{bw}(t)$)

line) and the total longshore sediment transport rate (LSST, heavy full line), for Test 1 and Test 3, respectively. In the Figures, circles are the measured suspended sediment transport rates obtained in the previous section and the triangles are the measured total LSST obtained from the volumes collected in the sand-traps installed at the downstream end of the straight beach in the LSTF (Wang et al., 2002). As seen in Figure 5-28 at Station 3 ($X \simeq -13\text{m}$), the measured longshore suspended sediment transport rate ($\simeq 170 \text{ m}^2/\text{year}$) is about four times larger than the total LSST ($\simeq 40 \text{ m}^2/\text{year}$). Similarly in Figure 5-29, the measured longshore suspended sediment transport at Station 3 ($\simeq 540 \text{ m}^2/\text{year}$) is larger than the total LSST ($\simeq 500 \text{ m}^2/\text{year}$). As discussed in the previous section, the estimation of the “measured” suspended sediment transport rates are rough because these values were obtained by integrating the products of the measured suspended sediment concentration and the measured current velocity. However, the estimated suspended sediment transport rates appear to be consistent with the measured total LSST except at Station 3. This is the reason why we suggested in the previous section that the measured concentration at Station 3 may be unreliable.

The model predicts peaks of the LSST near the shore-line for both Test 1 and 3 and the pronounced peak near the bar crest for Test 3. Near the shore-line, the model under-predicts the amount of peak LSST for Test 3 while it predicts nearly the same quantity as the measured peak LSST for Test 1. The under-prediction of the LSST near the shore-line may be partially due to the swash-zone transport, which our model does not explicitly account for. Surf-beat effects may be another reason for the observed under-predictions. In fact, the measured peaks of the LSST for both Test 1 and Test 3 are land-ward of our predicted shore-line, where the predicted mean water level and the beach elevation intersect. In order to explain the longshore sediment transport above the mean water level, the model must account for the swash-zone hydrodynamics such as wave run-up and low-frequency fluctuation of the mean water level due to surf-beat effects.

Although the model predicts the peak near the bar-crest for Test 3, the cross-shore range of the peak is narrower than the one measured and the model under-predicts the

total LSST near Station 3. As discussed in the comparisons of suspended sediment concentrations, the under-prediction of the suspended sediment transport at Station 3 may be improved if the lateral flux of the sediments due to advections and diffusions are accounted for.

Tables 5.5 and 5.6 summarize the measured and predicted local total LSST at each cross-shore location and the total LSST integrated over the cross-shore (x) direction and their relative errors for Test 1 and Test 3, respectively. The predictions are based on all diameter size classes (case iv) and (A), (B) and (C) in Tables 5.5 and 5.6 are predictions when wave-associated shear stress, $\tau_{ws}(t)$, is determined by $\tau_{ws}(t) \sim \cos \omega t$, $\tau_{ws}(t) \sim u_{bw}(t)$, and $\tau_{ws}(t) \sim |u_{bw}(t)| u_{bw}(t)$, respectively. Similar to the comparison of suspended sediment transport rates, relative errors, μ , are normalized by each prediction, i.e. $\mu = 1 - q_{y,meas.}/q_{y,pred.}$. Table 5.7 summarizes the number of data points whose relative errors fall within 30, 50, and 65% for the predictions (C) for Test 1 and Test 3, respectively. The total number of data points are twenty including two locations above the mean water level, where the model predicted zero sediment transport rates. In the rest of 18 locations, as summarized in Table 5.7, only one location is above 65%-error for Test 1 and two locations are above 65%-error for Test 3 ($X = -16.9(m)$ for Test 1 and $X = -13.1(m)$, $-3.4(m)$ for Test 3). In Test 1, both predicted and measured LSST at $X = -16.9(m)$ are very small compared to the other locations and hence the relatively large error at this point does not affect the predictive skill of the total LSST. In Test 3, $X = -3.4(m)$ is near the shore line and $X = -13.1(m)$ is at Station 3 where the model under-predicts the suspended sediment transport rates. As discussed in the comparisons of suspended sediment concentrations, this under-prediction may be improved by accounting for lateral suspended sediment fluxes due to diffusion and advections. The model also predicts the reasonable total LSST whose relative errors are 22% for Test 1 and -11% for Test 3.

Finally, Figure 5-30 compares Test 1 and Test 3 in terms of the cross-shore distributions of the bedload and suspended sediment transport rates. Table 5.8 shows predicted net bedload and suspended longshore sediment transport rates integrated

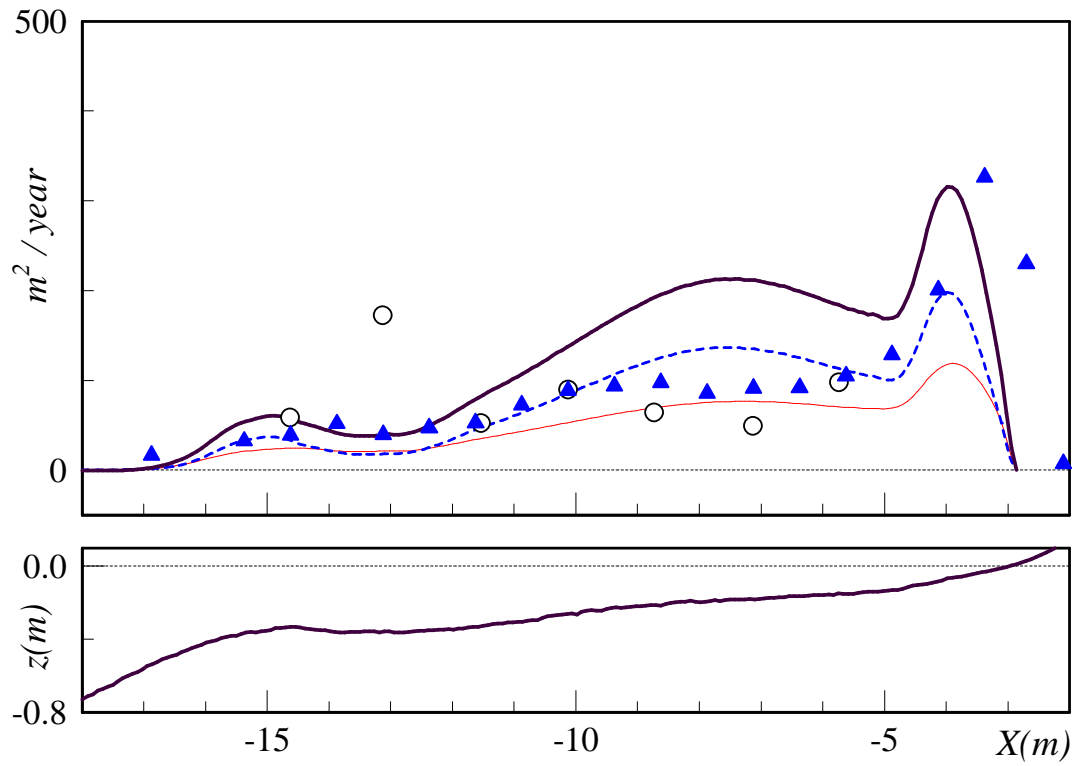


Figure 5-28: Cross-shore distributions of the predicted bedload (thin full line), suspended load (dashed line), and the total sediment transport rate (heavy full line) in the shore-parallel for Test 1. Measurements (circles, suspended load; and triangles, total LSST) are obtained by Wang et al. (2002).

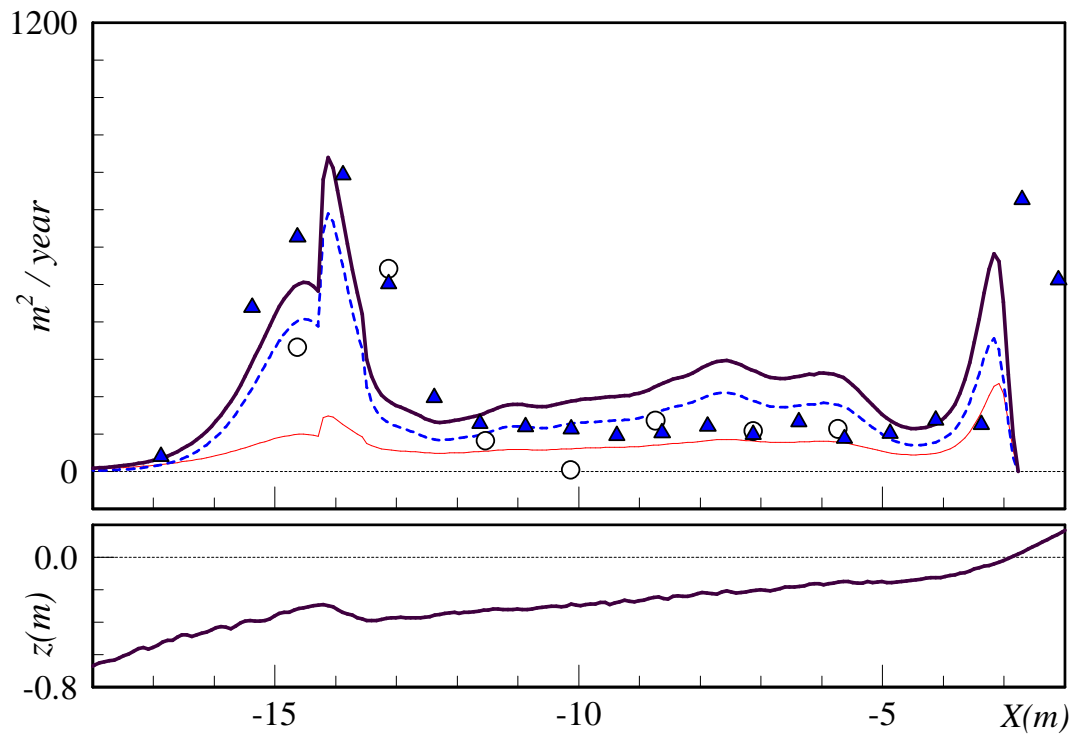


Figure 5-29: Cross-shore distributions of the predicted bedload (thin full line), suspended load (dashed line), and the total sediment transport rate (heavy full line) in the shore-parallel for Test 3. Measurements (circles, suspended load; and triangles, total LSST) are obtained by Wang et al. (2002).

Table 5.5: Measured and predicted local LSST and the total LSST integrated over the cross-shore (x) axis and their relative errors (Test 1, spilling breakers). Predictions are based on (A) $\tau_{ws}(t) \sim \cos \omega t$, (B) $\tau_{ws}(t) \sim u_{bw}(t)$, and (C) $\tau_{ws}(t) \sim |u_{bw}(t)| u_{bw}(t)$.

X(m)	\overline{q}_y (m ² /year)				relative error (μ)		
	meas.	(A)	(B)	(C)	(A)	(B)	(C)
-2.1	7	0	0	0			
-2.7	230	0	0	0			
-3.4	326	240	231	207	-0.36	-0.42	-0.58
-4.1	201	363	342	303	0.45	0.41	0.34
-4.9	129	197	197	170	0.35	0.35	0.24
-5.6	105	204	211	181	0.49	0.50	0.42
-6.4	92	225	234	199	0.59	0.61	0.54
-7.1	91	239	250	212	0.62	0.63	0.57
-7.9	86	238	250	211	0.64	0.66	0.59
-8.6	97	221	233	195	0.56	0.58	0.50
-9.4	94	192	203	169	0.51	0.54	0.45
-10.1	89	157	167	138	0.43	0.47	0.35
-10.9	72	122	130	107	0.41	0.44	0.33
-11.6	52	89	95	79	0.41	0.45	0.34
-12.4	47	53	58	50	0.11	0.19	0.04
-13.1	40	39	44	39	-0.02	0.09	-0.01
-13.9	52	41	46	41	-0.27	-0.13	-0.25
-14.6	39	61	66	58	0.35	0.41	0.32
-15.4	33	60	64	54	0.46	0.49	0.40
-16.9	16	1	2	3	-10.31	-6.12	-4.86
Total	1424	2060	2121	1816	0.31	0.33	0.22

Table 5.6: Measured and predicted local LSST and the total LSST integrated over the cross-shore (x) axis and their relative errors (Test 3, plunging breaker). Predictions are based on (A) $\tau_{ws}(t) \sim \cos \omega t$, (B) $\tau_{ws}(t) \sim u_{bw}(t)$, and (C) $\tau_{ws}(t) \sim |u_{bw}(t)| u_{bw}(t)$.

X(m)	\bar{q}_y (m ² /year)				relative error (μ)		
	meas.	(A)	(B)	(C)	(A)	(B)	(C)
-2.1	512	0	0	0			
-2.7	726	0	0	0			
-3.4	125	482	483	433	0.74	0.74	0.71
-4.1	138	174	140	127	0.21	0.02	-0.09
-4.9	101	175	149	136	0.42	0.32	0.26
-5.6	88	317	275	248	0.72	0.68	0.65
-6.4	132	338	286	254	0.61	0.54	0.48
-7.1	98	351	303	269	0.72	0.67	0.63
-7.9	120	379	323	284	0.68	0.63	0.58
-8.6	103	318	269	234	0.68	0.62	0.56
-9.4	96	269	231	200	0.64	0.58	0.52
-10.1	113	252	219	187	0.55	0.48	0.40
-10.9	119	234	208	177	0.49	0.43	0.33
-11.6	128	201	178	150	0.37	0.28	0.15
-12.4	197	177	160	133	-0.12	-0.23	-0.48
-13.1	501	236	224	187	-1.12	-1.24	-1.67
-13.9	792	778	756	671	-0.02	-0.05	-0.18
-14.6	626	751	642	499	0.17	0.02	-0.25
-15.4	439	431	373	290	-0.02	-0.18	-0.51
-16.9	40	37	37	35	-0.09	-0.07	-0.15
Total	3896	4571	4081	3510	0.15	0.05	-0.11

Table 5.7: Number of data points (out of 18 measured locations) whose relative errors fall within specified error ranges for the prediction case (C).

error	< 30	30 ~ 50	50~65	65 <
Test 1	4	8	5	1
Test 3	6	4	6	2

over the entire cross-shore range, Q_{SBy} and Q_{SSy} , and also shows predicted and measured total integrated LSST, Q_{Sy} , for both Test 1 and Test 3, respectively. In both cases, incident wave heights are nearly the same but Test 3 has longer waves than Test 1. Therefore the breaker types for the two cases are different, i.e. spilling breakers for Test 1 and plunging breakers for Test 3. Thus, by comparing the predicted sediment transport characteristics between Test 1 and Test 3, one can see the influence of the breaker types on the sediment transport characteristics. As seen in Figure 5-30, the longshore bedload transport rates are nearly the same in Test 1 and Test 3 except around the bar-crest ($X \simeq -14\text{m}$), where the bedload transport in Test 3 is about $100\text{m}^2/\text{year}$ larger than in Test 1. As seen in Table 5.8, predicted Q_{SBy} increases by about 30% from Test 1 to Test 3. On the other hand, Test 3 (plunging breaker) yields significantly larger suspended sediment transport rate than Test 1 around the bar crest and the predicted Q_{SSy} for Test 3 becomes more than twice as large as the one for Test 1 as seen in Table 5.8. In the vicinity of the bar crest, the reference concentration, which determines the magnitude of the suspended sediment concentrations, also increases from Test 1 to Test 3 (see Figures 5-17 and 5-18). However, the increase of the reference concentration is at most 30% while the suspended sediment transport rates in this vicinity for Test 3 are about 20 times larger than those for Test 1. We also observed that the predicted longshore current velocities are of the same order of magnitude for Test 1 and Test 3 (Figures 4-23 and 4-24). From these observations, one can deduce that the primary contribution to the significant increase of the suspended sediment transport in the bar-crest vicinity for the plunging breaker case is the increased turbulence due to the broken waves. In Test 3, most waves abruptly break on the bar crest and therefore yield strong turbulence intensities in the water column. This strong turbulence keeps larger amounts of sediment suspended in the water column and therefore increases the suspended sediment transport rate. The present model reasonably explains the increase of suspended sediment transport rates associated with plunging breakers.

From Table 5.8, the contributions of the suspended sediment transport to the total LSST is about 60% for Test 1 and about 70% for Test 3. In the natural field,

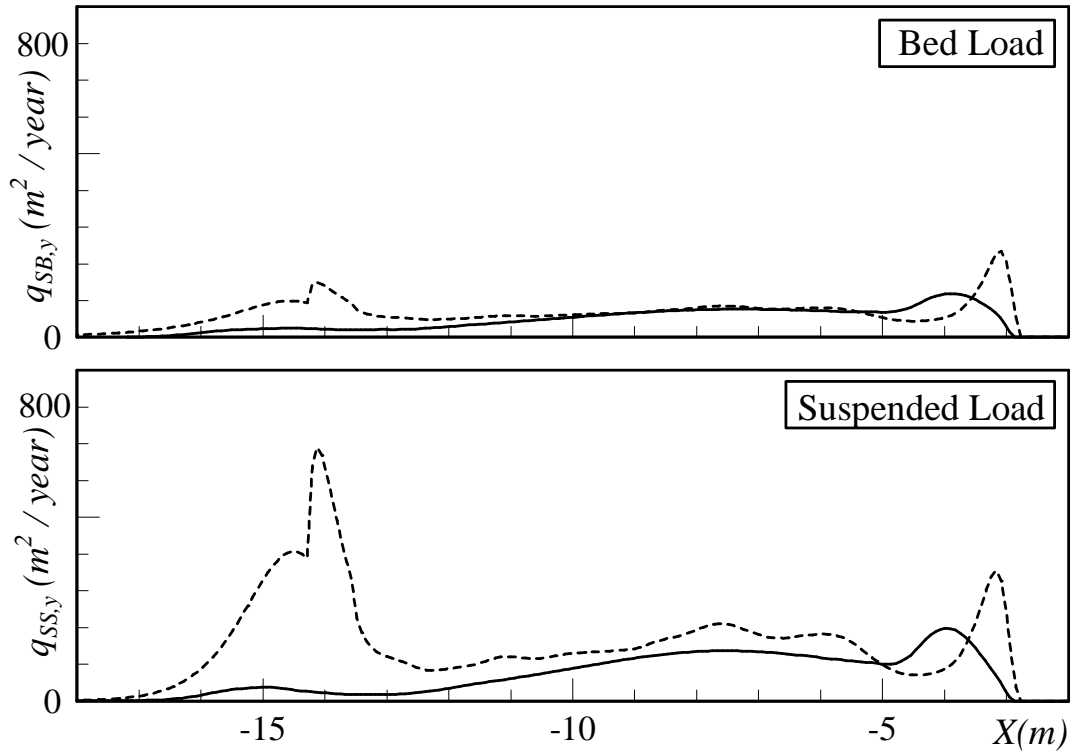


Figure 5-30: Comparisons of longshore bedload and suspended load transport rates between Test 1 (spilling breakers, full line) and Test 3 (plunging breakers, dashed line).

Table 5.8: Measured and predicted bed load, suspended load and total LSST integrated over the entire cross-shore region, $Q_{SB,y}$, $Q_{SS,y}$, and $Q_{Sy} = Q_{SB,y} + Q_{SS,y}$, respectively. Units of the measured and predicted LSST are in (m^3/year).

	predictions			meas.	relative error
	$Q_{SB,y}$	$Q_{SS,y}$	Q_{Sy}	Q_{Sy}	
Test 1	711	1105	1816	1424	0.22
Test 3	1043	2467	3510	3896	-0.11

waves may be much larger than those observed in the LSTF experiments while the bottom sand grain may be as large as those applied in the experiments. Thus we expect that the relative sediment grain size in the field becomes finer than those in the experiment. The contribution of the suspended sediment transport to the total LSST is therefore expected to be dominant for most field conditions.

5.7 Summary and Conclusion

Making use of the present near-shore hydrodynamics model, we extend the conceptual bedload sediment transport model and associated suspended sediment transport model (Madsen, 2001) to predictions for the local sediment transport rate in the surf zone. The surf zone hydrodynamic characteristics were accounted for in the present sediment transport model. For instance, increase of the turbulent eddy diffusivity due to broken waves changes the suspended sediment concentrations and the force balance of broken waves and surface rollers affect the bottom current shear stress.

The model was applied to the LSTF experiments, in which random waves are obliquely incident on a long, straight beach with a movable sand bed. The wave non-linearity and the bottom slope had significant influence on the bedload sediment transport rate in the cross-shore direction while neither of these characteristics had a significant influence on predictions of the longshore sediment transport rate and the reference concentrations for suspended load. Accounting for multiple grain size-classes, the predictions of the suspended sediment concentration profiles were improved considerably over those obtained for a single grain size, D_{n50} .

In the cross-shore (x) direction, the predicted mean suspended sediment transport rate agreed well with the measurements. The mean error of the predicted mean suspended sediment transport rate was about 15%. We also investigated the cross-shore balance of the total sediment transport on the equilibrium beach for Test 1 and Test 3. The non-linear wave effects significantly affected the cross-shore balance of the total sediment transport. Further model modifications and additional considerations are required in order to explain the cross-shore balance of the sediment transport on

equilibrium beaches especially in the swash-zone.

In the shore-parallel (y) direction, the model predicted peaks of LSST near the shore line both for Test 1 and Test 3 and the peak near the bar-crest for Test 3. The model slightly under-predicted the peak LSST near the shore-line for both Test 1 and Test 3. Since the measurements contain relatively large LSST land-ward the shore-line, i.e. above the predicted mean water level, some modifications for swash-zone hydrodynamics, such as wave run-up and surf-beat effects, may be required to improve the model predictions near the shore-line. Comparing the predicted LSST for Test 1 and Test 3, the present model reasonably explained the significant increase of the suspended sediment transport due to the plunging-type breaking waves. Although the model reasonably predicted the peak LSST near the bar-crest for Test 3, the predicted cross-shore extent of the peak was somewhat narrower than the measurements and the model under-predicted the LSST around the bar trough. This under-prediction may be improved by accounting for the lateral sediment flux due to advections and diffusions. Finally, quantitative predictive skills of the model was examined by comparing measured and predicted total LSST integrated over the cross-shore transects and the local suspended sediment transport rates. The mean errors of the predicted suspended sediment transport rates were about 30% in the longshore (y) direction both for Test 1 and Test 3. The error of the total LSST was about 22% for Test 1 and -11% for Test 3.

The model does not contain any empirical fitting coefficients except the resuspension parameter for the reference concentration model. The resuspension parameter was obtained from the separate experiments for unidirectional steady flows. Considering these facts the overall predictive skills of the model are considered good in its ability to capture both quantitative and qualitative features of longshore sediment transport along long, straight beaches.

Chapter 6

Summary and Concluding Remarks

In Chapter 2, we developed a model for predictions of nearshore wave characteristics. Numerical experiments with weakly non-linear periodic waves shoaling across a plane sloping bottom were used to establish simple expressions relating non-linear wave characteristics to those obtained when the waves were shoaled according to linear wave theory. Using the obtained expressions, non-linear wave characteristics may be reconstructed from knowledge of the characteristics of their linear equivalent. To obtain this knowledge a model, based entirely on linear wave theory, was developed for the evolution of wave heights as periodic waves travel from deep water up to their breaking point and as broken waves on into the surf zone where they dissipate their energy. Since this model for shoaling, breaking, and broken periodic waves is based on linear theory, a simple extension to random narrow-banded spectral waves was presented.

The excellent predictive skills of the model, in terms of its prediction of measured, and therefore non-linear, wave heights in the vicinity of the breaking point and inside the surf zone were demonstrated for periodic waves normally incident on a plane beach, random waves normally incident on a barred concrete beach, and random waves of small oblique incidence on barred movable bed beach profiles. The model was also shown to be successful in predicting non-linear characteristics (magnitude, skewness and asymmetry) of the near-bottom wave orbital velocity around the breaking point and inside the surf zone.

The present wave model is simple to apply because it is based on linear wave theory and the concept of an equivalent linear wave. Since the equivalent linear wave conserves energy flux the present model should be particularly well suited for the evaluation of radiation stresses driving long-shore and cross-shore currents. Combined with the surface roller model, this anticipation was supported by the demonstrated ability of the present model to accurately predict wave set-up for both periodic and random waves. Furthermore, the model's demonstrated ability to predict near-bottom orbital velocity features, which are of utmost importance in evaluation of flow resistance and sediment transport processes, suggests its suitability for adoption in models for hydrodynamic and sediment transport processes in the surf zone.

The concept of the surface roller was introduced in Chapter 3 to improve predictions of depth-averaged undertow velocity and wave set-up. Physical characteristics of the surface roller were determined as functions of the surface roller energy, E_{sr} , and an energy balance equation, which is consistent with the present wave model, was developed to capture the spatial evolution of the surface roller energy. A simple extension of the model to random waves was also proposed.

The validity of the model was tested against experimental data for periodic and random waves incident on plane uniformly sloping beaches with various slopes and random waves incident on a barred beach. Through comparisons of the predicted wave heights, wave set-up and depth-averaged undertow, excellent agreement verified the predictive skills of the model. It should be emphasized that no empirically fitted coefficient was applied in the present surface roller model.

The surface roller also had significant effects on the nearshore mean current velocity. Near the breaking point, for example, growing surface roller energy yields seaward acting momentum force and this force explained the sea-ward-leaning profiles of the undertow velocity observed near the breaking point. In the shore-parallel direction, the surface roller force balances the wave radiation stress force at the breaking point and gives a continuous longshore force across the breaking point. Some distance inside the surf zone, surface roller energy, E_{sr} , starts to decrease and the surface roller increases the longshore momentum force inside the surf zone. This feature shifts the

peak of the longshore current velocity shoreward.

In Chapter 4, we developed the near-shore mean shear current model. The near-shore mean current fields were determined from 2DH momentum equations integrated above the trough level and over the entire depth, respectively. Vertical profiles of the mean shear currents are analytically determined from a simple turbulent eddy viscosity model and a linearly varying mean shear stress obtained from the trough-level and the bottom shear stresses. Closed form solutions for the mean current velocity profiles were obtained and integrated to yield explicit expressions for forcings needed in the integrated momentum equations. This feature dramatically reduces the computational load for numerical applications of the model. The present near-shore current model is also applicable to random waves by using external forcings and volume fluxes for waves and surface rollers determined from our wave and surface roller models for random wave applications. Although we here limited the model application to long, straight beach conditions, the model concepts can be extended to arbitrary beach profiles including along-shore variability.

In the cross-shore (x) direction, forces due to the hydrostatic pressure, wave radiation stress, and the surface roller dominate the other forces such as bottom friction shear stress and mean-current-associated convective acceleration forces. Reasonable predictions of the wave set-up and set-down are therefore obtained from the force balance equations without bottom shear stress.

In the shore-parallel (y) direction, in contrast, mean-current-associated convective acceleration forces were comparable to the wave and the surface roller forces. In the depth-integrated momentum equations, similar to Svendsen and Putrevu's (1994) model, the mean-current-associated forces, such as the current-current, wave-current and surface roller-current interactions, had significant effects to disperse the longshore current velocity and, coupled with the surface roller model, to shift the peak of the longshore current velocity toward the shoreline. These mean-current-associated forces dominate the lateral mixing term due to turbulence and allow us to avoid an empirical lateral mixing to obtain smoothly varying near-shore current fields. The present model also accounted for the mean-current associated forces in the momentum

equations above the trough level and the trough shear stress obtained in this manner shifted the peak of the longshore current velocity further inside the surf zone and improved the predictive skills of the longshore current velocity profiles on the plane beach.

The modified Madsen (1994) wave-current bottom boundary layer model was adopted to specify the bottom boundary conditions for the near-shore current model. The application of Madsen's (1994) bottom boundary layer model reduces the specification necessary to evaluate the bottom shear stress term in the momentum equations to a specification of the bottom roughness. This bottom roughness may be known, e.g. in laboratory experiments with fixed-bed roughness, or it may be estimated for movable bed conditions, such as rippled or sheet flow beds, by introducing the equivalent bottom roughness through empirically determined relationships as functions of bottom sediment and flow characteristics. Some of these equivalent bottom roughness models were reviewed and adopted for computations.

Predictive skills of the near-shore current model were examined through comparisons with experimental data for periodic or random waves normally or obliquely incident on uniform plane and barred beaches. The validity of the adoption of the modified Madsen (1994) wave-current bottom boundary layer model was confirmed by comparing predicted depth-averaged longshore current velocity with experimental data by Visser (1991), in which both smooth concrete and gravel beaches were subjected to identical periodic incident wave conditions. The model successfully predicts the decrease of the longshore current velocity due to the increase in bottom roughness. From the model comparison with Visser's (1991) experiments, we observed that the longshore current velocity is sensitive to the value of the bottom roughness, k_N , if this is varied by an order of magnitude or more. Therefore, we can expect reasonable predictions of the longshore current velocity if we know the bottom roughness within an order of magnitude accuracy.

The model was also applied to the LSTF experiments with movable sand bed, in which the bed conditions are in a "break-off" range, i.e. intermediate to equilibrium (2D) ripples and sheet flow. The model with the sheet flow roughness slightly over-

predicted the longshore current velocity while it under-estimated with $k_N = k_{NR} \simeq \eta_r =$ the ripple height, which is about an order of magnitude larger than the sheet flow roughness.

No parameter was fitted against any near-shore mean current data. In the entire nearshore hydrodynamics models, the only parameters empirically fitted against experimental data were (i) the breaking criteria, $(u_c/C)_b$, (ii) the dissipation constant for broken waves, K_b , and (iii) the equivalent bottom roughness for a movable bed, k_N (Herrmann, 2004). For the fixed bed plane beach condition, predictive skills of the present model are still comparable to those of the best-fit classical Longuet-Higgins' (1970) longshore current model, in which the optimum empirical coefficients for the lateral dispersion, N , and the bottom friction, C_f , were calibrated. It should be pointed out that the movable bed roughness was separately obtained from steady flow experiments. Considering these facts, quantitative predictive skills of the longshore current model for the movable bed condition, whose mean prediction error of the depth-averaged longshore current velocity was $O(10\%)$, are also reasonably good.

Finally in Chapter 5, we introduced the predicted near-shore hydrodynamic characteristics and extended the conceptual bedload and suspended load sediment transport models (Madsen, 2001) to predictions for the local sediment transport rates in the surf zone. In this manner, the surf zone hydrodynamic characteristics were accounted for in the present sediment transport model. For instance, the increase of the turbulent eddy diffusivity due to broken waves changes the suspended sediment concentrations and the force balance of broken waves and surface rollers affect the bottom current shear stress.

The model was applied to the LSTF experiments. The wave non-linearity and the bottom slope had significant influence on the bedload sediment transport rate in the cross-shore direction while neither of these characteristics had pronounced contributions to the longshore sediment transport rates and the reference concentrations for suspended load. Accounting for multiple grain size-classes, the predictive ability for the suspended sediment concentration profiles was considerably improved over just using a single grain size, D_{50} .

In the cross-shore (x) direction, the predicted mean suspended sediment transport rate agreed well with the measured experimental data. The mean error of the predicted mean suspended sediment transport rate was about 15%. We also investigated the cross-shore balance of the total sediment transport on the equilibrium beach for Test 1 and Test 3. The wave non-linearity significantly affects the cross-shore balance of the total sediment transport and further refinements of the model for appropriate evaluations of non-linear wave effects are called for. Both for Test 1 and Test 3, predicted shore-ward bedload transport rate due to the skewness of the non-linear wave orbital velocity balanced with the sea-ward mean suspended sediment transport rates and yielded near-zero total cross-shore sediment transport rates in the surf zone. However, the sea-ward suspended sediment transport dominated the shore-ward bedload sediment transport due to wave non-linearity and yielded relatively large sea-ward transport rates near the swash zone for both Test 1 and Test 3 and near the bar-crest for Test 3, where the model predicted considerable suspended sediment concentrations due to the intensive turbulence caused by plunging-type broken waves. Therefore, in order to explain the cross-shore balance of the sediment transport on the equilibrium beaches, we require further model modifications and additional modelings that account for the swash-zone hydrodynamics and wave-wave suspended sediment transport.

In the shore-parallel (y) direction, in contrast to the shore-normal (x) direction, wave non-linearity has a negligible effect on the mean sediment transport rates because the waves propagate near-normal to the straight shore line. The model predicted peaks of LSST near the shore line both for Test 1 and Test 3 and the peak near the bar-crest for Test 3. The model, however, under-predicted the peak LSST near the shore-line for both Test 1 and Test 3. Since the measurements contains relatively large LSST land-ward the shore-line, i.e. above the predicted mean water level, the model may require additional modeling for swash-zone hydrodynamics such as wave run-up and surf-beat effects in order to improve the predictive skills near the shore-line. Comparing the predicted LSST for Test 1 and Test 3, the present model successfully explained the significant increase of the suspended sediment transport due to the

plunging-type breaking waves. Although the model reasonably predicted the peak LSST near the bar-crest for Test 3, the cross-shore range of the peak was slightly narrower than shown by the measurements and the model under-predicted the LSST around the bar-trough. This under-prediction may be improved by accounting for the lateral sediment flux due to advections and diffusions. Finally, quantitative prediction skills of the model were examined by comparing the model predictions with measured total LSST integrated over the cross-shore transects and the local suspended sediment transport rates. The mean prediction errors of suspended sediment transport rates were 24% for Test 1 and 33% for Test 3, in which $O(10\%)$ -over-predictions of the predicted longshore current velocity were included. Qualitative prediction skills of the model for the cross-shore distributions of LSST were also examined by comparing the predicted and measured local LSST at 20 cross-shore locations. Out of 20 points, which contain 3 points above the mean water level where the model yielded zero LSST, 12 and 10 points were within 50%-error for Test 1 and Test 3, respectively, and 16 points were within 65%-error for both Test 1 and Test 3. The error of the total integrated LSST was about 22% for Test 1 and -11% for Test 3. The model does not contain any empirical fitting coefficients except the resuspension parameter for the reference concentration model. The resuspension parameter was obtained from the separate experiments for unidirectional steady flows. Moreover, the model assumed sheet flow bed conditions although in the LSTF experiments the bed was covered by rounded ripples. Considering these facts the overall predictive skills of the model are considered good in its ability to capture both quantitative and qualitative features of longshore sediment transport along long, straight beaches.

Based on the conceptual sediment transport model (Madsen, 2001) and the present near-shore hydrodynamics model, we predicted both bedload and suspended load sediment transport rates for the LSTF experiments, the “intermediate” scale experiments to natural field and laboratories. In the LSTF experiments, the bed conditions are in a “break-off” range, i.e. between equilibrium (2D) rippled bed and sheet flow bed conditions. The predicted contribution of the longshore suspended sediment transport to the total LSST was about 60% for Test 1 and about 70% for Test 3. In the

larger scale natural field, waves may be much larger than those observed in the LSTF experiments while the bottom sand grain may be about the same size as those applied in the experiments. In the field, therefore, the bed should predominantly be the sheet flow condition and the relative sediment grain size should become finer than those in the LSTF experiment. The contribution of the suspended sediment transport to the total LSST is thus expected to be dominant for most field conditions. In this sense, we should more focus on the investigation of suspended sediment transports in order to accurately capture the sediment transport features and resulting beach morphology changes in the field.

Appendix A

Derivation of Expressions for Trough and Bottom Shear Stress

In most depth-averaged near-shore mean current models, depth-integrated momentum equations are commonly applied to define the relationship between bottom shear stress and other forces such as those due to wave radiation stresses, mean pressure, and mean current advections. Similar to Svendsen and Putrevu's (1994) approach, the present model accounts for the advective momentum force associated with mean currents. Svendsen and Putrevu (1994) showed, from their numerical application, that this feature reasonably explains distributions of the longshore current velocity in the cross-shore direction without introducing any empirical lateral eddy viscosity or dispersion coefficient. The most significant difference between the present derivations and those of Svendsen and Putrevu (1994) is that the present model also evaluates the mean shear stress at the wave trough level from the momentum equations integrated above the wave trough.

A.1 Pressure Force

The vertical momentum equation in the fluid reads

$$\rho \left(\frac{\partial w}{\partial t} + \frac{\partial uw}{\partial x} + \frac{\partial vw}{\partial y} + \frac{\partial w^2}{\partial z} \right)$$

$$= -\frac{\partial p}{\partial z} - \rho g + \frac{\partial \tau_{xz}}{\partial x} + \frac{\partial \tau_{yz}}{\partial y} + \frac{\partial \tau_{zz}}{\partial z} \quad (\text{A.1})$$

With the vertical axis, z , set to zero, i.e., $z = 0$ at the still water level, integrating (A.1) from wave trough level, $z = z_{tr}$, to the free surface, $z = \eta$ yields, with application of Leibnitz' rule,

$$\begin{aligned} & \rho \left[\frac{\partial}{\partial t} \int_{z_{tr}}^{\eta} w dz + \frac{\partial}{\partial x} \int_{z_{tr}}^{\eta} u w dz + \frac{\partial}{\partial y} \int_{z_{tr}}^{\eta} v w dz \right] \\ & - \rho w_{\eta} \left\{ \frac{\partial \eta}{\partial t} + u_{\eta} \frac{\partial \eta}{\partial x} + v_{\eta} \frac{\partial \eta}{\partial y} - w_{\eta} \right\} \\ & + \rho w_{tr} \left(u_{tr} \frac{\partial z_{tr}}{\partial x} + v_{tr} \frac{\partial z_{tr}}{\partial y} - w_{tr} \right) \\ = & -p_a + p_{tr} - \rho g (\eta - z_{tr}) \\ & + \int_{z_{tr}}^{\eta} \frac{\partial \tau_{xz}}{\partial x} dz + \int_{z_{tr}}^{\eta} \frac{\partial \tau_{yz}}{\partial y} dz + \tau_{zz,\eta} - \tau_{zz,tr} \end{aligned} \quad (\text{A.2})$$

where subscripts, η and tr , denote values at the free surface and at trough level, respectively. Terms in $\{ \} = 0$ by virtue of the kinematic free surface boundary condition and p_a is air pressure at the free surface. Rearranging (A.2) yields the pressure at the trough level

$$\begin{aligned} p_{tr} = & p_a + \rho g (\eta - z_{tr}) \\ & + \rho \left[\frac{\partial}{\partial t} \int_{z_{tr}}^{\eta} w dz + \frac{\partial}{\partial x} \int_{z_{tr}}^{\eta} u w dz \right. \\ & \left. + \frac{\partial}{\partial y} \int_{z_{tr}}^{\eta} v w dz - w_{tr}^2 \right] \\ & + \rho w_{tr} \left(u_{tr} \frac{\partial z_{tr}}{\partial x} + v_{tr} \frac{\partial z_{tr}}{\partial y} \right) \\ & - \int_{z_{tr}}^{\eta} \frac{\partial \tau_{xz}}{\partial x} dz - \int_{z_{tr}}^{\eta} \frac{\partial \tau_{yz}}{\partial y} dz - \tau_{zz,\eta} + \tau_{zz,tr} \end{aligned} \quad (\text{A.3})$$

A.2 Some simplifications

We separate the fluid velocity into mean and wave components according to

$$(u, v, w) = (U, V, W) + (\tilde{u}, \tilde{v}, \tilde{w}) \quad (\text{A.4})$$

In terms of order of magnitude, we allow the horizontal mean current velocity to be comparable to wave orbital velocities, i.e.

$$O(U) = O(V) = O(\tilde{u}) = O(\tilde{v}) \quad (\text{A.5})$$

In the vertical direction, however, we assume the horizontal length-scale for waves (L_w) to be considerably smaller than that of mean currents (L_m), and therefore assume

$$\begin{aligned} O(W) &= O(Uh/L_m) \\ &\simeq \frac{L_w}{L_m} O(\tilde{u}h/L_w) = \frac{L_w}{L_m} O(\tilde{w}) \ll O(\tilde{w}) \end{aligned} \quad (\text{A.6})$$

Since we are concerned with near-shore waters the waves approach long waves and \tilde{w} is already quite small. Thus $O(W) < O(\tilde{w})$ is sufficient to support the neglect of vertical mean current components from the dynamic pressure.

Viscous stresses are assumed to be exclusively due to mean current components, for instance,

$$\tau_{zx} = \rho\nu \frac{\partial U}{\partial z} \quad (\text{A.7})$$

and, as customary, normal viscous stresses are neglected, i.e.

$$\tau_{zz} \approx 0 \quad (\text{A.8})$$

since these appear together with and are dominated by hydrostatic pressures.

Since W is assumed to be small, shear stresses due to horizontal variance of W are also small, i.e.,

$$\frac{\partial \tau_{xz}}{\partial x}, \frac{\partial \tau_{yz}}{\partial y} \ll \frac{\partial \tau_{zi}}{\partial z} \quad (\text{A.9})$$

Much of our attention will focus on near-surface conditions, i.e. $z \geq z_{tr}$. In this proximity of the surface we assume wave orbital velocities and horizontal mean current velocities to be sufficiently accurately represented by a "surface value" independent

of z , i.e.

$$(\tilde{u}, \tilde{v}, \tilde{w}) \simeq (\tilde{u}_s, \tilde{v}_s, \tilde{w}_s) \quad (z \geq z_{tr}) \quad (\text{A.10})$$

and

$$(U, V) = (U_s, V_s) \quad (z \geq z_{tr}) \quad (\text{A.11})$$

Finally, we assume wave motions to be simply represented by linear wave theory, i.e.,

$$\begin{pmatrix} \tilde{u}_s \\ \tilde{v}_s \\ \tilde{w}_s \\ \tilde{\eta} \end{pmatrix} = \begin{pmatrix} \hat{u}_s \cos \varphi \\ \hat{v}_s \cos \varphi \\ \hat{w}_s \sin \varphi \\ a \cos \varphi \end{pmatrix} \quad (\text{A.12})$$

where $\varphi = k_x x + k_y y - \omega t$ is the wave phase, $a = H/2$ is the wave amplitude, and \hat{u}_s , \hat{v}_s , and \hat{w}_s are amplitudes of wave orbital velocities in the respective directions. The free surface elevation, η , and the trough level, z_{tr} , in (A.3) are therefore expressed as $z_{tr} = \bar{\eta} - a$, which is not a function of time as already anticipated in (A.2), and $\eta = \bar{\eta} + a \cos \varphi$, where $\bar{\eta}$ is the mean water level, i.e. the set-up.

A.3 Mean Pressure

Invoking the assumptions stated in the previous section, (A.3) may be simplified to read

$$\begin{aligned} p &= p_a + \rho g (\eta - z_{tr}) \\ &+ \rho \left[\frac{\partial}{\partial t} \int_{z_{tr}}^{\eta} \tilde{w}_s dz + \frac{\partial}{\partial x} \int_{z_{tr}}^{\eta} (U_s + \tilde{u}_s) \tilde{w}_s dz \right. \\ &\quad \left. + \frac{\partial}{\partial y} \int_{z_{tr}}^{\eta} (V_s + \tilde{v}_s) \tilde{w}_s dz - \tilde{w}_s^2 \right] \\ &+ \rho \tilde{w}_s \left((U_s + \tilde{u}_s) \frac{\partial z_{tr}}{\partial x} + (V_s + \tilde{v}_s) \frac{\partial z_{tr}}{\partial y} \right) \end{aligned} \quad (\text{A.13})$$

where the integrations are readily carried out since the integrands, by virtue of (A.10) and (A.11), are assumed constant, e.g.

$$\begin{aligned}\int_{z_{tr}}^{\eta} \tilde{w}_s dz &= \tilde{w}_s (\eta - z_{tr}) \\ &= \hat{w}_s a \sin \varphi (1 + \cos \varphi)\end{aligned}\tag{A.14}$$

Mean pressure at the trough level, \bar{p}_{tr} , is determined by introducing velocity components (A.12) into (A.13) and time-averaging to obtain

$$\bar{p}_{tr} = p_a + \rho g (\bar{\eta} - z_{tr}) - \overline{\rho \tilde{w}_s^2}\tag{A.15}$$

Mean pressure force above the trough level is determined from

$$P_s = \overline{\int_{z_{tr}}^{\eta} p dz}\tag{A.16}$$

Substituting the coordinate elevation $z_{tr} = z$ in (A.13) and use of (A.10) and (A.11), enable simple evaluations of the integrations in (A.16) and result in

$$\begin{aligned}P_s &= p_a (\bar{\eta} - z_{tr}) + \overline{\frac{\rho g}{2} (\eta - z_{tr})^2} \\ &\quad + \overline{\frac{\rho}{2} \frac{\partial}{\partial t} (\tilde{w}_s (\eta - z_{tr})^2)} \\ &\quad + \overline{\frac{\rho}{2} \frac{\partial}{\partial x} (\tilde{u}_s \tilde{w}_s (\eta - z_{tr})^2)} \\ &\quad + \overline{\frac{\rho}{2} \frac{\partial}{\partial y} (\tilde{v}_s \tilde{w}_s (\eta - z_{tr})^2)} - \overline{\rho \tilde{w}_s^2 (\eta - z_{tr})} \\ &= p_a a + \frac{E}{2} + \frac{\rho g a^2}{2} - a \overline{\tilde{w}_s^2}\end{aligned}\tag{A.17}$$

in which the terms represent atmospheric pressure force, mean wave-associated pressure force ($E = \rho g a^2 / 2$ is the wave energy), hydrostatic pressure force, and dynamic pressure force.

A.4 Trough Shear Stress

Shear stress at the trough level in the cross-shore direction, $\tau_{tr,zx}$, is determined by integrating the horizontal momentum equation,

$$\begin{aligned} & \rho \left(\frac{\partial u}{\partial t} + \frac{\partial u^2}{\partial x} + \frac{\partial uv}{\partial y} + \frac{\partial uw}{\partial z} \right) \\ &= -\frac{\partial p}{\partial x} + \frac{\partial \tau_{xx}}{\partial x} + \frac{\partial \tau_{yx}}{\partial y} + \frac{\partial \tau_{zx}}{\partial z} \end{aligned} \quad (\text{A.18})$$

from $z = z_{tr}$ to $z = \eta$ to obtain

$$\begin{aligned} & \rho \left[\frac{\partial}{\partial t} \int_{z_{tr}}^{\eta} u dz + \frac{\partial}{\partial x} \int_{z_{tr}}^{\eta} u^2 dz + \frac{\partial}{\partial y} \int_{z_{tr}}^{\eta} uv dz \right] \\ & + \rho u_{tr} \left[u_{tr} \frac{\partial z_{tr}}{\partial x} + v_{tr} \frac{\partial z_{tr}}{\partial y} - w_{tr} \right] \\ &= -\frac{\partial}{\partial x} \int_{z_{tr}}^{\eta} p dz + p_a \frac{\partial \eta}{\partial x} - \bar{p}_{tr} \frac{\partial z_{tr}}{\partial x} \\ & + \int_{z_{tr}}^{\eta} \frac{\partial \tau_{yx}}{\partial y} dz + \tau_{ax} + \tau_{srx} - \tau_{tr,zx} \end{aligned} \quad (\text{A.19})$$

where the kinematic free surface boundary condition was invoked. In (A.19), τ_{ax} represents the shear stress at the surface, e.g. due to winds, and τ_{srx} is an excess shear force due to the surface roller acting at the trough, determined in the following section. Time-averaging (A.19) over the wave period, with the assumption of vertical uniformity for horizontal velocity components, yields the mean current shear stress at the trough level, $\tau_{csx} = \tau_{tr,zx}$, as

$$\begin{aligned} \tau_{csx} &= -\frac{\partial}{\partial x} P_s + p_a \frac{\partial \bar{\eta}}{\partial x} - \bar{p}_{tr} \frac{\partial z_{tr}}{\partial x} \\ & - \rho \left[\frac{\partial}{\partial x} \overline{\int_{z_{tr}}^{\eta} u_s^2 dz} + \rho \frac{\partial}{\partial y} \overline{\int_{z_{tr}}^{\eta} u_s v_s dz} \right] \\ & - \overline{\rho u_s^2} \frac{\partial z_{tr}}{\partial x} - \overline{\rho u_s v_s} \frac{\partial z_{tr}}{\partial y} + \overline{\rho u_{tr} w_{tr}} \\ & + \int_{z_{tr}}^{\bar{\eta}} \frac{\partial \tau_{yx}}{\partial y} dz + \tau_{ax} + \tau_{srx} \end{aligned} \quad (\text{A.20})$$

in which $u_{tr} \simeq u_s$ and w_{tr} are velocity components at the trough to be determined in the following section. Introducing (A.10) and (A.11) simplifies the integrations in (A.20) with substitution of (A.15) and (A.17),

$$\begin{aligned}
\tau_{csx} = & -\frac{\partial}{\partial x} \left(p_a a + \frac{E}{2} + \frac{\rho g a^2}{2} - \rho a \overline{\tilde{w}_s^2} \right) \\
& + p_a \frac{\partial (\bar{\eta} - z_{tr})}{\partial x} - \left(\rho g a - \rho \overline{\tilde{w}_s^2} \right) \frac{\partial z_{tr}}{\partial x} \\
& - \rho \frac{\partial}{\partial x} \left((\tilde{u}_s + U_s)^2 (\eta - z_{tr}) \right) \\
& - \rho \frac{\partial}{\partial y} \left((\tilde{u}_s + U_s) (\tilde{v}_s + V_s) (\eta - z_{tr}) \right) \\
& - \rho \left(\overline{\tilde{u}_s^2} + U_s^2 \right) \frac{\partial z_{tr}}{\partial x} - \rho \left(\overline{\tilde{u}_s \tilde{v}_s} + U_s V_s \right) \frac{\partial z_{tr}}{\partial y} \\
& + \rho \overline{u_{tr} w_{tr}} \\
& + a \frac{\partial \tau_{yx}}{\partial y} + \tau_{ax} + \tau_{srx}
\end{aligned} \tag{A.21}$$

Finally, introducing (A.12) yields the complete expressions for the trough shear stress,

$$\begin{aligned}
\tau_{csx} = & -a \frac{\partial p_a}{\partial x} - \rho g a \frac{\partial \bar{\eta}}{\partial x} \\
& - \frac{\partial}{\partial x} \left(\frac{E}{2} \right) + \frac{\rho a}{2} \frac{\partial \hat{w}_s^2}{\partial x} + \frac{\rho \hat{w}_s^2}{2} \frac{\partial \bar{\eta}}{\partial x} \\
& - \rho a \frac{\partial}{\partial x} \left(\frac{\hat{u}_s^2}{2} + U_s^2 \right) - \rho a \frac{\partial}{\partial y} \left(\frac{\hat{u}_s \hat{v}_s}{2} + U_s V_s \right) \\
& - \rho \left(\frac{\hat{u}_s^2}{2} + U_s^2 \right) \frac{\partial \bar{\eta}}{\partial x} - \rho \left(\frac{\hat{u}_s \hat{v}_s}{2} + U_s V_s \right) \frac{\partial \bar{\eta}}{\partial y} \\
& - \rho \frac{\partial}{\partial x} (a \hat{u}_s U_s) - \frac{\rho}{2} \frac{\partial}{\partial y} (a \hat{u}_s V_s + a \hat{v}_s U_s) \\
& + \rho \overline{u_{tr} w_{tr}} \\
& + a \frac{\partial \tau_{yx}}{\partial y} + \tau_{ax} + \tau_{srx}
\end{aligned} \tag{A.22}$$

A.5 Momentum forces due to surface roller

Inside the surf zone, we account for the excess shear force due to the surface roller. We first assume that the mean fluid velocities in the surface roller are affected by the

mean current velocity near the surface, i.e.

$$(u_{sr}, v_{sr}) = (C \cos \theta + U_s, C \sin \theta + V_s) \quad (\text{A.23})$$

with θ denoting the angle of incidence of the waves. Time-averaged momentum flux components due to the roller are then determined, by use of the volume flux of the roller, $(q_{srx}, q_{sry}) = S_{sr}/T (\cos \theta, \sin \theta)$ to be

$$\begin{aligned} & \begin{pmatrix} M_{sr,xx} & M_{sr,yx} \\ M_{sr,xy} & M_{sr,yy} \end{pmatrix} \\ &= \rho \begin{pmatrix} R_{xx} + U_s q_{srx} & R_{yx} + U_s q_{sry} \\ R_{xy} + V_s q_{srx} & R_{yy} + V_s q_{sry} \end{pmatrix} \end{aligned} \quad (\text{A.24})$$

where R_{xx} , $R_{xy} = R_{yx}$, and R_{yy} are momentum flux components due to pure surface roller given by (4.10) and (4.11) in Chapter 4. The trough-level shear stress due to the roller, τ_{srj} ($j = 1, 2$), is determined from the change of these mean momentum fluxes, i.e.

$$\tau_{srj} = -\frac{\partial M_{sr,xj}}{\partial x} - \frac{\partial M_{sr,yj}}{\partial y} \quad (\text{A.25})$$

A.6 Mean vertical momentum flux at trough level

The vertical velocity at the trough level, w_{tr} , is determined from the continuity equation with application of Leibnitz' rule as

$$\begin{aligned} w_{tr} &= \frac{\partial}{\partial x} \left(\int_{z_{tr}}^{\eta} u_s dz + q_{srx} \right) + \frac{\partial}{\partial y} \left(\int_{z_{tr}}^{\eta} v_s dz + q_{sry} \right) \\ &\quad + u_s \frac{\partial z_{tr}}{\partial x} + v_s \frac{\partial z_{tr}}{\partial y} + \frac{\partial \eta}{\partial t} \end{aligned} \quad (\text{A.26})$$

Multiplying (A.26) by $u_{tr} = u_s$ and time-averaging yield the mean vertical momentum transfer force in (A.22),

$$\rho \overline{u_{tr} w_{tr}} = \rho \left(U_s \frac{\partial q_{sx}}{\partial x} + \left(U_s^2 + \frac{\hat{u}_s^2}{2} \right) \frac{\partial z_{tr}}{\partial x} \right)$$

$$\begin{aligned}
& +\rho \left(U_s \frac{\partial q_{sy}}{\partial y} + \left(U_s V_s + \frac{\hat{u}_s \hat{v}_s}{2} \right) \frac{\partial z_{tr}}{\partial y} \right) \\
& +\rho \hat{u}_s \left(\frac{\partial q_{wx}}{\partial x} + \frac{\partial q_{wy}}{\partial y} \right)
\end{aligned} \tag{A.27}$$

with mean wave volume flux and the total volume flux above the trough level denoting $q_{wx} = a\hat{u}_s/2$ and $q_{sx} = U_s a + q_{wx} + q_{srx}$, respectively.

A.7 Mean Trough Shear Stress

Substitution of (A.27) into (A.22) we obtain, after some algebraic manipulations, simplified expressions for the trough-level mean shear component,

$$\begin{aligned}
\tau_{csx} = & \tau_{ax} - a \frac{\partial p_a}{\partial x} - \rho g a \frac{\partial \bar{\eta}}{\partial x} - \frac{\partial}{\partial x} R_{xx} \\
& - \frac{\partial}{\partial x} \left(\frac{E}{2} \right) + \frac{\rho a}{2} \frac{\partial \hat{w}_s^2}{\partial x} + \frac{\rho \hat{w}_s^2}{2} \frac{\partial \bar{\eta}}{\partial x} \\
& - \rho \left[q_{sx} \frac{\partial U_s}{\partial x} + \left(q_{wx} + \frac{a U_s}{2} \right) \frac{\partial \hat{u}_s}{\partial x} \right] \\
& + a \frac{\partial \tau_{yx}}{\partial y} - \frac{\partial}{\partial y} R_{yx} \\
& - \rho \left[q_{sy} \frac{\partial U_s}{\partial y} + \left(q_{wy} + \frac{a V_s}{2} \right) \frac{\partial \hat{u}_s}{\partial y} \right]
\end{aligned} \tag{A.28}$$

where R_{xx} and $R_{yx} = R_{xy}$ are momentum flux components of the surface roller without mean current as derived in (4.10) and (4.11). The mean trough shear stress in the y -direction, τ_{csy} , is determined by replacing x by y , (\hat{u}, U) by (\hat{v}, V) and $\cos \theta$ by $\sin \theta$ and vice versa in (A.28).

A.8 Mean Bottom Shear Stress

To obtain an expression for the bottom shear stress, we start from (A.18) and integrate it from the bottom, $z = -h_0$ to the trough level, $z = z_{tr} = \bar{\eta} - a$ where h_0 is the still

water depth.

$$\begin{aligned}
& \rho \left[\frac{\partial}{\partial x} \int_{-h_0}^{z_{tr}} \overline{u^2} dz + \frac{\partial}{\partial y} \int_{-h_0}^{z_{tr}} \overline{uv} dz \right] \\
& - \rho u_{tr} \left[u_{tr} \frac{\partial z_{tr}}{\partial x} + v_{tr} \frac{\partial z_{tr}}{\partial y} - w_{tr} \right] \\
& - \rho u_b \left\{ u_b \frac{\partial h_0}{\partial x} + v_b \frac{\partial h_0}{\partial y} + w_b \right\} \\
= & - \frac{\partial}{\partial x} \int_{-h_0}^{z_{tr}} \bar{p} dz + \bar{p}_{tr} \frac{\partial z_{tr}}{\partial x} + \bar{p}_b \frac{\partial h_0}{\partial x} \\
& + \int_{-h_0}^{z_{tr}} \frac{\partial \tau_{yx}}{\partial y} dz + \tau_{tr, zx} - \tau_{b, zx}
\end{aligned} \tag{A.29}$$

Again, $\{ \} = 0$ from the kinematic bottom boundary condition and combining (A.29) with (A.20) determines the bottom shear stress

$$\begin{aligned}
\tau_{cbx} = & \tau_{ax} + \tau_{srx} \\
& - \frac{\partial}{\partial x} \left(P_s + \int_{-h_0}^{z_{tr}} \bar{p} dz \right) + p_a \frac{\partial \bar{\eta}}{\partial x} + \bar{p}_b \frac{\partial h_0}{\partial x} \\
& - \rho \left[\frac{\partial}{\partial x} \int_{z_{tr}}^{\bar{\eta}} \overline{u_s^2} dz + \frac{\partial}{\partial x} \int_{-h_0}^{z_{tr}} \overline{u^2} dz \right] \\
& - \rho \left[\rho \frac{\partial}{\partial y} \int_{z_{tr}}^{\bar{\eta}} \overline{u_s v_s} dz + \rho \frac{\partial}{\partial y} \int_{-h_0}^{z_{tr}} \overline{uv} dz \right] \\
& + \int_{-h_0}^{\bar{\eta}} \frac{\partial \tau_{yx}}{\partial y} dz
\end{aligned} \tag{A.30}$$

Introducing (A.4), (A.15) and (A.17) into (A.30) yields

$$\begin{aligned}
\tau_{cbx} = & \tau_{ax} + \tau_{srx} \\
& - h \frac{\partial p_a}{\partial x} - \rho g h \frac{\partial \bar{\eta}}{\partial x} \\
& - \frac{\partial}{\partial x} S_{xx} - \rho \tilde{w}_b^2 \frac{\partial h_0}{\partial x} \\
& - \rho \frac{\partial}{\partial x} \int_{-h_0}^{\bar{\eta}} U^2 dz - \rho \frac{\partial}{\partial x} (2q_{wx} U_s) \\
& - \frac{\partial}{\partial y} S_{yx} + \int_{-h_0}^{\bar{\eta}} \frac{\partial \tau_{yx}}{\partial y} dz \\
& - \rho \frac{\partial}{\partial y} \int_{-h_0}^{\bar{\eta}} UV dz - \rho \frac{\partial}{\partial y} (q_{wy} U_s + q_{wx} V_s)
\end{aligned} \tag{A.31}$$

where

$$S_{xx} = \rho \int_{-h_0}^{\bar{\eta}} (\bar{u}^2 - \bar{w}^2) dz + \frac{E}{2} \quad (\text{A.32})$$

$$S_{yx} = S_{xy} = \rho \int_{-h_0}^{\bar{\eta}} \bar{u} \bar{v} dz \quad (\text{A.33})$$

$$S_{yy} = \rho \int_{-h_0}^{\bar{\eta}} (\bar{v}^2 - \bar{w}^2) dz + \frac{E}{2} \quad (\text{A.34})$$

are the well-known wave radiation stresses and $h = h_0 + \bar{\eta}$ is a mean water depth. According to Mei (1989), the sixth term in (A.31), $\rho \bar{\tilde{w}}_b^2 \partial h_0 / \partial x$, is negligible for a gently sloping bottom.

Again, the bottom shear stress in the y -direction, τ_{cby} , is determined by replacing x by y , (\hat{u}, U) by (\hat{v}, V) and $\cos \theta$ by $\sin \theta$ and vice versa in (A.31).

A.9 Simplifications for Depth-Integrated Momentum Equations

To simplify the integrations in (A.31), we follow the similar approach to Svendsen and Putrevu (1994). We first separate the mean current velocity below the trough level into two components, i.e.

$$(U, V) = (U_0, V_0) + (U', V') \quad (\text{A.35})$$

where

$$(U_0, V_0) = \frac{1}{h_{tr}} \int_{-h_0}^{z_{tr}} (U, V) dz = \frac{1}{h_{tr}} (q_{bx}, q_{by}) \quad (\text{A.36})$$

are the “depth-averaged” mean current velocity components over the wave trough depth, $h_{tr} = h_0 + \bar{\eta} - a$, and (U', V') are the vertical distribution of the mean current departures from their depth-averaged values, and q_{bx} and q_{by} are the total volume fluxes below the trough in the x and y directions, respectively.

Svendsen and Putrevu (1994) assumed $O(U_0) \sim O(U') \ll O(\tilde{u})$ in the x -direction and neglected the second order terms of U_0 and U' . We also assume $O(U') \ll O(\tilde{u})$,

and neglect the second order terms of (U') . In contrast to their approach, we allow $O(U_0) \sim O(V_0) \sim O(\tilde{u})$ and keep all the second order terms of these mean current velocities. Terms of order U_0^2 can be non-trivial where abrupt changes of the current field may be expected, such as around the breaking point for periodic waves.

Introducing these expressions into (A.31) simplifies τ_{cbx} to

$$\begin{aligned}
\tau_{cbx} = & \tau_{ax} - h \frac{\partial p_a}{\partial x} - \rho g h \frac{\partial \bar{\eta}}{\partial x} \\
& - \frac{\partial}{\partial x} S_{xx} - \frac{\partial}{\partial x} R_{xx} - \rho \bar{w}_b^2 \frac{\partial h_0}{\partial x} \\
& - \rho \frac{\partial}{\partial x} ((q_{sx} + q_{wx}) U_s + q_{bx} U_0) \\
& - \frac{\partial}{\partial y} S_{yx} - \frac{\partial}{\partial y} R_{yx} \\
& - \rho \frac{\partial}{\partial y} (q_{sy} U_s + q_{wy} V_s + q_{by} U_0) \\
& + \int_{-h_0}^{\bar{\eta}} \frac{\partial \tau_{yx}}{\partial y} dz
\end{aligned} \tag{A.37}$$

The turbulent viscous term, τ_{yx} , is also approximately determined from depth-averaged velocity gradients, i.e.

$$\tau_{xy} = \tau_{yx} = \begin{cases} \rho \nu_{ts} \left(\frac{\partial V_s}{\partial x} + \frac{\partial U_s}{\partial y} \right) & (z \geq z_{tr}) \\ \rho \nu_{t0} \left(\frac{\partial V_0}{\partial x} + \frac{\partial U_0}{\partial y} \right) & (z \leq z_{tr}) \end{cases} \tag{A.38}$$

with ν_{ts} , eddy viscosity at the trough level, and ν_{t0} , depth-averaged eddy viscosity below the trough level, obtained from the turbulent eddy viscosity model discussed in Section 4.4.2.

For a long-straight beach condition, i.e. $\partial/\partial y = 0$, the total volume flux in x -direction below the trough, q_{bx} , is specified by requiring zero total volume flux in the x -direction, i.e. $q_{bx} = -q_{sx}$ and τ_{cbx} may be further simplified.

Appendix B

Model Application for Numerical Computations

This Appendix discusses the methodologies for application of the near-shore hydrodynamics model to numerical computations. The numerical model first computes the cross-shore distributions of wave and surface roller characteristics. Predicted wave and surface roller characteristics are then used to compute the near-shore mean current.

B.1 Waves and Surface Rollers

Since the present model is based entirely on the equivalent linear wave, it is simple to apply. We first discretize the cross-shore beach profiles with even horizontal intervals, Δx , and specify the incident wave conditions at the off-shore boundary.

The numerical computation starts at the off-shore grid point where both water depth and wave conditions are known. Assuming that the water depth at the off-shore boundary is sufficiently deep, we take both mean water level and surface roller energy to be zero at the off-shore boundary. Given all the variables at i -th grid point, linear wave theory determines the wave shoaling and refraction at the adjacent shoreward $(i + 1)$ -th grid point for non-breaking periodic wave conditions. Once the wave hits the breaking point, whose criteria is determined by (2.20), energy dissipation

equation (2.21) determines the equivalent linear wave height in the surf zone. For random waves, (2.27) is applied instead of (2.21) at all the grid points because a certain fraction of waves are assumed always broken even in the deep water. Similarly, either (3.13) or (3.16) is applied to determine the surface roller energy respectively for periodic or random wave conditions while wave characteristics are computed.

Once wave and surface roller characteristics at $(i+1)$ -th grid point are determined, (3.10) determines the elevation of the mean water level at $(i+1)$ -th grid point. Note that, when computing the wave and surface roller conditions, we require the mean water depth, i.e. the mean water level at $(i+1)$ -th grid point to estimate the wave phase velocity and group velocity from linear wave dispersion relationship. Since the mean water level is not yet known at $(i+1)$ -th grid point, we require numerical iteration to determine wave and surface roller characteristics and mean water level. In the numerical code, we first compute the wave and surface roller characteristics by initially taking $\bar{\eta}_{i+1} = \bar{\eta}_i$. From the obtained wave and surface roller characteristics at $(i+1)$ -th grid point, (3.10) is used to renew the prediction of $\bar{\eta}_{i+1}$. Using newly determined $\bar{\eta}_{i+1}$, wave and surface roller characteristics are repeatedly computed. Since the mean water elevation is relatively small compared to the still water depth, this numerical computation converges within a few numerical iterations. As shown in Chapter 4, the influence of the bottom shear stress on the wave setup determined in (3.10) is negligibly small. Thus, for computational efficiency, the numerical code neglects the bottom shear stress in (5.15) when determining the mean water level.

Following the above procedures, equivalent linear wave and surface roller characteristics are obtained and these characteristics are readily transformed to the non-linear wave characteristics from (2.2) through (2.6).

B.1.1 Effective Bottom Slope

As discussed in Chapters 2 and 3, one of the essential improvements of the present wave and surface roller models is that they account for the influence of the bottom slope. For application of the model to natural beaches with arbitrary profiles, we need to consider the appropriate local bottom slopes for evaluation of wave and surface

roller characteristics. For example, a natural movable bed beach may contain small scale geometry, such as ripples, which should affect the bottom roughness but not have significant influence on the local wave characteristics such as breaking wave dissipation rates and asymmetry and skewness of the near-bottom wave orbital velocity profiles. The beach profile may often be barred, i.e., we may have increasing water depth in the shoreward direction over a portion of the surf zone while our model is originally developed only for decreasing water depth, i.e., for a positive bottom slope throughout the surf zone. On an arbitrary beach profile, in which the local bottom slopes vary from place to place, it may be more realistic to expect that the characteristics of waves reaching a given depth reflect their history, i.e., the average slope of the bottom over which they have progressed prior to arrival in the given depth.

Accounting for these conceptual ideas, the numerical model determines the effective bottom slope through the following procedures: (i) remove the effect of ripples by taking a running average of the discretized depth data; (ii) make imaginary beach profile (A) by drawing a horizontal line from the bar-crest to the shoreward until the line hits the actual beach profile (dashed straight line A in Figure B-1); (iii) make another imaginary beach profile (B) by drawing a horizontal line from the bar-trough to the seaward until the line hits the actual beach profile (dashed straight line B in Figure B-1); (iv) define the effective bottom slopes for both beach profiles (A) and (B) as the average slope over some distance, Δx_L , seaward of the point of interest; and (v) if the effective bottom slopes for beach profiles (A) and (B) differ, take the maximum of the two. Figure B-1 illustrates the concept of this evaluation of the effective bottom slopes. The length of Δx_L may be scaled by local wave length and therefore vary with local depth. In this study, we take $\Delta x_L \simeq 0.5L$, with L , the local wave length. Note that this effective bottom slope is used only for the wave and surface roller model. The nearshore current model does not contain the explicit effect of the bottom slope. In the sediment transport model, the bottom slope for the bedload sediment transport model should be scaled by grain diameters. The bottom slope for the sediment transport model is therefore determined by the smallest horizontal interval, Δx , from the smoothed depth data, i.e. after removal of ripple effects.

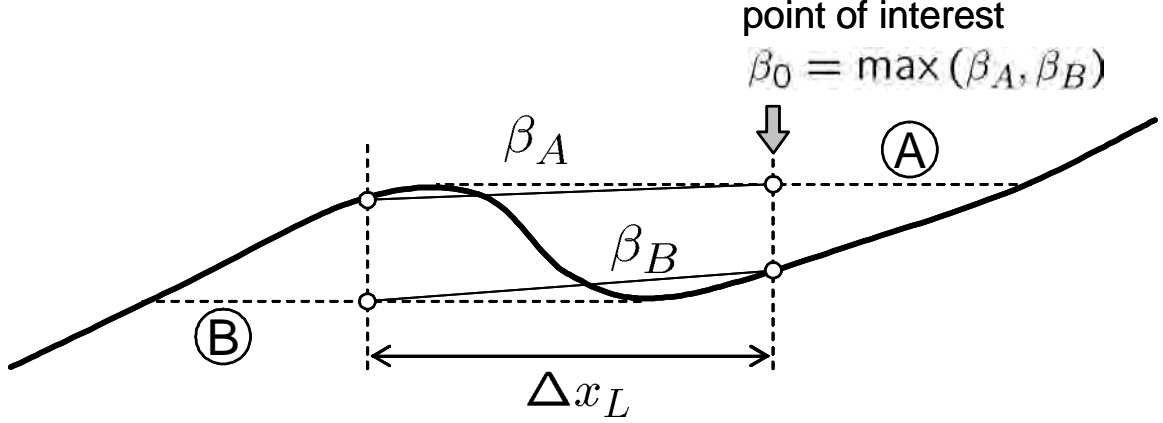


Figure B-1: Concept of the effective bottom slope

B.2 Nearshore Mean Current

Provided spatial distributions of wave and surface roller characteristics are already known, the near-shore mean current model determines unknown variables, (τ_{csx}, τ_{csy}) , (τ_{cbx}, τ_{cby}) , $\bar{\eta}$, and (q_{bx}, q_{by}) . All other variables can be determined as functions of these seven variables. In order to specify these seven variables, the following seven equations are applied: bottom boundary conditions, (4.29), momentum equations above the trough level, (4.33) and (4.41), momentum equations for the entire depth, (4.49) and (4.50). Some of the terms in the momentum equations, (4.33) and (4.49), are canceled out and further simplified formulae are applied in the numerical applications. Under the long-straight beach condition, $\partial/\partial y = 0$, q_{bx} is determined from mass conservation,

$$q_{bx} = -q_{sx} = -(q_{wx} + q_{srx} + aU_s) \quad (\text{B.1})$$

Numerical iteration is needed to solve these variables because non-linear advection terms are included in the momentum equations.

In order to obtain a steady state solution, we start from quiescence and ramp up the wave and surface roller forcings. During this initial stage we employ the unsteady form of (4.50) and solve

$$\rho \frac{\partial q_y}{\partial t} = r(t)(F_{bwy} + F_{sry}) + F_{bmy} + F_{bwm_y}$$

$$+F_{srm y} + F_{bvy} - \tau_{cby} \quad (\text{B.2})$$

where $q_y = q_{by} + aV_s + r(t)(q_{wy} + q_{sry})$ is the total mean volume flux in the alongshore y -direction. Note that $F_{bwy} + F_{sry}$ is a known variable obtained from wave and surface roller models. $r(t)$ is a ramp-up function that smoothly increases from zero to unity as t increases. For example, $r(t)$ may be defined as

$$r(t) = \begin{cases} 0.5 \left[1 - \cos\left(\frac{\pi t}{T_r}\right) \right] & 0 < t \leq T_r \\ 1 & T_r < t \end{cases} \quad (\text{B.3})$$

Ramp-up period, T_r , is set to be five wave periods in the numerical application. Starting from initial conditions of zero mean current, numerical computation of (B.2) is repeated until steady state condition, $\partial/\partial t = 0$ is obtained after $r(t)$ becomes unity. In the steady state, i.e., $\partial q_y/\partial t = 0$ and $r(t) = 1$, (B.2) becomes identical to (4.50). To ensure computational stability, $r(t)$ is also applied to known variables, q_{wj} and q_{srj} in the momentum equations, (4.33) and (B.2), and continuity equation, (B.1). Although adoption of a smaller time step, Δt , accomodates more stable numerical computations, the smaller Δt requires a larger number of iteration times to ensure the model to be sufficiently converged. In this sense, one should choose as large a Δt as possible while keeping computations stable. The magnitude of Δt should be related to the horizontal grid interval, Δx . The upper limit of Δt may be determined by $\Delta x/\Delta t > \max(|U| + \sqrt{gh})$. Here, U is a mean current velocity and \sqrt{gh} is a wave phase velocity in the shallow water. Because $|U|$ is an unknown variable, but often smaller than the wave phase velocity, $\Delta x/\Delta t > \sqrt{gh_{\max}}/2$, i.e. $\Delta t < 2\Delta x/\sqrt{gh_{\max}}$ may be the safer approximation for determination of Δt with h_{\max} , the maximum water depth in the system. The horizontal resolution, Δx , may be scaled by the wave length. In the LSTF experiment Test 1, for example, the length scale of Δx is roughly $\Delta x \simeq L_0/50$. Finally, the numerical scheme is summarized as follows.

1. Set $q_y = V_0 = V_s = U_s = \bar{\eta} = 0$.
2. Evaluate q_{bx} from (B.1)

3. Evaluate (τ_{csx}, τ_{csy}) from momentum equations above the trough level, (4.33) and (4.41)
4. Based on old (τ_{cbx}, τ_{cbx}) , evaluate bottom boundary layer thickness, δ , from (4.24)
5. Evaluate (τ_{cbx}, τ_{cbx}) from bottom boundary condition, (4.29)
6. Evaluate (U_s, V_s) from (4.27) with $\vec{\tau}_{cs}$ and $\vec{\tau}_{cb}$ obtained in steps (3) and (4)
7. Compute $\bar{\eta}$ from (4.49)
8. Obtain $q_y^{new} = q_y + (\partial q_y / \partial t) \Delta t$ where $(\partial q_y / \partial t)$ is obtained from (B.2)
9. Take $q_y = q_y^{new}$ and return to step (2) until steady state, $\left| \left(1 - q_y^{new} / q_y \right) T / \Delta t \right| \leq \varepsilon$ is obtained over the entire computational area with the convergence criterion, $\varepsilon = 0.001$.

B.2.1 Boundary Conditions

In order to solve the momentum equation (B.2) numerically, we require two boundary conditions, one at the off-shore boundary and the other at the on-shore boundary.

Off-Shore Boundary Condition

At the off-shore boundary, we assume that all variables are uniform in the cross-shore (x) direction, i.e. $\partial / \partial x = 0$ and take

$$X_{is-1} = X_{is} \quad (\text{B.4})$$

where X denotes variables such as U , V , U_s , V_s , and q_y , and is is the grid number at the off-shore boundary. In order to assure the assumption of $\partial / \partial x = 0$, input depth data near the off-shore boundary should also be uniform or sufficiently large so that the near-shore current becomes negligibly small.

On-Shore Boundary Condition

In order to avoid the unstable computation, the numerical code stops computation of (B.2) at $i = ie$ near the shore-line where the local trough depth, h_{tr} , becomes smaller than twice the local wave-current bottom boundary layer thickness, i.e. $h_{tr} \leq 2\delta$. We simply assume that the longshore current velocity becomes zero at the mean shore-line where the mean water depth becomes zero and the longshore current velocity at $i = ie + 1$, is linearly interpolated by

$$\bar{V}_{ie+1} = \bar{V}_{ie} \frac{(h_0 + \bar{\eta})_{ie+1}}{(h_0 + \bar{\eta})_{ie}} \quad (\text{B.5})$$

with local still water depth, h_0 .

Appendix C

Predictions of Ripple Geometry

C.1 Introduction

As discussed in Section 4.6.3, an ability to predict the ripple geometry is essential to determine the movable bed roughness of a rippled bed. Geometrical characteristics of sand ripples generated under waves have been studied both in laboratory experiments and through field observations (e.g., Inman, 1957; Keneddy and Falcon, 1965; Carstens et al., 1969; Mogridge and Kamphuis, 1972; Dingler, 1974; Miller and Komer, 1980; Nielsen, 1981; Madsen and Rosengaus, 1988; Sato and Horikawa, 1988; Traykovski et al., 1999; Li et al., 1998; Styles and Glenn, 2002). These observations indicate that ripple height and length immediately reach their equilibrium stage as wave stress increases and initiates the motion of sand grains. In this equilibrium stage, ripple length, λ , is roughly proportional to the near-bottom wave orbital diameter and ripple steepness, η_r/λ , with ripple height, η_r , is at the maximum and stays roughly constant. When the wave stress is further increased, ripple geometry enters a “breakoff” range where the ripple steepness starts to decrease and eventually vanishes. In the breakoff range, ripple length is roughly proportional to bottom sediment diameter and stays nearly constant while the ripple height decreases as the wave stress increases. These extensive observational studies of ripple geometries have yielded a number of models for predictions of ripple geometry (e.g. Nielsen, 1981; Grant and Madsen, 1982; Wikramanayake and Madsen, 1991; Mogridge et al., 1994;

Wiberg and Harris, 1994; Li et al., 1996; Traykovski et al., 1999; Styles and Glenn, 2002).

Some of these models are based on the laboratory experiment for periodic waves and others are developed from laboratory or field data for random waves. From a practical point of view, we focus on the models applicable to natural field, i.e. random wave, conditions. According to Nielsen (1981) and Wikramanayake and Madsen (1991), the ripples generated by random waves tends to become less steep and have rounder crests compared with ripples generated by periodic waves. While most models are based on pure wave conditions, Li and Amos (1998) suggested from their field observations that the shear stress due to mean current should also significantly affect the ripple geometry. In the surf zone, extensive turbulence due to broken waves and wave-induced nearshore currents may also affect ripple characteristics. In this Appendix, we first summarize existing models for prediction of ripple geometry under random wave conditions and compare these models with LSTF experimental data obtained by Wang, et al. (2002).

C.2 Existing Models

Nielsen (1992), on the basis of the field measurements obtained by Inman (1957) and Dingler (1974), proposed the following empirical formulae for predictions of ripple height, η_r , and length, λ , generated by random waves.

$$\lambda/A_{bm,s} = \exp\left(\frac{693 - 0.37 \ln^8 \Psi}{1000 + 0.75 \ln^7 \Psi}\right) \quad (C.1)$$

$$\eta_r/\lambda = 0.342 - 0.34\psi_{2.5}^{0.25} \quad (C.2)$$

$$\eta_r/A_{bm,s} = 21\Psi^{-1.85} \text{ for } \Psi > 10 \quad (C.3)$$

Here $A_{bms} = u_{bms}/\omega$ is bottom excursion amplitude with u_{bms} , amplitude of the near-bottom wave orbital velocity and $\omega = 2\pi/T$, wave frequency. Both A_{bms} and u_{bms} represent significant wave conditions for random waves, i.e. $u_{bm,s} \simeq \sqrt{2}u_{bm,rms}$. The

Mobility number, Ψ , introduced in (C.1) and (C.3), is defined by

$$\Psi = \frac{u_{bm,s}^2}{(s-1)gd} \quad (C.4)$$

and the Shields Parameter, $\psi_{2.5}$, is determined by

$$\psi_{2.5} = \frac{\frac{1}{2}f_{2.5}u_{bm,s}^2}{\rho(s-1)gD_{50}} \quad (C.5)$$

with Jonson's friction factor (Schwartz, 1974).

$$f_{2.5} = \exp \left(5.213 \left(\frac{2.5D_{50}}{A} \right)^{0.194} - 5.977 \right) \quad (C.6)$$

Wikramanayake and Madsen (1991) pointed out that the measured ripple geometries contain significant scatter compared with those obtained in laboratory experiments but have relatively strong correlations with a following non-dimensional parameter,

$$Z = \frac{\psi'_{rms}}{S_*} = \frac{2f'_{cw}\nu(A_{bm,rms}\omega)^2}{D[(s-1)gD]^{1.5}} \quad (C.7)$$

where maximum Shields parameter, ψ'_{rms} , is based on root-mean-square wave height and ' denotes the value for skin shear friction, i.e., f'_{cw} is determined from (4.26) with equivalent bottom roughness, $k'_N = D_{50}$. S_* is a sediment-fluid parameter,

$$S_* = \frac{D}{4\nu} \sqrt{(s-1)gD} \quad (C.8)$$

Based on the field data presented by Inman (1957), Dingler (1974) and Nielsen (1984), Wikramanayake and Madsen (1991) proposed

$$\frac{\eta_r}{A_{brms}} = \begin{cases} 0.018Z^{-0.5} & 0.016 < Z \leq 0.012 \\ 0.0007Z^{-1.23} & 0.012 \leq Z < 0.18 \end{cases} \quad (C.9)$$

$$\frac{\eta_r}{\lambda} = \begin{cases} 0.15Z^{-0.009} & 0.0016 < Z \leq 0.0158 \\ 0.0105Z^{-0.65} & 0.0158 \leq X < 0.18 \end{cases} \quad (C.10)$$

for predictions of ripple geometry in the field with random waves.

Alternately, Wikramanayake and Madsen (1991) also proposed the following empirical formulae based on the measurements of geometry of ripples generated by periodic waves in laboratory experiments.

$$\frac{\eta_r}{A_{bm}} = 0.27 - 0.33\sqrt{\psi'_m} \quad (\text{C.11})$$

$$\frac{\eta_r}{\lambda} = 0.16 - 0.36(\psi'_m)^{2.3} \quad (\text{C.12})$$

Comparing (C.12) with experimental data both for regular and random waves in the same experimental facilities (a wave tunnel, Sato and Horikawa, 1988; a wave flume, Rosengaus, 1987, and Mathisen, 1989), Wikramanayake and Madsen (1991) pointed out that if one were to represent the Shields Parameter for random waves by its root-mean-square value, the breakoff limit of the Shields number for random waves, where ripple steepness significantly decreases, is about a half of that for periodic waves. From this observation, (C.11) and (C.12) may be extended to random waves by substituting Shields parameter for significant waves because $\psi'_{m,s} \simeq 2\psi'_{m,rms}$.

Wiberg and Harris (1994) suggested that geometric ripple characteristics are classified into orbital, anorbital, and suborbital ripples depending on the relationship between sediment diameter, D , and the diameter of the orbital motion just above the bed defined by $d_0 = H/\sinh kh$ in linear theory. Here wave height, H , is represented by the significant wave height for a random sea. The measured data, Wiberg and Harris (1994) applied in their modeling, are Carstens et al. (1969), Mogridge and Kamphuis (1972), Dingler (1974), and Kennedy and Falcon (1965) for periodic waves in laboratory experiments and Inman (1957) and Dingler (1974) for field observations and therefore for random waves. Based on these measured data, Wiberg and Harris (1994) proposed that the length and the height of the orbital ripples, λ_{orb} and η_{orb} , are expressed as

$$\lambda_{orb} = 0.62d_0 \quad (\text{C.13})$$

$$\eta_{orb}/\lambda_{orb} = 0.17 \quad (\text{C.14})$$

Length of the anorbital ripples, λ_{ano} , in contrast to orbital ripples, is independent of d_0 but is proportional to sediment grain diameter, D , i.e.

$$\lambda_{ano} = 535D \quad (C.15)$$

Anorbital ripple height, η_{ano} , is then determined by numerically solving the following empirical formula obtained from field data.

$$\frac{\eta_{ano}}{\lambda_{ano}} = \begin{cases} 0.17 & d_0/\eta_{ano} < 10 \\ \exp \left[-0.095 \left(\ln \frac{d_0}{\eta_{ano}} \right)^2 + 0.442 \ln \frac{d_0}{\eta_{ano}} - 2.28 \right] & d_0/\eta_{ano} \geq 10 \end{cases} \quad (C.16)$$

If d_0/η_{ano} , determined in this manner, is smaller than 20, i.e. $d_0/\eta_{ano} < 20$, the predicted ripples are considered as orbital ripples whose geometric characteristics are determined by (C.13) and (C.14). If $d_0/\eta_{ano} > 100$, then the predicted ripples are considered as anorbital ripples whose geometric characteristics are defined by (C.15) and (C.16). If $20 < d_0/\eta_{ano} < 100$, then the predicted ripples are classified in suborbital ripples and their ripple length, λ_{sub} , becomes $\lambda_{ano} \leq \lambda_{sub} \leq \lambda_{orb}$. Wiberg and Harris proposed the following weighted geometric average of the two to determine λ_{sub} :

$$\lambda_{sub} = \exp \left[\left(\frac{\ln (d_0/\eta_{ano}) - \ln 100}{\ln 20 - \ln 100} \right) (\ln \lambda_{orb} - \ln \lambda_{ano}) + \ln \lambda_{ano} \right] \quad (C.17)$$

The height of suborbital ripple, η_{sub} , is also determined from (C.16) by replacing η_{ano} by η_{sub} and λ_{ano} by λ_{sub} . Note that (C.16) must be solved by numerical iteration, which may affect computational model efficiency.

Li et al. (1996) applied Nielsen (1981) and Grant and Madsen (1982) models to the field data observed at Duck, North Carolina, and the Scotian Shelf where both waves and mean currents were present. Comparing predicted ripple geometries with observations, Li et al. (1996) pointed out that Nielsen's (1981) model tends to under-predict while Grant and Madsen (1982) over-predicts the ripple heights. Li et al. (1996) re-calibrated the Grant and Madsen (1982) model against these field

measurements and proposed

$$\eta_r/A_{bm,s} = \begin{cases} 0.101S_r^{-0.16} & 1 < S_r < S_{rB} \\ 0.356S_r^{-1.5} & S_{rB} < S_r \end{cases} \quad (C.18)$$

$$\lambda/\eta_r = \begin{cases} 4.95S_r^{0.04} & 1 < S_r < S_{rB} \\ 3.03S_*^{-0.6}S_r & S_{rB} < S_r \end{cases} \quad (C.19)$$

where $S_r = \psi_{m,s}/\psi_{cr}$ is a ratio of maximum significant Shields Parameter, $\psi_{m,s}$, and critical Shields Parameter, ψ_{cr} , $S_{rB} = 1.8S_*^{0.6}$ is the breakoff limit of S_r . Li et al. (1998) analyzed the measured ripple data obtained from Sable Island Bank, Scotian Shelf and showed that the geometric characteristics are correlated with ratio of current shear stress and the wave shear stress.

Styles and Glenn (2002) pointed out that the Wikramanayake and Madsen (1991) model is physically inconsistent with the observed ripple geometric characteristics in that the predicted ripple height is independent of near-bottom excursion amplitude, A_{bm} , while a number of observations suggest that ripple geometry is scaled by A_{bm} . Styles and Glenn (2002) re-calibrated Wikramanayake and Madsen's (1991) model by adding LEO-15 data presented by Traykovski et al. (1999) to the field data used by Wikramanayake and Madsen (1991) and Wiberg and Harris (1994) and proposed

$$\frac{\eta_r}{A_{bm,s}} = \begin{cases} 0.30X^{-0.39} & X \leq 2 \\ 0.45X^{-0.99} & X \geq 2 \end{cases} \quad (C.20)$$

$$\frac{\lambda}{A_{bm,s}} = \begin{cases} 1.96X^{-0.28} & X \leq 2 \\ 2.71X^{-0.75} & X \geq 2 \end{cases} \quad (C.21)$$

$$X = \frac{\Psi_{mrms}}{S_*} = \frac{4\nu (A_{bm,rms}\omega)^2}{D [(s-1)gD]^{1.5}} \quad (C.22)$$

Note that significant excursion amplitude, $A_{bm,s}$, is applied in (C.20) and (C.21) while the original Wikramanayake and Madsen (1991) model uses $A_{bm,rms}$. In (C.22), Ψ_{mrms} is a mobility number defined in (C.4) with u_b represented by root-mean-square

wave conditions and S_* is a fluid-sediment parameter determined in (C.8).

C.3 Model Comparisons

We compare these empirical models with LSTF experimental data presented by Wang et al. (2002). Experimental conditions are summarized in Section 4.6.3. In the movable bed cases, Test 1 and Test 3, Wang et al. (2002) obtained the bottom bed elevations along cross-shore transects at intervals of 5mm. We first obtained the smoothed bottom profile by locally averaging the measurements over the length scale of ripple length ($\sim O(10cm)$). Displacements of the bed due to ripple forms were then determined from the fluctuations of the original 5mm-spaced elevations around the smoothed bottom profile. Height and length of each ripple are then defined from the obtained displacement data by zero-up-cross method. According to visual observations, the horizontal directions of the short-crested ripples were non-uniformly distributed. For this reason the ripple length estimated as an distance in the cross-shore direction will always be larger than the actual length while we can still expect reasonable estimations of ripple heights. Figures C-1 and C-2 show the shore-ward distributions of measured ripple heights, steepness and corresponding water depths for Test 1 and Test 3, respectively. In these Figures, solid circles are measurements and dashed lines are the locally averaged measured ripple geometry, which was applied to compute ripple roughness in Section 4.6.3. As seen in the Figures, ripple height and steepness tend to be smaller near the shoreline both in Test 1 and Test 3. In Test 3 (Figure C-2), ripple heights and steepness also decrease around the bar-crest where most waves start to break.

Figures C-3 and C-4 show comparisons of predicted and measured ripple heights and steepness as a function of non-dimensional parameter, $Z = \psi'_{w,rms}/S_*$, defined by (C.7). To determine corresponding Z -value for each measured ripple, we applied predicted local near-bottom wave orbital velocity by interpolating the predictions obtained from the present wave model. In Section 2, we confirmed that our wave model yields reasonable predictions of the near-bottom wave orbital velocity and

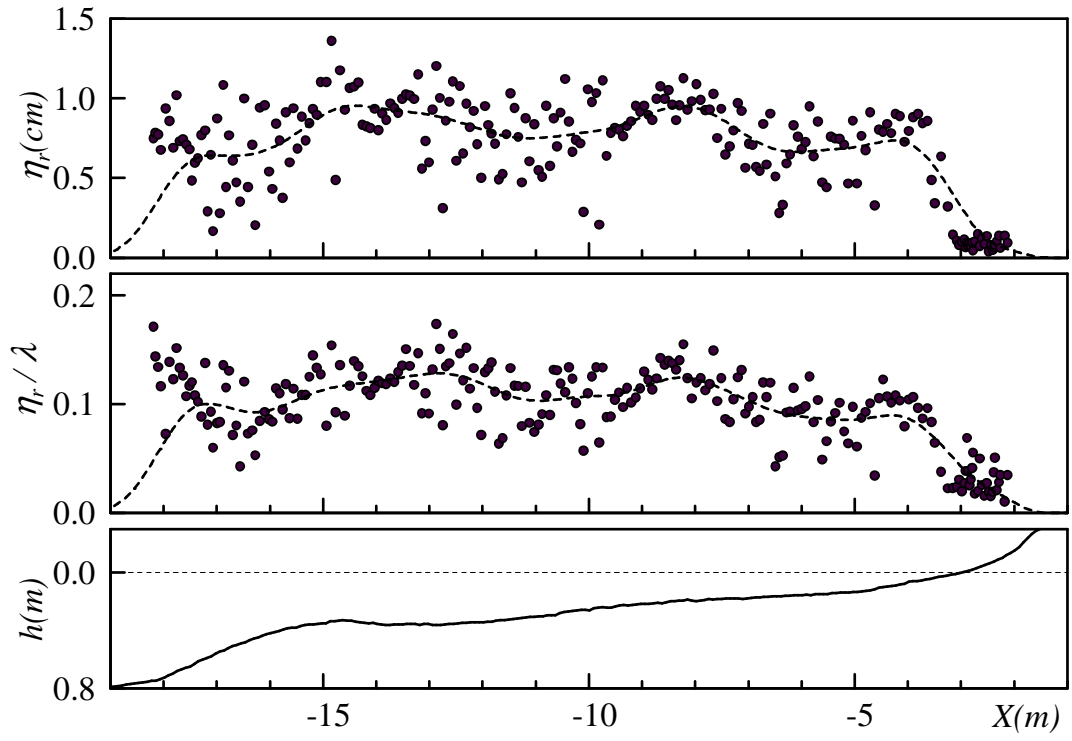


Figure C-1: Cross-shore distributions of measured ripple height, η_r , steepness, η_r/λ , and water depth. Measurements (Test 1: spilling breakers) by Wang et al. (2002) (full circles) and local average (dashed lines).

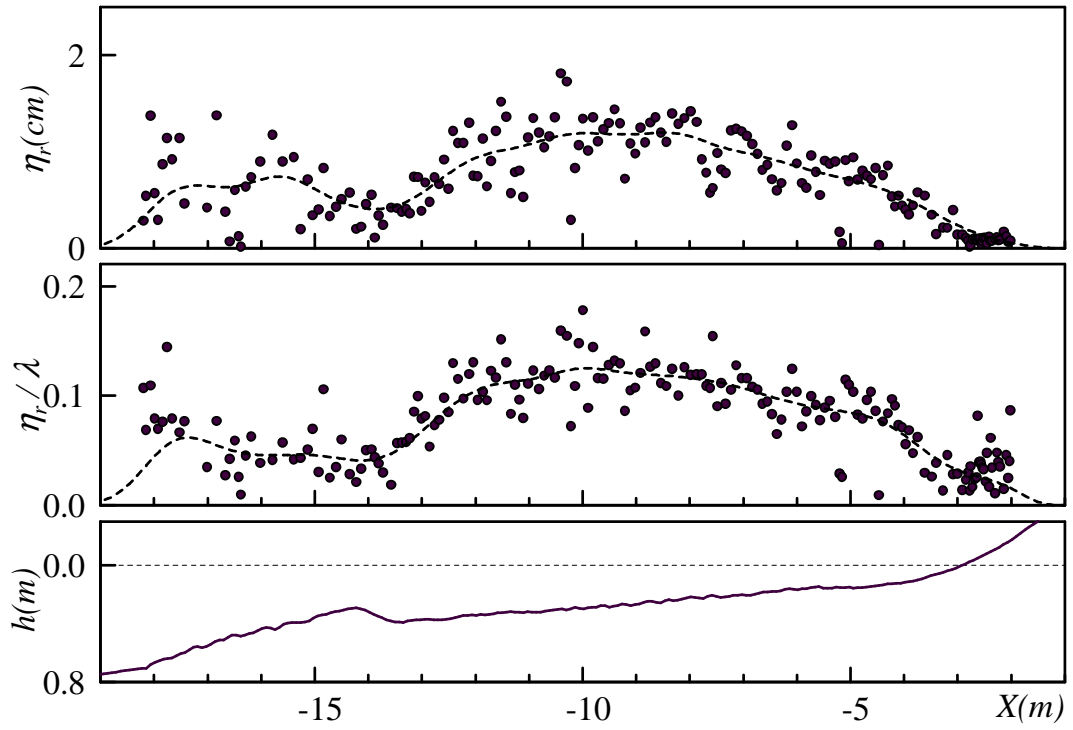


Figure C-2: Cross-shore distributions of measured ripple height, η_r , steepness, η_r/λ , and water depth. Measurements (Test 3; plunging breakers) by Wang et al. (2002) (full circles) and local average (dashed lines).

therefore we can expect the reasonable estimation of Z . Ripple geometries predicted by each predictive model are computed through the following procedures: (1) fix the wave period ($T = 1.5s$ for Test 1 and $T = 3.0s$ for Test 3) and the sediment diameter ($D_n = 0.167mm$) for each experimental case, Test 1 and Test 3; (2) take arbitrary $u_{b,rms}$ in certain broad range so that we can obtain wide-range of Z -values; (3) determine Z from given $u_{b,rms}$, T , and D_n ; and (4) obtain the predictions of ripple geometry from each model from given $u_{b,rms}$, T , and D_n . Note that single Z -value and the corresponding ripple geometry predictions are always determined once $u_{b,rms}$, T , and D_n are determined. In the figure, triangles are the measurements outside the surf zone ($X < -14m$ in Figures C-1 and C-2), open circles are the measurement near the shoreline ($X > -5m$) and solid circles are the rest of measurements. Abbreviations of each predictive model shown in the Figures are WM91F (Wikramanayake and Madsen, 1991, for field), WM91L (Wikramanayake and Madsen, 1991, laboratory), SG02 (Styles and Glenn, 2002), L96 (Li, et al., 1996), N81 (Nielsen, 1981), and WH94 (Wiberg and Harris, 1994), respectively. The sheet flow limit indicated in the figure was determined from Li and Amos (1999) as a function of sediment diameter ($\psi'_{up,rms} \simeq 0.42$ and $Z_{up} = \psi'_{up,rms}/S_* \simeq 0.23$, in this particular experiment). As seen in Figures C-3 and C-4, all predictive models exhibit decreasing ripple heights with increasing $\psi'_{w,rms}$ in the range where measured ripples are plotted. This feature supports our contention in Section 4.6.3 that ripples both in Test 1 and Test 3 are in the breakoff range. Most models still predict relatively large ripple heights even in the sheet flow range indicated in the figure. Ripple heights predicted by WM91L and N81 vanish around the sheet flow limit but N81 tends to under-predict the ripple height comparing with the measurements and other models. Measured data outside the surf zone (open triangles) agree well with most predictive models, especially with WM91L, L96, and SG02. Even inside the surf zone, these models agree reasonably well with measured ripples except near the shoreline. All models, however, over-predict ripple height and steepness near the shoreline (open circles) in both Test 1 and Test 3. This observation suggests that some other physical mechanisms must strongly affect the formation of ripples near the shoreline. For example, and most likely, broken wave

turbulence penetrates to the bottom boundary layer in the shallow water depth and cause wash-out of any bed forms.

Figures C-5 and C-6 exhibit the same distributions of measured ripple geometry as Figures C-1 and C-2 but also show predicted ripple geometries obtained from WM91L, which appears to yield relatively reasonable predictions in this particular experimental case. In the figure, dashed lines are predictions when skin friction wave Shields Parameter was used as originally proposed by Wikramanayake and Madsen (1991). Solid lines are predictions when the maximum skin friction Shields parameter, ψ'_m , based on combined wave and current flow, was substituted instead instead of $\psi'_{w,rms}$. Computation schemes for predictions of ψ'_m is discussed in Appendix D. Applying ψ'_m instead of $\psi'_{w,rms}$ somehow accounts for the increase of flow intensity due to the mean shear current while dashed lines only account for waves. The difference between solid lines and dashed lines are more significant in Test 3 (Figure C-6) because Test 3 is closer to the sheet flow bed condition and ripple height decreases more dramatically with increasing Z , as seen in Figures C-3 and C-4. As seen in Figure C-6, predictions based on ψ'_m (solid lines) yield smaller ripple height and steepness than those applying $\psi'_{w,rms}$ (dashed lines). This decrease of ripple height and steepness apparently improves the predictive skills of ripple geometry especially near the shoreline ($X(m) \simeq -3$). However, the model still over-predicts ripple heights at $-5 < X(m) < -3$ and $-14 < X(m) < -11$. It is interesting to note that these areas are where wave breaking is extensive. As seen in the Figure 2-22 in Chapter 2, most incident waves first break near the bar crest, $-14 < X(m) < -11$, and recovered broken waves resume breaking near the shoreline, $-5 < X(m) < -3$. This observation suggests that broken wave turbulence reaches the bottom in these regions and affect the ripple geometry.

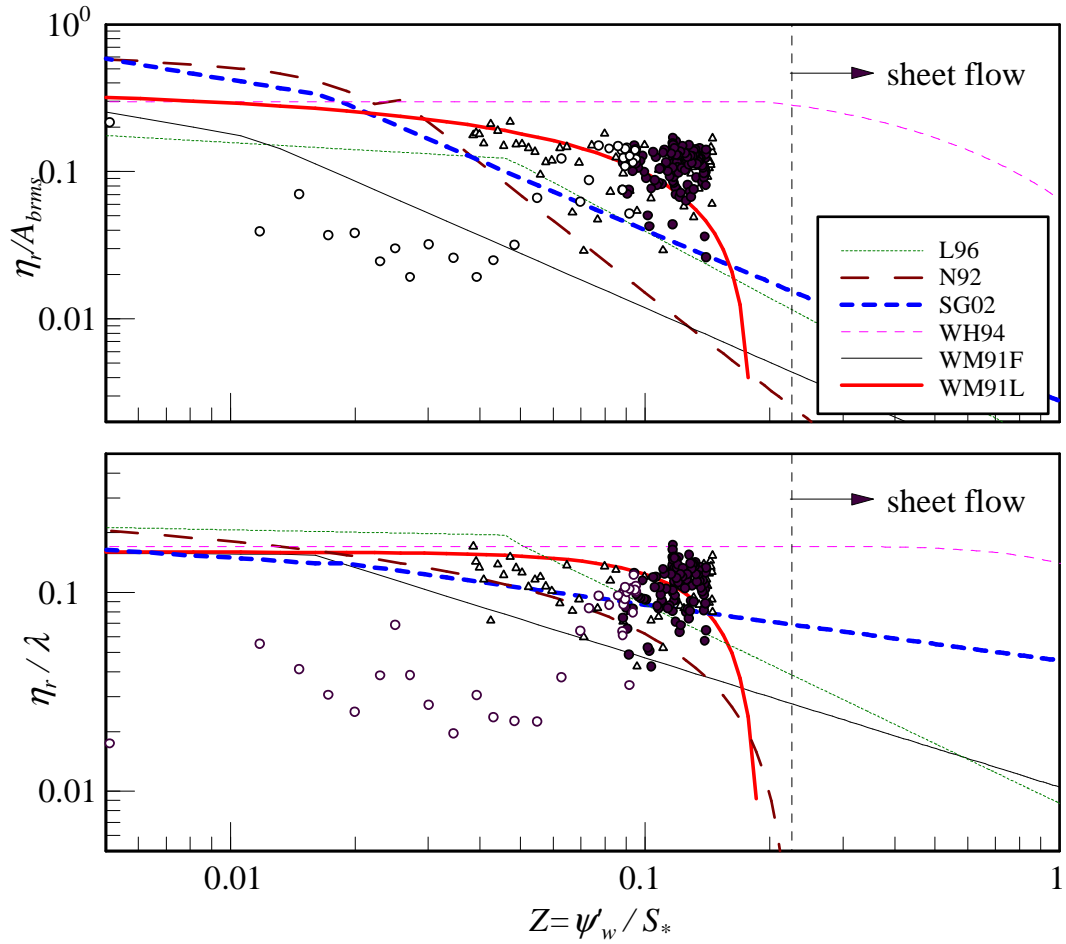


Figure C-3: Comparisons of predicted and measured ripple height, η_r , and steepness, η_r/λ , as a function of non-dimensional parameter, $Z = \psi'_{w,rms}/S_*$ for the experimental case by Wang et al. (2002) (Test 1; spilling breakers). Measurements outside the surf zone ($X(m) < -14$, triangles), inside the surf zone ($-14 < X(m) < -5$, full circles), and near the shoreline ($X(m) > -5$, open circles). Models are WM91F (Wikramanayake and Madsen, 1991, field), WM91L (Wikramanayake and Madsen, 1991, laboratory), SG02 (Styles and Glenn, 2002), L96 (Li et al., 1996), N81 (Nielsen, 1981), and WH94 (Wiberg and Harris, 1994).

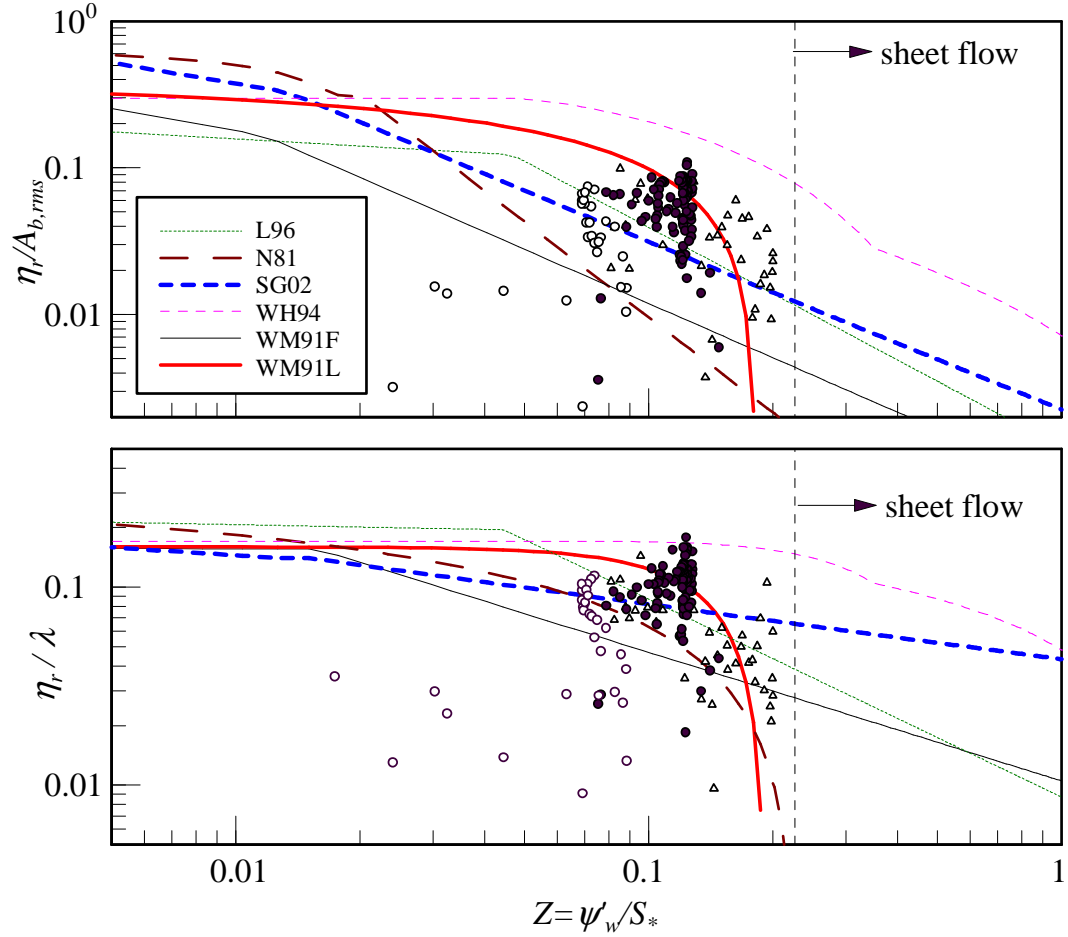


Figure C-4: Comparisons of predicted and measured ripple height, η_r , and steepness, η_r/λ , as a function of non-dimensional parameter, $Z = \psi'_{w,rms}/S_*$ for the experimental case by Wang et al. (2002) (Test 3; plunging breakers). Measurements outside the surf zone ($X(m) < -14$, triangles), inside the surf zone ($-14 < X(m) < -5$, full circles), and near the shoreline ($X(m) > -5$, open circles). Models are WM91F (Wikramanayake and Madsen, 1991, field), WM91L (Wikramanayake and Madsen, 1991, laboratory), SG02 (Styles and Glenn, 2002), L96 (Li et al., 1996), N81 (Nielsen, 1981), and WH94 (Wiberg and Harris, 1994).

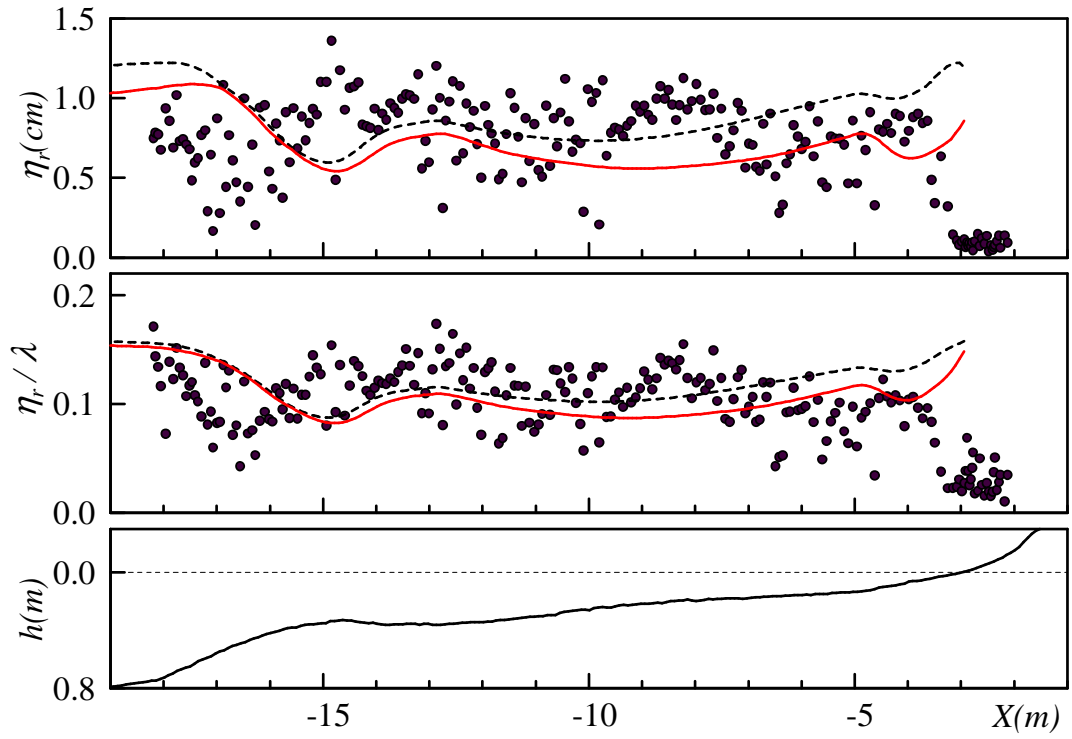


Figure C-5: Cross-shore distributions of measured and predicted ripple height, η_r , steepness, η_r/λ , and water depth. Measurements (Test 1: spilling breakers) by Wang et al. (2002) (full circles) and predictions by Wikramanayake and Madsen (1991) (dashed line based on $\psi'_{w,rms}$; full line based on ψ'_m).

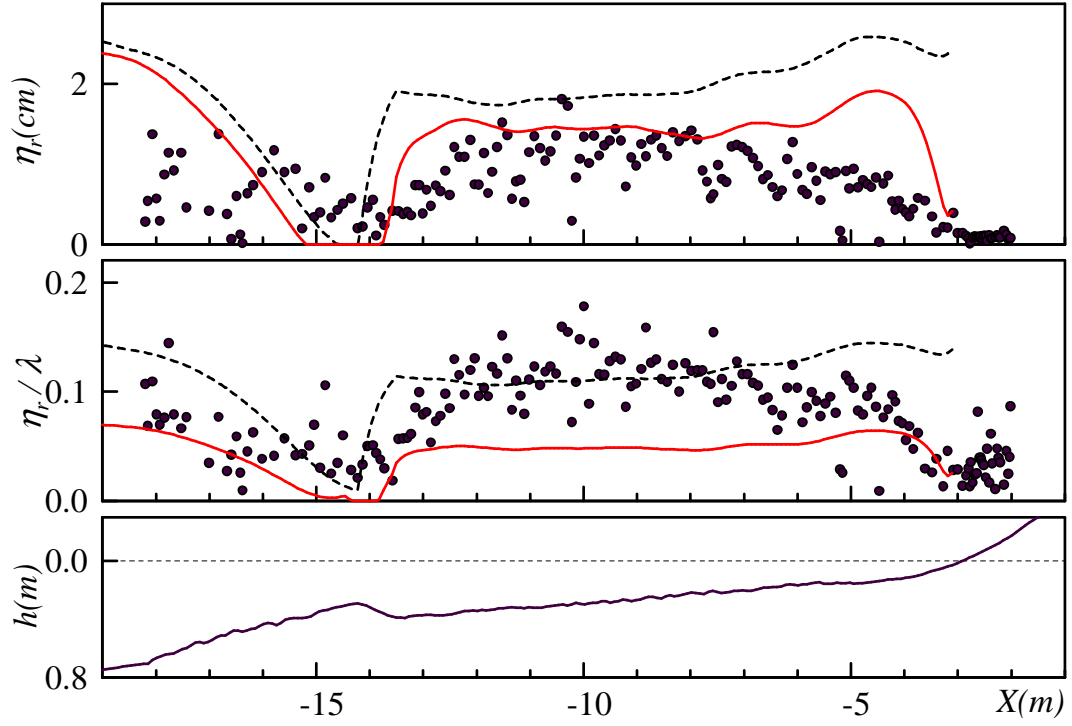


Figure C-6: Cross-shore distributions of measured and predicted ripple height, η_r , steepness, η_r/λ , and water depth. Measurements (Test 3: plunging breakers) by Wang et al. (2002) (full circles) and predictions by Wikramanayake and Madsen (1991) (dashed line based on $\psi'_{w,rms}$; full line based on ψ'_m).

Appendix D

Estimation of Skin Friction Shear Stress under Combined Wave and Current Fields

Under combined wave and current conditions, we require a special treatment to compute skin friction shear stress. Provided that the equivalent bottom roughness, k_N , is known, the present nearshore current model yields wave bottom boundary layer thickness, δ , and the mean current velocity at the outer edge of the wave bottom boundary layer, $\vec{U}_\delta = (U_\delta, V_\delta)$. From these current conditions and near-bottom wave orbital velocity, skin friction shear stress is determined by the modified Madsen's (1994) wave-current bottom boundary layer model with skin friction bottom roughness, k'_N . Within the bottom boundary layer, $z \leq \delta$, a new bottom boundary condition, based on the skin friction shear velocity, is then determined by

$$U_{\delta'} = \frac{\tau'_c}{\kappa \rho u'_{*m}} \ln \left(\frac{\delta'}{z_0} \right) \quad (\text{D.1})$$

where $z_0 = k'_N/30$ and u'_{*m} is the maximum combined wave-current skin friction shear velocity, defined as

$$u'^2_{*m} = \tau'_m / \rho = C'_\mu \tau'_{wm} / \rho \quad (\text{D.2})$$

with

$$C'_\mu = \sqrt{1 + 2 |\cos \phi_{wc}| \frac{\tau'_c}{\tau'_{wm}} + \left(\frac{\tau'_c}{\tau'_{wm}} \right)^2} \quad (\text{D.3})$$

$$\tau'_{wm} = \frac{1}{2} \rho f'_{cw} u_{bm}^2 \quad (\text{D.4})$$

where ϕ_{wc} denotes the angle between wave and current skin friction shear stress, τ'_c . The skin friction boundary layer thickness, δ' , is determined by

$$\delta' = A \frac{\kappa u'_{*m}}{\omega} \quad (\text{D.5})$$

$$A = \exp \left[2.96 \left(C'_\mu A_{bm} / k'_N \right)^{-0.071} - 1.45 \right] \quad (\text{D.6})$$

The skin friction factor, f'_{cw} , introduced in (D.4) is the combined wave-current skin friction factor, u_{bm} ($= U_{b*}/2$ for periodic waves or $= U_{brms}/2$ for random waves) is the amplitude of the near-bottom wave orbital velocity obtained from the wave model and $A_{bm} = u_{bm}/\omega$ is the corresponding bottom excursion amplitude. f'_{cw} can be obtained from (4.26) in Chapter 4 by replacing k_N by k'_N , i.e.

$$f_{cw} = \max \begin{cases} C_\mu \exp(7.02 X'^{-0.078} - 8.82) & 0.2 < X' < 10^2 \\ C_\mu \exp(5.61 X'^{-0.109} - 7.30) & 10^2 < X' \end{cases} \quad (\text{D.7})$$

with $X' = C'_\mu A_{bm} / k'_N$. Combined with the bottom boundary condition, (D.1), the mean current velocity above the skin friction boundary layer but below the outer edge of the bottom boundary layer, i.e. $\delta' \leq z \leq \delta$, is expressed as

$$\begin{aligned} U &= \frac{\tau'_c}{\rho \kappa u'_{*c}} \ln \frac{z}{\delta'} + U_{\delta'} \\ &= \frac{1}{\kappa} \left(u'_{*c} \ln \frac{z}{\delta'} + \frac{u'^2_{*c}}{u'_{*m}} \ln \frac{\delta'}{z_0} \right) \end{aligned} \quad (\text{D.8})$$

with $z'_0 = k'_N/30$. The skin friction current shear stress, $\tau'_c = \rho u'^2_{*c}$ is determined by substituting $U = U_\delta$ at $z = \delta$ in (D.8) as

$$u'_{*c} = u'_{*m} \frac{\ln \frac{\delta}{\delta'}}{\ln \frac{\delta'}{z_0}} \left(-\frac{1}{2} + \sqrt{\frac{1}{4} + \kappa \frac{U_\delta}{u'_{*m}} \frac{\ln \frac{\delta'}{z_0}}{\left(\ln \frac{\delta}{\delta'}\right)^2}} \right) \quad (\text{D.9})$$

The direction of the mean skin friction shear stress, $\bar{\tau}'_c$, is parallel to the mean current velocity at the outer edge of the bottom boundary layer, i.e. $\vec{U}_\delta = (U_\delta, V_\delta)$. The newly obtained u'_{*c} is applied to compute C'_μ in (D.3) and the same procedures are repeated until u'_{*c} converges.

Bibliography

- [1] Bagnold, R. A., 1963. Mechanics of Marine Sedimentation, *The Sea: Ideas and Observations*, vol.3, Interscience, NewYork.
- [2] Bailard, J. A., 1981. An Energetics Total Load Sediment Transport Model for a Plane Sloping Beach, *Journal of Geophysical Research*, vol.86(C11), pp.10,938–10,954.
- [3] Barton, J. R., and P. N. Lin, 1955. A study of the sediment transport in alluvial streams, *Technical Report*, Colorado A&M College, Civil Engineering Department, Fort Collins, CO, USA.
- [4] Battjes, J. A., 1974. Computation of set-up, longshore currents, run-up and overtopping due to wind-generated waves, *Communications on Hydraulics, Dept. of Civil Eng., Delft Univ. of Technology*, Rept. No.74-2.
- [5] Battjes, J. A., 1975. Modeling of turbulence in the surf zone, *Symposium on Modeling Technique*, pp.1050–1061.
- [6] Bodge, K. R. and R. G. Dean, 1987. Short-Term Impoundment of Longshore Sediment Transport, *Proceedings of Coastal Sediments '87*, ASCE, pp.468–483.
- [7] Bowen, A. J. 1969. The Generation of Longshore Currents on a Plane Beach, *J. Marine Res.*, 27, No.2, pp.206–215.
- [8] Bowen, A. J., D. L. Inman, and V. P. Simmons, Wave “set-down” and set-up, *Journal of Geophysical Research*, vol.73, No.8, pp.2569–2576.

- [9] Brooks, N. H., 1954. Laboratory studies of the mechanics of motion of streams flowing over a movable bed of fine sand, PhD thesis, California Institute of Technology.
- [10] Carstens, M. R., F. M. Neilson, and H. D. Altinbielk, 1969. Bed forms generated in the laboratory under an oscillatory flow: Analytical and experimental study, *Tech. Memo. 28*, USACE, 39pp.
- [11] Chen, Q., J. T. Kirby, R. A. Dalrymple, A. B. Kennedy, and A. Chawla, 2000. Boussinesq modeling of wave transformation, breaking and runup. II: Two horizontal dimensions, *Journal of Waterway, Port, Coastal and Ocean Engineering*, 126, pp.48–56.
- [12] Coastal Development Institute of Technology of Japan, 2001. Research and development of a numerical wave flume: CADMAS-SURF, *Report of the research group for development of numerical wave flume for the design of maritime structures*, 296p.
- [13] Cox, D.T. and N. Kobayashi, 1996. Undertow Profiles in the Bottom Boundary Layer under Breaking Waves, *Proc. 25th Int. Conf. on Coast. Eng.*, pp.3194–3206.
- [14] Cox, D., N. Kobayashi and A. Okayasu, 1995. Experimental and Numerical Modeling of Surf Zone Hydrodynamics, *Report No. CACR-95-97*, Center for Applied Coastal Research, University of Delaware.
- [15] Cruz, E., H. Yokoki, M. Isobe, and A. Watanabe, 1993. Nonreflecting boundary conditions for non-linear wave equation, *Proceedings of Coastal Engineering*, JSCE, Vol.40, pp.46–50 (in Japanese).
- [16] Dally, W. R., R. G. Dean and R. A. Dalrymple, 1985. Wave Height Variation Across Beaches of Arbitrary Profile, *Journal of Geophysical Research*, 90(C6), pp.11,917–11,927.

- [17] Dally, W. R. and C. A. Brown, 1995. A modeling investigation of the breaking wave roller with application to cross-shore currents, *J. Geophys. Res.*, 100 (C12), pp.24,873–24,883.
- [18] De Vriend, H. J., and M. J. F. Stive, 1987. Quasi-3D modeling of nearshore currents, *Coastal Engineering*, 11, pp.565–601.
- [19] Dean, R. G., 1965. Stream Function Representation of Nonlinear Ocean Waves, *Journal of Geophysical Research*, 70(C18), pp.4561–4572.
- [20] Deigaard, R., P. Justesen and J. Fredsoe, 1991. Modeling of undertow by a one-equation turbulence model, *Coastal Eng.*, 15, pp.431–458.
- [21] Dingler, J. R., 1974. Wave-formed ripples in nearshore sands, *PhD thesis, University of California, San Diego*.
- [22] Dingler, J. R., and D. L. Inman, 1976. Wave-dormed ripples in nearshore sands, *Proceedings of the 15th Internatilnal Conference on Coastal Engineering*, pp.2109–2126.
- [23] Dobbins, W. E., 1944. Effect of turbulence on sedimentation, *Trans. Am. Soc. Civ. Eng.*, 109, pp.629–678.
- [24] Drake, T. G., and J. Calantoni, 2001. Discrete particle model for sheet flow sediment transport in the nearshore, *Journal of Geophysical Research*, 106(C9), pp.19,859–19,868.
- [25] Ebersole, B., and R. A. Dalrymple, 1980. Numerical modeling of nearshore circulation. In: Edge, B. L. (Ed.), *Proceedings of the 17th International Conference on Coastal Engineering*, pp.2710–2725.
- [26] Einstein, H. A., 1950. The bed load functions of sediment transportation in open channel flows. *US Dept. Agric. Soil Conserv. Serv. Tech. Bull.* 1026, pp.1–71.

- [27] Einstein, H. A., and N. Vhien, 1955. Effects of heavy sediment concentration near the bed on velocity and sediment distribution, *Technical Report*, University of California, Institute of Engineering Research, Berkeley, California.
- [28] Feddersen, F., R. T. Guza, S. Elgar, and T. H. C. Herbers, 1998. Alongshore momentum balances in the nearshore, *Journal of Geophysical Research*, 103(C8), pp.15,667–15,676.
- [29] Gallagher, E. L., Elgar, S., and R. T. Guza, 1998. Observations of Sand Bar Evolution on a Natural Beach, *Journal of Geophysical Research*, Vol.103(C2), pp.3203–3215.
- [30] Gallagher, E. L., E. B. Thornton, and T. P. Stanton, 2003. Sand bed roughness in the nearshore, *Journal of Geophysical Research*, Vol.108(C2), 21-1–21-8.
- [31] Glenn, S. M., and W. D. Grant, 1987. A suspended sediment correction for combined wave and current flows, *Journal of Geophysical Research*, 92(C8), pp.8244–8264.
- [32] Goda, Y., 1970. A Synthesis Breaker Indices. *Proc. of the Japan Soc. of Civil Engineers.*, No.180, pp.39–49. (in Japanese)
- [33] Goda, Y., 1964. Wave forces on a vertical circular cylinder: experiments and a proposed method of wave force computation, *Rep. Port and Harbour Res. Inst.*, Ministry of Transport, No.8, 74p.
- [34] Gobbi, M. F. and Kirby, J. T., 1996. A fourth order Boussinesq-type wave model, *Proceedings of 25th International Conference on Coastal Engineering*, pp.1116–1129.
- [35] Grant, W.D. and Madsen O. S. 1982. Movable bed roughness in oscillatory flow, *Journal of Geophysical Research*, 87(C1), pp.469–481.
- [36] Grant, W.D. and Madsen O. S. 1986. The Continental Shelf Bottom Boundary Layer, M. Van Dyke, ed., *Annual Review of Fluid Mechanics*, Vol. 18, pp.265–305.

- [37] Gravens, M. B., Kraus, N. C., and H. Hanson, 1991. GENESIS: Generalized Model for Simulating Shoreline Change, *Instruction Report CERC-89-19*, U.S. Army Engineer Waterways Experiment Station, Vicksburg, MS.
- [38] Green, M. O., R. G. Bell, T. J. Dolphin, and A. Swales, 2000. Silt and sand transport in a deep tidal channel of a large estuary (Manukau Harbour, New Zealand), *Mar. Geol.*, 38, pp.115–141.
- [39] Hamilton, D. G. and Ebersole, B. A., 2001. Establishing Uniform Longshore Currents in a Large-Scale Laboratory Facility, *Coastal Eng.*, 42, pp.199–218.
- [40] Hansen, J. B. and I. A. Svendsen, 1984. A Theoretical and Experimental Study of Undertow. *Proc. 19th Int. Conf. on Coastal Eng.*, ASCE, pp.2246–2262.
- [41] Hanson, H. and N. C. Kraus, 1989. GENESIS: Generalized Numerical Modeling System for Simulating Shoreline Change, *Report 1, Technical Reference Manual, Technical Report CERC-89-19*, U.S. Army Engineer Waterways Experiment Station, Coastal Engineering Research Center, Vicksburg, MS.
- [42] Herrmann, J. M., 2004. Effect of stratification due to suspended sediment on velocity and concentration distribution in turbulent flows, *Master's thesis in Massachusetts Institute of Technology*, 152p.
- [43] Hill, P. S., A. R. M. Nowell, and P. A. Jumars, 1988. Flume evaluation of the relationship between suspended sediment concentration and excess shear stress, *Journal of Geophysical Research*, 93, pp.12,499–12,509.
- [44] Hirt, C. W., and B. D. Nichols, 1981, Volume of fluid (VOF) method for dynamics of free boundaries, *J. Comput. Phys.*, 39, pp.201–225.
- [45] Hoefel, F. and S. Elgar, 2003. Wave-induced sediment transport and sandbar migration, *Science magazine*, vol.299, pp.1885-1887.
- [46] Hoffman, J. D., 1992. Numerical methods for engineers and scientists, McGraw-Hill, Inc., 825P.

- [47] Horikawa, K., 1985. Nearshore Dynamics and Coastal Processes, *University of Tokyo Press*, 522p. (in Japanese)
- [48] Horikawa, K. and C. T. Kuo, 1966. A Study on Wave Transformation inside the Surf Zone. *Proc. 10th Int. Conf. on Coastal Eng.*, ASCE, pp.217–233.
- [49] Hunt, J. N., 1952. Viscous damping of waves, *La Houille Balanche*, 7, pp.836–842.
- [50] Hunt, J. N., 1954. The turbulent transport of suspended sediment in open channels, *Proc. R. Soc. London Ser. A*, 224, pp.322–335.
- [51] Inman, D.L., 1957. Wave generated ripples in nearshore sands, *Tech. Memo. 100*, beach erosion board, USACE, 66pp.
- [52] Isobe, M., 1979. Hozonha no Setsudo-kai no Hako ni yoru Hyouji, *Annual Conference, JSCE*, II-394, pp.760–761 (in Japanese).
- [53] Isobe, M., 1985. Calculation and application of first-order Cnoidal wave theory, *Coastal Engineering*, 9, pp.309–325.
- [54] Isobe, M., 1987. A Parabolic Equation Model for Transformation of Irregular Waves Due to Refraction, Diffraction and Breaking, *Coastal Eng. in Japan*, 30, pp.33–47.
- [55] Isobe, M., 1994. Time-dependent mild-slope equations for random waves, *Proceedings of 24th International Conference on Coastal Engineering*, pp.285–299.
- [56] Iversen, H. W., 1951. Laboratory study of breakers, *Proc. Symposium on Gravity Waves*, Circular 521, pp.9–32.
- [57] Jimenez, J. A. and O. S. Madsen, 2003. A simple formula to estimate settling velocity of natural sediments, *Journal of Waterway, Port, Coastal and Ocean Engineering*, 129(2), pp.70–78.

- [58] Kalinske, A. A., and C. L. Pien, 1943. Experiments on eddy diffusion and suspended material transportation in open channels, *Eos Trans. AGU*, 24, pp.530–536.
- [59] Kanayama, S., H. Tanaka, and N. Shuto, 1998. A multi-level model for non-linear dispersive water waves, *Proceedings of 26th International Conference on Coastal Engineering*, pp.576–588.
- [60] Kennedy, J. F. and M. Falcon, 1965. Wave generated sediment ripples, *Rep. 86, Hydrodyn. lab.*, MIT.
- [61] King, D. B., Jr. 1991. The effect of beach slope on oscillatory flow bedload transport, *Proceedings Coastal Sediments '91*, Vol. 1, pp.734–744.
- [62] Kirby, J. T., G. Wei, Q. Chen, A. B. Kennedy, and R. A. Dalrymple, 1998. FUN-WAVE 1.0 fully nonlinear Boussinesq wave model documentation and user's manual, *Research Report CACR-98-06*, Center for Applied Coastal Research, University of Delaware.
- [63] Kobayashi, N. and B. D. Johnson, 2001. Sand, suspension, storage, advection, and settling in surf and swash zones. *Journal of Geophysical Research*, 106(C5), pp.9363–9376.
- [64] Kobayashi, N., and K. S. Han, 1988. Erosion at Bend of Gravel Causeway Due to Waves, *Journal of the Waterway, Port, Coastal and Ocean Engineering Division*, ASCE, Vol 114, pp.297–314.
- [65] Kothe, D. B., R. C. Mjolsness, and M. D. Torrey, 1991. *RIPPLE*: A computer program for incompressible flows with free surfaces, Los Alamos National Laboratory, LA-12007-MS.
- [66] Kurata, Y. and M. Hattori, 2000. A breaking wave model taking account of surface rollers, *Proceedings of Coastal Engineering*, JSCE, Vol.47(1), pp.166–170. (in Japanese)

- [67] Kuriyama, Y., 1994. Numerical model for longshore current distribution on a bar-trough beach, *Proceedings 24th International Conference on Coastal Engineering*, pp.2237–2215.
- [68] Kuriyama, Y., and T. Nakatsukasa, 2000. A one-dimensional model for undertow and longshore current on a barred beach, *Coastal Engineering*, 40, pp.39–58.
- [69] Kuroiwa, M., Noda, H., and Y. Matsubara, 1998. Applicability of a quasi-three dimensional numerical model to nearshore currents, *Proceedings 26th International Conference on Coastal Engineering*, pp.815–828.
- [70] Lee, T. H., and D. M. Hanes, 1996. Comparison of field observations of the vertical distribution of suspended sand and its prediction by models, *Journal of Geophysical Research*, 101, pp.3561–3572.
- [71] Lee, G., C. T. Friedrichs, and C. E. Vincent, 2002. Examination of diffusion versus advection dominated sediment suspension on the inner shelf under storm and swell conditions, Duck, North Carolina, *Journal of Geophysical Research*, 107(C7), pp.21-1–21-22.
- [72] Lee, G., W. B. Dade, C. T. Friedrichs, and C. E. Vincent, 2003. Spectral estimates of bed shear stress using suspended-sediment concentrations in a wave-current boundary layer, *Journal of Geophysical Research*, 108(C7), pp.1-1–1-15.
- [73] Li, M. Z., L. D. Wright, C. L. Amos, 1996. Predicting ripple roughness and sand resuspension under combined flows in a shoreface environment, *Marine Geology* 130, pp.139–161.
- [74] Li, M.Z. and C.L. Amos, 1998. Predicting ripple geometry and bed roughness under combined waves and currents in a continental shelf environment, *Continental Shelf Research*, 18, pp.941–970.
- [75] Li, M. Z. and C. L. Amos, 1999. Sheet flow and large wave ripples under combined waves and currents: field observations, model predictions and effects on boundary layer dynamics, *Continental Shelf Research*, 19, pp.637–663.

- [76] Lin, P. and P. L.-F. Liu, 1998. A numerical study of breaking waves in the surf zone, *Journal of Fluid Mechanics*, 359, pp.239–264.
- [77] Lippmann, T. C., Thornton, E. B., and A. J. R. M. Reniers, 1995. Wave stress and longshore current on barred profiles, *Proceedings Coastal Dynamics '95*, pp.401–412.
- [78] Liu, P. L.-F. and T.-J. Hsu, 2003. Modeling cross-shore sediment transport using two-phase flow approach, *Proceedings of the International Conference on Coastal Sediments 2003*. CD-ROM Published by World Scientific Publishing Corp. and East Meets West Productions, Corpus Christi, Texas, USA. ISBN 981-238-422-7.
- [79] Longuet-Higgins, M. S., 1970. Longshore currents generated by obliquely incident sea waves, *Journal of Geophysical Research*, 75, pp.6778–6789.
- [80] Longuet-Higgins, M. S. and R. W. Stewart, 1962. Radiation stresses and mass transport in gravity waves with applications to surf-beats, *Journal of Fluid Mechanics*, 13, pp.481–504.
- [81] Ludwig, K. A. and D. M. Hanes, 1990. A laboratory evaluation of optical backscatterance suspended solids sensors exposed to sand-mud mixtures, *Marine Geology*, 94, pp.173–179.
- [82] Luque, F. R. and R. van. Beek, 1976. Erosion and transport of bedload sediment, *Journal of Hydraulic Research*, 14(2), pp.127–144.
- [83] Lyn, D. A., 1986. Turbulence and turbulent transport in sediment-laden open-channel flows, PhD thesis, California Institute of Technology.
- [84] Madsen, O. S., 1991. Mechanics of Cohesionless Sediment Transport in Coastal Waters, *Proceedings Coastal Sediments '91*, ASCE, Vol.1, pp.15-27.
- [85] Madsen, O. S. 1993. Sediment Transport Outside the Surf Zone, *unpublished Technical Report*, U.S. Army Engineer Waterways Experiment Station, Vicksburg, MS.

- [86] Madsen, O. S., 1994. Spectral Wave-Current Bottom Boundary Layer Flows, *Proc. 24th Int. Conf. on Coast. Eng.*, pp.384–398.
- [87] Madsen, O. S., 2001. Chapter 6 in *Coastal Engineering Manual*. U.S. Army Corps of Engineers, Engineer Manual 1110-2-1100, U.S. Army Corps of Engineers, Washington, D.C.
- [88] Madsen, O. S., L. D. Wright, J. D. Boon, and T. A. Chisholm, 1993. Wind stress, bed roughness and sediment suspension on the inner shelf during an extreme storm event, *Continental Shelf Research*, 13(11), pp.1303–1324.
- [89] Madsen, O. S. and M. M. Rosengaus, 1988. Spectral wave attenuation by bottom friction: experiments, *Proceedings of 21st International Conference on Coastal Engineering*, vol.2, pp.1093–1112.
- [90] Madsen, O.S. and P. N. Wikramanayake, 1991. Simple model for turbulent wave-current bottom boundary layer flow, *DRP-91-1, Ralph M. Parsons Laboratory, Massachusetts Institute of Technology*, 150pp.
- [91] Madsen, O. S. and P. Salles, 1998. Eddy Viscosity Models for Wave Boundary Layers, *Proc. 26th Int. Conf. on Coast. Eng.*, pp.2615–2627.
- [92] Madsen, O. S. and W. D. Grant, 1976. Quantitative description of sediment transport by waves, *Proceedings of the 15th International Conference on Coastal Engineering*, pp.1093–1112.
- [93] Madsen, O. S., Y. Tajima, and B.A. Ebersole, 2003. Longshore Sediment Transport: A Realistic Order-of-Magnitude Estimate, *Proceedings of the International Conference on Coastal Sediments 2003*. CD-ROM Published by World Scientific Publishing Corp. and East Meets West Productions, Corpus Christi, Texas, USA. ISBN 981-238-422-7.
- [94] Madsen, P. A., B. Banjamali, H. A. Schaffer, and O. R. Sorensen, 1996. Boussinesq type equations with high accuracy in dispersion and nonlinearity, *Proceedings of 25th International Conference on Coastal Engineering*, pp.95–108.

- [95] Madsen, P. A., O. R. Sorensen, H. A. Schaffer, 1997a. Surf zone dynamics simulated by a Boussinesq type model. Part I. Model description and cross-shore motion of regular waves, *Coastal Engineering*, 32, pp.255–287.
- [96] Madsen, P. A., O. R. Sorensen, H. A. Schaffer, 1997b. Surf zone dynamics simulated by a Boussinesq type model. Part II. Surf beat and swash oscillations for wave groups and irregular waves, *Coastal Engineering*, 32, pp.289–320.
- [97] Mathisen, P. P., 1989. Experimental study on the response of fine grained sediments to wave agitation and associated attenuation, *M.S. Thesis, Department of Civil Engineering, Massachusetts Institute of Technology*.
- [98] McLean, S. R., 1992. On the calculation of suspended load for noncohesive sediments, *Journal of Geophysical Research*, 97(C4), pp.5759–5770.
- [99] Mei, C. C., 1989. The Applied Dynamics of Ocean Surface Waves, *Advanced Series on Ocean Eng.*, 1, 740P.
- [100] Meyer-Peter, E. and R. Muller, 1948. Formulas for bed-load transport, *Proceedings of the 2nd Congress of International Association for Hydraulic Structures Research*, pp.39–64.
- [101] Miche, R., 1951. Le pouvoir réfléchissant des ouvrages maritime exposés à la action de la houle, *Annales Ponts et Chaussees*, 121 Annee, pp.285–319.
- [102] Michell, J. H., 1893. On the highest wave in water, *Phil. Mag.*, 5th series, Vol.36, pp.430–437.
- [103] Miller, M. C. and P. D. Komar, 1980. Oscillation sand ripples generated by laboratory apparatus, *J. Sediment Petrol.* 50, pp.173–182.
- [104] Miller, M. C. and P. D. Komar, 1980. A field investigation of the relationship between oscillation ripples spacing and the near-bottom water orbital motions, *J. Sediment Petrol.* 50, pp.183–191.

- [105] Mizuguchi, Y., Tsujioka, K. and K. Horikawa, 1978. Wave height attenuation in the surf zone, *Proceedings of Coastal Engineering*, JSCE, Vol.25, pp.166–170. (in Japanese)
- [106] Mogridge, G. R. and J. W. Kamphuis, 1972. Experiments on bed-form generation by wave action, *Proceedings 13th Coastal Engineering Conference*, pp.1123–1142.
- [107] Mogridge, G. R., M. H. Davies, and D. H. Willis, 1994. Geometry prediction for wave-generated bedforms, *Coastal Engineering*, 22, pp.255–286.
- [108] Nadaoka, K., S. Beiji, and Y. Nakagawa, 1994. A fully-dispersive non-linear wave model and its numerical solutions, *Proceedings of 24th International Conference on Coastal Engineering*, pp.427–441.
- [109] Nadaoka, K., T. Kondo, and N. Tanaka, 1982. The Structure of Velocity Fields within the Surf Zone Revealed by Means of Laser-Doppler Aemometry, *Report of the Port and Harbour Research Institute*, vol.21, No.2, pp.50–120 (in Japanese).
- [110] Nagayama, S., 1983. Study on the Change of Wave Height and Energy in the Surf Zone. *Bach. Thesis in Civil Eng., Yokohama National Univ., Japan*.
- [111] Nairn, R. B., and H. N. Southgate, 1993. “Deterministic Profile Modeling of Nearshore Processes, Part2. Sediment Transport and Beach Development,” *Coastal Engineering*, vol.19, pp.57–96.
- [112] Nielsen, P., 1981. Dynamics and geometry of wave-generated ripples, *Journal of Geophysical Research*, 86, pp.6467–6472.
- [113] Nielsen, P., 1983. Entrainment and distribution of different sand sizes under water waves, *J. Sedimentary Petrology*, vol.53, No.2, pp.423–448.
- [114] Nielsen, P., 1992. *Coastal bottom boundary layers and sediment transport*. World Scientific, Singapore, 324p.

- [115] Nikuradse, J., 1933. Stromungsgsetze in glatten und rauhen rohren, *VDI Forschungsheft 361*. (English translation, 1950. *NACA Tech. Memo. 1292, Natl. Advis. Comm. for Aeronaut.*)
- [116] Noda, E. K., C. J. Sonu, V. C. Rupert, and J. I. Collins, 1974. Nearshore circulations under sea breeze conditions and wave-current interactions in the surf-zone, *Tetra Tech Rep.*, TC-149-4.
- [117] Nomicos, G. N., 1956. Effects of sediment load on the velocity field and friction factor of turbulent flow in an open channel, PhD thesis, California Institute of Technology.
- [118] Nwogu, O., 1993. Alternative form of Boussinesq equations for nearshore wave propagation, *J. Waterway, Port, Coastal and Ocean Eng.*, 119(6), pp.618-638.
- [119] Nwogu, O., 1996. Numerical Prediction of Breaking Waves and Currents with Boussinesq Model, *Proc. 25th Int. Conf. on Coast. Eng.*, pp.4807-4820.
- [120] Osiecki, D. A., and W. R. Dally, 1996. The influence of rollers on longshore currents, *Proceedings of the 25th International Conference on Coastal Engineering*, pp.3419-3430.
- [121] Okayasu, A., A. Watanabe and M. Isobe, 1990. Modeling of Energy Transfer and Undertow in the Surf Zone, *Proceedings of the 22nd International Coastal Engineering Conference*, ASCE, pp.123-135.
- [122] Okayasu, A. and H. Katayama, 1992. Distribution of Undertow and Long-Wave Component Velocity due to Random Waves, *Proceedings of the 23rd International Conference on Coastal Engineering*, pp.883-893.
- [123] Okayasu, A., K. Hara, and T. Shibayama, 1994. Laboratory experiments on a 3-D nearshore currents and a model with momentum flux by breaking waves, *Proceedings of the 24th International Conference on Coastal Engineering*, pp.2461-2475.

- [124] Okayasu, A., T. Shibayama, and K. Horikawa, 1988. Vertical Variation of Undertow in the Surf Zone. *Proceedings of the 21st International Conference on Coastal Engineering*, ASCE, pp.478–491.
- [125] Peregrin, D. H., 1967. Long waves on a beach, *Journal of Fluid Mechanics*, 27, pp.815–827.
- [126] Perlin, M., and R. G. Dean, 1983. A Numerical Models to Simulate Sediment Transport in the Vicinity of Coastal Structures, *Miscellaneous Report No. 83-10*, CERC, U.S. Army Corps of Engineers, Fort Belvoir, VA.
- [127] Phillips, O. M., 1977. Dynamics of the upper ocean, *2nd Edition*, Cambridge University Press, London.
- [128] Puleo, J. A., Holland, K. T., Slinn, D. N., Smith, E., and B. M. Webb, 2002, Numerical modelling of swash zone hydrodynamics, *Proceedings of the 28th International Conference on Coastal Engineering*, 1, pp.968–979.
- [129] Putrevu, U., and I. A. Svendsen, 1992. A mixing mechanism in the nearshore region, *Proceedings of the 23rd International Conference on Coastal Engineering*, pp.2758–2771.
- [130] Qin, W., I. A. Svendsen, B. A. Ebersole, and E. R. Smith, 2002. Modeling sediment transport at the LSTF at CHL, *Proceedings of the 28th International Conference on Coastal Engineering*, pp.3020–3032.
- [131] Rankin, K. L., and R. I. Hires, 2000. Laboratory measurement of bottom shear stress on a movable bed, *Journal of Geophysical Research*, 105, pp.17,011–17,019.
- [132] Reniers, A. J. H. M., and J. A. Battjes, 1997. A laboratory study of longshore currents over barred and non-barred beaches, *Coastal Engineering*, 30, pp.1–22.
- [133] Reniers, A. J. H. M., E. B. Thornton, and T. C. Lippmann, 1995. Longshore currents over barred beaches, *Coastal Dynamics '95*, pp.413–424.

- [134] Ribberink, J. S., and A. A. Al-Salem, 1994. Sediment transport in oscillatory boundary layers in cases of rippled beds and sheet flow, *Journal of Geophysical Research*, 99, pp.12,707–12,727.
- [135] Rose, C. P., and P. D. Thorne, 2001. Measurements of suspended sediment transport parameters in a tidal estuary, *Continental Shelf Research*, 21, pp.1555–1575.
- [136] Rosengaus, M. M., 1987. Experimental study of wave-generated bedforms and resulting wave attenuation, *Sc.D. Thesis, Department of Civil Engineering, Massachusetts Institute of Technology*.
- [137] Rouse, H., 1938. Experiments on the mechanics of sediment suspension, *Proc. Int. Congr. Appl. Mech. 5th*, pp.550–554.
- [138] Ruessink, B. G., Miles, J. R., Feddersen, F., Guza, R. T., and S. Elgar, 2001. Modeling the Alongshore Current on Barred Beaches, *J. Geophys. Res.*, 106 (C10), pp.22,451–22,463.
- [139] Saeki and Sasaki, 1974. Saiha go no Nami no Henkei ni Kansuru Kenkyu, *Proceedings of the 21st Japanese conference on Coastal Engineering*, JSCE, pp.39–44. (in Japanese)
- [140] Sanchez-Arcilla, A., Collado, F., and A. Rodriguez, 1992. Vertically varying velocity field in Q-3D nearshore circulation, *Proc. 23rd Int. Conference on Coastal Engineering*, pp.2811–2824.
- [141] Sanchez-Arcilla, A., Collado, F., Lemos, M., and A. Rodriguez, 1990. Another quasi-3D model for surf-zone flows, *Proc. 22nd Int. Conference on Coastal Engineering*, pp.316–329.
- [142] Sato, S., T. Isayama, and T. Shibayama, 1988. Measurements of Near-Bottom Velocities in Random Waves on a Constant Slope. *Coastal Engineering in Japan*, JSCE vol.31, pp.219–229.

- [143] Sato, S. and K. Horikawa, 1988. Sand ripple geometry and sand transport mechanism due to irregular oscillatory flows, *Proceedings of 21st International Conference on Coastal Engineering*, vol.2, pp.1748–1762.
- [144] Savage, R. P., 1962. Laboratory determination of Littoral Transport Rates, *Journal of the Waterway, Port, Coastal, and Ocean Division*, ASCE, No. WW2, pp.69–92.
- [145] Scheffner, N. W., and J. D. Rosati, 1987. A Users Guide to the N-Line Model: A Numerical Model to Simulate Sediment Transport in the Vicinity of Coastal Structures, *Instruction Report CERC-87-4*, U.S. Army Engineer Waterways Experiment Station, Vicksburg, MS.
- [146] Sheng, J. and A. E. Hay, 1995. Sediment eddy diffusivities in the nearshore zone, from multifrequency acoustic backscatter, 1995. *Continental Shelf Research*, 15, pp.129–147.
- [147] Sleath, J. F. A., 1982. The suspension of sand by waves, *J. Hydraulic Research*, 20, pp.439–452.
- [148] Sleath, J. F. A. and S. Wallbridge, 2002. Pickup from rippled beds in oscillatory flow, *Journal of Waterway, Port, Coastal and Ocean Engineering*, 128(6), pp.228–237.
- [149] Smith, I. D., and S. R. McLean, 1977. Spatially Averaged Flow over a Wavy Surface, *Journal of Geophysical Research*, Vol.82(C12), pp.1,735–1,754.
- [150] Soulsby, R., 1997. Dynamics of Marine Sands, *Thomas Telford*, London.
- [151] Soulsby, R. L. and R. J. S. W. Whitehouse, 1997. Threshold of sediment motion in coastal environments, *Proceedings Pacific Coasts and Ports 1997 Conference*, 1, pp.149–154.
- [152] Stive, M. J. F. and H. G. Wind, 1986. Cross-shore mean flow in the surf zone, *Coastal Engineering*, vol.10, pp.325–340.

- [153] Styles, R. and S. M. Glenn, 2002. Modeling bottom roughness in the presence of wave-generated ripples, *Journal of Geophysical Research Vol.107 C8*, pp.24-1 – 24-15.
- [154] Svendsen, I. A., 1984. Mass flux and undertow in a surf zone, *Coastal Engineering*, Vol.8, pp.303–329.
- [155] Svendsen, I. A. and U. Putrevu, 1994. Nearshore mixing and dispersion, *Proc. Math. and Phys. Sciences*, Vol.445, Issue1925, pp.561–576.
- [156] Svendsen, I. A., Qin, W., and B. A. Ebersole, 2003. Modeling waves and currents at the LSTF and other laboratory facilities, *Coastal Engineering*, 50, pp.19–45.
- [157] Svendsen, I. A., Sancho, F. E., Oltman-Shay, J., and E. B. Thornton, 1997. Modeling nearshore circulation under field conditions, *Proceedings ASCE Waves'97 conference*, pp.765–776.
- [158] Tajima, Y., 2001. Surf zone hydrodynamics, *Master's thesis in Massachusetts Institute of Technology*, 157p.
- [159] Tajima, Y. and O. S. Madsen, 2002. Shoaling, breaking and broken wave characteristics, *Proc. 28th Int. Conf. on Coast. Eng.*, pp.222–234.
- [160] Tajima, Y. and O. S. Madsen, 2003. Modeling Near-Shore Waves and Surface Rollers, *2nd Int. Conf. on Asian and Pacific Coasts*, (to appear in 2004 press).
- [161] Takahashi, S., Kotake, Y., Fujiwara, R., and M. Isobe, 2002. Performance evaluation of perforated-wall caissons by VOF numerical simulations, *Proceedings of the 28th International Conference on Coastal Engineering*, 2, pp.1364–1376.
- [162] Thornton, E. B. and R. T. Guza, 1981. Longshore currents and bed shear stress, *Proceedings Conference on Directional Wave Spectra Applications*, ASCE, 147–164.

- [163] Thornton, E. B. and R. T. Guza, 1986. Surf zone longshore currents and random waves: field data and models, *Journal of Physical Oceanography*, 16, pp.1165–1178.
- [164] Ting, F. C. K. and J. T. Kirby, 1996. Dynamics of surf-zone turbulence in a spilling breaker, *Coastal Engineering*, 27, pp.131–160.
- [165] Toyoshima, O., M. Tominaga, and H. Hashimoto, 1968. Experimental study on wave deformation inside surf zone, *Doboku-Kenkyu-sho-hokoku*, 133, pp.121–129.
- [166] Traykovski, P. A., E. Hay, J. D. Irish, and J. F. Lynch, 1999. Geometry, migration, and evolution of wave orbital ripples at LEO-15, *Journal of Geophysical Research*, 104, pp.1505–1524.
- [167] Trowbrige, J. H., and O. S. Madsen, 1984. Turbulent wave boundary layers, 1: Model formulation and first-order solution, *Journal of Geophysical Research*, 89(C5), pp.7989–7997.
- [168] Trowbrige, J. H., and O. S. Madsen, 1984. Turbulent wave boundary layers, 1: Second-order theory and mass transport, *Journal of Geophysical Research*, 89(C5), pp.7997–8007.
- [169] U.S. Army Corps of Engineers. 2001. *Coastal Engineering Manual*. Engineer Manual 1110-2-1100, U.S. Army Corps of Engineers, Washington, D.C.
- [170] U.S. Army Corps of Engineers. 1977. *Shore Protection Manual*. 3rd ed., 2 Vol, U.S. Army Engineer Waterways Experiment Station, U.S. Government Printing Office, Washington, DC.
- [171] U.S. Army Corps of Engineers. 1984. *Shore Protection Manual*. 4th ed., 2 Vol, U.S. Army Engineer Waterways Experiment Station, U.S. Government Printing Office, Washington, DC.

- [172] Van Dongeren, A. R., Reniers, A. J. H. M., Battjes, J. A., and I. A. Svendsen, 2003. Numerical modeling of infragravity wave response during Delilah, *Journal of Geophysical Research*, 108(C9).
- [173] Van Dongeren, A. R., Sancho, F. E., Svendsen, I. A., and U. Putrevu, 1994. SHORECIRC: A quasi 3-D nearshore model, *Proceedings 24th International Conference on Coastal Engineering*, pp.2741–2754.
- [174] Van Rijn, L. C., 1984. Suspended transport, part II: suspended load transport, *J. Hydr. Eng.*, 110, pp.1613–1641.
- [175] Vincent, C. E. and A. Downing, 1994. Variability of suspended sand concentrations, transport and eddy diffusivity under non-breaking waves on the shoreface, 1994. *Continental Shelf Research*, 14, pp.223–250.
- [176] Vincent, C. E. and P. D. Osborne, 1995. Prediction suspended sand concentration profiles on a macro-tidal beach, *Continental Shelf Research*, 13, pp.1497–1514
- [177] Visser P. J., 1991. Laboratory Measurements of Uniform Longshore Currents, *Coastal Engineering*, 15, pp.563–593.
- [178] Wang, P., E. R. Smith, and B. A. Ebersole, 2002. Large-Scale laboratory measurements of longshore sediment transport under spilling and plunging breakers, *Journal of Coastal Research*, vol.18, No.1, pp.118–135.
- [179] Watanabe A. and M. Dibajnia, 1988. A Numerical Model of Wave Deformation in Surf Zone, *Proc. 21st Int. Conf. on Coastal Eng.*, ASCE, pp.579–587.
- [180] Watanabe A., T. Hara and K. Horikawa, 1984. Study on Breaking Condition for Compound Wave Trains., *Coastal Eng. in Japan*, JSCE, vol.27, pp.71–82.
- [181] Watanabe, A. and Z. Elnaggar, 2000. Variations of Orbital Velocity and Undertow in the Nearshore Zone, *Proc. 27th Int. Conference on Coastal Engineering*, Vol.1, pp.769–782.

- [182] Webb, M. P., and C. E. Vincent, 1999. Comparison of time-averaged acoustic backscatter concentration profile measurements with existing predictive models, *Mar. Geol.*, 162, pp.71–90.
- [183] Wei, G., J. T. Kirby, S. T. Grilli, and R. Subramanya, 1995. A fully nonlinear Boussinesq model for surface waves. part 1. Highly nonlinear unsteady waves, *Journal of Fluid Mechanics*, vol.294, pp.71–92.
- [184] Wen, L. and J. T. Kirby, 2003. Cross-shore sediment transport model based on the Boussinesq equations and an improved Bagnold formula, *Proceedings of the International Conference on Coastal Sediments 2003*. CD-ROM Published by World Scientific Publishing Corp. and East Meets West Productions, Corpus Christi, Texas, USA. ISBN 981-238-422-7.
- [185] Wiberg, P. L. and C. K. Harris, 1994. Ripple geometry in wave-dominated environments, *Journal of Geophysical Research*, 99(C1), pp.775–789.
- [186] Wijetunge, J. J. and J. F. A. Sleath, 1998. Effects of sediment transport on bed friction and turbulence, *Journal of waterway, port, coastal, and ocean engineering*, 124, pp.172–178.
- [187] Wikramanayake, P.N. and O. S. Madsen, 1991. Calculation of movable bed friction factors, *Technical report DACW-39-88-K-0047*, Coastal Engineering Research Center USACE, 105pp.
- [188] Wikramanayake, P. N. and O. S. Madsen, 1994. Calculation of Suspended Sediment Transport by Combined Wave-Current Flows, *Contract Report DRP-94-7*, U.S. Army Engineer Waterways Experiment Station, Vicksburg, MS.
- [189] Wilson, K. C., 1965. Application of the minimum-entropy-production principle to problems in two-phase flow, Ph.D. Thesis presented to Queen's University at Kingston, Canada.
- [190] Wilson, K. C., 1966. Bed-load transport at high shear stress, *Journal of Hydraulic Engineering*, 92(6), pp.49–59.

- [191] Wilson, K. C., 1987. Analysis of bed-load motion at high shear stress, *Journal of Hydraulic Engineering*, 113(1), pp.97–103.
- [192] Wilson, K. C., 1989. Mobile-bed friction at high shear stress, *Journal of Hydraulic Engineering*, 115(6), pp.825–830.
- [193] Wu, C.-S., and L.-F. Liu, 1985. Finite element modeling of nonlinear coastal currents, *Journal of Waterway, Port, Coastal and Ocean Engineering*, 111(2), pp.417–432.
- [194] Xu, J. P. and L. D. Wright, 1995. Tests of bed roughness models using field data from the Middle Atlantic Bight, *Continental Shelf Research*, 15, pp.1409–1434.
- [195] Yalin, M. S., 1963. An expression for bed-load transportation. *J. Hydr. Div.*, 89(HY3), pp.221–250.

REPORT DOCUMENTATION PAGE				Form Approved OMB No. 0704-0188	
Public reporting burden for this collection of information is estimated to average 1 hour per response, including the time for reviewing instructions, searching existing data sources, gathering and maintaining the data needed, and completing and reviewing this collection of information. Send comments regarding this burden estimate or any other aspect of this collection of information, including suggestions for reducing this burden to Department of Defense, Washington Headquarters Services, Directorate for Information Operations and Reports (0704-0188), 1215 Jefferson Davis Highway, Suite 1204, Arlington, VA 22202-4302. Respondents should be aware that notwithstanding any other provision of law, no person shall be subject to any penalty for failing to comply with a collection of information if it does not display a currently valid OMB control number. PLEASE DO NOT RETURN YOUR FORM TO THE ABOVE ADDRESS.					
1. REPORT DATE (DD-MM-YYYY) August 2005		2. REPORT TYPE Final report		3. DATES COVERED (From - To)	
4. TITLE AND SUBTITLE Waves, Currents, and Sediment Transport in the Surf Zone along Long, Straight Beaches				5a. CONTRACT NUMBER	
				5b. GRANT NUMBER	
				5c. PROGRAM ELEMENT NUMBER	
6. AUTHOR(S) Yoshimitsu Tajima and Ole S. Madsen				5d. PROJECT NUMBER	
				5e. TASK NUMBER	
				5f. WORK UNIT NUMBER	
7. PERFORMING ORGANIZATION NAME(S) AND ADDRESS(ES) Massachusetts Institute of Technology Department of Civil Engineering Cambridge, MA 02139				8. PERFORMING ORGANIZATION REPORT NUMBER	
9. SPONSORING / MONITORING AGENCY NAME(S) AND ADDRESS(ES) Coastal and Hydraulics Laboratory U.S. Army Engineer Research and Development Center 3909 Halls Ferry Road, Vicksburg, MS 39180-6199				10. SPONSOR/MONITOR'S ACRONYM(S)	
				11. SPONSOR/MONITOR'S REPORT NUMBER(S) ERDC/CHL CR-05-1	
12. DISTRIBUTION / AVAILABILITY STATEMENT Approved for public release, distribution is unlimited.					
13. SUPPLEMENTARY NOTES					
14. ABSTRACT This study presents a theoretical model for predictions of nearshore hydrodynamic characteristics and the local sediment transport rate along long, straight beaches. The wave may be periodic or random, the beach may be plane or barred, and the bed may be concrete or covered with movable natural sand grains. The present model must be efficient and flexible so that it can accommodate iterative computations for time-varying and, hence, arbitrary beach profiles. The nearshore hydrodynamics model consists of wave, surface roller, and nearshore current models. Both wave and surface roller models are based on simple energy balance equations and, based on these models, the nearshore current is determined from two-layer 2DH momentum equations. Coupled with a simple turbulent eddy viscosity model, vertical profiles of mean shear current are analytically obtained. The model accounts for advective interactions between waves, surface rollers, and currents and, coupled with the surface roller model, explain the shoreward shift of the peak longshore current velocity. The model applies a modified version of Madsen's (1994) wave-current bottom boundary layer model to specify the bottom boundary condition from knowledge of equivalent bottom roughness scaled by a sediment diameter. (Continued)					
15. SUBJECT TERMS See reverse.					
16. SECURITY CLASSIFICATION OF:			17. LIMITATION OF ABSTRACT	18. NUMBER OF PAGES	19a. NAME OF RESPONSIBLE PERSON
a. REPORT UNCLASSIFIED	b. ABSTRACT UNCLASSIFIED	c. THIS PAGE UNCLASSIFIED			19b. TELEPHONE NUMBER (include area code)

14. ABSTRACT (continued)

Introducing the predicted nearshore hydrodynamic characteristics, we extend the conceptual bedload and associated suspended load sediment transport models (Madsen 2001) to the surf zone. The extended sediment transport model accounts for breaking wave effects such as an increase of turbulence due to broken waves and change of the momentum force balances due to breaking waves and surface rollers. The model predicted the peaks of longshore sediment transport observed near the shoreline and the wave breaking point for plunging breakers.

15. SUBJECT TERMS

Bedload sediment transport
Longshore currents
Longshore sediment transport
Near-shore current modeling
Near-shore hydrodynamics
Numerical model
Sediment transport
Suspended load sediment transport
Wave modeling